Effects of carbon nanomaterials on the performance of symmetric pseudocapacitors

by

Katlego Makgopa

Thesis submitted in fulfilment of the requirements for the degree of

Doctor of Philosophy (Chemistry)

In the Faculty of Natural and Agricultural Sciences

University of Pretoria

May 2016

Supervisor: Professor K. I. Ozoemena

Declaration

I, Katlego Makgopa, hereby declare that:

I understand what plagiarism is, and I am aware of the University of Pretoria's policy in this regard. The work contained in this thesis is my original work, and I did not refer to work of current or previous students, lecture notes, handbooks or any other study material without proper referencing. Where another research work is used, this has been adequately acknowledged and referenced. I have not allowed anyone to copy any part of my thesis. I have not previously in its entirety or part submitted this thesis at any university for a degree.

Signature of student:

Name of student:

Student number:

Date:

Dedication

To my beautiful & loving wife Mpho

And

My children, Gabriella (Hlogi) and Nathan (Itu).

"Who can find a virtuous wife? For her worth is far above rubies. The heart of her husband safely trusts her; So he will have no lack of gain." (Proverb 31:10).

"Behold, children are a heritage from the Lord, The fruit of the womb is a reward." (Psalms 173:3)

Acknowledgements

Firstly, I would like to express my sincere gratitude to my Lord and Almighty Saviour Jesus Christ by whose grace I had begun and completed this study (*Glory To His Name*).

I would also like to thank the following people for their support and assistance during this degree:

- My supervisor, mentor, and motivator, Prof. Kenneth I. Ozoemena, who has absorbed me into his research and gave me countless opportunities. Thank you for everything that you have helped me throughout this period of study. Indeed, it has been a privilege working in conjunction with one of the leading scientists in South Africa and across the Globe. It has been a long good journey indeed.
- Dr. Paul Madus Ejikeme, for his continual advice and support during his visit to University of Pretoria, South Africa.
- A colleague and friend Dr. Charl Jafta, for all the encouragement and academic insights.
- All my colleagues at University of Pretoria (Dr. A. Bello, Dr. D Momodu, Dr. J. Madito, Dr. D. Molefe, Mr. J. Lekitima and Ms. T. Masikhwa) and Energy Materials, CSIR (Dr. K. Raju and Ms. F. Nkosi), thank you for all your contributions and scientific discussions. Indeed you have been pillars of strength at times of need.
- My mother, Sinah, brothers Eddie & Thabo, sister Vinoliah, all my cousin (esp. Papiki) and my dear friend Selby Shubane. Thank you for everything.
- My in-laws, for such enormous support and interest in my work. Much gratitude.
- My wife Mpho Makgopa, for her great support, patience, and sacrifices during this period and throughout our life. You are a virtuous woman indeed.
- The NRF, for the Ph.D. scholarship.

Abstract

This thesis reports on the study of carbon nanomaterials integrated with nanostructured birnessite-type MnO_2 and tetragonal hausmannite-type Mn_3O_4 as electrode materials for enhanced performance in symmetric pseudocapacitors. This work further explores the synergistic effect of graphene oxide decorated with particles of nickel (II) tetraaminophthalocyanine as electrode materials for improved performance (power and energy densities) in symmetrical pseudocapacitor device. Physical properties of the synthesised electrode materials were investigated using scanning electron microscopy (SEM), transmission electron microscopy (TEM), energy dispersive X-ray spectroscopy (EDX), X-ray powder diffraction (XRD), X-ray photoelectron spectroscopy (XPS), gas adsorption technique (BET), infra-red spectroscopy, Raman spectroscopy and thermogravimetric analysis (TGA) techniques. Electrochemical properties of synthesised electrode materials were investigated using cyclic voltammetry (CV), galvanostatic charge-discharge (GCD) and electrochemical impedance spectroscopy (EIS). From the study of carbon nanomaterials integrated with nanostructured birnessite-type MnO_2, it has been discovered that OLC/MnO_2 nanohybrid exhibited better performance (regarding specific capacitance, rate capability, and energy density) compared to other nanohybrids such as CNT/MnO_2, GO/MnO_2, and AC/MnO_2. This device gave maximum specific capacitance of 255 F g^{-1}, the specific energy density of 5.6 Wh kg^{-1} and excellent power density of 74.8 kW kg^{-1}. The CNT/MnO_2, exhibited a maximum specific capacitance, energy and power density of 174 F g^{-1}, 4.9 Wh kg^{-1}, and 55.1 kW kg^{-1}, respectively, while, the GO/MnO_2 displayed 135 F g^{-1}, 3.9 Wh kg^{-1}, and 35.8 kW kg^{-1}, and AC/MnO_2 was 110 F g^{-1}, 3.3 Wh kg^{-1}, and 30.0 kW kg^{-1}, respectively. From the study of carbon nanomaterials integrated with nanostructured tetragonal hausmannite-type Mn_3O_4, OLC/Mn_3O_4 nanohybrid exhibited

better performance (regarding specific capacitance, rate capability, and energy density) compared to other nanohybrid electrode materials (i.e., CNT/Mn_3O_4 GO/Mn_3O_4, and AC/Mn_3O_4). This device exhibited a maximum specific capacitance of 195 F g^{-1}, the specific energy density of 4.3 Wh kg^{-1} and power density of 52 kW kg^{-1}. The CNT/Mn_3O_4 exhibited a maximum specific capacitance, energy and power density of was 180 F g^{-1}, 3.9 Wh kg^{-1}, and 33 kW kg^{-1}, respectively. While the GO/Mn_3O_4 displayed values of 160 F g^{-1}, 3.6 Wh kg^{-1}, 24 kW kg^{-1} and AC/Mn_3O_4 was 124 F g^{-1}, 2.8 Wh kg^{-1}, 18 kW kg^{-1}, respectively. The study on the synergistic effect of graphene oxide (GO) decorated with particles of nickel (II) tetraaminophthalocyanine (NiTAPc) resulted in GO/NiTAPc nanohybrid displaying better pseudocapacitive performance relative to its precursor (i.e., GO and NiTAPc). This pseudocapacitor device exhibited a maximum specific capacitance of 163 F g^{-1}, the specific energy density of 3.6 Wh kg^{-1} and high-power density of 140 kW kg^{-1}. These values are much higher than those of its individual precursors NiTAPc (60 F g^{-1} and 1.3 Wh kg^{-1}) and GO (15 F g^{-1} and 0.3 Wh kg^{-1}). This excellent capacitive performance shows promising opportunities for the development of aqueous-based pseudocapacitors made of carbon nanomaterials with transitional metal oxides and metallophthalocyanine (MPc) complexes (N4-macrocyclic metal compounds). Interestingly, this study also shows the significance of the use of novel carbon nanomaterials apart from the well-studied activated carbon for the development of high-power electrochemical capacitors.

Table of Content

List of Abbreviations and Symbols

AC	Activated carbon
BTU	British Thermal Units
CB	Carbon Black
CV	Cyclic Voltammetry
CNT	Carbon Nanotubes
ECs	Electrochemical Capacitors
EDLC	Electrical Double Layer Capacitor
EDX	Energy dispersive X-ray spectroscopy
ESD	Energy storage devices
ESR	Equivalent series resistance
EIS	Electrochemical Impedance Spectroscopy
FESEM	Field Emission Scanning Electron Microscopy
FTIR	Fourier Transform Infra-Red
GCD	Galvanostatic Charge Discharge
GO	Graphene Oxide
HEV	Hybrid Electric Vehicle
IEA	International Energy Agency
IEO2013	International Energy Outlook 2013
IHP	Inner Helmholtz plane
LIBs	Lithium Ion Batteries
MTAPc	Metallotetraaminophthalocyanine
MWCNT	Multi-Walled Carbon Nanotubes
MnO_2	Manganese Dioxide
NEC	Nippon Electric company
NiTAPc	Nickel (II) Tetraaminophthalocyanine

NMP	N-Methyl-2-Pyrolidone
OHP	Outer Helmholtz plane
OLC	Onion-Like Carbon
PVDF	Polyvinylidene Fluoride
P-XRD	Powder X-ray diffraction
Redox	Reduction-Oxidation
SEM	Scanning Electron Microscopy
SOHIO	Standard Oil of Ohio
SWCNT	Single-Walled Carbon Nanotubes
T	Temperature
TGA	Thermo-Gravimetry Analysis
UV-Vis	Ultraviolet-visible
XPS	X-ray Photoelectron Spectroscopy
XRD	X-ray Diffraction
A	Ampere
Ag/AgCl	Silver/Silver Chloride
φ	Phase shift
°C	Degree Celsius
C	Charge or Discharge Rate
C_{ox}	Concentration of the Oxidized Species
C_{red}	Concentration of the Oxidized Species
C_{sp}	Specific Capacitance
E	Energy Density
E_0	Standard Potential
E_-^0	Negative Electrode Potential
E_+^0	Positive Electrode Potential
E_{cell}^0	Standard Cell Potential

E_{cell}	Cell Potential
F	Faraday Constant
i	Current
m	Mass
M	Molar Mass
n	Number of Electrons
P	Power Density
R	Gas Constant
U_0	Cell Potential
V	Volt
V_{oc}	Open Circuit Potential
ΔE_0	Difference in the Electrode Potentials
ΔG_0	Gibbs Free Energy
ε_0	Dielectric Constant
ε_r	Electrolyte Dielectric Constant

List of Tables

List of Figures

CHAPTER 1: INTRODUCTION

1.1 Global Interest in Renewable Energy

Today's society is highly dependent on hydrocarbons as the primary source of energy due to their low cost as well as high specific energy and power per weight or per volume. Nevertheless, there exists a change in energy paradigm due to the growth in civilization as well as more countries in the developing world seeking an improved standard of living, hence, generating high energy demand. Therefore, the development of technology that is compatible with the resources provided by nature is essential to have sustainable development. According to the International Energy Outlook 2013 (IEO2013) [1], Global energy use will continue to rise rapidly with total world consumption jumping from 524 quadrillion British thermal units (BTUs) in 2010 to an estimated 820 quadrillion in 2040. A net increase of 56% (BTU represents the amount of energy needed to heat one pound of water by one degree Fahrenheit). As a result, every country across the globe put a lot of effort in innovation towards sustainable and renewable energy. The term "renewable energy" is defined in several ways, but generally, it refers to those energy resources and technologies whose common characteristic is that they are non-depletable or naturally replenishable [2]. The definition of renewable energy according to the International Energy Agency is as follows: *"The energy derived from natural processes that replenish constantly. In its various forms, it derives directly or indirectly from the sun, or from heat generated within the earth. Also defined as the energy generated from solar, wind, biomass, geothermal, hydropower and ocean resources*" [3]. Fig. 1.1 indicates some of the examples of the modernized technologies in renewable energy applications. Out of these distinguished types of renewable energies, wind and solar (PVs) are the most feasible and can be scaled accordingly, in almost any part of the world, to provide power. The challenge with these technologies is their inability to store the as-produced energy, thus placing

ECs and other electrochemical energy storage devices (i.e., Batteries) of national and strategic significance in a highly competitive international market.

Figure 1.1: Illustration of the electric grid modernization and windmill technology as an example of renewable energy applications [4].

Although petroleum and other liquids remain the largest source of energy, the liquid fuels share of world marketed energy consumption falls from 34 percent in 2010 to 28 percent in 2040. Therefore, fossil fuels are expected to continue supplying much of the energy worldwide. Unfortunately, this type of energy supply provides hostility to the environment. Thus, renewable energy and nuclear power have been observed to be the world's fastest-growing energy sources, each increasing by 2.5 percent per year; even though fossil fuels continue to supply almost 80 percent of the global energy use through 2040, (see fig. 1.2).

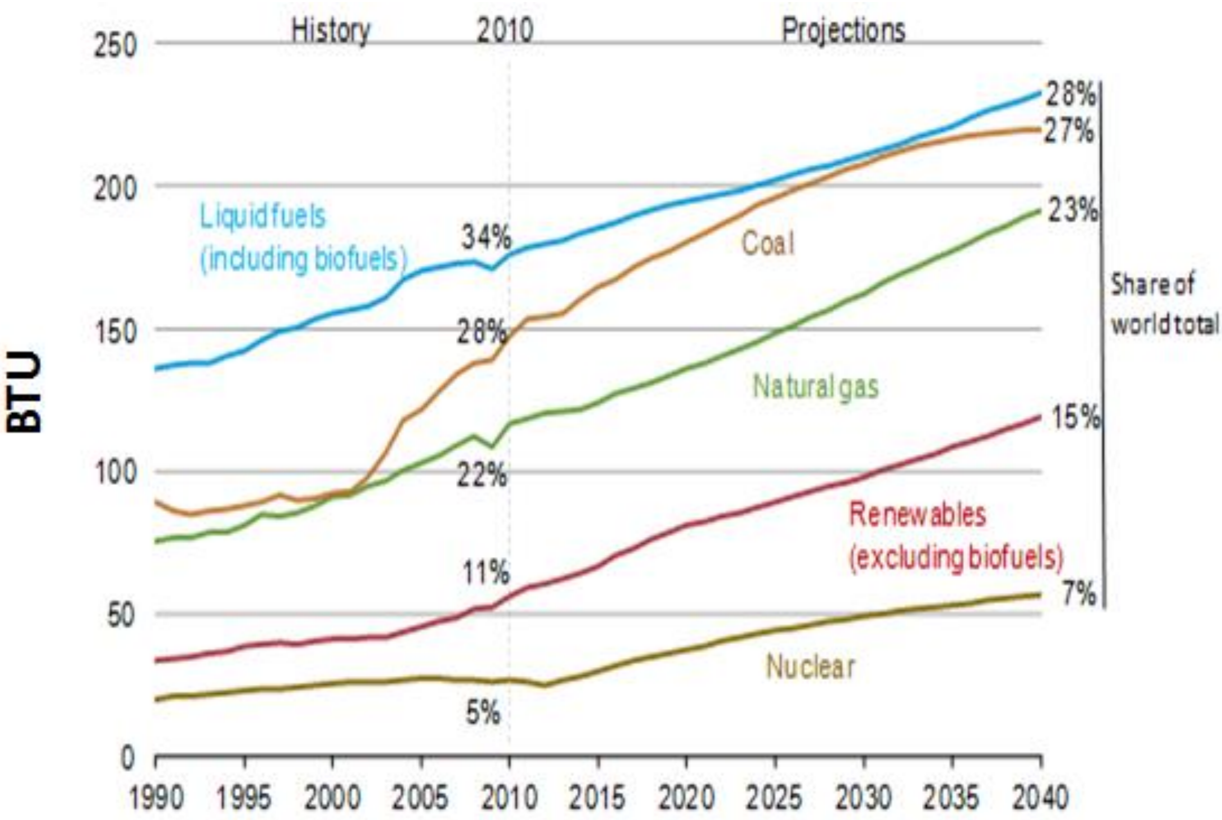

Figure 1.2: Projections indicating increased world consumption of energy from all fuel sources through 2040 [1].

It is indeed a fact that from the discovery and exploitation of fossil fuels, and the result of profound scientific and technological innovations, life has been exceedingly comfortable over the past two centuries regarding energy reliability. But we cannot shy away from the fact that we are on course to consume these non-renewable energy sources within several hundreds of years and also avoid the unknown medium-to-long term implications of burning carbonaceous fuels and CO_2 emissions that continue being harmful to the environment. Hence, it is evident that scientific and technological interference are necessary with renewable energy resources at the forefront. Thus, creating a major demand for alternative energy storage mechanism that will be coupled together with the renewables [5].

1.2 Energy Storage Systems (ESS)

As much as the renewable energy shows to be the escalating solution towards the uprising cruelty to the environment, a key stumbling block in renewables is the technical difficulties of electricity storage and transmission. Grid energy storage is a critical component of the integration of renewable technologies and ensuring reliable distribution of electricity [6]. But the August 2003 blackout in the Northeast, the September 2011 power failure that extended from Southern California to Mexico and Arizona and 2008-2015 loads shedding by ESKOM electricity grid in South Africa are more widely publicized examples in which power outages affected and still continue to affect many millions of consumers across the globe. From a broader perspective, such power outage events underscore the complex set of issues associated with the generation and use of electricity as well as the use of Grid to store energy [7]. Indeed, EES can be seen as an established, valuable approach for improving the reliability and overall use of the entire power system (see fig. 1.3). EES technology is attractive for providing many grid services, and also, it can deliver services to solve more localized power quality issues and reactive power support [8]. It is evident that the synergy between the energy storage systems and renewable energy resources will be a major contributor to resolving the current energy crisis.

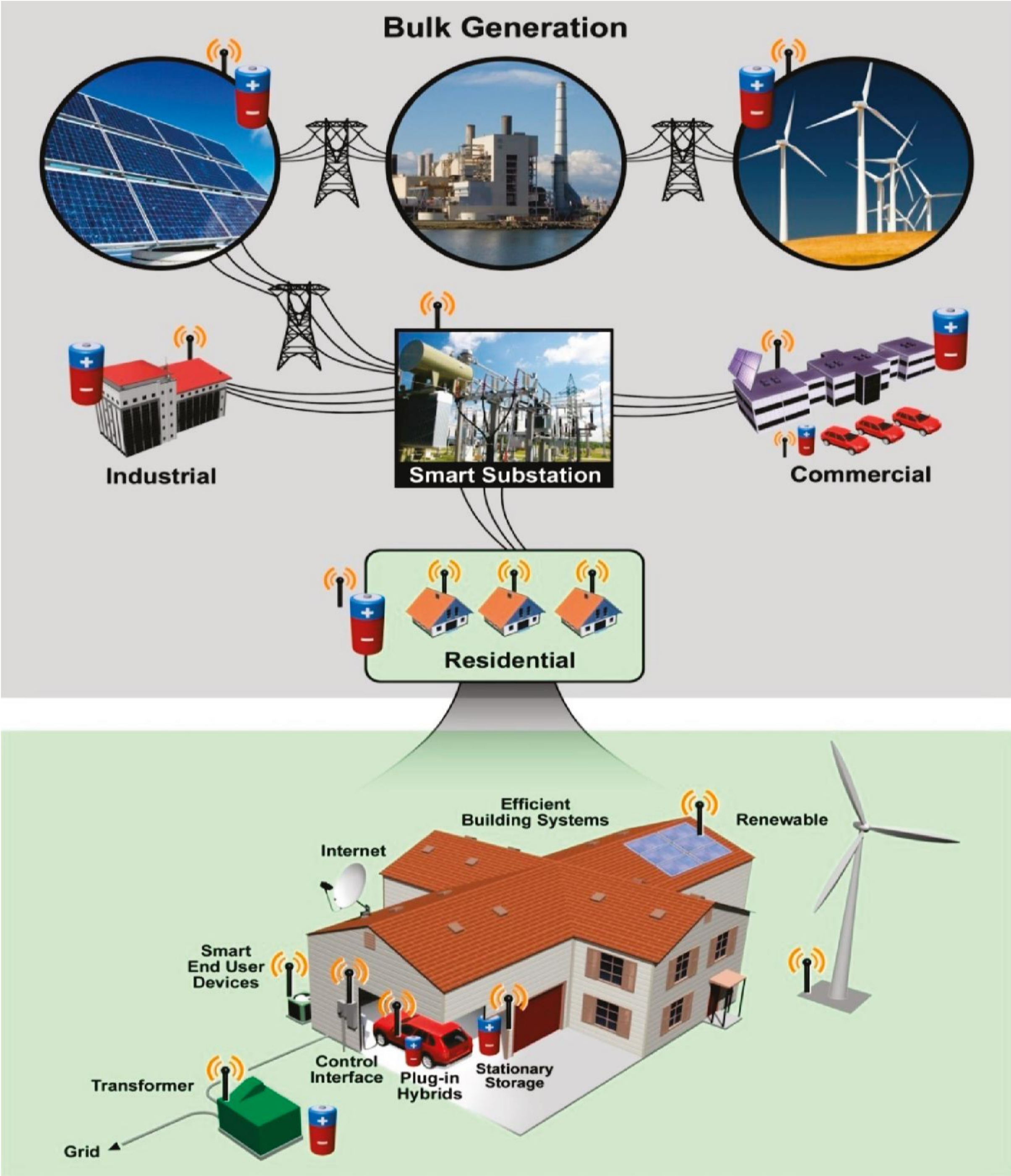

Figure 1.3: Schematic representation of applications of electricity storage for a generation, transmission, distribution, and end customers and future smart grid that integrates with intermittent renewables and plug-in hybrid vehicles through two-way digital communications between loads and production or distribution networks [8].

1.3 Electrochemical Energy Storage Systems (EESs)

The implementation of renewable energy sources, such as solar or wind power, causes paramount challenges to power grid management and stability due to their significant fluctuations in electricity generation due to high energy demand. A shift towards the establishment of various technologies is being developed to complement the existing ones to achieve this task, ranging from mechanical, physical, thermal, chemical, and electrochemical energy storage systems. In considering a reliable, stable, and sustainable large-scale use of renewables, electrochemical capacitors (ECs) and batteries play a fundamental role in advanced and highly efficient energy storage and management [9]. Thus, EES in the form of electrochemical capacitors (ECs) and batteries can be used not only as a backup energy supply but also as the power source for smaller devices such as laptops, cell phones and in medical implants. They are also used as pacemakers, defibrillators, and also in transportation such as electric vehicles, defence, or aerospace applications (see fig. 1.4) [10]. Batteries and ECs are now a commodity of national and strategic significance in a highly competitive international arena [11].

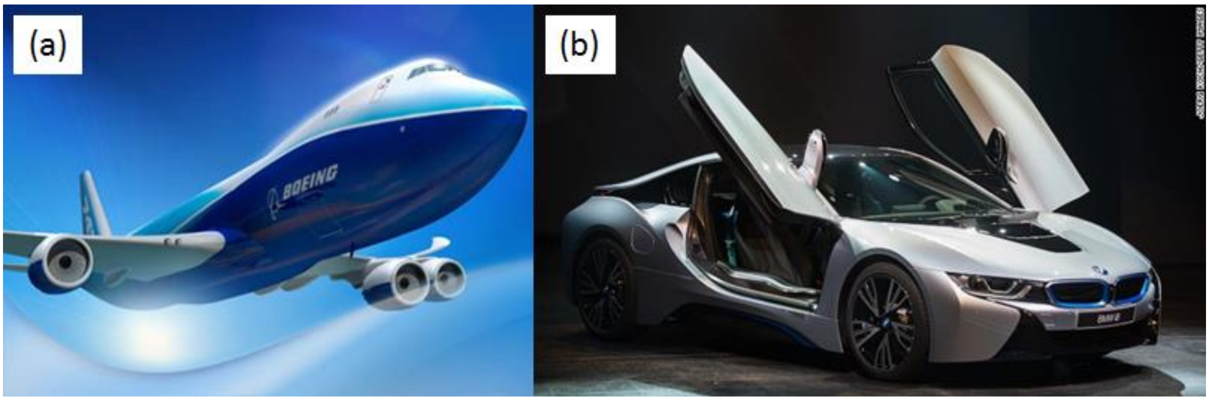

Figure 1.4: Illustration of some of the recent applications of ECs in (a) aerospace and (b) transportation [12], [13].

Electrochemical energy storage systems characterize an opportunity for fundamental and applied researchers to overcome collectively challenging scientific and technological barriers that directly address a critical societal and environmental necessity. In particular, development of high energy and power density ECs and batteries that are safe to operate in an environmental premise could make a global electrified transportation industry a reality. ECs can be used together with LIBs for their high power attribute to compliment LIBs that possesses relatively high energy density, or they can be utilized independently as new research demonstrates that these energy storage systems have good energy density. Therefore, research and development in the field of ECs are focused on increasing the energy density of these energy storage systems as well as their stability [5], [14], [15].

1.4 The Objectives / Scope of this Study

Their high power densities characterise ECs with moderate to low energy densities, and widely used in most of today's portable electronics and electric vehicles (EVs). But unfortunately, regardless of their commercial success, ECs still fall short of satisfying high energy needs for applications such as power tools and efficient utilisation of renewable energies such as solar and wind power. The performance of ECs is intimately dependent on the properties of their electrode materials; as such it is not surprising that greater attention is devoted to research and development of electrode materials [16]. There is a need to improve substantially their performance such as cycle stability, safety, high energy density and cost to meet the requirements of future systems. Breakthroughs in the development of new materials hold the key to new generations of ECs as against the *status quo*. Such materials will lead to the development of ECs that can meet the current needs (i.e., safety, affordability, with high energy and stability for use in mobile electronic devices and large scale devices). The demand for high power capabilities (especially for more major system applications), full capacity retention, high charging rate, lowering of cost, safety issues and ensuring a constant supply of power can be achieved. One of the main parameters playing a role in the development of ECs is the surface area of the electrodes, pore volume, and pore distribution which makes nanosizing of electrode material an important part of this research. Nanoscale design of the structure and chemistry of electrode materials may enable researchers/scientist to develop a new generation of devices that approach the theoretical limit for electrochemical storage and deliver electrical energy rapidly and efficiently [17]. Nanomaterials of about the length scale of less than 100 nm, have received increasing interest owing to their fundamental scientific significance as well as their potential applications that derive from their fascinating electrical, magnetic, and catalytic properties [18]. The manganese oxide based (MnO) materials (e.g., MnO_2 and Mn_3O_4) and carbon nanomaterials (e.g., carbon nanotubes (CNTs), onion-like carbons (OLCs) and graphene) are well recognised for their environmental friendliness and are safer compared to other materials such as RuO_2. Therefore, the use of such nanomaterials in ECs is a very attractive quest for research due to availability in nature [19]–[21]. Since the development of high-performance ECs is at the forefront of energy research globally, it has been shown that the capacitance and lifetime of electrodes are controlled by the (i) synthesis method, (ii) the size and type of the electrode material, and (iii) the nature of the electrolyte involved. Thus, the primary objectives of this thesis are as follows:

I. To synthesise single phase birnessite-type MnO_2 on to various carbon allotropes (i.e., OLC, CNT, GO, and AC) and forming carbon/MnO_2 nanohybrids using simple chemistry technique of reflux.

II. To synthesise tetragonal Hausmannite Mn_3O_4 by high-temperature annealing of multiphase electrolytic manganese dioxide (EMD) and decoration of synthesised tetragonal Hausmannite Mn_3O_4 material on to various carbon allotropes (i.e., OLC, CNT, GO, and AC) to make carbon/Mn_3O_4 nanohybrids.

III. To explore the synergistic effect of graphene oxide (GO) decorated with particles of nickel (II) tetraaminophthalocyanine (NiTAPc) (i.e., GO/NiTAPc) as electrode materials.

IV. To investigate the morphology of the synthesised nanohybrid materials with techniques such as field-emission scanning electron microscopy (FESEM), transmission electron microscopy (TEM).

V. To study the texture and elemental composition of the materials with Raman spectroscopy, energy dispersive X-ray (EDX), X-ray diffraction (XRD), X-ray photoelectron spectroscopy (XPS), Fourier transform infrared spectroscopy (FTIR), Brauer-Emmett-Teller (BET) and thermogravimetric analysis (TGA).

VI. Investigation of the pseudocapacitive performance of carbon nanomaterials decorated with metal oxides or metallophthalocynines by understanding the principle of its charge storage mechanism and the bonding properties of the carbon nanomaterials and each of the metal oxide or metallophthalocynines materials using cyclic voltammetry (CV), galvanostatic charge-discharge (GCD) and electrochemical impedance spectroscopy (EIS).

1.5 Outline of the Dissertation

This dissertation is divided into seven chapters with **Chapter 1** discussing the increasing demand for energy and the hostile implications of the use of the current power source. This chapter also touches on renewable energy and how it affects society today and in the future. In this section, electrochemical energy storage, and its dynamic growth is put into perspective. **Chapter 2** is a literature review that gives a broad background in electrochemistry and the core principles of ECs with the three different types of ECs discussed in a detailed form. Different electrode materials are reviewed in a more comprehensive way in this chapter. Brief overviews of the techniques used for microscopic, spectroscopic and electrochemical analysis are presented. In **Chapter 3**, the experimental techniques and methods are presented. This chapter also discusses a synthetic procedure of various Mn_xO_y-based nanohybrid materials and GO-NiTAPc composite. The fabrications of electrochemical cells with electrode materials are presented. **Chapter 4-6** reports on the results obtained in the study. **Chapter 7** gives concluding remarks showing the significance of this study and also paves the way forward with some recommendations and possible future work.

References

[1] IEA, "With Projections to 2040," *International Energy Outlook 2014:*, 2014. [Online]. Available: www. eia. gov/ieo/. [Accessed: 10-Dec-2014].

[2] H. Bang, A. E. Ellinger, J. Hadjimarcou, and P. A. Traichal, "Consumer concern, knowledge, belief, and attitude toward renewable energy: an application of the reasoned action theory," *Psychol. Mark.*, vol. 17, no. 6, pp. 449–468, 2000.

[3] UNEP, "Green Economy and Trade – Trends, Challenges and Opportunities," *United Nations Environment Programme*, 2013. .

[4] "Ionova Technologies." [Online]. Available: http://www.ionova.com/img/home slideshow images/iStock_000016895670_MediumLargeRenewables.jpg. [Accessed: 09-Feb-2015].

[5] M. M. Thackeray, C. Wolverton, and E. D. Isaacs, "Electrical energy storage for transportation—approaching the limits of, and going beyond, lithium-ion batteries," *Energy Environ. Sci.*, vol. 5, p. 7854, 2012.

[6] K. B. Hatzell, M. Boota, E. C. Kumbur, and Y. Gogotsi, "Flowable Conducting Particle Networks in Redox-Active Electrolytes for Grid Energy Storage," *J. Electrochem. Soc.*, vol. 162, no. 5, pp. A5007–A5012, 2015.

[7] B. Dunn, H. Kamath, and J.-M. Tarascon, "Electrical Energy Storage for the Grid: A Battery of Choices," *Science (80-.).*, vol. 334, no. Li, pp. 928–935, 2011.

[8] Z. Yang, J. Zhang, M. C. W. Kintner-meyer, X. Lu, D. Choi, and J. P. Lemmon, "Electrochemical energy storage for green grid.pdf," *Chem. Rev.*, vol. 111, pp. 3577–3613, 2011.

[9] F. Béguin, V. Presser, A. Balducci, and E. Frackowiak, "Carbons and electrolytes for advanced supercapacitors.," *Adv. Mater.*, vol. 26, no. 14, pp. 2219–51, 2283, Apr. 2014.

[10] A. Burke and H. Zhao, "Review of the Present and Future Applications of Supercapacitors in Electric and Hybrid Vehicles Review of the Present and Future Applications of Supercapacitors in Electric and Hybrid Vehicles," *Inst. Transp. Stud.*, no. December, 2014.

[11] "Capacitors and SuperCapacitors," *Electropaedia*. [Online]. Available: http://www.mpoweruk.com/supercaps.htm. [Accessed: 16-Feb-2015].

[12] P. Harrop, "Supercapacitors to the rescue." [Online]. Available: http://www.energyharvestingjournal.com/articles/5106/supercapacitors-to-the-rescue. [Accessed: 16-Feb-2015].

[13] "Super-fast and green? How the new breed of sports cars is getting a makeover." [Online]. Available: http://www.cnn.com/2014/10/27/world/europe/porsche-spyder-918-luxury-hybrid/. [Accessed: 16-Feb-2015].

[14] P. Simon and Y. Gogotsi, "Materials for electrochemical capacitors.," *Nat. Mater.*, vol. 7, no. 11, pp. 845–54, Nov. 2008.

[15] Q. Li, X.-F. Lu, H. Xu, Y.-X. Tong, and G.-R. Li, "Carbon/MnO(2) double-walled nanotube arrays with fast ion and electron transmission for high-performance supercapacitors.," *ACS Appl. Mater. Interfaces*, vol. 6, no. 4, pp. 2726–33, Feb. 2014.

[16] G. Wang, L. Zhang, and J. Zhang, "A review of electrode materials for electrochemical supercapacitors.," *Chem. Soc. Rev.*, vol. 41, no. 2, pp. 797–828, Jan. 2012.

[17] Y. Gogotsi, "What nano can do for energy storage," *ACS Nano*, vol. 8, no. 1, pp. 5369–5371, 2014.

[18] C. Burda, X. Chen, R. Narayanan, and M. A. El-sayed, "Chemistry and Properties of Nanocrystals of Different Shapes," *Chem. Rev.*, vol. 105, no. 4, pp. 1025– 1102, 2005.

[19] F. Béguin and E. Frackowiak, *Supercapacitors: Materials, Systems and Applications*. John Wiley & Sons, Weinheim, 2013.

[20] T. K. Gupta, B. P. Singh, V. N. Singh, S. Teotia, A. P. Singh, I. Elizabeth, S. R. Dhakate, S. K. Dhawan, and R. B. Mathur, "MnO2 decorated graphene nanoribbons with superior permittivity and excellent microwave shielding properties," *J. Mater. Chem. A*, vol. 2, no. 12, p. 4256, 2014.

[21] D. P. Dubal, D. S. Dhawale, R. R. Salunkhe, V. J. Fulari, and C. D. Lokhande, "Chemical synthesis and characterization of Mn3O4 thin films for supercapacitor application," *J. Alloys Compd.*, vol. 497, no. 1–2, pp. 166–170, 2010.

CHAPTER 2: LITERATURE STUDIES / BACKGROUND

2.1 Electrochemical Capacitors (ECs): An Overview

The understanding of ECs requires brief background knowledge on electrochemistry, even though this chapter will not dive deep into the overall concept of electrochemistry but focus on the sections that directly describe the ECs. Electrochemistry is a branch of chemistry that examines chemical effects that involve the transfer of electrons to and from any substance (i.e., molecules or ions, etc.). These mentioned reactions are known as redox (**red**uction-**ox**idation) reactions. There are two processes in electrochemistry; (i) Electrolytic processes, and (ii) Galvanic or Voltaic processes. In the first process, chemical reactions occur by the passage of an electric current, while the chemical reactions result in the production of electrical energy (e.g. ECs and Batteries) in the second process [1]–[3]. Capacitors, one of the examples of the energy storage devices, can be classified into three categories namely: electrostatic capacitors, electrolytic capacitors and electrochemical capacitors [4]. Electrochemical capacitors (ECs) also known as ultracapacitors or supercapacitors are energy storage devices that are currently investigated in various academic and industrial laboratories because they can be used as complementary charge storage devices to conventional batteries in different applications that require peak power pulses [5], [6]. With a fast-growing market for portable electronic devices and the development of hybrid electric vehicles, there has been an ever-increasing demand for high energy and power densities storage devices [7]. ECs emerge as promising energy storage device since it serves as a gap between conventional capacitors and batteries. Batteries store energy chemically (bulk phenomenon) while ECs store energy physically through dielectric polarization or electronic double layer of ions and electron (surface phenomenon). Batteries are known to store relatively large amounts of energy as compared with ECs but have relatively slow power delivery or uptake, short cycle life, and thermal management issues. On the contrary, ECs are power devices that can be fully charged or discharged in seconds resulting in a much higher power delivery or uptake in shorter times; consequently resulting in their energy densities being lower than that of batteries [4]. Figure 2.1 is the Ragone plot which shows the various comparisons within the energy systems.

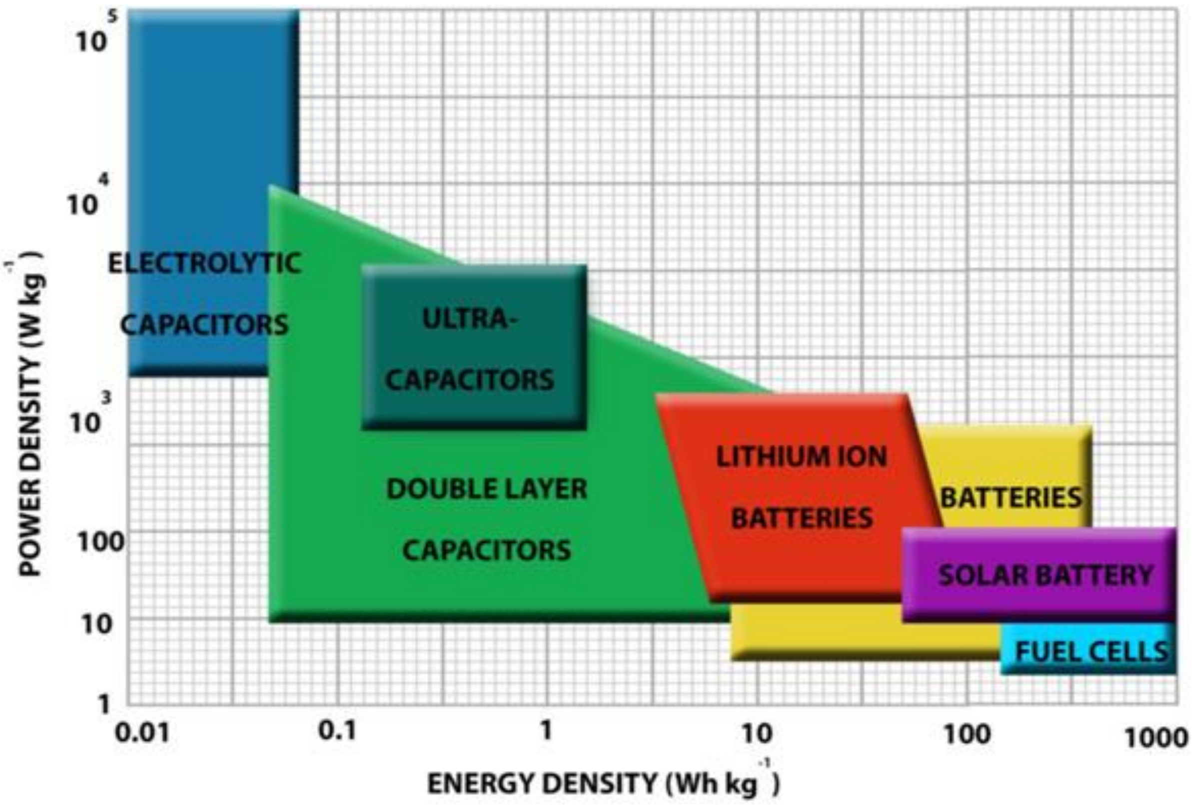

Figure 2.1: Ragone Plot is depicting energy vs. power densities of standard power devices including ECs [8].

From the Ragone plot, it can be seen that batteries usually exhibit higher energy densities as compared to ECs while suffering from low power densities. There are two types of fundamental storage mechanisms involved in ECs, viz: (a) ‘‘electrochemical double layer capacitor’’ (EDLC) and (b) ‘‘pseudocapacitors’’. The operation mechanism of the former involves the non-Faradaic separation of charges at the ‘‘double-layer’’ (i.e., electrode/electrolyte interface) while the latter involves fast Faradaic, redox reaction of electroactive materials at the interface [9]. EDLCs are obtained from carbon materials such as activated carbons, graphene, onion-like carbons and carbon nanotubes while pseudocapacitors are from redox-active materials such as polymeric complexes and metal oxides. Hybrid materials incorporating EDLC and pseudocapacitor materials are thought to give the next generation high-performance supercapacitor devices [6], [10]. Most packaged ECs devices are two-terminal systems and can be either symmetric or asymmetric depending on the arrangement of the electrodes. The former involves two similar electrodes (i.e., material type, thickness, mass, etc.) sandwich together whereas the latter is made of two electrodes with a variation of electrode materials. In most cases, carbon materials such as activated carbon are used as the anode while polymeric complexes and metal oxides or the composites as cathodes. Under these conditions, of course, an overall evaluation of the *two-electrode* system (without the utilization of a reference electrode) is obtained giving vital electrochemical information such as energy densities and power densities that are not easily obtainable using data collected at individual electrodes in *three-electrode* cells (reference electrode included). Nevertheless, many researchers still opt for the *three-electrode* system since its measurements allow one to have fundamental informative on the behavior of electrode of an ECs device [4].

UNIVERSITEIT VAN PRETORIA
UNIVERSITY OF PRETORIA
YUNIBESITHI YA PRETORIA

2.2 Historical Background of Electrochemical Capacitors (ECs)

The concept of the double-layer capacitance dates back to a German physicist, Hermann von Helmholtz, in 1853 [4]. In 1957, a scientist by the name of Howard I. Becker at General Electric Company first patented ECs based on the double- layer capacitance structure (Fig. 2.2a). This capacitor consisted of porous carbon electrodes using the double-layer capacitance mechanism for charging [11]. In 1966, Robert A. Rightmire, a chemist working at the Standard Oil Company, Cleveland, Ohio (SOHIO) patented a device that stored energy in the double layer interface (Fig. 2.2b) [12]. At this time, SOHIO acknowledged that "the 'double-layer' at the interface behaves like a capacitor of relatively high specific capacity." SOHIO went on to patent a disc-shaped capacitor in 1970 utilizing a carbon paste soaked in an electrolyte under Donald L. Boos as an inventor [13]. The trade name of the first commercial ECs device made by Nippon Electric Company (NEC) of Japan under the licensed technology from SOHIO was called "supercapacitor" and the first ECs products were introduced to the marketplace as memory backup devices in computers, in 1978. Many other product models were introduced in the 1980s to meet new application requirements with several patents being filed up. In 1982 sales of ECs products with different optimisations (i.e. new model series) began. As early as January 1982, Pinnacle Research Institute (PRI) were already involved in capacitor technology incorporated metal-oxide electrodes and was designed for military applications such as laser weaponry and missile guidance systems and they called them "ultracapacitor" [14]. Nevertheless, whatever the trade name of ECs are known as, they all refer to a capacitor, which stores electrical energy in the interface between an electrolyte and a solid electrode [15]. There are several large companies such as NessCap, CAP-XX, Nippon Chemi-Con (NCC), Maxwell, etc. that contributed to the developmental growth of the ECs. In the mid-1980s, Panasonic manufactured button-cell capacitors in several different sizes. These became very popular for solar-powered wrist watches [16]. Early electrochemical capacitors (ECs) were rated at a few volts and had capacitance values measured from fractions of farads up to several farads. Today's trend is for cells with the size ranging from small millifarad-size devices with exceptional pulse power performance up to devices rated at several kilo farads. The technology is experiencing increasingly broader use especially originating from the "humble" beginning, both replacing batteries in some cases and in others complementing their performance [17].

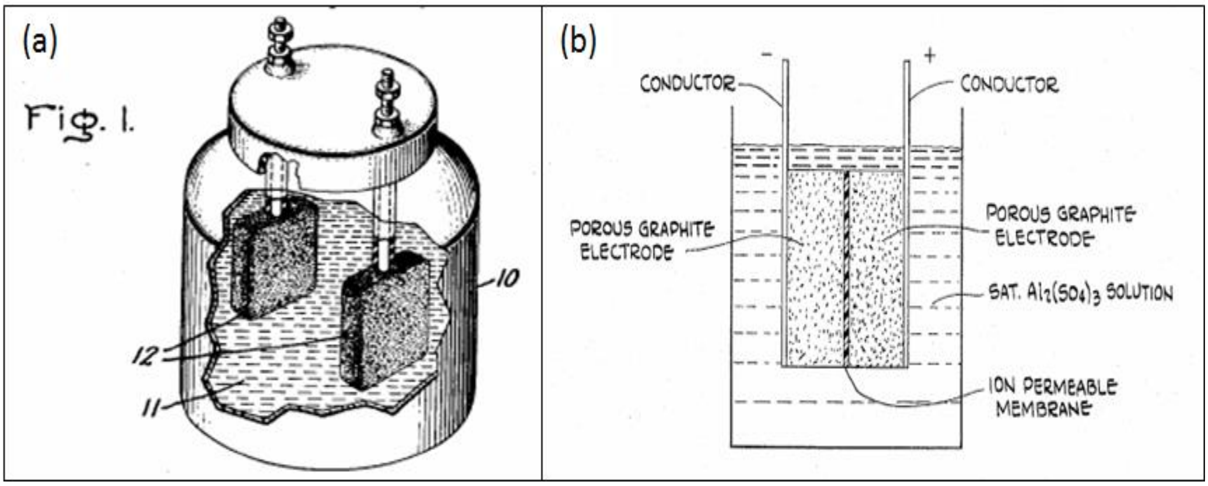

Figure 2.2: An illustration of (a) the capacitor patented by General Electric in 1957 [11] and (b) an electrolytic energy storage device patented by SOHIO in 1966 [12].

2.3 Basic Principles of Electrochemical Capacitors (ECs)

Electrochemical capacitors (ECs) developed as energy storage devices upon the understanding of their physical processes that take place at the electrode/electrolyte interface. ECs operate using the same principle as the conventional capacitors. Capacitors are divided into three types, (1) Electrostatic capacitors, (2) Electrolytic capacitors and (3) Electrochemical capacitors (which is the topic of this section) [15]. Electrostatic capacitors mostly referred to as conventional capacitors are energy storage devices made of two metal plates separated by a dielectric that is a non-conducting material (i.e. air or ceramic) as illustrated in Figure 2.3a. Electrolytic capacitors are structurally similar to electrostatic capacitors except that they possess a conductive electrolyte that is in direct contact with the electrodes (see Fig. 2.3b). A thin oxide layer formed on the two plates serve as the dielectric, which is typically Al_2O_3 on Al plates and this result in an increased capacitance per unit volume as compared to the electrostatic capacitors [4].

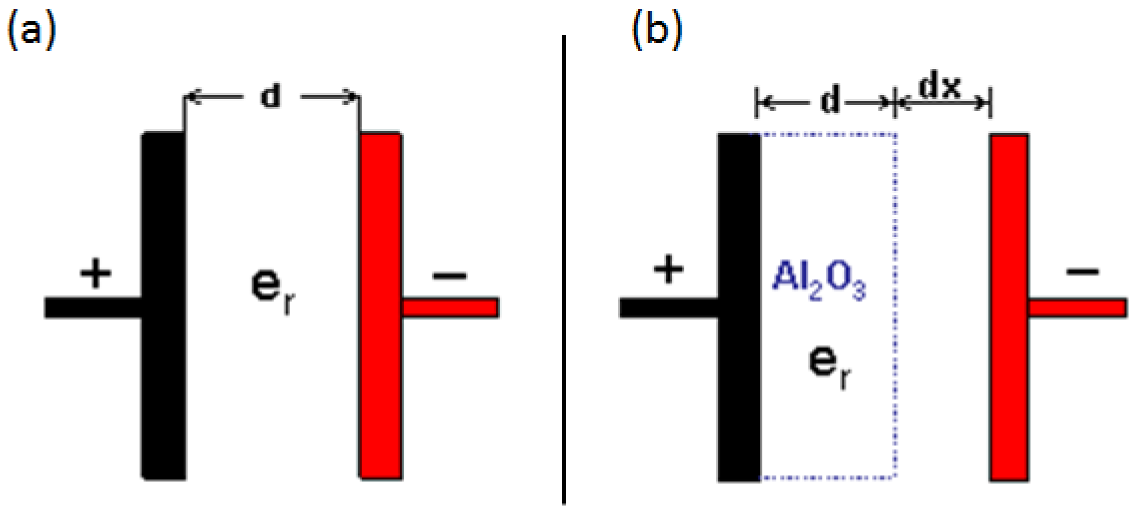

Figure 2.3: Diagrams of (a) a typical electrostatic capacitor and (b) a conventional electrolytic capacitor.

There is a potential difference (ΔV) that exists between these two plates that carry equal magnitude charge with opposite sign. The amount of charge stored on the plates measured in Coulombs (Q) is directly proportional to the potential difference between the conducting plates. Therefore, the capacitance of the capacitor, defined as the ability of a capacitor to store electrical charge, measured in Farads (F), can be calculated using the equation 2.1:

$$C = \frac{Q}{\Delta V} \tag{2.1}$$

The capacitance resulted from the charge stored on the plates is thus also proportional to the surface area (A) of the plates and inversely proportional to the distance between the plates (d). The vacuum dielectric constant (ε_0) adjust the proportionality. These relationships can be described as:

$$C = \frac{\varepsilon_0 A}{d} \quad 2.2$$

ECs are divided into three different groups; (i) electrochemical double layer capacitors (EDLC), (ii) pseudocapacitors and (iii) Hybrid capacitors. The EDLC store energy using ion adsorption, while the pseudocapacitors store energy using the fast surface redox reactions mechanism. Hybrid capacitors take into account the combined storage mechanism of the EDLCs and the pseudocapacitors [18]–[20]. The ECs can further be constructed in either symmetric or asymmetric configuration depending upon the cell packaging (see section 2.1). Figure 2.4 illustrate an example of the EDLC-type of the ECs.

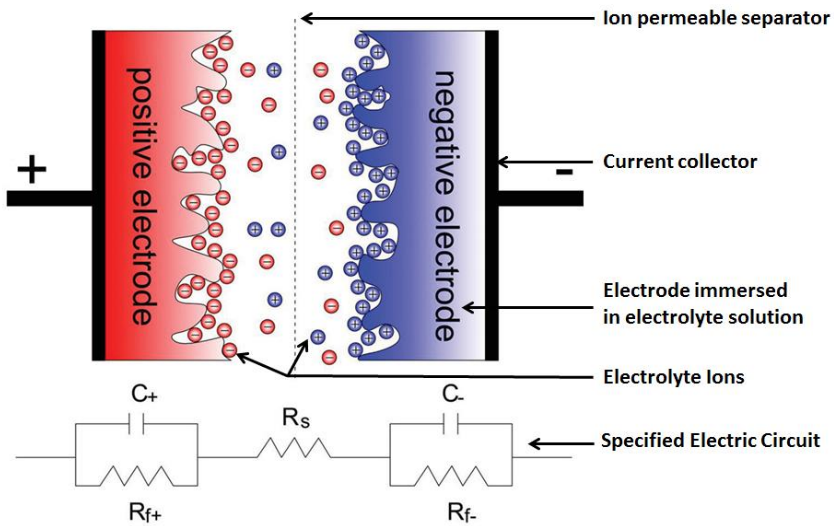

Figure 2.4: A typical design of the electrochemical double layer capacitor (EDLC) [21].

In such a device, each electrode–electrolyte interface represents a capacitor so that the complete cell can be considered as two capacitors in series (see Fig. 2.4). The electrostatic charge existing on each electrode–electrolyte interface allows reversible ion adsorption from the electrolyte onto the electrode active material that is electrochemically stable. The capacitance of two separated arrays of charges increases inversely with their separation distance. Hence, a large capacitance value would arise in the case of point charge ions close to the electrode surface. Charge separation occurs on polarization at the electrode-electrolyte interface producing the double layer capacitance defined by the following equation:

$$C = \frac{\varepsilon_r \varepsilon_0 A}{d} \qquad 2.3$$

where ε_r is the electrolyte dielectric constant, (ε_0) vacuum dielectric constant, d is the charge separation distance (the effective thickness of the double layer) and A the surface area of the electrode [22], [23].

2.3.1 Energy Storage in Electrical Double Layer Capacitors (EDLCs)

The construction of ECs is similar to that of batteries in the sense that they consist of two electrodes immersed in an electrolyte, with an ion permeable separator located between the electrodes (see Fig. 2.4) [24]. ECs based on electrochemical double layer capacitance (EDLC) are electrical energy storage devices that store and release energy by nanoscopic charge separation at the electrochemical interface between an electrode and an electrolyte. The electrostatic charge storing allows reversible ion adsorption from the electrolyte onto active material that is electrochemically stable and has a high surface area [25], [26]. Typically, the electrodes used for EDLC's are carbon materials [9], [21]. Charge separation occurs upon polarization at the electrode-electrolyte interface producing the double layer capacitance. This energy storage mechanism was first defined by Helmholtz in 1879 as shown in Fig. 2.5a. Gouy and Chapman later modified the Helmholtz model upon the extensive consideration of a continuous distribution of cations and anions in the electrolyte solution which is driven by thermal motion referred to as the diffuse layer (see Fig. 2.5b). Later, Stern combined the Helmholtz model with the Gouy–Chapman model that showed two regions of ion distribution: the inner region called the compact layer or Stern layer and the outer region called the diffuse layer (see Fig. 2.5c) [20], [21], [26].

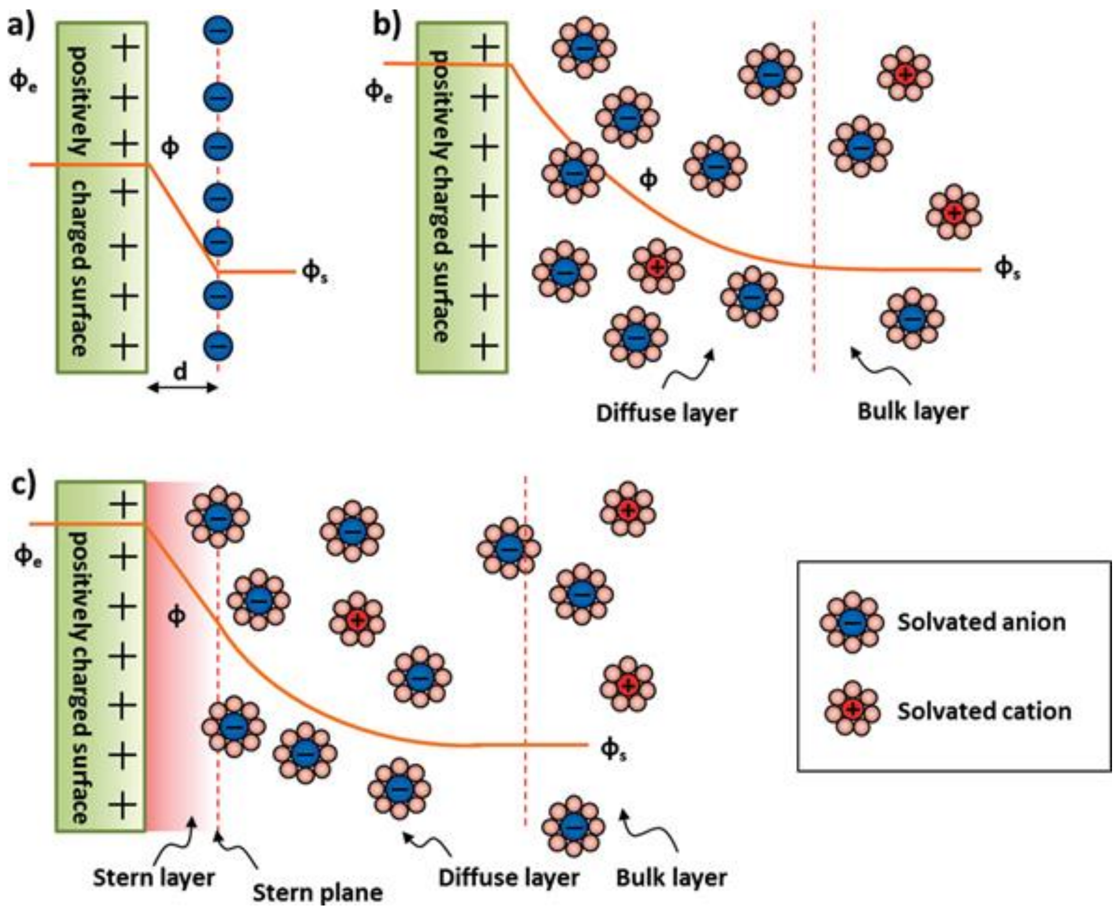

Figure 2.5: Models of the electrical double layer at a positively charged surface in the aqueous electrolyte: (a) the Helmholtz model, (b) the Gouy–Chapman model, and (c) the Stern model [21].

Several factors that the Helmholtz model (i.e. the diffusion of ions in the solution and the interaction between the dipole moment of the solvent and the electrode) and Gouy-Chapman model (i.e., It's insufficiency for highly charged double-layers) could not take into account led to Stern's discovery of his model. The two layers in Stern model are equivalent to two capacitors in series (i.e., C_H (Helmholtz layer) and C_D (diffuse layer)) and from these two layers; the total capacitance of the electrode (C_{DL}) can be calculated using the following equation:

$$\frac{1}{C_{DL}} = \frac{1}{C_H} + \frac{1}{C_D} \quad 2.4$$

Determination of EDL capacitive performance of the electrode is influenced by the following factors: (i) The electric field across the electrode, (ii) Types of the electrolyte ions, (iii) Solvent in which the electrolyte are dissolved in and (iv) The chemical affinity between the adsorbed ions and electrode surface. By applying an electric potential difference between the electrodes in the EDLC, the positive charge carriers, protons, in the positively polarized electrode are balanced by an equal number of negative anions at the electrode/electrolyte interface, while cations electrically balance the holes stored in the negatively polarized electrode. Since there are no redox reactions taking place at the EDLC electrodes due to the electrostatic charge storage, this mechanism allows very fast energy uptake and delivery interpreted as high power performance. Also, this energy storage mechanism also allows for a large amount of cycling due to the reversibility of the process. However, as a consequence of the electrostatic surface charging the mechanism of the EDLC suffer from a limited energy density [19], [27]–[29].

2.3.2 Energy Storage in Pseudocapacitors (PCs)

Pseudocapacitor differs from the EDLC by the means of its energy storage mechanism, where it makes use of some electro-sorption processes, fast redox reactions on the surface of the electrodes with the electrolytes and intercalation of ions through a porous electrode material. In contrast to the double layer capacitance generated from the potential dependence of surface density and electrostatically (non-Faradaic) storing of charges; pseudocapacitance arises from thermodynamic conditions and is due to charge acceptance (Δq) and voltage change (ΔV). The accumulation of electrons on the surface of the electrode is due to the faradaic process where the electrons produced transferred across the electrode-electrolyte interface [4], [30], [31]. This process is similar to the charging and discharging processes that occur in batteries [18]. Three distinguished Faradaic processes happen in pseudocapacitors, namely: reversible adsorption of electrons (adsorption-desorption), redox reactions of transition metal oxides, and reversible electrochemical doping and un-doping of polymer-based electrodes [4], [32]. Electron adsorption-desorption pseudocapacitance results from a reversible process where ions are deposited on the surface of the electrode, creating a monolayer that gives rise to Faradaic charge transfer. The following equation defines the process mentioned above:

$$\underset{c}{A^{\pm}} + \underset{1-\theta_A}{S} + \underset{V}{e^{-}} \leftrightharpoons \underset{\theta_A}{SA_{ads}} \qquad 2.5$$

where A is the ionic species, S is the substrate, c is the concentration of deposited ions, 1-θ_A is the fractional free surface area available for adsorption at coverage, θ_A, and V are the electrode potential.

By the understanding of Langmuir adsorption equation the electrode surface coverage can be defined by the following equation:

$$\frac{\theta_A}{1-\theta_A} = K\exp\left(\frac{-\mathrm{VF}}{\mathrm{RT}}\right) \qquad 2.6$$

where K is an electrochemical equilibrium constant for chemisorption with charge transfer. The capacitance derived from this mechanism is obtained by differentiating the above equation 2.6, and the following equation represents this relation:

$$C_{\varphi} = \frac{q_1 F}{RT} \frac{Kc\pm exp\left(\frac{-VF}{RT}\right)}{\left(1+Kc\pm exp\left(\frac{-VF}{RT}\right)^2\right)} \qquad 2.7$$

where q_1 is the faradaic charge necessary for the complete formation or dispersion of the monolayer, V is the electrode potential, R is the gas constant, T is the absolute temperature while F is the Faraday's constant. A reversible reduction-oxidation (redox) process of transition metal involves an electron transfer process between an oxidized species, Ox and a reduced species, Red. And this mechanism can be defined by the following equation:

$$\mathrm{Ox} + \mathrm{z}e^{-} \leftrightharpoons \mathrm{Red} \tag{2.8}$$

From the above equation (i.e. equation 2.8) the potential, E can be achieved from the Nernst equation 2.9:

$$E = E_0 + \frac{RT}{zF} ln \frac{\Re}{1-\Re} \tag{2.9}$$

where E is the cell potential, E_0 is the standard potential and $\Re$ defined as [ox]/([ox]+[red]). The redox capacitance derived from this mechanism obtained by differentiating the above equation 2.9, and the following equation represents this relation:

$$C_{\Phi} = \left(\frac{q(zF)^2}{RT}\right) \frac{\Re}{1-\Re} \tag{2.10}$$

In pseudocapacitor, Faradaic charge transfer takes place directly within the electrode material, and its capacitance has demonstrated to be higher than the capacitance from the EDLC due to the extended working voltage [33]. Even though the capacitive response of this capacitor is better than the EDLC, the major disadvantage of the pseudocapacitor system is their surface degradation, thermal expansion, and redox-dependent stable state kinetics. These factors affect the electrochemical behaviour of the pseudocapacitors, leading to low power performance due to poor electrical conductivity and lack of stability during cycling, compared to pure EDLCs systems [26], [32], [34].

2.3.3 Energy Storage in Hybrid Capacitors (HCs)

The other two relevant parameters of a capacitor apart from the capacitance are its energy and power densities discussed in details in the coming sections. Since EDLCs gives such a high power out as compared to the pseudocapacitors while the latter is capable of high energy output, a high energy and high power density at high rates are not simultaneously achievable by either one of the two storage mechanism (i.e. EDLCs or pseudocapacitors). Therefore, to achieve high performance, hybrid capacitors integrate both energy storage mechanisms of the two stated mechanisms in their operation synergistically. Hybrid capacitors utilize both the faradaic and non-faradaic processes to store charges. Hybrid capacitors are recognizable in three classes, namely composite, asymmetric and battery-type hybrids. This types of capacitors are tailored to meet the following requirements for a high-performance ECs, namely: good electron conductivity, highly accessible specific surface area and efficient mass transport [32]. The most common design of the hybrid capacitor typically consists of a battery-type electrode (e.g., a faradic or intercalating metal oxide) and an EDLC-type electrode (high surface area carbon) as represented schematically by Figure 2.6.

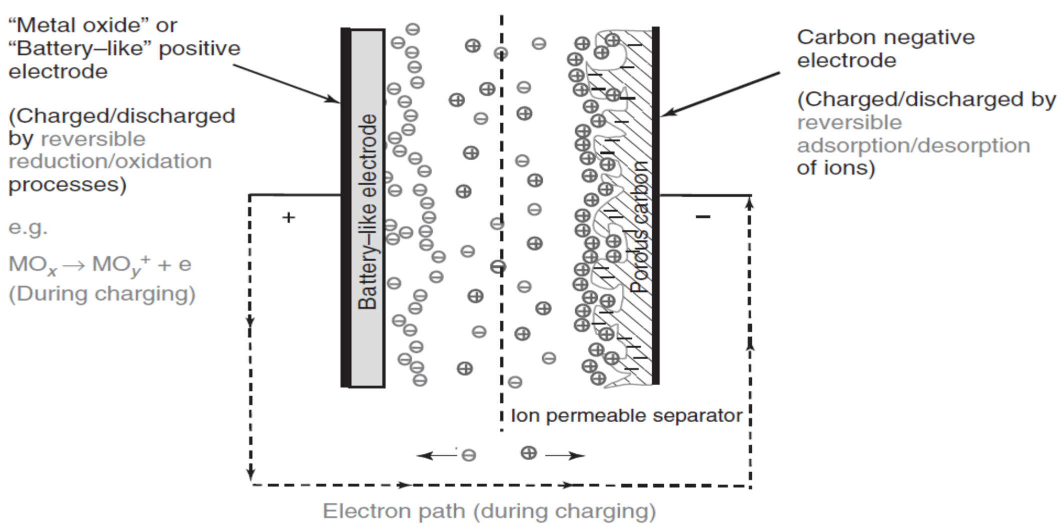

Figure 2.6: A schematic representation of a charged asymmetric electrochemical capacitor (e.g., MnO_2-AC) [29].

A composite hybrid capacitor consists of an electrode made from a carbon material incorporated into a conducting polymer or metal oxide material. Several studies conducted with electrically conducting polymers and metal oxides incorporated into various carbon materials are reported [23], [34]–[37]. Recently, Hu and co-workers [38] reported a specific capacitance of about 1090.8 F g^{-1} for PANI/CP composite electrode which possessed much better capacitance that is higher than that of its precursor CP and PANI. Metal oxides are known to exhibit poor conductivity. Thus, incorporation of carbon materials (i.e. AC, MWCNTs, graphene, and OLCs) into these materials helps to circumvent the lack of electrical conductivity resulting in improved performance [23], [39]. Asymmetric hybrid capacitors at times referred to as capacitor-type/capacitor-type capacitor are capacitors with a different positive and negative electrode. These types of capacitors, from the literature perspective, mostly are made of carbon materials as an anode (negative electrode) while the cathode (positive electrode) usually manufactured from any capacitive materials. These capacitors usually have a high operating potential window that accounts for an increase in the ECs performance. Therefore, several studies have been done on the development of this ECs to achieve high energy densities [40]–[46]. Recently, Moosavifard and co-workers [42] reported an energy density of about 19.7 Wh kg^{-1} on an asymmetric capacitor. Their system consists of AC (anode) and CuO (cathode) electrodes. While in 2012, Yan *et al.* [47] obtained a remarkably high energy density of 77.8 Wh kg^{-1} on an asymmetric capacitor made up of porous graphene (anode) and $Ni(OH)_2$/graphene (cathode). Battery-type hybrid capacitors are referred to sometimes as battery-type/capacitor-type capacitor (e.g., Lithium Ion Capacitors) since these capacitors incorporate materials that behave as batteries. They are also asymmetric, and their negative electrode is similar to an anode of the lithium-ion battery. The demand for high energy, great cycling, and stability devices have increased consistently in the past years since neither LIBs nor EDLCs can satisfy these requirements based on the development of current technology. A strategic design of developing a high voltage device (i.e., high power and energy density) that will be convenient is the creation of a hybrid system that combines both lithium-ion battery electrodes with ECs electrodes. Hence, thus far, the lithium ion capacitor (LIC) has captured attention as one of the most impressive ECs since it displays an operating voltage of about 3.8-4.0 V with high energy (≥ 20 Wh kg^{-1}) and cycle life that is between that of LIBs and EDLCs. The flow diagram is shown in Fig. 2.7 clearly illustrates the taxonomy of the ECs system.

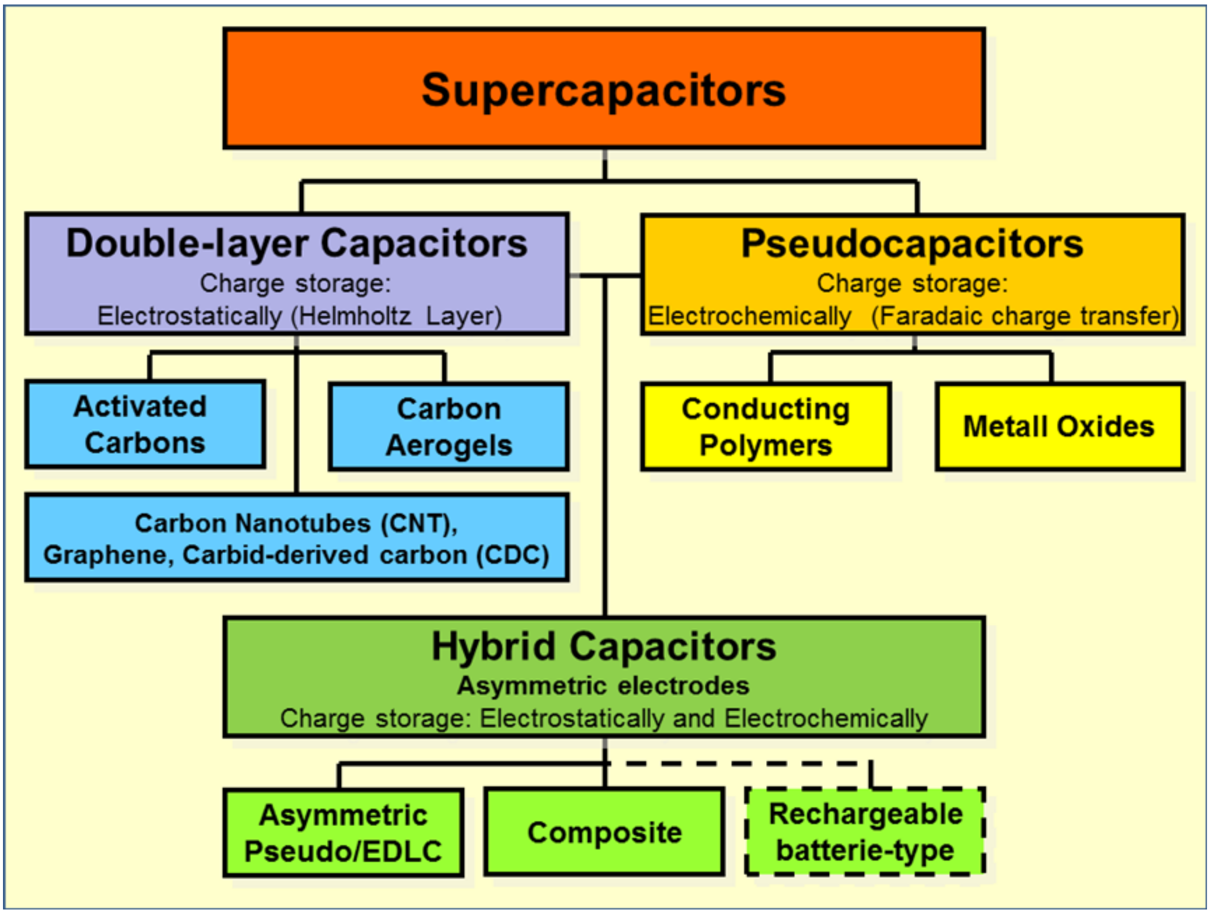

Figure 2.7: The flow diagram showing the taxonomy of the ECs. Double-layer capacitors, pseudocapacitors, and hybrid capacitors defined by the design of their electrode.

2.3.4 Performance of Electrochemical Capacitors (ECs)

An electrochemical capacitor (ECs) consists of two porous electrode materials, generally carbon materials such as activated carbon (AC) for the EDLCs, metal oxides or conducting polymers such as MnO_2 or PANI for pseudocapacitors which are in direct contact with the current collector and separated by a porous separator impregnated with an electrolyte solution. These two porous electrodes of the ECs are equivalent to two capacitors connected in series. The resulting capacitance (C) obtained after polarization of electrodes by applying potential difference (voltage) between them can be expressed according to the following equation:

$$\frac{1}{C_{cell}} = \frac{1}{C_+} + \frac{1}{C_-} \quad 2.11$$

where C_{cell}, C_+, and C_- are the capacitance (in Farad = Coulomb/Volt) of the resulting device or cell, of the positive electrode, and of the negative electrode, respectively. With the capacitance (C_{cell}) determined from the cyclic voltammetry (CV) and the slope of the discharge curve of the galvanostatic charge-discharge (GCD) profile using equation 2.12.

$$C_{cell}(F) = \frac{i}{\Delta V/\Delta t} \quad 2.12$$

where i (A) is the applied current, $\Delta V/\Delta t$ (V s^{-1}) the slope of the discharge curve after the initial iR drop. In a symmetrical system where the two electrodes (positive and negative electrode) are similar with similar morphological and electronic properties ($C_+ = C_-$), the cell capacitance (C_{cell}), from equation 2.11 will therefore be defined according to the following equations:

$$C_{cell} = \frac{C_e}{2} \quad 2.13$$

where $C_e = C_+ = C_-$.

The electrode capacitance is calculated using the following equation:

$$C_e = 2C_{cell} \quad 2.14$$

In ECs, to provide a basis for comparison between different electrode materials, it is a common practice to provide a specific (gravimetric) capacitance, which is related to the capacitance of one single electrode, $C_{e,sp}$ (F/g). Hence, dividing equation 2.14 by the mass of the single electrode, equation 2.15 can be used:

$$C_{e,sp}(F\ g^{-1}) = \frac{2C_{cell}}{m_e} \qquad 2.15$$

where $C_{e,sp}$ is the measured specific capacitance of each electrode in F g^{-1} (C_e/m), and m_e (g) is the mass of the single electrode. Note that Equations 2.13-2.15 simply remind the researchers that when reporting or comparing the values of capacitance from different literature one must explicitly specify if the values are those of the electrodes or cells. The value of a single electrode derived from a *three-electrode* (half-cell) measurement will be higher than the actual cell capacitance obtained from a *two-electrode* (full-cell) measurement.

For a symmetric system, the specific (gravimetric) capacitance of the two electrodes (C_{sp}) is given by:

$$C_{sp}(F\ g^{-1}) = \frac{4C_{cell}}{M} \qquad 2.16$$

where M is the total mass of the active materials of the two electrodes (i.e., M = $2m_e$ since the weight of each electrode is the same). The multiplier of 4 only adjusts the capacitance of the cell and the combined weight of two electrodes to the capacitance and mass of a single electrode[28], [48].

The other two relevant parameters of a capacitor apart from the C_{sp} are its energy and power density [23]. The energy (E) stored in a capacitor is related to the charge (Q) at each interface and the potential difference between the two plates. Therefore, energy is directly proportional to the capacitance as shown by the following equation:

$$E_{sp}(Wh\ kg^{-1}) = \frac{C_{cell}V^2}{2M} \qquad 2.17$$

where M (kg) is the mass of the ECs and V (V) is the maximum voltage of electrochemical stability. The maximum power of the device is calculated using the following equation:

$$P_{max}(W.kg^{-1}) = \frac{V^2}{4R_sM} \qquad 2.18$$

The internal resistance R_s is calculated from the voltage drop at the beginning of a discharge curve and is shown by the following equation:

$$R_s(\Omega) = \frac{\Delta V_{IR}}{2i} \qquad 2.19$$

where ΔV_{IR} is the voltage drop between the first two points from the start of the discharge curve.

For an asymmetric system, Equations 2.16-2.19 are also applied. However, before they are implemented to the asymmetric system, it is very critical first to perform *'mass-balancing'* from the *three-electrode* experiment for each of the electrodes. In the symmetric supercapacitor, the applied voltage is split equally between the two electrodes due to the use of the same material having the same mass in each electrode. In the asymmetric supercapacitors, however, the voltage split is dependent on the capacitance of the active material in each electrode of its two electrodes. The capacitance is usually related to the mass and the specific capacitance of the active material [49], [50]. Thus, to split voltage equally, the mass balance between the two electrodes must be optimize using the following relationship: $q_+ = q_-$, where q_+ means the charges stored at the positive electrode and q_- means the charges stored at the negative electrode. The following equation is used to express the stored charge:

$$q = C_{sp}.m.\Delta E \qquad 2.20$$

or:

$$\frac{m_+}{m_-} = \frac{C_{sp-}}{C_{sp+}}.\text{x}\,\frac{\Delta E_-}{\Delta E_+} \qquad 2.21$$

where m, C_{sp} and ΔE represent the mass, specific capacitance, and potential range obtained from the charging/discharging process of three-electrode configuration of the individual positive and negative electrode, respectively.

The electrolyte that is itself an electronic insulator but also an ionic conductor serves as the medium for transfer of charge as ions between the anode and the cathode. The choice of electrolyte solutions plays a crucial role when it comes to the performance of the ECs [48], [51]. Three types of electrolytes mainly used in ECs are aqueous, organic, or liquid salts (frequently known as ionic liquids). There are two main criteria involved in the selection of an electrolyte: the electrochemical stability window (which is crucial in maximizing the specific energy values according to equation 2.17), and the ionic conductivity (which has a significant influence on the values of specific power according to equation 2.18). Aqueous electrolytes include acid-based (e.g., H_2SO_4), alkali-based (e.g., KOH) and neutral-based (e.g., Na_2SO_4) which have a higher conductivity (up to ~1 S/cm). Due to the relatively high conductivity of this electrolyte-type, the system results in a higher power performance. Nevertheless, this system suffers from the narrow electrochemical stability window (1.23 V) due to water electrolysis, leading to a relatively small (~1 V) operating voltage and consequently, limiting the energy stored in the device [48], [52]. Acid-based and alkali-based aqueous electrolytes come along with other disadvantage properties such as being unfriendly to the environment and harmful to work with [29]. Electrolytes with neutral pH such as Na_2SO_4 and Li_2SO_4 are investigated to mitigate the corrosive character of the acid and alkali media. These neutral electrolytes have high voltage values. Good charge/discharge cycle life have been observed in carbon materials such as AC for symmetric cells using Na_2SO_4 and Li_2SO_4 while also this neutral electrolyte has been applied in asymmetric cell construction using AC as a negative electrode and MnO_2 as positive electrode [40], [53]–

[58]. It is worth mentioning that the overpotential for electrolyte decomposition varies, depending on the used carbon with the temperature playing an important role in the degradation mechanism [21]. Organic electrolytes composed of salt dissolved in an organic solvent (i.e., Propylene carbonate (PC) and acetonitrile (AN)) provide a wider electrochemical stability window (ranging from 2.7-2.8 V) as compared to Acid-Alkali based aqueous electrolytes due to their resistance to hydrolysis. Nonetheless, they suffer relatively low ionic conductivity and high viscosity that results in lower specific capacitance (100‑150 F g^{-1}) as compared to Acid-Alkali based aqueous electrolytes [59]–[62]. However, the wide electrochemical stability window in organic electrolytes is advantageous to the ECs as it helps to deliver a higher specific energy stored as compared to Acid-Alkali based aqueous ECs systems and for this reason, the majority of industrial systems are currently produced with organic electrolytes. Salts commonly applied in organic electrolytes are quaternary ammonium salts out of which tetraethylammonium tetrafluoroborate (TEA-BF_4) is the most widely used salt for commercial supercapacitors. Other salts includes EMIM-BF_4 (1-ethyl-3-methylimidazolium tetrafluoroborate), MEPY- BF_4 (1-ethyl-1-methylpyrrolidinium tetrafluoroborate), TMPY-BF_4 (tetramethylene-pyrrolidinium tetrafluoroborate), and TEMA-BF_4 (triethylmethylammonium tetrafluoroborate) [29], [63]. Recently, ionic electrolytes have been explored by researchers as an alternative by fine-tuning electrolytes that result in an increase energy density of the ECs. Ionic liquids (ILs) also called room temperature ionic liquids (RTILs) are organic salts that are likely liquids at room temperature [64]. This type of salts is called molten salts. Their desirable properties make them promising candidates for ECs electrolytes. These electrolytes have a very low vapor pressure because no solvent is required, hence, limiting environmental exposure and preventing the risk of explosion. ILs possess interesting

properties, such as high thermal stability at elevated temperatures (beyond the ~80° C limit of organic electrolytes), low flammability and a broad electrochemical stability window (ranging from 2 to 6 V, typically about 4.5 V). These properties are extremely higher than that of organic and aqueous electrolytes [51], [65]. However, the ionic conductivity of ILs, specifically at room temperature, is lower than that of organic electrolytes, therefore reducing the power performance of IL-based ECs [66]–[69].

2.4 Electrode Materials for the ECs

It is essential to understand that if the two electrodes of ECs are the same, namely, $C_+ = C_-$, the overall capacitance C_{tot} would be half of either individual's capacitance, the corresponding system is called a symmetric ECs system while in the case of $C_+ \neq C_-$ (the anode and the cathode have two different electrode materials, the corresponding system is called an asymmetric ECs system), C_{tot} is mainly dominated by the electrode with smaller capacitance. In general, the capacitance and stored energy essentially depend on the electrode material used. Hence in order to increase overall cell capacitance, both electrode capacitances have to be increased. Thus, extensive development of electrode materials becomes one of the key approaches in ECs research and development (R&D). This section looks into some of the electrode materials utilised in the ECs application.

2.4.1 Carbon Structure and Porous Texture on EDLC Performance

Carbon is the choice material as an electrode for industrial applications. Due to its excellent properties including such as its natural abundance, non-toxicity, low cost, higher specific surface area (~1 to >2000 m^2 g^{-1}), high chemical stability and excellent electronic conductivity. They have controlled pore structure, wide operating temperature range and compatibility in composite materials as compared to some other potential ECs electrode materials [15], [70]. Carbon exists in different allotropes (i.e., graphite, diamond, fullerenes or nanotubes), various micro-textures (i.e., more or less ordered) due to the degree of graphitization, a variety of dimensionality from 0 to 3D. It also exists in different forms (i.e., powders, fibres, foams, fabrics, etc.).

a) Activated Carbon

Among other reasons, one of the great universal attractions of using carbon as an electrode material in ECs due to it ability to exists in a different form with a very high specific surface area. The process employed to increase carbon surface area and porosity from a carbonised organic precursor is referred to as 'activation'. Hence, the resulting group of these materials referred to as activated carbons. Activated carbon can be manufactured from various carbonaceous raw materials such as coal, coconut shell, apricot shell, pines wood, etc. through carbonization and activation of organic molecules. There are several studies on activated carbons (ACs) as the electrode materials for the EDLCs due to its high surface area. This type of carbon material can be readily obtained commercially or synthesised in the laboratory for various research activities. A developed surface area of greater than 2000 m^2 g^{-1}, including a controlled distribution of pores during the activation process, can be reached during carbon activation [9], [19]. Activation opens up the pores in carbon precursor, thus creating additional porosity which results in an improved surface area. A Control over the resulting porosity together with pore size distribution is manipulated by varying the carbon precursor and activation conditions (i.e., temperature, gaseous environment and time). Two well-known general categories of carbon activation include thermal activation (also referred to as physical activation) and chemical activation [71], [72]. Thermal activation of carbon precursor requires controlled gasification, generally at temperatures that are between 700 and 1100 °C in the presence of suitable oxidising agents that are gases such as carbon dioxide (CO_2), steam, air, or even mixtures of these gases [9], [73]. The oxidising atmosphere, during gasification process, is the one responsible for an increased pore volume and surface area of the carbon precursor as it creates carbon 'burn-off' while also eliminating volatile pyrolysis products. An increased burn-off of the carbon precursor yields a high degree of activation. Nevertheless, the extent of carbon activation can also be achieved by the additional activity resulting from a decrease in carbon strength, reduced yield, lower density, and the widening of pores. The second category, chemical activation, is different from the thermal activation by the fact that it is usually carried out at temperatures that are slightly lower (~400–700 ◦C) [72]. Chemical activation also involves certain chemical agents such as phosphoric acid (H_2PO_4), zinc chloride ($ZnCl_2$) and potassium hydroxide (KOH) to achieve dehydration. In this type of activation, post-activation washing of the carbon product is usually required to remove residual reactants as well as any inorganic contaminant that originates from the carbon precursor (or the ones introduced during activation). Activated carbons with exceptionally high surface area materials (>2500 m^2 g^{-1}) were prepared and reported in the literature [71], [74].

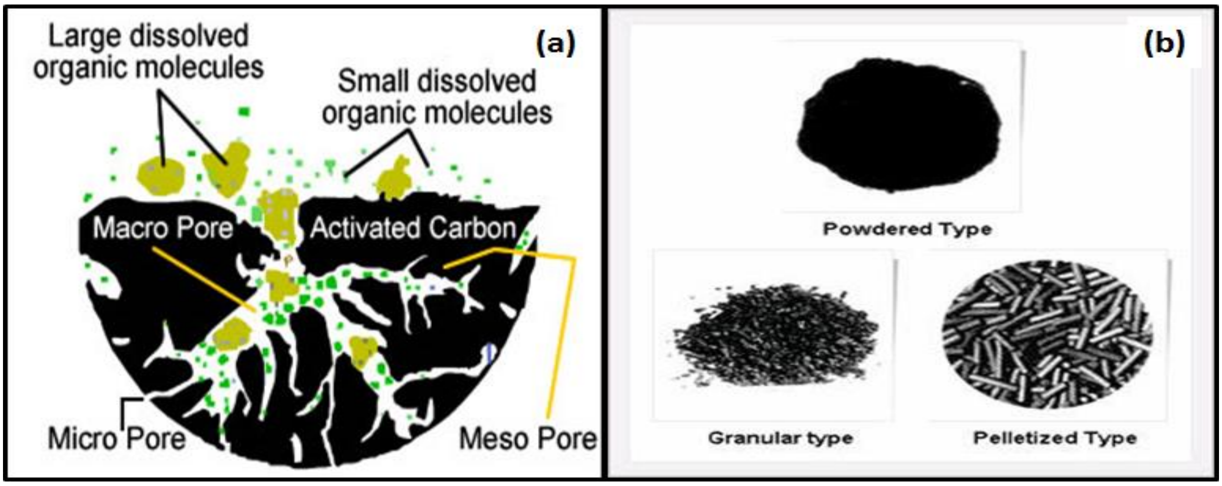

Figure 2.8: (a) Schematic representation of activated carbon showing various internal pores size responsible for the high surface area, (b) different forms of

activated carbon [75], [76]. Micropores (ø < 2 nm), Mesopores (2 nm < ø < 50 nm), Macropores (ø ≥ 50 nm).

Apart from its many uses, activated carbon has been widely used as an ECs electrode. In 2003, Lozano-Castello´ *et al*. reported a specific capacitance as high as 220 F g^{-1} from a KOH-activated carbon with a large surface area more than 2000 m^2 g^{-1} [74] in a three electrode system. Yuan *et al.* at around 2005 reported specific capacitance value of about 194 F g^{-1} for the composite of activated carbon decorated with NiO (AC/NiO) as the electrode material [77]. In 2010, Xu *et al.* showed that the use of apricot shell as a carbon source results in an improved specific capacitance of about 339 F g^{-1} [78]. Saha *et al.* reported on the activated carbon derived from the lignin with a surface area of around 1148 m^2 g^{-1} and specific capacitance of about 102 F g^{-1} for KOH-activated derivatives [79]. Recently the hybrid materials made of Co_3O_4 nanoparticles on the surface of activated carbon (AC) provided a specific capacitance up to 491 F g^{-1} at the current density of 0.1 A g^{-1} in a 6 M KOH electrolyte [80].

b) Graphene and Graphene Oxide

Graphene is one-atom-thick, two-dimensional (2D), sp^2 hybridized allotrope of carbon with its atoms arranged in a honeycomb crystal lattice that has a hexagonal pattern (see Fig. 2.9a) which possess a broad range of extraordinary properties [81]–[83]. There have been many theoretical reports on graphene. In 2004, two scientists from the University of Manchester namely Andre Geim and Kostya Novoselov managed to extract, for the very first time, these one atom thick crystallites from the bulk graphite and this outstanding work saw them winning the prestigious award, Nobel Price, in 2010 [84], [85]. The oxide form of this carbon material is called graphene oxide (see Fig. 2.9b).

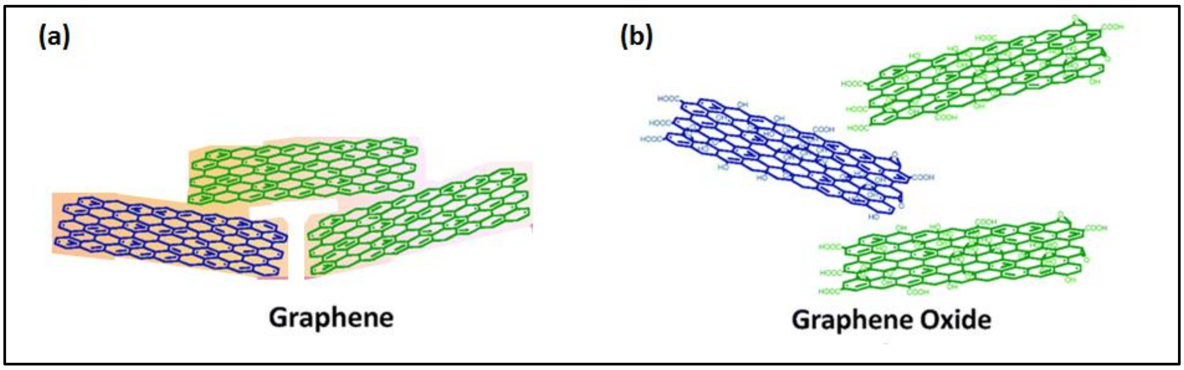

Figure 2.9: Representations of (a) Graphene sheet, and (b) Graphene oxide sheet [86], [87].

Graphene has emerged as one of the most exciting material for research in the last few years [88], [89]. The extraordinary properties of graphene include a high theoretical specific surface area (2630 m^2 g^{-1}), high Young's modulus (~ 1 TPa) entailing strong mechanical strength and compared to other carbon allotropes in Table 2.1 [89]–[91]. Graphene is synthesized by several processes such as mechanical exfoliation of graphite, chemical vapour deposition (CVD), unzipping of carbon nanotubes, also through reduction of graphene oxide, etc. [92], [93]. The chemical method via reduction of graphene oxide (see Fig. 2.10) is considered a scalable approach to synthesizing graphene and has been widely utilized to synthesize chemically derived graphene also known as reduced graphene oxide (rGO) [94]. Table 2.1 shows comparative properties of graphene with those of various carbon allotropes.

Table 2.1: A comparison of intrinsic properties of graphene with those of various carbon allotropes.

Allotropes of Carbon	**Graphite**	**Diamond**	**Fullerene**	**Carbon nanotubes**	**Graphene**
Dimensionality	Three (3D)	Three (3D)	Zero (0D)	One (1D)	Two (2D)
Hybridization	Sp^2	Sp^3	Mainly Sp^2	Mainly Sp^2	Sp^2
Crystal system	Hexagonal	Octahedral	Tetragonal	Icosahedral	Hexagonal
Experimental specific surface area ($m^2 g^{-1}$)	~10-20	~20-160	~80-90	~1300	~2675
Density ($g\ cm^{-3}$)	2.09-2.23	3.5-3.53	1.72	>1	>1
Electrical conductivity ($S\ cm^{-1}$)	Anisotropic 2,3 x10^4a, x10^6b	–	10^{-10}	Depends on the particular structure	2000
Electronic properties	Conductor	Insulator, Semiconductor	Insulator	Metallic or semiconducting	Semimetal, zero gap semiconductor
Thermal conductivity ($W\ m^{-1}K^{-1}$)	1500-2000a 5-10c	900-2320	0.4	3500	4848-5300
Hardness tenacity	High	Ultrahigh	Highly elastic	High flexible elastic	Highest flexible elastic (single layer)
Optical properties	Uniaxial	Isotropic	Non-linear optical response	Structural dependent	97.7% optical transmittance

Key: a, b, c = directions relative to the plane.

The chemical method involves the oxidation of graphite, to graphene oxide (GO) using the Hummers method [95] or the modified Hummers method [24] then after, the obtained GO is then reduced using reducing agents such as hydrazine solution, sodium borohydride ($NaBH_4$) or any other reducing agents [96], [97].

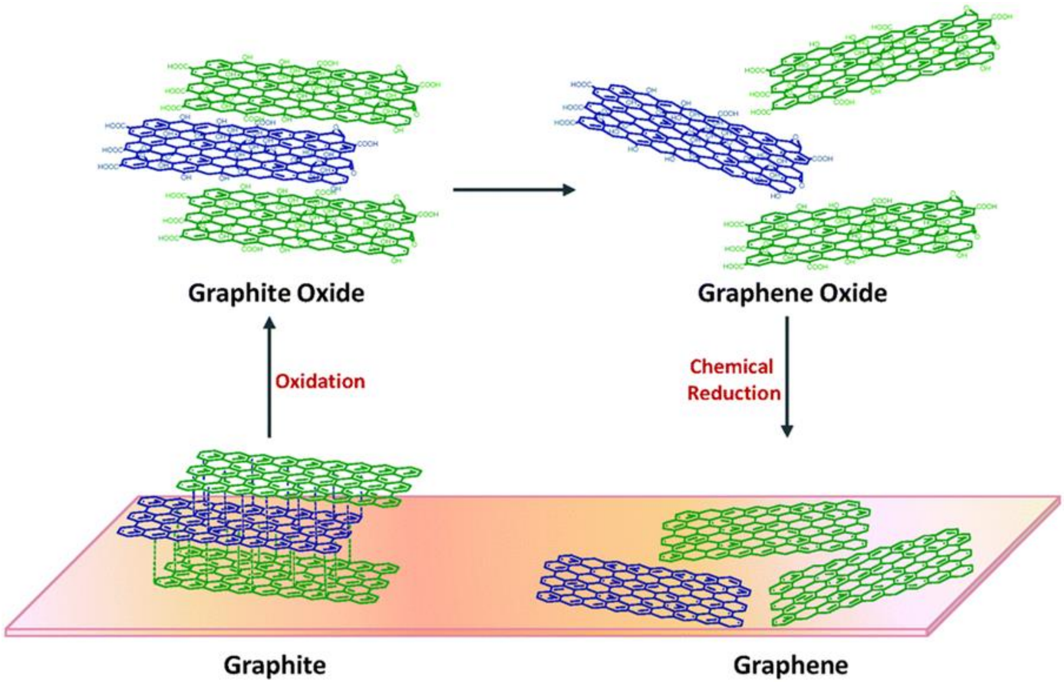

Figure 2.10: An illustration of the chemical route to the synthesis of chemically derived graphene from graphite via graphene oxide [97].

Due to graphene's high theoretical specific surface area, graphene has found attention as a potential electrode material for ECs application [24], [98]–[102]. However, graphene sheet has a high tendency of restacking during electrode formation due to strong π–π interactions between neighbouring layers. This interaction leads to a significant decrease in the surface area, consequently resulting in lower specific capacitance values. Several measures such as decoration of graphene sheets with pseudocapacitive materials (i.e., transition metal oxides and conducting polymers) and functionalization of graphene (with chemical moieties such as carbonyl and hydroxyl groups) that ultimately prevents the restacking of graphene has been employed [99], [103]–[107]. The advantage of the above approach is that the surface area of graphene can be maximally accessed and thus improve the specific capacitance through the non-Faradaic contribution of graphene and also the Faradaic contribution of the pseudocapacitive materials and chemical moieties [108]. In 2008, Stoller *et al*. reported a specific capacitance as high as 135 F g^{-1} and 99 F g^{-1} from a graphene in aqueous (KOH) and organic (TEABF4/AN) electrolytes respectively [24]. Wang *et al.* in 2009 managed to improve the specific capacitance value of graphene by chemical treatment of GO and obtained the value of about 205 F g^{-1} in aqueous electrolyte [109]. Not long ago, in 2012, El-Kady and his co-workers showed that graphene can be synthesised as easy as burning a disc coated with GO with laser and the obtained graphene (rGO) resulted with an improved specific capacitance of about 276 F g^{-1} in ionic liquid (EMIMBF4) as an electrolyte [110]. Recently, in 2014, Qi *et al.* reported a remarkable specific capacitance of about 704 μF cm^{-2} for a 3D few-layered graphene (VFG) grown by plasma-enhanced chemical vapor deposition [111].

c) Carbon Nanotubes (CNTs)

Carbon nanotubes (CNTs) are one of carbon allotropes made of the cylindrical nanostructure of carbon molecules with novel properties that make them useful in a wide variety of applications in the field of nanotechnology, electronics, optics and other fields of material science. They are sp^2 hybridized form of carbon atoms made from graphene/graphite sheets that are rolled into cylindrical shaped seamless tubes and capped at the end with fullerene-type hemispheres. There are two main types of CNTs with high structural perfection, namely, Single-Walled Carbon Nanotubes (SWCNTs) and Multi- Walled Carbon Nanotubes (MWCNTs) shown in Fig. 2.11. In essence, SWCNTs are strips of a single layer graphene sheet that are rolled around a hollow central core forming a tube-like structure with a nanoscale diameter (~ 1 nm) whereas MWCNTs are made up of two or more layers of graphene sheet rolled up in a similar fashion as SWCNTs (see Fig. 2.12).

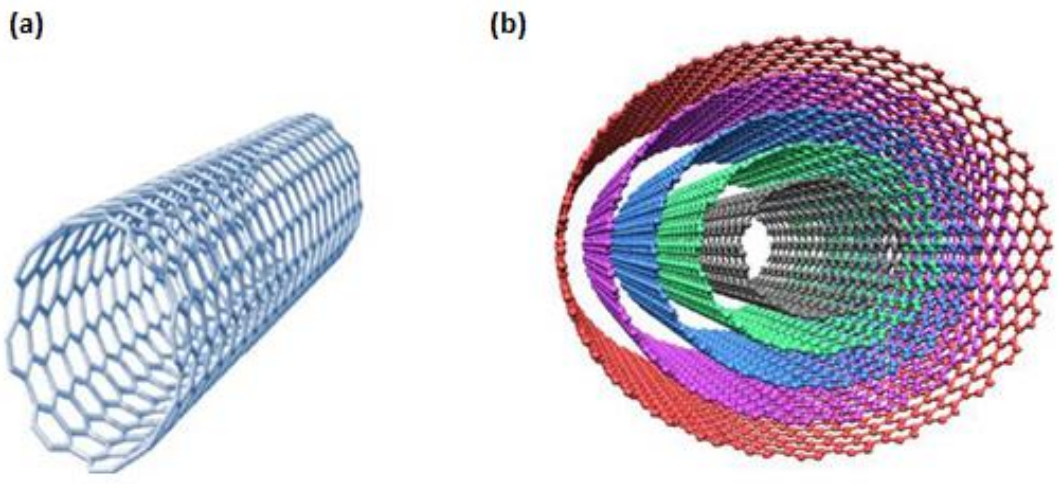

Figure 2.11: An illustration of (a) Single-Walled Carbon Nanotubes and (b) Multi-Walled Carbon Nanotubes.

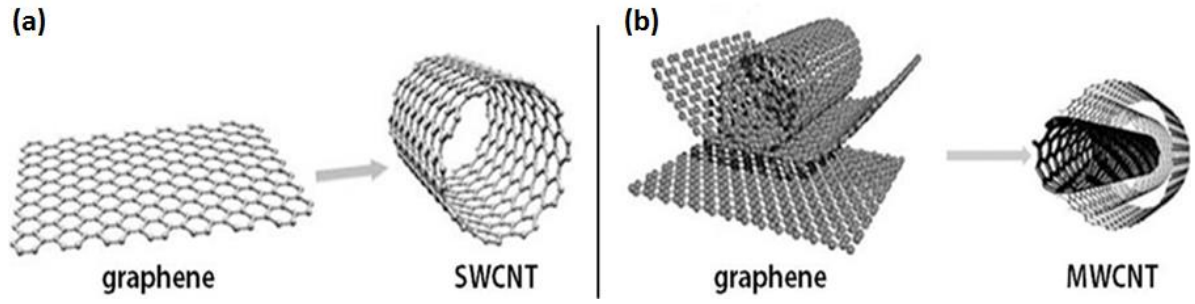

Figure 2.12: Formation of (a) Single-Walled Carbon Nanotubes and (b) Multi-Walled Carbon Nanotubes, from graphene sheet.

The discovery of carbon nanotubes (CNTs) dates back to 1950s though the theory was not clear at that time. Roger Bacon saw a strange new carbon fibre, in the late 1950s, while studying carbon under conditions near its triple point. He saw linear, hollow tubes of carbon that seemed to be of graphitic layers of carbon. These similar tubes were observed again by Morinobu Endo at around 1970s, produced by a gas-phase process. In 1991, Sumio Iijima of NEC reported multi-walled CNTs synthesised from a carbon arc discharge and two years later at around 1993, Sumio Iijima and Donald Bethume (from IBM) worked independently and found single-walled CNTs [112]–[117].

Carbon nanotubes (CNTs) can be classified by the manner in which the graphitic backbone consisting of the sp^2 carbon atoms is rolled and be described by the two indices (n, m) in a shorthand notation. The properties of the CNTs depend on the atomic arrangement, the diameter and length of the tubes and the morphology. The atomic structure of CNTs is described using the tube chirality (or helicity) and the angle of chirality. The chirality angle measures the extent of the twist within the tube [118]. The chirality angle property results in the single-walled CNT being able to be differentiated into zig-zag and armchair as shown in Fig. 2.13. Regarding the roll-up vector, the zig-zag carbon nanotube is described as (n, 0) and the armchair carbon nanotube as (n, n).

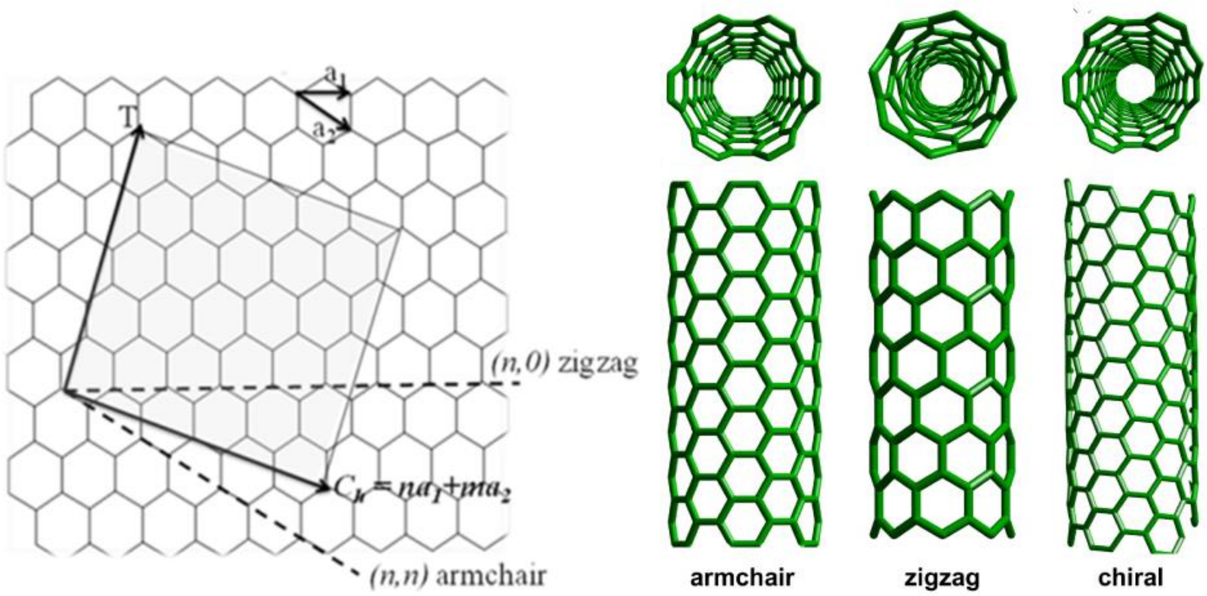

Figure 2.13: Graphene sheet rolled up to show different chirality of the single-walled CNTs [119], [120].

The chirality of the CNTs provides significant effects on the properties especially the electronic properties. Some of these properties of CNT compared with the properties of other carbon allotropes shown in Table 2.1. Carbon nanotubes have been widely synthesised using various techniques such as arc discharge [114], laser ablation [121], high-pressure carbon monoxide disproportionation [122] and chemical vapour deposition (CVD) [123]. Carbon nanotubes can be functionalized at the surfaces with functional groups such as carboxylic acid (-COOH) and sulfonic acid (-SO_3H) to give functionalized carbon nanotubes (*f*-CNTs where *f* = -COOH or (-SO_3H)) [124]. Due to CNTs intrinsic properties fine-tuned, CNT has found its path as the energy storage electrode material in ECs application [125], [126]. By the year 1999, already work was done on CNT, and its electrochemical capacitive performance reported [127]. In 2000, Frackowiak *et al.* reported on the pure electrostatic attraction of ions of a pure multi-walled CNT as well as quick pseudo-faradaic reactions on the functionalized multi-walled CNT, detected upon varying surface functionality of the CNT. The specific capacitance values obtained varied from 4 to 135 F g^{-1} (depending on the type of nanotubes and their post treatments) [128]. In 2005, Du *et al.* reported on a thin film formed using multi-walled CNTs. This electrode material displayed a high packing density and local alignment with an electrical double layer performance that maintained a close to rectangular shape cyclic voltammogram even at a high scan rate of 1000 mV s^{-1}. This performance lead to fast rate capability with a high specific power density of about 30 kW kg^{-1} [129]. The tremendous performance of CNT as ECs electrode material continued with time without any disappointment, by the year 2010, Izadi-Najafabadi and co-workers managed to design a high energy and power performance ECs by operating at the higher voltage range of 4 V in organic electrolyte using single-walled CNT. Their results were as a consequence of the combination of high surface area and electrochemical doping that enabled them to achieve an improved specific capacitance if around 160 F g^{-1} while simultaneously enhancing the specific energy density to more than 50 Wh Kg^{-1} [130]. Recently, CNTs have been employed in several fabrications to make composites with other potential electrode materials for ECs applications [7], [131]–[133].

d) Onion-like Carbons (OLCs)

Carbon nanomaterials are widely studied and used in several applications (i.e., energy storage, electronics, etc.,). Nevertheless, carbon onions discovered long ago (i.e., before fullerenes and carbon nanotubes) remained unpopular and were poorly investigated. Recently, this type of carbon allotropes have found attention and are increasing being investigated. Onion-like carbons (OLCs) also known as carbon nano-onions (CNOs) are another type of carbon allotrope that are made up of spherical carbon shells that resemble the concentric layered structure of onion, hence, the origin of their name. OLCs range from the diverse sizes of the concentric shells, from the nested fullerenes to small (< 100 nm) polyhedral nanostructures. The knowledge of OLCs dates back to 1980 when Sumio Iijima saw isolated single layers of hexagonal nets of carbon atoms formed inside the shells of the graphitised carbon particles from the carbon black using a transmission electron microscope [134]. At this time, it was rather difficult to synthesise OLCs in a bulk form but instead was mostly observed as a by-product from the synthesis of carbon black. In late 1992, a scientist by the name of Daniel Ugarte showed a precise mechanism of producing the spherical graphitic structure by focusing an electron beam on an amorphous carbon sample where OLCs are observed forming *in situ*. The onion grows under an electron beam when the amorphous carbon begins to curl due to graphitization and the graphitic structure closes on itself after being exposed to an electron beam for sufficient time. The curving and closure of the carbon onion structure occur as to minimize the surface energy of the newly formed edge planes of graphite [135]. The method used by Daniel Urgate to synthesise the OLCs with the diameter of ~45 nm and other synthetic methods explored in previous years were not adequate to produce bulk quantities of OLCs [136]–[141]. To achieve large-scale production of OLCs, Vladimir Kuznetsov, and co-workers in 1994 proposed and applied the vacuum annealing to prepare a large scale production (gram quantities) of OLCs by graphitization of nanodiamond (ND) precursors at a temperature between 1000 and 1800 ^{o} C [142], [143]. This approach has become a very useful method to prepare OLCs with a diameter of 6-8 nm. At around 2001, Sano and co-workers used a similar method to vacuum annealing and managed to produce exceptionally large quantities (in tons) of OLCs (with a diameter of 4-36 nm) by annealing in inert gases to transform nanodiamond [144]. Because the yield of OLCs produced in this method is close to 100% and the limitation of the volume manufactured the size of the furnace, this approach falls among others that have great potential in industrial applications. The conversion of nanodiamond to OLC can be represented using a molecular dynamics (MD) simulation (see Fig. 2.14a-c). Using a representation of the MD simulation, a nanodiamond particle (Fig. 2.14a) was annealed at 1400 ^{0} C causing the outer layers of the nanodiamond to convert to graphitic carbon (Fig. 2.14b); nevertheless, the annealing temperature was not high enough to turn the entire particle. A further increase in temperature to 1800 ^{0} C converts the whole particle to an OLC particle (Fig. 2.14c) [145]. It is observed that the OLC particles start to polygonize when exposed to the highest annealing temperatures ($\geq$ 200 ^{0} C) due to their structure becoming more ordered as shown in (Fig. 2.14d) [146]. The particles size of the OLC made from the vacuum annealing of nanodiamond precursor adopts more or less similar size of the ND, hence, in general, a 5 nm in diameter ND produces an OLC particles in the range of 5-10 nm [147].

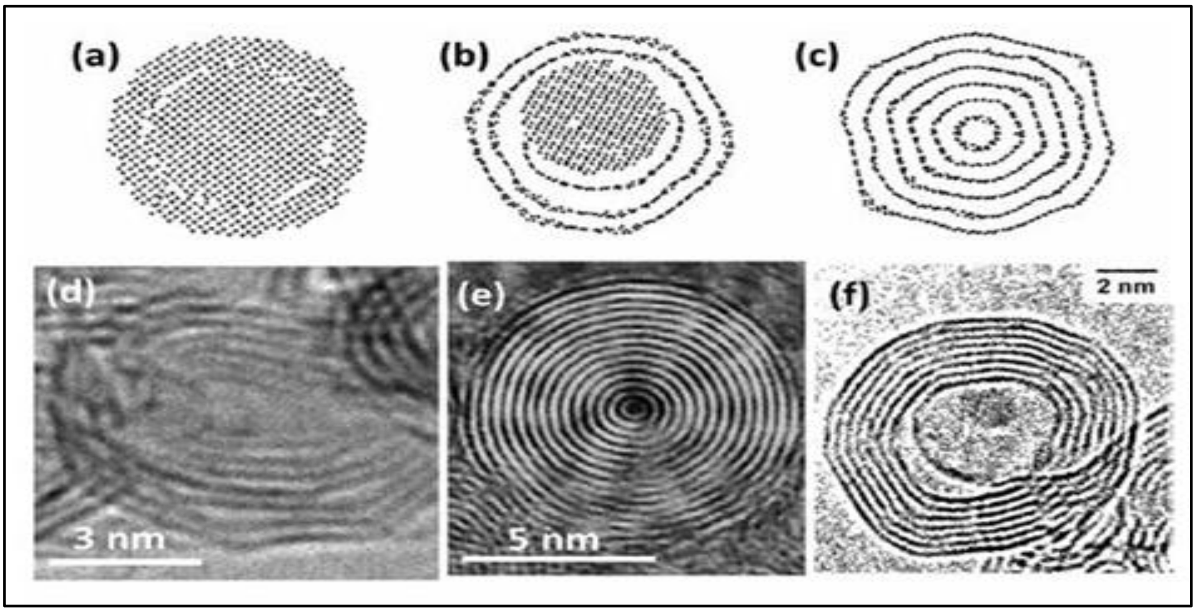

Figure 2.14: Molecular dynamics simulations (a) pristine nanodiamond, (b) nanodiamond annealed at 1400 °C, (c) nanodiamond annealed at 1800 °C. TEM images of OLCs synthesized via (d) annealing of nanodiamond at 2000 °C, (e) arc discharge between two carbon electrodes in water, and (f) electron beam irradiation [146].

The structural properties of the OLC differ significantly due to the method and conditions of synthesis as well as the nature of the carbon precursor used. In general, the specific surface area (SSA) of the OLC derived from the vacuum annealing of the nanodiamond (in temperatures between 1200-1800 ^{0}C) ranges between 400-600 m^2g^{-1}. The specific surface area of the OLC entirely depends on the density of the material and the surface of the particles since there is no accessible internal porosity of the material [148]. Due to the inaccessibility of the internal pores of the OLCs, scientist developed a way of penetrating through the rigid structure of the OLC by activating it using chemical activation technique (see Fig. 2.15) [149]. Onion-like carbons (OLCs) gained interest as energy storage material in EDLCs at around 2006 and 2007 when investigated in both aqueous and organic electrolytes [150], [151].

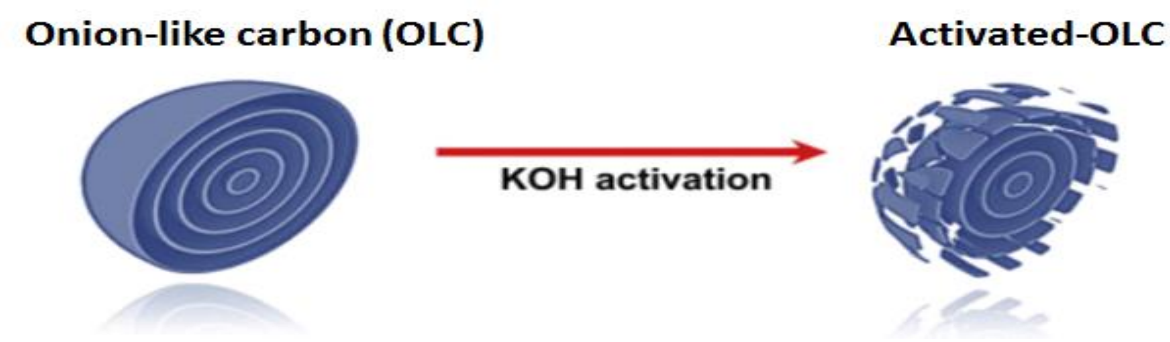

Figure 2.15: A representation of chemical activation of OLC [149].

In 2007, Portet *et al.* [151] showed that the OLCs are capable of delivering remarkable electrochemical properties. They exhibited high power density of about 63 kW Kg^{-1}, the maximum specific capacitance of ~40 F g^{-1} at the lower current density and ~30 F g^{-1} at higher current density. The stability of the OLCs was tested extensively, and it remained clear that these materials are useful when it come to the overbearing of both high current densities and voltages which becomes a great deal for industrial applications [152]. Due to the above reason, in 2010, David Pech and co-workers [153] constructed a micro-ECs system using interdigital onion-like carbon electrodes and compared to other ECs system of the same length scale. The micro-ECs system was able to operate efficiently at extremely higher scan rates of ~100 V s^{-1} and hence, to show much faster performance compared to other pure EDLCs systems that run at the scan rates at around 1 V s^{-1} and below. It is worth noting that the power performance of the EDLCs is higher than that of other ECs systems. Nevertheless, the power performance of the ECs made from the OLC electrodes is 10x greater than that of ECs made from activated carbon (AC) electrodes. But the energy density of the OLC system is lower than that of the activated carbon due to the low specific surface area of the OLCs compared to the activated carbon [146], [153]. The curvature effect of OLCs has been demonstrated to be of positive gain towards energy storage as the particle sizes of the OLCs decreases. Thus, the reason many scientists prefers the nano-onions (with small diameters and particle sizes) derived from the vacuum annealing of the nanodiamond for electrochemical capacitors [148], [154], [155]. Onion-like carbons have been used to make composites with other capacitive materials such as conducting polymers and transition metal oxide to improve their stability and capacitive performance. The as-synthesised OLC-PANI composites have demonstrated a remarkable specific capacitance of 640 F g^{-1} in symmetric two electrode system and a stable rate capability even after 10000 cycles [156]. In 2013, Gao *et al.* demonstrated that the increase of the OLC porosity in outer shells through chemical activation results in an improved electrochemical performance of the ECs system. A maximum specific capacitance of 122 F g^{-1}, the remarkable high power density of 153 kW Kg^{-1} and excellent energy density of 8.5 Wh Kg^{-1} was achievable after OLC activation [149]. Due to the relatively high conductivity of the OLC observed from the smooth flow of electrolyte ions on its surface area and the high rate capability reported in the literature, scientist began to explore this material as conductive additives to replace carbon black [157], [158]. It is evident from the literature's perspective that OLCs as compared to another carbon allotrope is insufficiently studied. According to the Web of Science search, fullerenes discovered by Smalley *et al.* [159] in 1985 has 30 000 results. CNT identified in 1991 have 123 000 results. Graphene found ten years ago already has 52 000 results while OLCs discovered 30 years ago has only 1400 results with almost 280 related to energy and only 40 results specifically related to electrochemical capacitors [160]. There is still much to be learned about this material as the energy storage material for ECs applications. Hence, one of the focus of this study is to explore the OLCs electrodes.

2.4.2 Transition Metal Oxide (i.e., Mn_xO_y) as Pseudocapacitor Materials

Reduced sizes of bulk materials into the nanoscale significantly affect the physical and chemical properties of the materials. Nanomaterials are estimated to bring significant improvements for energy storage devices as the size reduction of materials increases the contact surface area between the electrode and the electrolyte, and decreases the transport path length for both electrons and ions. Transition metal oxides nanomaterials are estimated to bring significant improvements for energy storage devices as the size reduction of materials increases the contact surface area between the electrode and the electrolyte, and decreases the transport path length for both electrons and ions in pseudocapacitors (PCs) [161], [162]. Ruthenium oxide, RuO_2, appeared to be a promising electrode material due to its high capacitance, good conductivity, excellent electrochemical reversibility and high rate capability. However, the cost, lack of abundance, and toxic character required seeking alternatives. Considerable attention is devoted to manganese oxide based materials, due to their environmental friendliness in nature. Manganese dioxides, characterized by their high theoretical specific surface area (1370 m^2 g^{-1}), high theoretical capacitance, low-cost and abundance in nature have attracted significant interest in ECs applications. Manganese oxide can be presented in various oxidation states and phases as mentioned above. The most often studied phases are MnO_2 with an oxidation state of +4, Mn_2O_3 with an oxidation state of +3 and Mn_3O_4 with the oxidation state of both +2 and +3.

a) MnO_2

MnO_2 nanomaterials can exist in different types of structural phases α-, β-, γ-, δ-, ε- and λ-types, when the basic structural unit ([MnO_6] octahedron) is linked in different ways [163]. The properties of MnO_2 are significantly affected by their phases and morphologies; moreover, the operating properties of ECs also depend on the phase of

MnO_2. In this regard, more energy has been focused toward the preparation of MnO_2 with different phases and shapes [164]. Several structural forms of MnO_2 with different nanoarchitectures such as nanowires [165], nanorods [166], single crystal nanotubes [163], nanourchins [167] and amorphous [168] have been synthesised using hydrothermal techniques. Some other techniques used for the synthesis of MnO_2 nanostructures include thermal decomposition, co-precipitation [169], [170], simple reduction [171], sol-gel [172], solid-state process and microwave process [173]. Research on manganese dioxide (MnO_2) as a potential electrode material for ECs surfaced very slowly at around 1999, with the study from Lee and Goodenough [174] when they were investigating pseudocapacitive behaviour of an amorphous manganese dioxide (MnO_2) in aqueous electrolyte (2 M KCl) as a way to compensate the cost disadvantage brought by the use of RuO_2. In 2002, there was an improved outcome in terms of the literature regarding synthesis and testing of manganese oxide-based ECs electrode materials [175], [176]. An amorphous hydrous manganese oxide (a-$MnO_2 \cdot nH_2O$) was anodically deposited onto a graphite substrate showing an improved maximum specific capacitance of 330 F g^{-1} and 320 F g^{-1} achieved from cyclic voltammetry and galvanostatic charge-discharge measurements respectively using Na_2SO_4 (0.1 M) as electrolyte [175]. It can be said that before year 2004, the fundamental understanding of the reaction involved in the electrode/electrolyte interface of the manganese oxide-based electrode was not yet clearly understood. Toupin and co-workers later published their work with the aim of getting a better understanding of the charge storage mechanism in manganese dioxide electrodes when cycled in aqueous electrolyte [6]. It has been established that pseudocapacitive (Faradic) reactions occurring on the surface and in the bulk of the electrode are the major charge storage mechanisms for manganese oxides. The surface reaction involves the adsorption of electrolyte cations ($C^+ = H^+$, Li^+, Na^+ and K^+) on the manganese oxide whereas the bulk Faradaic reaction relies on the intercalation or de-intercalation of electrolyte cations in the bulk of the manganese oxide and are illustrated by equation 2.22 and 2.23 respectively [6], [177]:

$$(MnO_2)_{surface} + C^+ + e^- \longleftrightarrow (MnO_2^- C^+)_{surface} \quad (2.22)$$

$$MnO_2 + C^+ + e^- \longleftrightarrow MnOOC \quad (2.23)$$

In the established charge storage mechanisms, a redox reaction between the III and IV oxidation states of Mn ions occurs [177]. At this time it was clear that the crystal structure of the crystallized Mn_xO_y-based materials play an important role in the improvement of the electrochemical properties of the electrode material and also, preparation of composites with other materials does improve the electrocapacitive performance [170], [178], [179]. However, owing to the high resistivity of *a*-$MnO_2 \cdot nH2O$, a conducting additive, such as carbon materials, CNTs or Graphene, and OLCs, are required for the realization of ECs electrodes [180], [181]. As a result, *a*-MnO_2 has been prepared on the SWCNT by a simple precipitation technique with good cycle power at the current density of 2 A g^{-1} [182]. In 2007, Ma *et al.* [183] synthesised birnessite-type MnO_2 coated uniformly on multi-walled carbon nanotubes (CNTs). The specific surface area of 200 m^2 g^{-1} obtained after a spontaneous direct redox reaction between the multi-walled CNTs and permanganate ions (MnO_4^-). A high specific capacitance of 250 F g^{-1} at a high current density of 1 A g^{-1} (MnO_2/CNT nanocomposite) was reported. In 2013, Jafta *et al.* [58] synthesised α-MnO_2 from the raw electrolytic manganese dioxide (EMD) using the hydrothermal technique in the presence of a surfactant (SDS) and decorated them on the surface of the graphene oxide (GO). The electrochemical properties of nanostructured α-MnO_2/GO composite fabricated in an aqueous asymmetric electrochemical capacitor exhibited high energy density of 35 Wh kg^{-1} and specific capacitance of 280 F g^{-1} at high voltage window of 1.8 V using 1 M Li_2SO_4 as the electrolyte. These remarkable electrochemical properties coupled with long-term cycling stability clearly indicated that the nanocomposite may be suitable for future development of low-cost asymmetric electrochemical capacitors (ECs).

b) Mn_3O_4

Manganese oxide can be presented in various oxidation states and phases as mentioned above. The most often studied phases are MnO_2 with an oxidation state of +4, Mn_2O_3 with an oxidation state of +3 and Mn_3O_4 with the oxidation state of both +2 and +3. Manganese (II, III) oxide is the chemical compound with formula Mn_3O_4. It exists in two oxidation states, +2 and +3, and its formula written as $MnO.Mn_2O_3$. Manganese (II, III) oxide, Mn_3O_4, is found in nature as the mineral hausmannite. Hausmannite Mn_3O_4 consist of a spinel structure with tetragonal distortion elongated along the c-axis due to Jahn-Teller effect on the Mn^{3+} ion. Manganese ions occupy the octahedral B-site (Mn^{3+}) and tetrahedral A-site (Mn^{2+}) corresponding to a normal spinel structure. There are 32 oxygens and 24 cations in the unit cell [184]. Several studies were conducted to improve Mn_3O_4 electrode materials in ECs. Subsequently, to improve the electro-capacitive behaviour of Mn_3O_4, the nanosized particles of Mn_3O_4 have been prepared by various methods. Some of these methods include successive ionic layer adsorption and reaction (SILAR) [185], hydrothermal [186], solution combustion [187], chemical bath deposition [188], sonochemical [189], microwave irradiation and microwave assisted techniques [190]–[193]. Manganese (II, III) oxide (Mn_3O_4) as a potential electrode material for ECs showed up just after the researchers discovered MnO_2 as a pseudocapacitive electrode material. In 2003, a novel class of electrochemical capacitor electrode material had been electrochemically synthesized from a manganese halide complex in water-containing acetonitrile electrolyte at room temperature. Spectroscopic analysis showed a good agreement of the as-synthesised material with those of tetragonal hausmannite, Mn_3O_4. This thin film electrode material displayed electrochemical properties with a specific capacitance of 92 F g^{-1} in aqueous electrolyte and 58 F g^{-1} in organic electrolyte from cyclic voltammetry at the scan rate of 20 mV s^{-1} [194]. In the following years even though the study of manganese oxide continued, it was still not convincing that this material can find its prime time in the energy storage applications though there was still an on-going research [195], [196]. In 2005, Wu and Hu [197] studied a mixture, consisting of Mn_3O_4 and MnOOH crystals and reported specific capacitance ranging between 45-71 F g^{-1}. In the same year, Djurfors *et al.* [198] showed that Mn_3O_4 film prepared by either thermal and electrochemical oxidation of Mn/MnO films have an effect on the capacitive performance of the electrode material. Nagarajan *et al.* later followed the principle of Djurfors *et al.* to form a spinel Mn_3O_4 phase at 300 ◦C with an improved specific capacitance value of 445 F g^{-1} in 0.25 M Na_2SO_4 aqueous electrolyte [199]. As a race in finding a stable and suitable electrode derived from the Mn_3O_4 material, researchers developed composites of this material from carbon templates. In 2008, a low-temperature, efficient and one-step deposition technique, in which $Mn(CH_3COO)_2{\cdot}4H_2O$ serves as precursor and O_2 as the oxidant, was employed to deposit Mn_3O_4 nanoparticles on multiwalled carbon nanotubes (MWCNTs) in ethanol solution at 150 and 200 ◦C. The electrochemical performance of the Mn_3O_4/MWCNT composites as an electrode material was examined using cyclic voltammetry and obtained a maximum specific capacitance of 330 F g^{-1} [200]. In 2010, Wang *et al.* [201] used graphene sheet as a template for the decoration of Mn_3O_4 by mixing graphene suspension in ethylene glycol with MnO_2 organosol, followed by subsequent ultrasonication processing and heat treatment. The Mn_3O_4/graphene nanocomposite electrode materials for ECs exhibited a high specific capacitance of 175 F g^{-1} in 1 M Na_2SO_4 electrolyte and 256 F g^{-1} in 6M KOH electrolyte, respectively was achieved. Dubal *et al.* have employed two other simple techniques such as chemical bath deposition (CBD) and successive ionic layer adsorption and reaction (SILAR) to fabricate Mn_3O_4 nanoparticles on stainless steel. The capacitive performance of Mn_3O_4 thin film synthesised from CBD and SILAR independently exhibited a maximum capacitance of 284 and 314 F g^{-1} respectively in 1 M Na_2SO_4 electrolyte [184], [188]. In 2013, Dubal and Holze [202] reported a novel kind of all-solid-state flexible electrochemical capacitor configuration consisting of two slightly separated Mn_3O_4 thin films as electrodes and H_2SO_4-PVA gel as the solid-state electrolyte. The device showed good electrochemical performances, such as high specific capacitance of about 127 F g^{-1} and well enough energy and power density values of more than 10 Wh Kg^{-1} and 5 kW Kg^{-1} respectively with 89% of capacity retention after 2000 cycles. Recently, in 2015, Qiao *et al.* [203] synthesised micro/nano-structured Mn_3O_4 with an open 3D flower-like morphology by a facile solvothermal approach using hexadecyltrimethylammonium bromide as a surfactant and ethanol as a solvent. The Mn_3O_4 microspheres used exhibited electrochemical performance with a specific capacitance of 286 F g^{-1} at a low current density (0.5 A g^{-1}), and still retained 80% (230 F g^{-1}) and 73% (210 F g^{-1}) at higher current densities of 5 A g^{-1} and 10 A g^{-1}, respectively.

c) Mn_2O_3

Manganese (III) oxide, Mn_2O_3 and Manganese (II) oxide, MnO are other types of the oxides of manganese derivatives. There are substantially few literature reviews on these materials as ECs materials. Two forms are recognizable in Mn_2O_3, α-Mn_2O_3, and γ-Mn_2O_3. The α-Mn_2O_3 has the cubic bixbyite structure while pure Mn_2O_3 has an orthorhombic structure γ-Mn_2O_3 has a structure related to the spinel structure of Mn_3O_4 with the oxide ions firmly packed in the cubic form [204]. MnO, just like any monoxides, adopts the rock salt structure, with anions and cations being both octahedrally coordinated [205]. Just as much as any manganese oxide material, Mn_2O_3 nanospheres have been synthesized using hydrothermal and sonochemical techniques by Nathan *et al.* as an ECs electrode material [206]. Chen *et al.* has successfully synthesised of γ-Mn_2O_3 nanowire bundles [207]. Recently, Li *et al.* synthesised nanocubes Mn_2O_3 using the hydrothermal technique for the ECs application [208]. Nano-sized manganese oxide (Mn_2O_3) was synthesized by Chiang *et al.* using a solvothermal method [209]. There is limited literature on the synthesis of Mn_2O_3 for ECs application even though several of this material have been widely synthesised using various techniques such as chemical oxidation [210], Calcination of MnO_2 and hydrothermal [211]. These two forms of manganese oxide-based materials (i.e., Manganese (III) oxide, Mn_2O_3 and Manganese (II) oxide, MnO) have been synthesised using several techniques and tested for various applications, but their interrogation as ECs electrode materials is still not well reported. The study of Mn_2O_3 as an electrode material for electrochemical capacitors (ECs) surfaced at around 2006 when Chiang *et al.* [209] reported on the synthesis and the examination of the nanoparticles of Mn_2O_3 as a potential electrode. The electrode material exhibited a maximum specific capacitance of about 197 F g^{-1} from cyclic voltammetry at the scan rate of 10 mV s^{-1}. In 2008, Yu *et al.* [212] managed to synthesise Mn_2O_3 particles made of micropores. The electrochemical capacitive performance of these microporous particles improved to specific capacitance as high as 350 F g^{-1}. The improved performance is believed to be as a result of a relatively high specific surface area of 283 m^2 g^{-1}. Carbon materials are known to have a synergistic effect that brings stability to the manganese oxide-based electrode materials, Zhang *et al.* [213] reported the study of nano-sized Mn_2O_3, which was homogenously incorporated into mesoporous carbon template to form Mn_2O_3/C nanocomposite. The results obtained showed an improved electrochemical performance with the maximum specific capacitance of 600 F g^{-1}, the value that is almost twice the one achieved by Yu *et al.* and also close to the values obtained when using RuO_2 as an electrode material. In 2011, Wang and co-workers [214] showed that a composite of Mn_2O_3 and carbon aerogel microbead (CAMB) can be achieved by using an in situ encapsulation technique and be used as an electrode material for ECs. The capacitive behaviour of the Mn_2O_3/CAMB electrode resulted from an optimization of mass variation of the Mn_2O_3 (10 wt. %) displayed a maximum specific capacitance of 368 F g^{-1}, emphasising the fact that indeed this type of the manganese oxide material is well suited to be employed in the ECs applications. Recently in 2015, Li *et al.* developed a novel Mn_2O_3 nanocubins that are porous, through the hydrothermal technique that was followed by calcination in air. The as-synthesised Mn_2O_3 nanocubins exhibited a specific capacitance of 191 F g^{-1} at a current density of 0.1 A g^{-1}. This electrode material showed relatively high rate capability at a high current density of 5.0 A g^{-1} and excellent long-term cycle stability even after 3000 cycles. According to the obtained electrochemical results are shown above, Mn_2O_3-based electrode material presented itself as a promising material best suited for the advancement of ECs technology [215]. Unfortunately, its growth and attention have been dramatically slow as compared to other manganese oxide-based electrode such as MnO_2 and Mn_3O_4 [216]. To the best of our knowledge, there is no literature on the use of manganese mono oxide (MnO) as an electrode material for electrochemical capacitors (ECs) application.

In conclusion, the Mn_xO_y-based electrodes substantially display promising properties for the development of the state-of-the-art energy storage device coupled with relatively low cost and environmentally friendly.

2.4.3 Transition Metallophthalocyanines (i.e., MPc) as Pseudocapacitor Materials

Phthalocyanines (Pcs) are 18π-electron aromatic macrocycles that have a characteristic blue, green colour that makes them materials of choice for making dyes. They have adopted their name from Greek where Phthal originated from Naphtha, which means a rock oil while cyanine means blue. Phthalocyanines made of 16 carbon and eight nitrogen atoms with more than 70 different metals and non-metals incorporated in them [217], [218]. PCs are a unique class of compounds that have a similar structure as tetraazoporphyrin with additional four fused benzo rings. Metallophthalocyanines attracted enormous attention worldwide due to their attractive properties such as thermal and chemical stability, chemical inertness, very colouring properties, catalytic activity, semi-conductivity, and photoconductivity. The ability to incorporate ring substituent in the peripheral and non-peripheral position with its properties like solubility obtained by changing the central metal ions and axial ligand have resulted in this class of compound having a broad range of applications [219]. The metal ion in the central cavity of the phthalocyanine moiety provides the ability to study redox chemistry on this compound. Redox reactions of this molecules occur either at the central metal atom, in the phthalocyanine ring itself or on both. Synthesis of phthalocyanines can be achieved using different routes depending on the desired type of phthalocyanine; metal free, symmetrical and asymmetrical metallophthalocyanines. Various precursors such as phthalonitrile, phthalic acid, phthalic acid anhydride, phthalimide, diiminoisoindoline, and o-cyanobenzamide developed for the synthesis of metallophthalocyanines complexes [217], [220]. Figure 2.16 illustrates the structure of metallophthalocyanine (Ni^{2+} as a central metal).

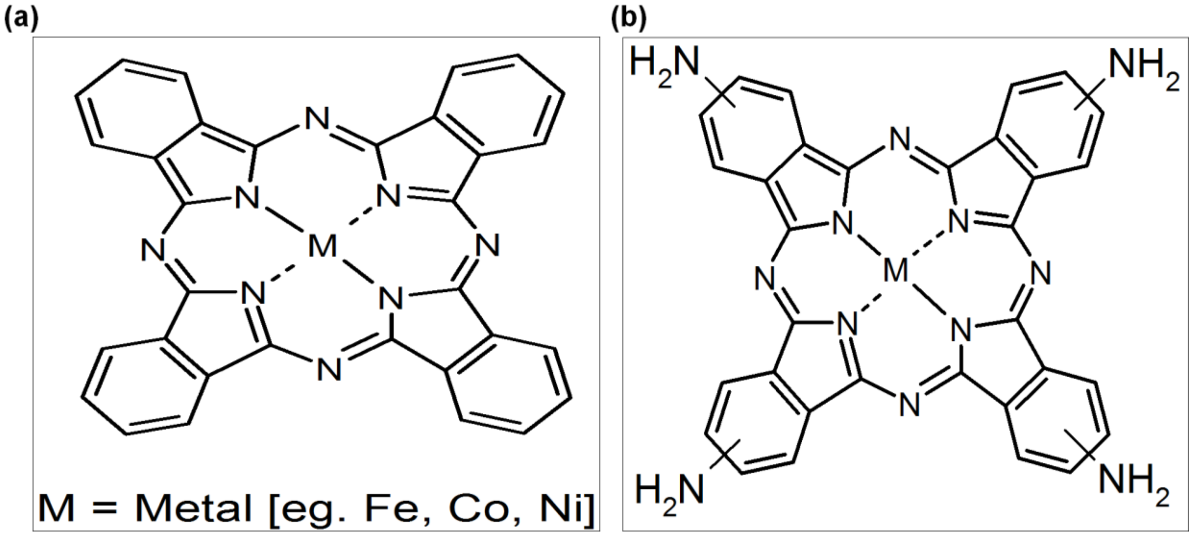

Figure 2.16: Molecular structure of (a) Metallophthalocyanine and (b) Metallo-tetraaminophthalocyanine (MTAPc) complex.

The insolubility of PCs to several aqueous solvents has hampered their use in many applications. Although its solubility in some organic solvents, phthalocyanines, have found applications in ink jet printing, electrophotography, electrochemical sensors and energy storage such as supercapacitors. Extensive research work has been carried out to improve the electrical conductivity of phthalocyanines via doping mechanism and polymerization methods. And this modification opens the even more extra application for this tremendous class of complexes [217], [221]–[225].

Transition-metal phthalocyanines (MPc's) are considered as active electrode materials for pseudocapacitors [26], [226]. A significant aspect of the development of advanced ECs is the improvement of their energy density without sacrificing their high power density and cycle ability by designing composite material with high surface area, excellent conductivity, and proper pore size distribution.

Metallophthalocyanine (MPc) complexes and their derivatives are the well-known class of N4-macrocyclic metal compounds with attractive physical and chemical properties [223]. They are employed in a possible range of technological applications such as electrochemical capacitors, sensors, field effect transistors photocatalysis and electrocatalysts [124], [222], [224], [227]. MPc complexes such as nickel (II) tetraaminophthalocyanine (NiTAPc) have been supported on multi-walled carbon nanotubes (MWCNTs) and tested as a pseudocapacitance device in 1 M H_2SO_4 electrolyte and has shown exciting electrochemical capacitive performance [10], [228].

2.5 Electrochemical Characterization Techniques for ECs Applications

This section takes account of the basic principles of all the electrochemical techniques used for the characterization of all electrodes material in ECs applications.

2.5.1 Cyclic Voltammetry (CV)

Cyclic voltammetry is a potentiodynamic electroanalytical technique that is used to provide qualitative information about electrochemical processes that happen at the electrode/electrolyte interphase in a voltaic cell. In most of the ECs data collection, CV is usually the first electrochemical characterization tool utilised to measure the thermodynamics of the redox potentials taking place on the assembled half cells of the energy storage electrode materials [229]. The relationship between the measured current and the applied potential describe the nature of the process that happens at the electrode/ electrolyte interphase, and this includes information on the charge separation as well as electron-transfer reactions which are hugely valuable resources in ECs. A potentiostat connected to a three-electrode system (Fig 2.17a) or two-electrode system (Fig 2.17b) used to acquire data from the electrochemical cells is employed. A three-electrode system consists of a working electrode (WE), a counter electrode (CE) and a reference electrode (RE). The working electrode is usually made of inert materials and serves as a platform where the electrochemical reaction occurs. The reference electrode is an electrode which has stable and known electrode potential and is usually used as a benchmark in the determination of the potential of a WE while the counter electrode is used to complete the circuit. A two-electrode system consists of the positive electrode (cathode) and a negative electrode (anode). Cyclic voltammetry experiment comprises of scanning the potential of the working electrode for a particular period using a triangular waveform as depicted in Fig 2.18a. The electrode potential is thus increased linearly with time at a specific scan rate with the time range t_0 – t_2

representing the first cycle t_1 indicating the start of the reverse sweep and $t_2 - t_4$ indicating the second cycle. During these potential sweeps the current, which results from the electrochemical reactions taking place at the electrode interface, is measured as a function of the potential. Therefore, a cyclic voltammogram is a plot of a current response versus the applied potential (Fig. 2.18b).

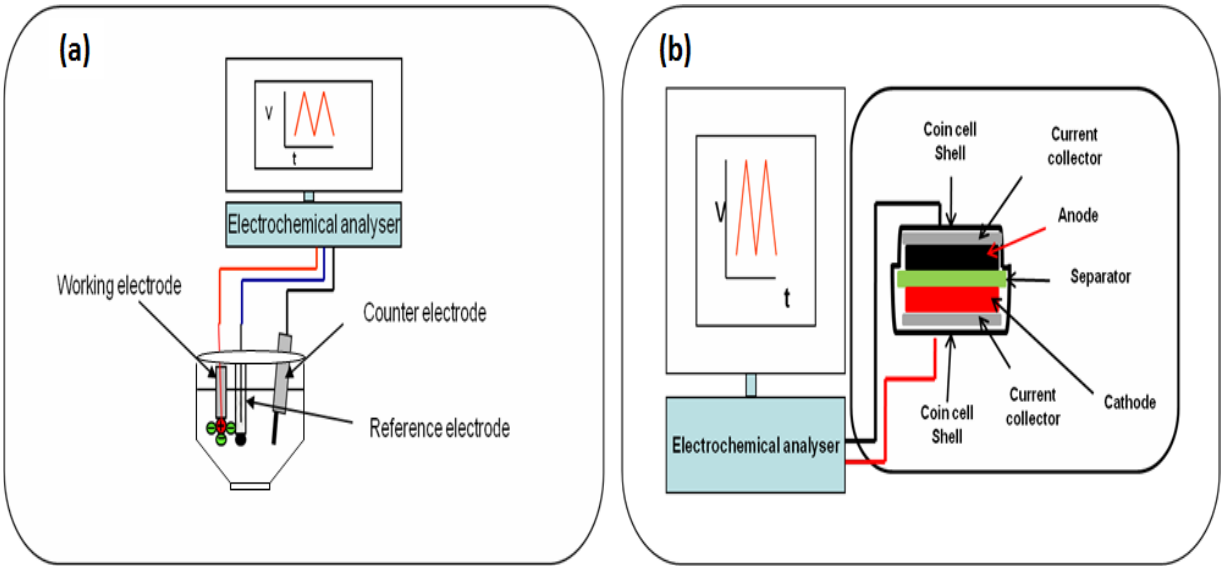

Figure 2.17: The schematic diagram is representing (a) a three electrode, half-cell, system and (b) a two electrode system, connected to an electrochemical analyser [230].

Figure 2.18b shows the behaviour of the electrode material as either pseudocapacitive or electrochemical double layer capacitive systems. The cyclic voltammograms of the ideal electric double layer capacitance are rectangular in shape [158]. This measurement shows that the charge storage is purely double layer capacitance which is due to non-faradaic processes. One prominent observation from this kind of behaviour is that applied current is independent of applied voltage. The reverse scan of an ideal electric double layer material is a mirror image of the forward scan [231]. The shape of a parallelogram shown in Fig. 2.18b indicates that there is resistance to the transfer of charges between an electrode and the electrolyte. As discussed earlier, the electrode materials that display Faradaic processes give cyclic voltammogram that deviates from a rectangular shape since charges accumulated on the electrode is dependent on the applied potential. For pseudocapacitors, the CVs have redox peaks that show the involvement of faradaic reactions [232].

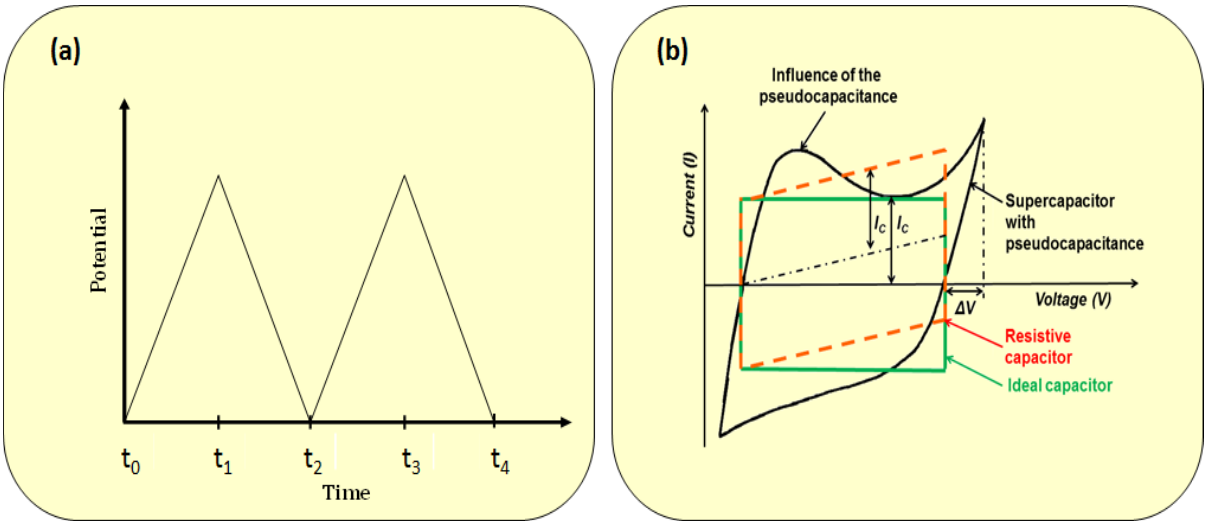

Figure 2.18: The representation of (a) a potential profile for two cyclic voltammetry scans and (b) typical cyclic voltammograms of different capacitive electrodes.

Cyclic voltammetry is a powerful analytical tool that provides information on the thermodynamics of redox processes, kinetics of heterogeneous electron transfer reactions and adsorption processes [233]. In CV, the electron transfer processes occurring at the surface of the electrode material can be labeled as reversible, irreversible or quasi-reversible depending on the nature of the electrode material evaluated. The summary of some of the crucial parameters used as diagnostic criteria for evaluating these processes is listed in Table 2.2.

Table 2.2: The diagnostic criteria for reversible, irreversible and quasi-reversible cyclic voltammetric process

Parameter	Cyclic Voltammetry Process		
	Reversible	*Irreversible*	*Quasi-reversible*
E_p	Independent of ν	Shifts cathodically by 30/αn mV for a 10-fold increase in V	Shifts with ν
$E_{pc} - E_{pa}$	~ 59/n mV at 25°C and independent of ν	–	May approach 60/n mV at low ν but increases as ν increases
$i_p / \nu^{1/2}$	Constant	Constant	Virtually independent of ν
i_{pa} / i_{pc}	Equals 1 and independent of ν	No current on the reverse side	Equals 1 only for α = 0.5

It is worth noting that in ECs analysis, specific (or gravimetric) capacitance can be calculated from the cyclic voltammograms using the equation 2.20 and 2.21:

$$C_{sp}(F\ g^{-1}) = \frac{\int idt}{\Delta Vm} \qquad 2.20$$

where $\int idt$ is the total charge (A s) obtained by integration of current (A), V (V) is the maximum voltage (V) and m is the mass of active electrode (g).

$$C_{sp}(F\ g^{-1}) = \frac{i}{\nu m} \qquad 2.21$$

where i is the current (A), ν is the scan rate (V s^{-1}), and m is the mass of active electrode (g).

2.5.2 Galvanostatic Charge-Discharge (GCD)

The galvanostatic charge-discharge technique is the widely used method in ECs application and the most important characterization tool for the determination of the electrochemical performance of the ECs electrode materials. From this characterization technique, most of the relevant parameters such as the specific capacitance, the power and energy densities, the rate capability and the Coulombic efficiency of the ECs system can be extracted. In GCD application, a constant current is applied, and the potential of the working electrode is monitored relative to reference electrode with time (see Fig 2.19a). Upper and lower potential limits are set for the working electrodes. Once one of this limit is reached the charge or the discharge curve stop and the current reverses, the next step in the cycle begins as depicted in Fig 2.19b.

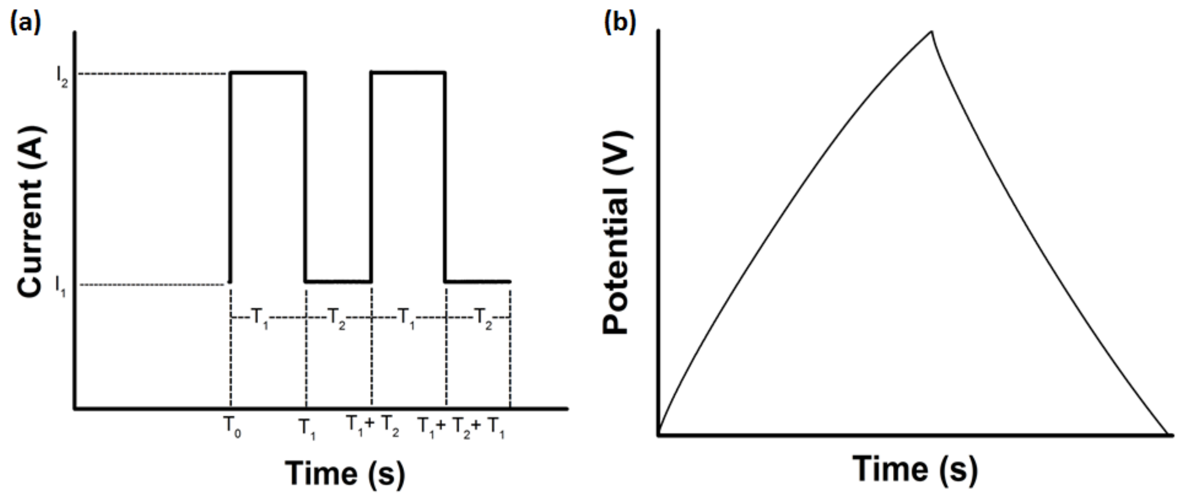

Figure 2.19: The representation of (a) current versus time profile and (b) potential versus time profile, during galvanostatic charge-discharge in ECs.

The pattern at which the GCD curve display, gives information on the type and behavior of the electrode material fabricated. The relationship between potential and time for the EDLCs capacitor is linear resulting in a GCD curves that are a mirror image of each other as shown in Fig 2.19b, while for pseudocapacitors, the relationship between measured voltage and time is non-linear resulting in the GCD curves that are not mirror images of each other. The GCD curves of pseudocapacitive material have at least a hump on their profile to illustrate the redox activity of the material whereas the GCD curves of the EDLCs materials have no hump as there is no redox activity taking place on their surface but only a pure electrostatic charge separation. To gain understanding of the power performance as well as the ability of the electrode material to retain its capacitance, a variation of current density on the GCD technique must be employed. The power of the electrode material considerably increases when charge-discharge measurements evaluated at higher current density with the stable electrode material. To attain higher energy density, usually the maximum voltage window is increased by the use of different electrolytes that are stable at a higher voltage (i.e., Organic and Ionic electrolytes). Equations 2.16-2.18 are used to determine all the electrochemical performance (i.e., specific capacitance, energy and power density) of an ECs system using information from the GCD technique. Another important parameter in an ECs electrode material evaluation is the deliverable energy efficiency also known as Coulombic efficiency, obtained by equation 2.21 [234].

$$\eta\ (\%) = \frac{t_d}{t_c} \times 100\% \qquad 2.21$$

where t_d is the discharge time and t_c is the charging time.

One other important aspect of ECs electrode materials is that they must have longer cycle life with the stability in the order of thousands of cycles. Recently, voltage-holding over several hours has been recommended as the ideal method of testing the stability of the ECs electrode material instead of the traditional rapid cycling over an extended period [235].

2.5.3 Electrochemical Impedance Spectroscopy (EIS)

In today's scientific community, the concept of electrical resistance is well known mainly in electrical systems. Electrical resistance is the ability of a circuit element to resist the flow of electrical current. The electrochemical impedance spectroscopy has gained popularity as a vital electrochemical characterization technique that can measure and give feedback on the electrical resistance of several systems such as ECs and LIBs. The promise of EIS is that a broad range of physical and chemical phenomena characterised by a single experimental run covering a sufficient range of frequencies. The analytic process in EIS depends on diffusion of reactants (ions from electrolytes in ECs) toward or away from the surface that has a particular low-frequency character. It measures the dielectric properties of a medium as a function of frequency, based on the interaction of an external field with the electric-dipole-moment of the sample, often expressed by permittivity (see Fig 2.20)

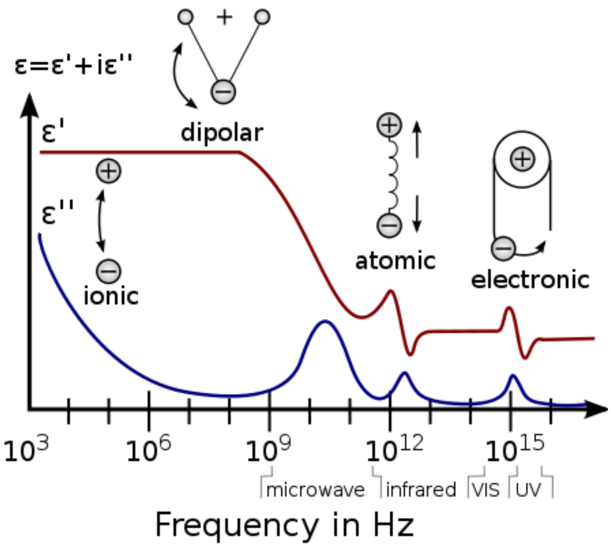

Figure 2.20: Representation of a dielectric permittivity spectrum over a wide range of frequencies. The real and imaginary parts of permittivity and various processes depicted: ionic and dipolar relaxation and atomic and electronic resonances at higher energies.

This electrochemical technique is used to study and determine many parameters useful in ECs applications. The general concept begins with the Ohm's law that gives the relationship between current and resistance at a constant voltage. According to Ohm's law the resistance (R) is equal to the potential (V) over the current (I):

$$R = \frac{V}{I} \qquad 2.22$$

The unfortunate limitation of this relation is that it is only applicable to one circuit element referred to as the "ideal resistor". The ideal resistor has several simplifying properties, such as (i) the "ideal resistor" follows Ohm's law at all currents and voltages, (ii) its resistance is independent of frequency and (iii) current and voltage signals through a resistor are in phase with each other. But this is not the case in the real world applications where much more complex circuit elements are involved. Therefore, impedance concept is the parameter used since is a more general circuit parameter instead of the simple concept of resistance [236]. Impedance defined as the measure of the ability of a circuit to resist the flow of electrical current (similar to resistance), it does not involve the simplifications mentioned above used for the ideal resistor. Electrochemical impedance is ordinarily measured using a small excitation signal obtained by applying an AC potential that is sinusoidal to the electrochemical cell and then measuring the current through the cell. This measurement is carriedout so that the cell's response is pseudo-linear. In a linear (or pseudo-linear) system, the current response to a sinusoidal potential will be a sinusoid at the same frequency but shifted in phase (see Fig 2.21a). This current response can be analysed as a sum of sinusoidal functions at the same frequency but at a different phase (a Fourier series).

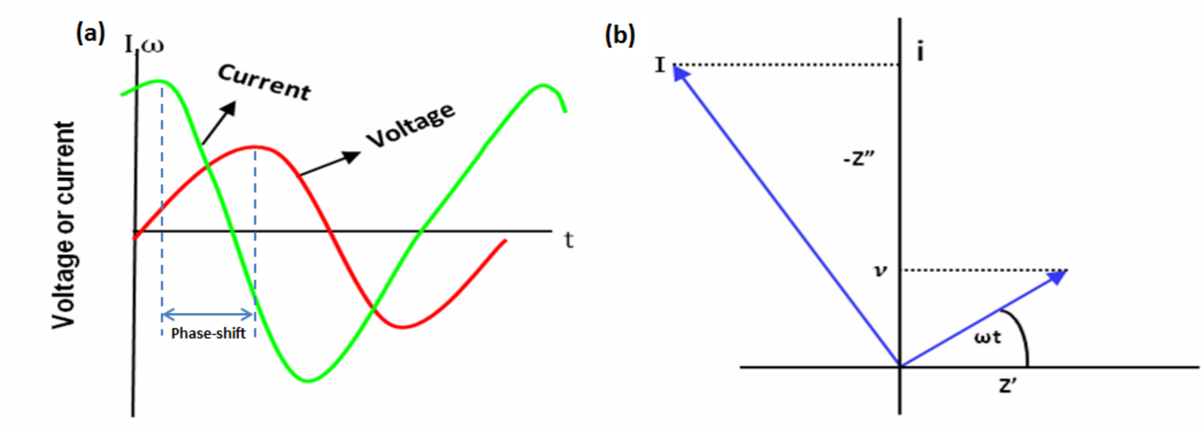

Figure 2.21: Representation of (a) two graphs showing a current response curve from an applied sinusoidal voltage curve and (b) vector depicting real and imaginary impedance.

The excitation signal, expressed as a function of time, has the form:

$$V(t) = V_0 \sin(\omega t) \qquad 2.23$$

where *V(t)* is the potential at time t, V_0 the amplitude of the signal and ω is the radial frequency expressed as:

$$\omega = 2\pi f \qquad 2.24$$

The current response signal is express as:

$$I(t) = I_0 \sin(\omega t + \varphi) \qquad 2.25$$

where *I(t)* is the response signal at time t, I_0 the amplitude of the response signal and φ is the phase shift. An expression analogous to Ohm's law allows for the calculation of impedance as:

$$Z = \frac{V(t)}{I(t)} = \frac{V_0 \sin(\omega t)}{I_0 \sin(\omega t + \varphi)} = Z_0 \frac{\sin(\omega t)}{\sin(\omega t + \varphi)} \qquad 2.26$$

The impedance is express in terms of a magnitude, Z_0, and a phase shift, φ. By making use of Euler's relation:

$$exp(j\varphi) = \cos(\varphi) + j\sin(\varphi) \qquad 2.27$$

it is possible to express the impedance as a complex function:

$$Z(\omega) = Z_0 \frac{\sin(\omega t)}{\sin(\omega t+\varphi)} = Z_0 \exp(j\varphi) = Z_0[\cos(\varphi) + j\sin(\varphi)] \qquad 2.28$$

The expression for *Z(ω)* shown in equation 2.28 is made up of a real and an imaginary part where the real part is a plot on the x-axis and the imaginary part on the y-axis producing the "Nyquist plot" shown in Fig. 2.22a. Nyquist plots in Fig. 2.22b shows the manner at which the impedance of a fast charge transfer reaction under diffusion control behaves at a planar electrode. This Nyquist plot result is fitted using the electrical equivalent circuit (EEC) as shown in Fig. 2.23. Every point in this graph represents the impedance at a particular frequency. A Rs value indicates the solution resistance that exists between the surface of the working electrode and reference electrode. A Rct (or Rf) value is known as the charge transfer resistance. Warburg impedance element ω characterizes the diffusional process happening in the reaction. ESR is the equivalent series resistance, and it consist of solution resistance, resistance to the porous layer and contact resistance between current collector and an electrode. EDR is the equivalent distributed resistance in the Warburg region when the Warburg has a slope of 45°. For an ideal capacitor, the impedance plane plot is parallel to the imaginary axis while that of EDLC, at high frequency it makes a 45° angle at low frequency and is nearly parallel to the imaginary axis of the complex plane impedance plot. There are two or more regions (the high and low-frequency regions) on an impedance plot and the area where this two meet is called knee frequency.

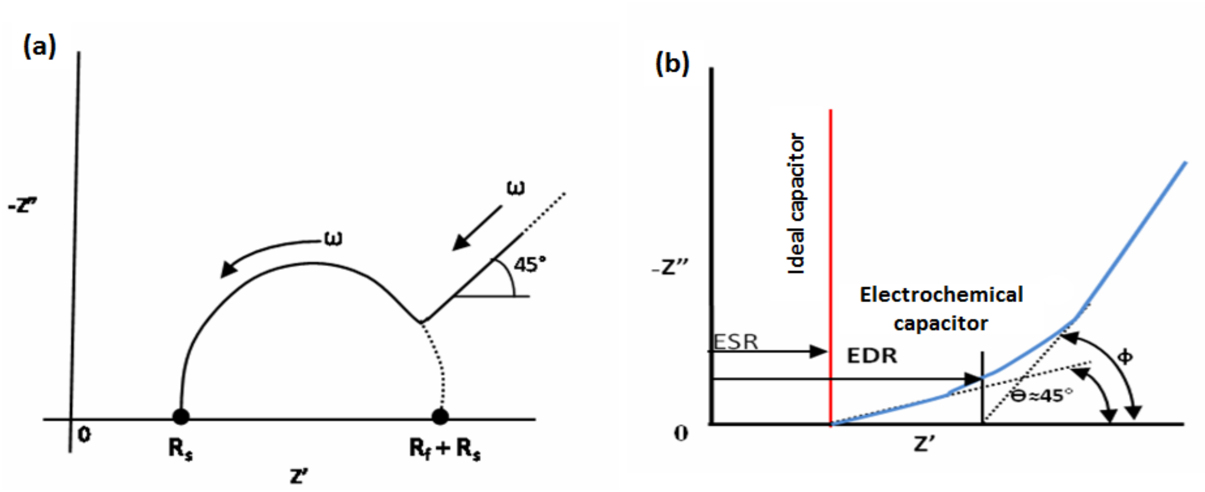

Figure 2.22: Nyquist plot of (a) a diffusion controlled faradaic process and (b) ideal and electrochemical double layer capacitors.

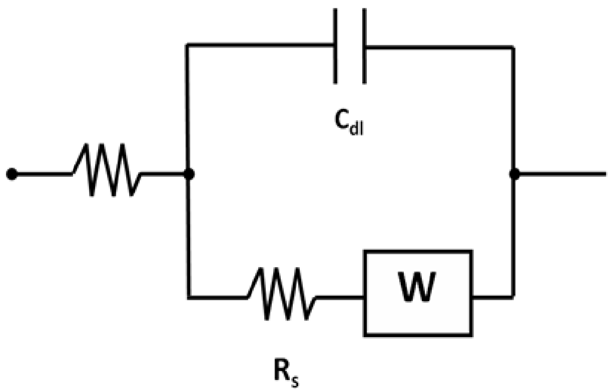

Figure 2.23: Randles equivalent circuit of fast charge transfer reaction that involves diffusion.

2.6 Microscopic, Spectroscopic and Thermal Characterization Techniques for Energy Storage Electrodes In ECs Application

This section takes account of the basic principles of all the microscopic, spectroscopic and thermal techniques used for the characterization of all electrodes material in ECs applications.

2.6.1 Scanning Electron Microscopy (SEM)

The scanning electron microscope utilizes electrons instead of light to form an image. SEM has emerged as one of the powerful characterisation tools used in nanomaterials research today. It has been utilised to image small particles of the electrode powders, where possible, a resolution of up to 10 nm have been recorded, depending on the system type, and generating high-resolution images of shapes of objects and to show spatial variations in chemical compositions [237]. In a typical SEM as shown in Fig. 2.24, an electron beam is thermionically emitted from an electron gun fitted with tungsten (W) filament cathode. Tungsten is usually the best choice in thermionic electron guns due to its highest melting point, lowest vapour pressure and cost effectiveness as compared to all other metals. Apart from tungsten (W), other types of electron emitters include lanthanum hexaboride (LaB_6) cathodes [238].

These types of electron guns produce an electron beam with an average diameter of ~ 15 – 20 μm. A Field Emission (FE) electron gun is used to decrease the electron beam diameter to around 0.5 – 5 nm, and thus obtaining the resolution of the image. This FE electron gun is a W wire, with the tip of a single crystal with a radius of ~ 100 nm.

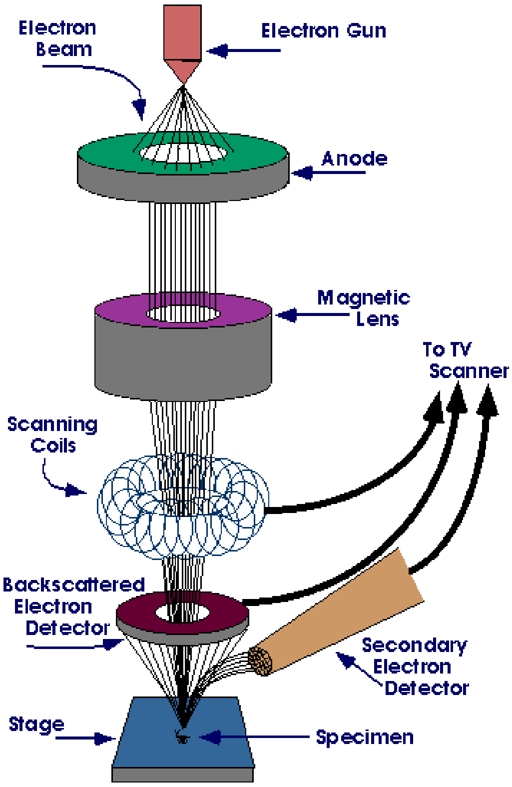

Figure 2.24: Schematic diagram of a typical Scanning Electron Microscope (SEM) [239].

The beam produced, by electrons that are pulled out from the tip by the high electric field, passes through pairs of scanning coils or pairs of deflector plates in the electron column. To avoid ion bombardment to the tip from the residual gas ultra-high vacuum (UHV, ~ 10^{-9} Torr) is needed. When the primary electron beam interacts with the sample, the electrons lose energy by repeated random scattering and absorption within a teardrop-shaped volume of the specimen known as the interaction volume. The energy exchange between the electron beam and the sample results in the reflection of high-energy electrons by elastic by elastic scattering, emission of secondary electrons by inelastic scattering and the emission of electromagnetic radiation, each of which can be detected by specialized detectors.

2.6.2 Transmission Electron Microscopy (TEM)

The transmission electron microscope is a very powerful tool for material science. This instrument utilizes a high energy beam of electrons that is shone through the sample to create an image. The interactions between the electrons and the atoms can be used to observe features such as the crystal structure, growth of layers and interactions of composites materials [240]. In a typical TEM as shown in Fig. 2.25, the source of illumination is a beam of electrons of very short wavelength (high energy), emitted from a tungsten filament at the top of a cylindrical column. Electrons with high accelerating voltage pass through the sample and are scattered in different degree, losing or prevailing initial energy. The elastically scattered electrons produce an imaging contrast. [241]. The spatial variation in this information (the "image") is then magnified by a series of magnetic lenses until the information is collected by hitting a fluorescent screen, photographic plate, or light sensitive sensor like CCD (charge-coupled device) camera. The image detected by the CCD is displayed in real time on a monitor or computer [242].

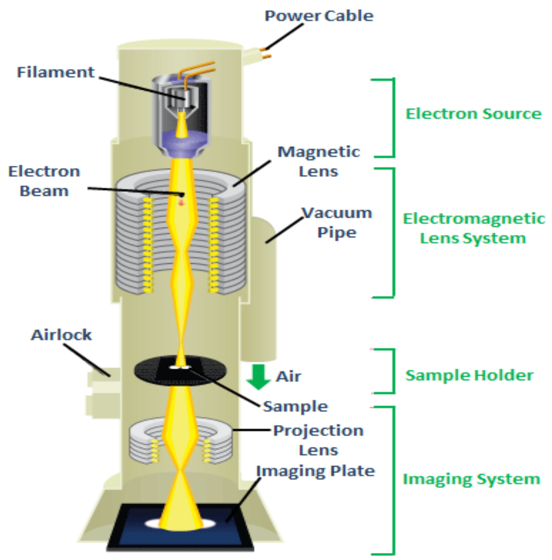

Figure 2.25: Schematic diagram of a typical Transmission Electron Microscope (TEM) [243].

2.6.3 Energy Dispersive X-ray Spectroscopy (EDX)

Energy dispersive X-ray spectroscopy (EDX, EDS, or XEDS), sometimes referred to as dispersive X-ray analysis (EDXA) or energy dispersive X-ray microanalysis (EDXMA), is an analytical tool used to determine elemental composition or chemical characterization of a sample. This analysis is performed to achieve both the qualitative and quantitative elemental composition of the prepared samples. For consistency sake, this technique is abbreviated as EDX throughout the dissertation. EDX systems are typically integrated into SEM or TEM instrument and include a sensitive X-ray detector, a liquid nitrogen dewar for cooling, and software that collect and analyse energy spectra [244].The detector is used to separate the characteristic X-rays of different elements into an energy spectrum while the software is used to examine the energy spectrum to determine the specific elements present in the sample. To stimulate the emission with the X-rays characteristic of a specimen a high energy beam of charged particles such as electrons is focused directly onto the sample having atoms at rest with their electrons at the ground state (or unexcited) in the electron shells bound to the nucleus (see Fig. 2.26). The incident beam may then excite an electron in an inner shell, thereby ejecting it from the shell and creating an electron-hole from its original position. An electron from an outer, higher-energy shell then fills the formed hole, and the difference in energy resulted from the higher-energy shell and the lower energy shell released in the form of an X-ray. An energy-dispersive spectrometer can, therefore, measure the emitted X-rays from a specimen. Since the energies of the X-rays are characteristic of the difference in energy between the two shells and of the atomic structure of the emitting element, EDX allows the elemental composition of the sample to be measured.

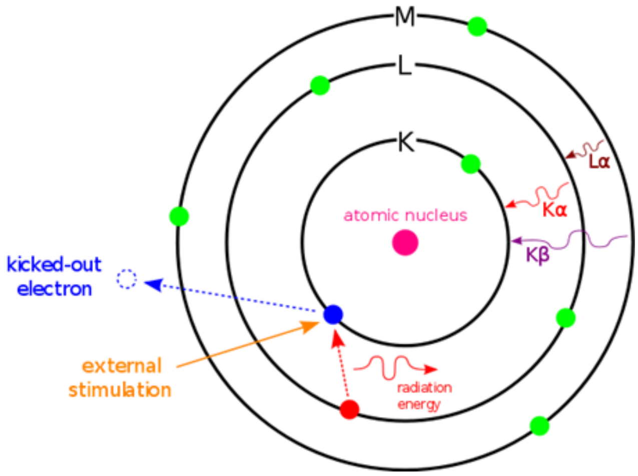

Figure 2.26: Schematic diagram representing the principle operation of EDX.

2.6.4 X-Ray Diffraction (XRD)

X-ray powder diffraction (XRD) is an analytical technique used for phase identification of crystalline powder materials. This method is also useful for unit cell dimensions, determination of purity and crystallinity of investigated samples. XRD consist of three basic elements namely an X-ray tube, a sample holder, and an X-ray detector, and they all lie on the circumference of the circle, which is known as the focusing circle [245]. The analysis of XRD is based on constructive interference of monochromatic X-rays and a crystalline sample. When a sample bombarded with the x-rays, constructive interference of X-ray radiation occurs in the material when Bragg's law is satisfied:

$$n\lambda = 2dsin\theta;\ n = 1, 2, 3, \qquad 2.29$$

where n is an integer, λ is the wavelength of the incident wave, d is the distance between two planes in the atomic lattice, and θ is the angle between the incident beam and the scattering planes.

A detector records and processes this X-ray signal and converts the signal to a count rate which is then output to a device such as a printer or a computer monitor [246]. A

Rietveld refinement gives information such as lattice parameters and phase distribution.

2.6.5 X-Ray Photoelectron Spectroscopy (XPS)

X-Ray Photoelectron Spectroscopy (XPS) also known as Electron Spectroscopy for Chemical Analysis (ESCA) is the most widely used surface-sensitive analysis technique due to its ability to be applied to a broad range of investigated materials. XPS is a photoelectric effect where electrons are emitted from solids (or other mediums) when they absorb energy from X-ray photons ($h\nu$) [247]. Thus, electrons emitted in this manner are called photoelectrons. This technique measures the elemental composition at the parts per thousand range, empirical formula, chemical state and electronic state of the elements that exist within a material [248]. The sample, in ultra-high vacuum (UHV; P < 10−9 millibar), is irradiated with the X-ray radiation, photoionization occurs and the kinetic energy of the ejected photoelectrons is measured by an electron energy analyser (see Fig. 2.27).

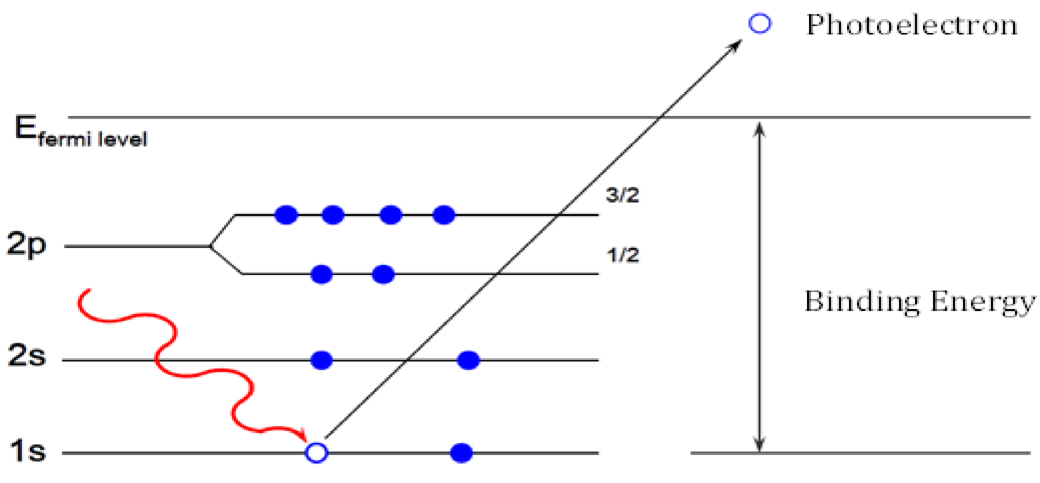

Figure 2.27: Schematic diagram of a principle operation of XPS.

The X-ray radiation (1 – 15 keV) usually applied is capable of inducing electrons not only from the outer shells but also from core levels of elements. Determination of the kinetic energy of the photoejected electrons permits identification of the elemental composition of the composite surface. The binding energy (E_b) of the core electron is given by the Einstein relation:

$$h\nu = E_b + E_k + \phi \qquad 2.29$$

or

$$E_b = h\nu - E_k - \phi \qquad 2.30$$

where $h\nu$ is the X-ray photon energy (for this study it is either monochromated Al K_α, = 1486.6 eV or Mg K_α, = 1253.6 eV), E_k the kinetic energy of the photoelectron and ϕ is the work function induced by the analyser.

A significant advantage of XPS is its ability to obtain information on chemical states from the variations in binding energies, or chemical shifts, of the photoelectron lines.

2.6.6 Infrared Spectroscopy

Infra-red spectroscopy is a qualitative analytical tool used to obtain information on the molecular structures of virtual all type of samples in any physical state (solid, liquid or gas). An infra-red spectrum obtained when an infra-red radiation of a continuous wavelength pass through a sample is absorbed by the vibrating molecules at a particular wavelength, thus giving rise to an absorption peak at that same wavelength [249]. The various molecular vibrations in a sample produce a vast number of absorptions which are uniquely characteristic of the functional groups of that molecule. FT-IR spectrometers are highly sensitive instruments that have good resolutions [250].

2.6.7 Gas Adsorption Technique

The gas adsorption technique is known to measure the specific surface area, porosity, pore sizes and pore size distribution of powdered or solid materials. In gas adsorption analysis, a dry sample is usually evacuated of all gas and cooled to a temperature of 77K (or -196.15 °C), commonly using liquid N_2. At this temperature, inert gases such as nitrogen, argon and krypton physically adsorb on the surface of the sample [251]. This adsorption process can be considered to be a reversible condensation or layering of molecules on the sample surface during which heat is produced. Nitrogen gas is a perfect choice for measuring surface area and pore size distribution. To determine the surface area, solid sample is pre-treated by applying some combination of heat, vacuum, and flowing gas to remove adsorbed contaminants acquired (typically H_2O and CO_2) from atmospheric exposure. The solid sample is then cooled, under vacuum, usually to cryogenic temperature (77K or -196.15 °C). An adsorptive (i.e., nitrogen) is dosed to the solid in controlled increments and followed by allowing the pressure to equilibrate after each dose of an adsorptive, and thus, the quantity adsorbed is determined [252]. The amount adsorbed at each pressure and temperature defines an adsorption isotherm, from which the amount of gas required to form a monolayer on the external surface of the solid is determined. The surface area can be then calculated using the area covered by each adsorbed gas molecule known [253]. The data collected is displayed in the form of a Brunauer-Emmett-Teller (BET) isotherm, which plots the amount of gas adsorbed as a function of the relative pressure.

2.6.8 Raman Spectroscopy

Raman spectroscopy is a technique used to observe vibrational, rotational, and other low-frequency modes in a system. Raman scattering is perceived as the change in frequency for a small percentage of the intensity in a monochromatic beam as the result of coupling between the incident radiation and vibrational energy levels of molecules. A vibrational mode will be Raman active only when it changes the polarizability of the molecule [254]. In a typical Raman experiment, the sample is irradiated with a monochromatic radiation (laser) then this laser light will interact with the sample in some fashion. It may be reflected, absorbed or even scattered in some manner. If the sample is transparent, most of the light will be transmitted resulting in a small fraction being elastically (Rayleigh) scattered and also a tiny portion being inelastically (Raman) scattered. It is the change in wavelength of the inelastically scattered light which provides the chemical, and structural information is displayed as a Raman spectrum by plotting the intensity of the inelastically scattered light as a function of energy or the shift in the wavenumber of the radiation [254]–[256]. Low-frequency Raman modes (below 400 cm^{-1}) are associated with metal-ligand bonds. If one is interested in studying very low-frequency Raman modes which lie close to the laser line, it is important to choose a filter or filtering technique that provides a sharp transition between deep blocking of the Rayleigh scatter and transmission of the Raman signal.

2.6.9 Thermo-Gravimetric Analysis (TGA)

Thermogravimetry analysis is a method used for the determination of the material thermal's stability and % composition. In TGA analysis, the change of a known amount of material weight is recorded as a function of temperature or time under inert or reactive atmosphere.

Reference

[1] A. J. Bard and R. L. Faulkner, *Electrochemical Methods: Fundamentals and Applications*. New York: John Willey & Sons, 1996.

[2] R. Kötz and M. Carlen, "Principles and applications of electrochemical capacitors," *Electrochim. Acta*, vol. 45, pp. 2483–2498, 2000.

[3] M. M. Thackeray, C. S. Johnson, J. T. Vaughey, N. Li, and S. A. Hackney, "Advances in manganese-oxide 'composite' electrodes for lithium-ion batteries," *Journal of Materials Chemistry*, vol. 15, no. 23. p. 2257, 2005.

[4] B. E. Conway, *Electrochemical Supercapacitors Scientific Fundamentals and Technological Applications*. 1999.

[5] A. Burke, "Ultracapacitors: why, how, and where is the technology," *J. Power Sources*, vol. 91, pp. 37–50, 2000.

[6] M. Toupin, T. Brousse, and D. Be, "Charge Storage Mechanism of MnO 2 Electrode Used in Aqueous Electrochemical Capacitor," *Chem. Mater.*, vol. 16, no. 9, pp. 3184–3190, 2004.

[7] H. Jiang, P. S. Lee, and C. Li, "3D carbon based nanostructures for advanced supercapacitors," *Energy Environ. Sci.*, vol. 6, no. 1, p. 41, 2013.

[8] S. Holmberg, A. Perebikovsky, L. Kulinsky, and M. Madou, "3-D micro and nano technologies for improvements in electrochemical power devices," *Micromachines*, vol. 5, no. 1, pp. 171–203, 2014.

[9] E. Frackowiak and F. Béguin, "Carbon materials for the electrochemical storage of energy in capacitors," *Carbon N. Y.*, vol. 39, no. 6, pp. 937–950, May 2001.

[10] A. T. Chidembo, K. I. Ozoemena, B. O. Agboola, V. Gupta, G. G. Wildgoose, and R. G.

Compton, "Nickel(ii) tetra-aminophthalocyanine modified MWCNTs as potential nanocomposite materials for the development of supercapacitors," *Energy Environ. Sci.*, vol. 3, no. 2, p. 228, 2010.

[11] H. I. Becker, "Low voltage electrolytic capacitor," 1957.

[12] R. A. Rightmire, "Electrical energy storage apparatus," 1966.

[13] D. L. Boos, "Electrolytic Capacitor having carbon paste electrodes," 1970.

[14] G. L. Bullard, H. B. Sierra-Alcazar, H. L. Lee, and J. L. Morris, "Operating principles of the ultracapacitor.," *IEEE Trans. Magn.*, vol. 25, no. 1, pp. 102–106, 1989.

[15] P. Sharma and T. S. Bhatti, "A review on electrochemical double-layer capacitors," *Energy Convers. Manag.*, vol. 51, no. 12, pp. 2901–2912, 2010.

[16] J. R. Miller, "HISTORY OF TECHNOLOGY A brief history of supercapacitors," *Battey+energy Technol.*, vol. ISSN521452, pp. 61–78, 2007.

[17] J. R. Miller and A. F. Burke, "Electrochemical capacitors: Challenges and opportunities for real-world applications," *Electrochem. Soc.*, vol. 17, pp. 53–57, 2008.

[18] S. Liu, S. Sun, and X.-Z. You, "Inorganic nanostructured materials for high performance electrochemical supercapacitors.," *Nanoscale*, vol. 6, pp. 2037–45, 2014.

[19] G. Pandolfo and F. Hollenkamp, "Carbon properties and their role in supercapacitors," *J. Power Sources*, vol. 157, no. 1, pp. 11–27, 2006.

[20] B. E. Conway, V. Birss, and J. Wojtowicz, "The role and utilization of pseudocapacitance for energy storage by supercapacitors," *J. Power Sources*, vol. 66, no. 1–2, pp. 1–14, May 1997.

[21] F. Béguin, V. Presser, A. Balducci, and E. Frackowiak, “Carbons and electrolytes for advanced supercapacitors.,” *Adv. Mater.*, vol. 26, no. 14, pp. 2219–51, 2283, Apr. 2014.

[22] E. Frackowiak, “Carbon materials for supercapacitor application.,” *Phys. Chem. Chem. Phys.*, vol. 9, no. 15, pp. 1774–85, Apr. 2007.

[23] M. Zhi, C. Xiang, J. Li, M. Li, and N. Wu, “Nanostructured Carbon-Metal Oxide Composite Electrodes for Supercapacitors: Review,” *Nanoscale*, pp. 72–88, 2012.

[24] M. D. Stoller, S. Park, Y. Zhu, J. An, and R. S. Ruoff, “Graphene-based ultracapacitors.,” *Nano Lett.*, vol. 8, no. 10, pp. 3498–502, Oct. 2008.

[25] Y. Zhai, Y. Dou, D. Zhao, P. F. Fulvio, R. T. Mayes, and S. Dai, “Carbon materials for chemical capacitive energy storage.,” *Adv. Mater.*, vol. 23, no. 42, pp. 4828–4850, Nov. 2011.

[26] L. L. Zhang and X. S. Zhao, “Carbon-based materials as supercapacitor electrodes.,” *Chem. Soc. Rev.*, vol. 38, no. 9, pp. 2520–31, Sep. 2009.

[27] S. Bose, T. Kuila, A. K. Mishra, R. Rajasekar, N. H. Kim, and J. H. Lee, “Carbon-based nanostructured materials and their composites as supercapacitor electrodes,” *J. Mater. Chem.*, vol. 22, p. 767, 2012.

[28] D. Qu, D. Qu, H. Shi, and H. Shi, “Studies of activated carbons used in double-layer capacitors,” *J. Power Sources*, vol. 74, pp. 99–107, 1998.

[29] F. Béguin and E. Frackowiak, *Supercapacitors: Materials, Systems and Applications*. John Wiley & Sons, Weinheim, 2013.

[30] T. Brezesinski, J. Wang, S. H. Tolbert, and B. Dunn, “Ordered mesoporous alpha-MoO3 with iso-oriented nanocrystalline walls for thin-film pseudocapacitors.,”

Nat. Mater., vol. 9, no. 2, pp. 146–151, 2010.

[31] L. Bai, D. a. Harrington, and B. E. Conway, "Behavior of overpotential—deposited species in Faradaic reactions—II. ac Impedance measurements on H2 evolution kinetics at activated and unactivated Pt cathodes," *Electrochim. Acta*, vol. 32, pp. 1713–1731, 1987.

[32] C. Z. Yuan, B. Gao, L. F. Shen, S. D. Yang, L. Hao, X. J. Lu, F. Zhang, L. J. Zhang, and X. G. Zhang, "Hierarchically structured carbon-based composites: Design, synthesis and their application in electrochemical capacitors.," *Nanoscale*, vol. 3, pp. 529–545, 2011.

[33] S. Pilban Jahromi, A. Pandikumar, B. T. Goh, Y. S. Lim, W. J. Basirun, H. N. Lim, and N. M. Huang, "Influence of particle size on performance of a nickel oxide nanoparticle-based supercapacitor," *RSC Adv.*, vol. 5, pp. 14010–14019, 2015.

[34] E. Frackowiak, V. Khomenko, K. Jurewicz, K. Lota, and F. Béguin, "Supercapacitors based on conducting polymers/nanotubes composites," *J. Power Sources*, vol. 153, pp. 413–418, 2006.

[35] J. Zhang and X. S. Zhao, "Conducting polymers directly coated on reduced graphene oxide sheets as high-performance supercapacitor electrodes," *J. Phys. Chem. C*, vol. 116, pp. 5420–5426, 2012.

[36] L. L. Zhang, S. Zhao, X. N. Tian, and X. S. Zhao, "Layered graphene oxide nanostructures with sandwiched conducting polymers as supercapacitor electrodes," *Langmuir*, vol. 26, no. 11, pp. 17624–17628, 2010.

[37] K. Lota, V. Khomenko, and E. Frackowiak, "Capacitance properties of poly(3,4-ethylenedioxythiophene)/carbon nanotubes composites," *J. Phys. Chem. Solids*, vol. 65, pp. 295–301, 2004.

[38] C. Hu, S. He, S. Jiang, S. Chen, and H. Hou, "Natural source derived carbon paper supported conducting polymer nanowire arrays for high performance supercapacitors," *RSC Adv.*, vol. 5, pp. 14441–14447, 2015.

[39] A. T. Chidembo, S. H. Aboutalebi, K. Konstantinov, C. J. Jafta, H. K. Liu, and K. I. Ozoemena, "In situ engineering of urchin-like reduced graphene oxide–Mn2O3–Mn3O4 nanostructures for supercapacitors," *RSC Adv.*, vol. 4, no. 2, p. 886, 2014.

[40] J. N. Lekitima, K. I. Ozoemena, C. J. Jafta, N. Kobayashi, Y. Song, D. Tong, S. Chen, and M. Oyama, "High-performance aqueous asymmetric electrochemical capacitors based on graphene oxide/cobalt(ii)-tetrapyrazinoporphyrazine hybrids," *J. Mater. Chem. A*, vol. 1, no. 8, p. 2821, 2013.

[41] A. Bello, F. Barzegar, D. Momodu, J. Dangbegnon, F. Taghizadeh, M. Fabiane, and N. Manyala, "Asymmetric supercapacitor based on nanostructured graphene foam / polyvinyl alcohol / formaldehyde and activated carbon electrodes," *J. Power Sources*, vol. 273, pp. 305–311, 2015.

[42] S. E. Moosavifard, M. F. El-Kady, M. S. Rahmanifar, R. B. Kaner, and M. F. Mousavi, "Designing 3D Highly Ordered Nanoporous CuO Electrodes for High-Performance Asymmetric Supercapacitors," *ACS Appl. Mater. Interfaces*, vol. 7, pp. 4851–4860, 2015.

[43] J. Liu, L. Zhang, H. Bin Wu, J. Lin, Z. Shen, and X. W. (David) Lou, "High-performance flexible asymmetric supercapacitors based on a new graphene foam/carbon nanotube hybrid film," *Energy Environ. Sci.*, vol. 7, pp. 3709–3719, 2014.

[44] N. Kurra, R. Wang, and H. N. Alshareef, "All conducting polymer electrodes for asymmetric solid-state supercapacitors," *J. Mater. Chem. A*, vol. 00, pp. 1–7, 2015.

[45] V. Khomenko, E. Raymundo-Piñero, E. Frackowiak, and F. Béguin, "High-voltage asymmetric supercapacitors operating in aqueous electrolyte," *Appl. Phys. A Mater. Sci. Process.*, vol. 82, pp. 567–573, 2006.

[46] J. Zhang, J. Jiang, H. Li, and X. S. Zhao, "A high-performance asymmetric supercapacitor fabricated with graphene-based electrodes," *Energy Environ. Sci.*, vol. 4, p. 4009, 2011.

[47] J. Yan, Z. Fan, W. Sun, G. Ning, T. Wei, Q. Zhang, R. Zhang, L. Zhi, and F. Wei, "Advanced asymmetric supercapacitors based on Ni(OH) 2/graphene and porous graphene electrodes with high energy density," *Adv. Funct. Mater.*, vol. 22, pp. 2632–2641, 2012.

[48] M. D. Stoller and R. S. Ruoff, "Review of Best Practice Methods for Determining an Electrode Material's Performance for Ultracapacitors," *Energy Environ. Sci.*, vol. 3, pp. 1294–1301, 2010.

[49] T. Cottineau, M. Toupin, T. Delahaye, T. Brousse, and D. Bélanger, "Nanostructured transition metal oxides for aqueous hybrid electrochemical supercapacitors," *Appl. Phys. A Mater. Sci. Process.*, vol. 82, no. 4 SPEC. ISS., pp. 599–606, 2006.

[50] P. Chen, G. Shen, Y. Shi, H. Chen, and C. Zhou, "Preparation and Characterization of Flexible Asymmetric Supercapacitors Based on Transition-Metal-Oxide Nanowire/Single-Walled Carbon Nanotube Hybrid Thin-Film Electrodes," *ACS Nano*, vol. 4, no. 8, pp. 4403–4411, 2010.

[51] G. Wang, L. Zhang, and J. Zhang, "A review of electrode materials for electrochemical supercapacitors.," *Chem. Soc. Rev.*, vol. 41, no. 2, pp. 797–828, Jan. 2012.

[52] V. Ruiz, C. Blanco, E. Raymundo-Piñero, V. Khomenko, F. Béguin, and R.

Santamaría, "Effects of thermal treatment of activated carbon on the electrochemical behaviour in supercapacitors," *Electrochim. Acta*, vol. 52, pp. 4969–4973, 2007.

[53] K. Fic, G. Lota, M. Meller, and E. Frackowiak, "Novel insight into neutral medium as electrolyte for high-voltage supercapacitors," *Energy Environ. Sci.*, vol. 5, p. 5842, 2012.

[54] Q. Gao, L. Demarconnay, E. Raymundo-Piñero, and F. Béguin, "Exploring the large voltage range of carbon/carbon supercapacitors in aqueous lithium sulfate electrolyte," *Energy Environ. Sci.*, vol. 5, p. 9611, 2012.

[55] P. Staiti, a. Arenillas, F. Lufrano, and J. Á. Menéndez, "High energy ultracapacitor based on carbon xerogel electrodes and sodium sulfate electrolyte," *J. Power Sources*, vol. 214, pp. 137–141, 2012.

[56] L. Zhao, Y. Qiu, J. Yu, X. Deng, C. Dai, and X. Bai, "Carbon nanofibers with radially grown graphene sheets derived from electrospinning for aqueous supercapacitors with high working voltage and energy density.," *Nanoscale*, vol. 5, pp. 4902–4909, 2013.

[57] K. Fic, E. Frackowiak, and F. Béguin, "Unusual energy enhancement in carbon-based electrochemical capacitors," *J. Mater. Chem.*, vol. 22, pp. 24213–24223, 2012.

[58] C. J. Jafta, F. Nkosi, L. le Roux, M. K. Mathe, M. Kebede, K. Makgopa, Y. Song, D. Tong, M. Oyama, N. Manyala, S. Chen, and K. I. Ozoemena, "Manganese oxide/graphene oxide composites for high-energy aqueous asymmetric electrochemical capacitors," *Electrochim. Acta*, pp. 2–7, Jul. 2013.

[59] M. Arulepp, L. Permann, J. Leis, a. Perkson, K. Rumma, a. Jänes, and E. Lust,

"Influence of the solvent properties on the characteristics of a double layer capacitor," *J. Power Sources*, vol. 133, pp. 320–328, 2004.

[60] P. Liu, M. Verbrugge, and S. Soukiazian, "Influence of temperature and electrolyte on the performance of activated-carbon supercapacitors," *J. Power Sources*, vol. 156, pp. 712–718, 2006.

[61] R. Q. Wang, "Studies and Characterisations of Activated Carbons Used for Carbon / Carbon Supercapacitors," *J. Power Sources*, vol. 5, pp. 866–868, 2011.

[62] D. Jiang and J. Wu, "Unusual effects of solvent polarity on capacitance for organic electrolytes in a nanoporous electrode.," *Nanoscale*, vol. 6, pp. 5545–50, 2014.

[63] P. Kurzweil and M. Chwistek, "Electrochemical stability of organic electrolytes in supercapacitors: Spectroscopy and gas analysis of decomposition products," *J. Power Sources*, vol. 176, pp. 555–567, 2008.

[64] J. S. Wilkes, "A short history of ionic liquids—from molten salts to neoteric solvents," *Green Chem.*, vol. 4, pp. 73–80, 2002.

[65] A. Balducci, R. Dugas, P. L. Taberna, P. Simon, D. Plée, M. Mastragostino, and S. Passerini, "High temperature carbon-carbon supercapacitor using ionic liquid as electrolyte," *J. Power Sources*, vol. 165, pp. 922–927, 2007.

[66] Oxford Dictionaries, *Alternative energy*, vol. 4, no. 4. 2010.

[67] A. Balducci, U. Bardi, S. Caporali, M. Mastragostino, and F. Soavi, "Ionic liquids for hybrid supercapacitors," *Electrochem. commun.*, vol. 6, pp. 566–570, 2004.

[68] C. Arbizzani, M. Biso, D. Cericola, M. Lazzari, F. Soavi, and M. Mastragostino, "Safe, high-energy supercapacitors based on solvent-free ionic liquid electrolytes," *J. Power Sources*, vol. 185, pp. 1575–1579, 2008.

[69] D. Weingarth, H. Noh, a. Foelske-Schmitz, a. Wokaun, and R. Kötz, "A reliable determination method of stability limits for electrochemical double layer capacitors," *Electrochim. Acta*, vol. 103, pp. 119–124, 2013.

[70] Y. Zhang, H. Feng, X. Wu, L. Wang, A. Zhang, T. Xia, H. Dong, X. Li, and L. Zhang, "Progress of electrochemical capacitor electrode materials: A review," *Int. J. Hydrogen Energy*, vol. 34, no. 11, pp. 4889–4899, 2009.

[71] K. Kierzek, E. Frackowiak, G. Lota, G. Gryglewicz, and J. Machnikowski, "Electrochemical capacitors based on highly porous carbons prepared by KOH activation," *Electrochim. Acta*, vol. 49, pp. 515–523, 2004.

[72] M. J. Bleda-Martínez, D. Lozano-Castelló, E. Morallón, D. Cazorla-Amorós, and a. Linares-Solano, "Chemical and electrochemical characterization of porous carbon materials," *Carbon N. Y.*, vol. 44, pp. 2642–2651, 2006.

[73] M. J. Bleda-Martínez, J. a. Maciá-Agulló, D. Lozano-Castelló, E. Morallón, D. Cazorla-Amorós, and a. Linares-Solano, "Role of surface chemistry on electric double layer capacitance of carbon materials," *Carbon N. Y.*, vol. 43, pp. 2677–2684, 2005.

[74] D. Lozano-Castello, D. Lozano-Castello, D. Cazorla-Amoros, D. Cazorla-Amoros, a Linares-Solano, a Linares-Solano, S. Shiraishi, S. Shiraishi, H. Kurihara, H. Kurihara, a Oya, and a Oya, "Influence of pore structure and surface chemistry on electric double layer capacitance in non-aqueous electrolyte," *Carbon N. Y.*, vol. 41, pp. 1765–1775, 2003.

[75] "Activated carbon." [Online]. Available: http://www.sushrutchemicals.com/images/diagramedimage.jpg. [Accessed: 14-Mar-2015].

[76] "Activated carbon." [Online]. Available:

http://fotos.infoisinfo.co.in/acuro_organics_limited/3480171_8050. [Accessed: 14-Mar-2015].

[77] G. H. Yuan, Z. H. Jiang, A. Aramata, and Y. Z. Gao, "Electrochemical behavior of activated-carbon capacitor material loaded with nickel oxide," *Carbon N. Y.*, vol. 43, pp. 2913–2917, 2005.

[78] B. Xu, Y. Chen, G. Wei, G. Cao, H. Zhang, and Y. Yang, "Activated carbon with high capacitance prepared by NaOH activation for supercapacitors," *Mater. Chem. Phys.*, vol. 124, no. 1, pp. 504–509, 2010.

[79] D. Saha, Y. Li, Z. Bi, J. Chen, J. K. Keum, D. Hensley, A. Grappe, H. M. Meyer, S. Dai, M. P. Paranthaman, A. K. Naskar, K. Dale, H. a Grappe, H. M. M. Iii, and M. Parans, "Studies on Supercapacitor Electrode Material from Activated Lignin-Derived Mesoporous Carbon Studies on Supercapacitor Electrode Material from Activated Lignin-Derived Mesoporous Carbon," *Langmuir*, vol. 30, pp. 900–910, 2014.

[80] F. Zhou, Q. Liu, J. Gu, W. Zhang, and D. Zhang, "A facile low-temperature synthesis of highly distributed and size-tunable cobalt oxide nanoparticles anchored on activated carbon for supercapacitors," *J. Power Sources*, vol. 273, pp. 945–953, 2015.

[81] A. K. Geim and K. S. Novoselov, "The rise of graphene.," *Nat. Mater.*, vol. 6, pp. 183–191, 2007.

[82] R. R. Nair, P. Blake, a N. Grigorenko, K. S. Novoselov, T. J. Booth, T. Stauber, N. M. R. Peres, and a K. Geim, "Fine structure constant defines visual transparency of graphene.," *Science*, vol. 320, p. 1308, 2008.

[83] F. Bonaccorso, L. Colombo, G. Yu, M. Stoller, V. Tozzini, a. C. Ferrari, R. S. Ruoff, and V. Pellegrini, "Graphene, related two-dimensional crystals, and hybrid

systems for energy conversion and storage," *Science (80-.).*, vol. 347, no. 6217, pp. 1246501–1246509, 2015.

[84] K. S. Novoselov, A. K. Geim, S. Morozov, D. Jiang, Y. Zhang, S. Dubonos, I. Grigorieva, and A. Firsov, "Electric field effect in atomically thin carbon films.," *Science*, vol. 306, no. 5696, pp. 666–9, Oct. 2004.

[85] "The Nobel Price in Physics 2010." [Online]. Available: http://www.nobelprize.org/nobel_prizes/physics/laureates/2010/. [Accessed: 15-Mar-2015].

[86] S. Radic, N. K. Geitner, R. Podila, A. Käkinen, P. Chen, P. C. Ke, and F. Ding, "Competitive binding of natural amphiphiles with graphene derivatives.," *Sci. Rep.*, vol. 3, p. 2273, 2013.

[87] "Graphene Oxide." [Online]. Available: http://en.wikipedia.org/wiki/Graphite_oxide#/media/File:Graphite_oxide.svg. [Accessed: 05-Mar-2015].

[88] Y. Huang, J. Liang, and Y. Chen, "An overview of the applications of graphene-based materials in supercapacitors," *Small*, vol. 8, no. 12, pp. 1805–1834, 2012.

[89] Y. Zhu, S. Murali, W. Cai, X. Li, J. W. Suk, J. R. Potts, and R. S. Ruoff, "Graphene and graphene oxide: Synthesis, properties, and applications," *Adv. Mater.*, vol. 22, pp. 3906–3924, 2010.

[90] T. J. Booth, P. Blake, R. R. Nair, D. Jiang, E. W. Hill, U. Bangert, A. Bleloch, M. Gass, K. S. Novoselov, M. I. Katsnelson, and a. K. Geim, "Macroscopic graphene membranes and their extraordinary stiffness," *Nano Lett.*, vol. 8, pp. 2442–2446, 2008.

[91] J.-W. Jiang, J.-S. Wang, and B. Li, "Young's modulus of Graphene: a molecular

dynamics study," *Phys. Rev. B*, vol. 80, no. 113405, pp. 15–18, 2009.

[92] S. Russo, M. F. Craciun, T. Khodkov, M. Yamamoto, M. Koshino, and S. Tarucha, *Graphene – Synthesis, Characterization, Properties and applications*. Intech open acess, 2011.

[93] L. L. Zhang, R. Zhou, and X. S. Zhao, "Graphene-based materials as supercapacitor electrodes," *J. Mater. Chem.*, vol. 20, no. 29, p. 5983, 2010.

[94] C. Li and G. Shi, "Three-dimensional graphene architectures," *Nanoscale*, vol. 4, no. 18, p. 5549, 2012.

[95] J. William S. Hummers and R. E. Offeman, "Preparation of Graphitic Oxide," *J. Am. Chem. Soc*, vol. 80, no. 1937, p. 1339, 1958.

[96] D. R. Dreyer, S. Park, C. W. Bielawski, and R. S. Ruoff, "The chemistry of graphene oxide.," *Chem. Soc. Rev.*, vol. 39, no. 1, pp. 228–240, 2010.

[97] C. K. Chua and M. Pumera, "Chemical reduction of graphene oxide: a synthetic chemistry viewpoint.," *Chem. Soc. Rev.*, vol. 43, no. 1, pp. 291–312, 2014.

[98] Y. Wang, Y. Wu, Y. Huang, F. Zhang, X. Yang, Y. Ma, and Y. Chen, "Preventing Graphene Sheets from Restacking for High-Capacitance Performance," *J. Phys. Chem. C*, vol. 115, no. 46, pp. 23192–23197, Nov. 2011.

[99] Y. Zhu, S. Murali, M. D. Stoller, K. J. Ganesh, W. Cai, P. J. Ferreira, A. Pirkle, R. M. Wallace, K. A. Cychosz, and M. Thommes, "Carbon-based supercapacitors produced by activation of graphene," *Science (80-.).*, vol. 332, no. 6037, pp. 1537–1541, 2011.

[100] Y. Chen, X. Zhang, D. Zhang, P. Yu, and Y. Ma, "High performance supercapacitors based on reduced graphene oxide in aqueous and ionic liquid electrolytes,"

Carbon N. Y., vol. 49, no. 2, pp. 573–580, Feb. 2011.

[101] Z. Bo, X. Shuai, S. Mao, H. Yang, J. Qian, J. Chen, J. Yan, and K. Cen, "Green preparation of reduced graphene oxide for sensing and energy storage applications.," *Sci. Rep.*, vol. 4, p. 4684, Jan. 2014.

[102] C. Liu, Z. Yu, D. Neff, A. Zhamu, and B. Z. Jang, "Graphene-Based Supercapacitor with an Ultrahigh Energy Density.," *Nano Lett.*, pp. 4863–4868, Nov. 2010.

[103] H. Wang, Q. Hao, X. Yang, L. Lu, and X. Wang, "Graphene oxide doped polyaniline for supercapacitors," *Electrochem. commun.*, vol. 11, no. 6, pp. 1158–1161, Jun. 2009.

[104] Z. Fan, J. Yan, T. Wei, L. Zhi, G. Ning, T. Li, and F. Wei, "Asymmetric Supercapacitors Based on Graphene/MnO2 and Activated Carbon Nanofiber Electrodes with High Power and Energy Density," *Adv. Funct. Mater.*, vol. 21, no. 12, pp. 2366–2375, Jun. 2011.

[105] X. Zhang, Y. Feng, S. Tang, and W. Feng, "Preparation of a graphene oxide–phthalocyanine hybrid through strong π–π interactions," *Carbon N. Y.*, vol. 48, no. 1, pp. 211–216, Jan. 2010.

[106] S. D. Perera, M. Rudolph, R. Mariano, N. Nijem, J. P. Ferraris, Y. J. Chabal, and K. J. Balkus Jr, "Manganese oxide nanorod "graphene/vanadium oxide nanowire "graphene binder-free paper electrodes for metal oxide hybrid supercapacitors," *Nano Energy*, 2013.

[107] X. Zhao, L. Zhang, S. Murali, M. D. Stoller, Q. Zhang, Y. Zhu, and R. S. Ruoff, "Incorporation of manganese dioxide within ultraporous activated graphene for high-performance electrochemical capacitors.," *ACS Nano*, vol. 6, no. 6, pp. 5404–12, Jun. 2012.

[108] B. Xu, S. Yue, Z. Sui, X. Zhang, S. Hou, G. Cao, and Y. Yang, "What is the choice for supercapacitors: graphene or graphene oxide?," *Energy Environ. Sci.*, vol. 4, no. 8, p. 2826, 2011.

[109] Y. Wang, Z. Shi, Y. Huang, Y. Ma, C. Wang, M. Chen, and Y. Chen, "Supercapacitor Devices Based on Graphene Materials.pdf," *J. Phys. Chem. C*, vol. 113, pp. 13103–13107, 2009.

[110] M. F. El-kady, V. Strong, S. Dubin, and R. B. Kaner, "Laser Scribing of High-Performanceand Flexible Graphene-BasedElectrochemical Capacitors," *Science (80-.).*, vol. 335, pp. 1326–1330, 2012.

[111] J. L. Qi, X. Wang, J. H. Lin, F. Zhang, J. C. Feng, and W.-D. Fei, "A high-performance supercapacitor of vertically-oriented few-layered graphene with high-density defects," *Nanoscale*, vol. 7, no. 8, pp. 3675–3682, 2015.

[112] "The History of Carbon Nanotubes – Who Invented The Nanotube?" [Online]. Available: http://nanogloss.com/nanotubes/the-history-of-carbon-nanotubes-who-invented-the-nanotube/#axzz3VUGkmKR4. [Accessed: 26-Mar-2015].

[113] "Carbon Nanotubes - History and Development of Carbon Nanotubes (Buckytubes)." [Online]. Available: http://www.azonano.com/article.aspx?ArticleID=982. [Accessed: 26-Mar-2015].

[114] S. Iijima, "Helical microtubules of graphitic carbon," *Nature*, vol. 354, no. 6348. pp. 56–58, 1991.

[115] S. Iijima and T. Ichihashi, "Single-shell carbon nanotubes of 1-nm diameter," *Nature*, vol. 363, pp. 603–604, 1993.

[116] D. S. Bethune, C. H. Kiang, M. S. de Vries, G. Gorman, R. Savoy, J. Vazquenz, and R.

Beyers, "Cobalt-catalysed growth of carbon nanotubes with single-atomic-layer walls," *Nature*, vol. 363, pp. 605–607, 1993.

[117] A. Oberlin, M. Endo, and T. Koyama, "Filamentous growth of carbon through benzene decomposition," *J. Cryst. Growth*, vol. 32, pp. 335–349, 1976.

[118] E. T. Thostenson, Z. Ren, and T.-W. Chou, "Advances in the science and technology of carbon nanotubes and their composites: a review," *Compos. Sci. Technol.*, vol. 61, pp. 1899–1912, 2001.

[119] V. Choudhary and A. Gupta, "Polymer / Carbon Nanotube Nanocomposites," *INTECH*. pp. 66–90, 2001.

[120] H. Terrones and M. Terrones, "Curved nanostructured materials," *New J. Phys.*, vol. 5, pp. 126.1–126.37, 2003.

[121] Jiangtao Hu, Teri W. Odom, and Charles M. Lieber, "Chemistry and Physics in One Dimensions: Syntesis and Properties of Nanowires and Nanotubes," *Acc. Chem. Res.*, vol. 32, no. 5, pp. 435–445, 1999.

[122] M. J. Bronikowski, P. a. Willis, D. T. Colbert, K. a. Smith, and R. E. Smalley, "Gas-phase production of carbon single-walled nanotubes from carbon monoxide via the HiPco process: A parametric study," *J. Vac. Sci. Technol. A Vacuum, Surfaces, Film.*, vol. 19, no. 4, p. 1800, 2001.

[123] J. Liu, S. Fan, and H. Dai, "Recent Advances in Methods of Forming Carbon Nanotubes," *MRS Bull.*, vol. 29, no. 04, pp. 244–250, 2004.

[124] B. O. Agboola, J. Pillay, K. Makgopa, and K. I. Ozoemena, "Electrochemical Characterization of Mixed Self-Assembled Films of Water-Soluble Single-Walled Carbon Nanotube-Poly(m-aminobenzene sulfonic acid) and Iron(II)

Tetrasulfophthalocyanine," *J. Electrochem. Soc.*, vol. 157, no. 11, p. F159, 2010.

[125] C. Liu and H.-M. Cheng, "Carbon nanotubes for clean energy applications," *J. Phys. D. Appl. Phys.*, vol. 38, no. 14, pp. R231–R252, 2005.

[126] M. F. L. De Volder, S. H. Tawfick, R. H. Baughman, and a J. Hart, "Carbon nanotubes: present and future commercial applications.," *Science*, vol. 339, no. 6119, pp. 535–9, 2013.

[127] R. . Ma, J. Liang, B. . Wei, B. Zhang, C. . Xu, and D. . Wu, "Study of electrochemical capacitors utilizing carbon nanotube electrodes," *J. Power Sources*, vol. 84, no. 1, pp. 126–129, 1999.

[128] E. Frackowiak, K. Metenier, V. Bertagna, and F. Beguin, "Supercapacitor electrodes from multiwalled carbon nanotubes," *Appl. Phys. Lett.*, vol. 77, no. 15, p. 2421, 2000.

[129] C. Du, J. Yeh, and N. Pan, "High power density supercapacitors using locally aligned carbon nanotube electrodes," *Nanotechnology*, vol. 16, no. 4, pp. 350–353, 2005.

[130] A. Izadi-Najafabadi, S. Yasuda, K. Kobashi, T. Yamada, D. N. Futaba, H. Hatori, M. Yumura, S. Iijima, and K. Hata, "Extracting the full potential of single-walled carbon nanotubes as durable supercapacitor electrodes operable at 4 v with high power and energy density," *Adv. Mater.*, vol. 22, no. 35, pp. 235–241, 2010.

[131] H. Zanin, E. Saito, H. J. Ceragioli, V. Baranauskas, and E. J. Corat, "Reduced graphene oxide and vertically aligned carbon nanotubes superhydrophilic films for supercapacitors devices," *Mater. Res. Bull.*, vol. 49, no. 1, pp. 487–493, 2014.

[132] F. Zeng, Y. Kuang, N. Zhang, Z. Huang, Y. Pan, Z. Hou, H. Zhou, C. Yan, and O. G.

Schmidt, “Multilayer super-short carbon nanotube/reduced graphene oxide architecture for enhanced supercapacitor properties,” *J. Power Sources*, vol. 247, pp. 396–401, 2014.

[133] H. Wang, H. Yi, X. Chen, and X. Wang, “Asymmetric supercapacitors based on nano-architectured nickel oxide/graphene foam and hierarchical porous nitrogen-doped carbon nanotubes with ultrahigh-rate performance,” *J. Mater. Chem. A*, vol. 2, no. 9, p. 3223, 2014.

[134] S. Iijima, “DIRECT OBSERVATION OF THE TETRAHEDRAL BONDING IN GRAPHITIZED CARBON BLACK BY,” *J. Christal Growth*, vol. 50, no. 3, pp. 675–683, 1980.

[135] Daniel Urgate, “Curling and closure of graphitic networks under electron-beam irradiation.,” *Nature*, vol. 359, no. 6397, pp. 707–709, 1992.

[136] B. . Xu and S.-I. Tanaka, “Formation of giant onion-like fullerenes under Al nanoparticles by electron irradiation,” *Acta Mater.*, vol. 46, no. 15, pp. 5249–5257, 1998.

[137] A. G. Nasibulin, A. Moisala, D. P. Brown, and E. I. Kauppinen, “Carbon nanotubes and onions from carbon monoxide using Ni(acac)2 and Cu(acac)2 as catalyst precursors,” *Carbon N. Y.*, vol. 41, no. 14, pp. 2711–2724, 2003.

[138] Y. Yang, X. Liu, X. Guo, H. Wen, and B. Xu, “Synthesis of nano onion-like fullerenes by chemical vapor deposition using an iron catalyst supported on sodium chloride,” *J. Nanoparticle Res.*, vol. 13, no. 5, pp. 1979–1986, 2011.

[139] T. Cabioc’h, M. Jaouen, E. Thune, P. Guérin, C. Fayoux, and M. . Denanot, “Carbon onions formation by high-dose carbon ion implantation into copper and silver,” *Surf. Coatings Technol.*, vol. 128–129, pp. 43–50, 2000.

[140] M. Bystrzejewski, M. H. Rummeli, T. Gemming, H. Lange, and A. Huczko, "Catalyst-free synthesis of onion-like carbon nanoparticles," *New Carbon Mater.*, vol. 25, no. 1, pp. 1–8, 2010.

[141] M. Zhao, H. Song, X. Chen, and W. Lian, "Large-scale synthesis of onion-like carbon nanoparticles by carbonization of phenolic resin," *Acta Mater.*, vol. 55, no. 18, pp. 6144–6150, 2007.

[142] V. L. Kuznetsov, A. L. Chuvilin, Y. V. Butenko, I. Y. Mal'kov, and V. M. Titov, "Onion-like carbon from ultra-disperse diamond," *Chem. Phys. Lett.*, vol. 222, no. 4, pp. 343–348, May 1994.

[143] V. L. Kuznetsov, Y. V. Butenko, V. I. Zaikovskii, and a. L. Chuvilin, "Carbon redistribution processes in nanocarbons," *Carbon N. Y.*, vol. 42, no. 5–6, pp. 1057–1061, 2004.

[144] N. Sano, H. Wang, M. Chhowalla, I. Alexandrou, and G. A. J. Amaratunga, "Nanotechnology: Synthesis of carbon 'onions' in water," *Nature*, vol. 414, no. 6863, pp. 506–507, Nov. 2001.

[145] L. Hawelek, A. Brodka, S. Tomita, J. C. Dore, V. Honkimäki, and A. Burian, "Transformation of nano-diamonds to carbon nano-onions studied by X-ray diffraction and molecular dynamics," *Diam. Relat. Mater.*, vol. 20, no. 10, pp. 1333–1339, 2011.

[146] J. McDonough and Y. Gogotsi, "Carbon Onions: Synthesis and Electrochemical Applications," *Electrochem. Soc. Interface*, vol. 22, no. 3, pp. 61–66, 2013.

[147] M. E. Plonska-Brzezinska and L. Echegoyen, "Carbon nano-onions for supercapacitor electrodes: recent developments and applications," *J. Mater. Chem. A*, vol. 1, no. 44, p. 13703, 2013.

[148] J. K. McDonough, A. I. Frolov, V. Presser, J. Niu, C. H. Miller, T. Ubieto, M. V. Fedorov, and Y. Gogotsi, "Influence of the structure of carbon onions on their electrochemical performance in supercapacitor electrodes," *Carbon N. Y.*, vol. 50, no. 9, pp. 3298–3309, Aug. 2012.

[149] Y. Gao, Y. S. Zhou, M. Qian, X. N. He, J. Redepenning, P. Goodman, H. M. Li, L. Jiang, and Y. F. Lu, "Chemical activation of carbon nano-onions for high-rate supercapacitor electrodes," *Carbon N. Y.*, vol. 51, pp. 52–58, Jan. 2013.

[150] E. G. Bushueva, A. V. Okotrub, P. S. Galkin, V. L. Kuznetsov, and S. I. Moseenkov, "Electrochemical supercapacitors based on carbon materials," *Nanocarbon nanodiamond Conf. St. Petersburg, Russ.*, pp. 11–15, 2006.

[151] C. Portet, G. Yushin, and Y. Gogotsi, "Electrochemical performance of carbon onions, nanodiamonds, carbon black and multiwalled nanotubes in electrical double layer capacitors," *Carbon N. Y.*, vol. 45, no. 13, pp. 2511–2518, Nov. 2007.

[152] C. Portet, J. Chmiola, Y. Gogotsi, S. Park, and K. Lian, "Electrochemical characterizations of carbon nanomaterials by the cavity microelectrode technique," *Electrochim. Acta*, vol. 53, no. 26, pp. 7675–7680, 2008.

[153] D. Pech, M. Brunet, H. Durou, P. Huang, V. Mochalin, Y. Gogotsi, P.-L. Taberna, and P. Simon, "Ultrahigh-power micrometre-sized supercapacitors based on onion-like carbon.," *Nat. Nanotechnol.*, vol. 5, no. 9, pp. 651–4, Sep. 2010.

[154] J. Huang, B. G. Sumpter, V. Meunier, G. Yushin, C. Portet, and Y. Gogotsi, "Curvature effects in carbon nanomaterials: Exohedral versus endohedral supercapacitors," *J. Mater. Res.*, vol. 25, no. 08, pp. 1525–1531, 2010.

[155] G. Feng, D. Jiang, and P. T. Cummings, "Curvature Effect on the Capacitance of Electric Double Layers at Ionic Liquid / Onion-like Carbon Interfaces Curvature

Effect on the Capacitance of Electric Double Layers at Ionic Liquid / Onion-like Carbon Interfaces," *J. Chem. Theory Comput.*, vol. 8, pp. 1058–1063, 2012.

[156] I. Kovalenko, D. G. Bucknall, and G. Yushin, "Detonation Nanodiamond and Onion-Like-Carbon-Embedded Polyaniline for Supercapacitors," *Adv. Funct. Mater.*, vol. 20, no. 22, pp. 3979–3986, Nov. 2010.

[157] N. Jäckel, D. Weingarth, M. Zeiger, M. Aslan, I. Grobelsek, and V. Presser, "Comparison of carbon onions and carbon blacks as conductive additives for carbon supercapacitors in organic electrolytes," *J. Power Sources*, vol. 272, pp. 1122–1133, 2014.

[158] D. Weingarth, M. Zeiger, N. Jäckel, M. Aslan, G. Feng, and V. Presser, "Graphitization as a Universal Tool to Tailor the Potential-Dependent Capacitance of Carbon Supercapacitors," *Adv. Energy Mater.*, vol. 4, no. 13, pp. 1–13, 2014.

[159] H. W. Kroto, J. R. Heath, S. C. O'Brien, R. F. Curl, and R. E. Smalley, "C 60-buckminsterfullerene," *Nature*, vol. 318, pp. 162–163, 1985.

[160] J. K. McDonough, "Onion-like Carbon for Electrochemical Capacitors," Ph.D. Thesis, Drexel University, 2014.

[161] C. Burda, X. Chen, R. Narayanan, and M. A. El-sayed, "Chemistry and Properties of Nanocrystals of Different Shapes," *Chem. Rev.*, vol. 105, no. 4, pp. 1025– 1102, 2005.

[162] X. Liu, C. Chen, Y. Zhao, and B. Jia, "A review on the synthesis of manganese oxide nanomaterials and their applications on lithium-ion batteries," *Journal of Nanomaterials*, vol. 2013. 2013.

[163] W. Xiao, H. Xia, J. Y. H. Fuh, and L. Lu, "Growth of single-crystal ??-MnO2

nanotubes prepared by a hydrothermal route and their electrochemical properties," *J. Power Sources*, vol. 193, pp. 935–938, 2009.

[164] Y. Zhang, C. Sun, P. Lu, K. Li, S. Song, and D. Xue, "Crystallization design of MnO2 towards better supercapacitance," *CrystEngComm*, vol. 14, no. 18, p. 5892, 2012.

[165] H. Y. Wang, F. X. Xiao, L. Yu, B. Liu, and X. W. Lou, "Hierarchical α-MnO2 nanowires@Ni1-xMn xOy nanoflakes core-shell nanostructures for supercapacitors," *Small*, vol. 10, no. 1, pp. 3181–3186, 2014.

[166] J. Wu, H. Huang, L. Yu, and J. Hu, "Controllable Hydrothermal Synthesis of MnO 2 Nanostructures," *Adv. Mater. Phys. Chem.*, vol. 3, pp. 201–205, 2013.

[167] M. Xu, L. Kong, W. Zhou, and H. Li, "Hydrothermal synthesis and pseudocapacitance properties of Î±-MnO2 hollow spheres and hollow urchins," *J. Phys. Chem. C*, vol. 111, no. 51, pp. 19141–19147, 2007.

[168] K. B. Hatzell, L. Fan, M. Beidaghi, M. Boota, E. Pomerantseva, E. C. Kumbur, and Y. Gogotsi, "Composite manganese oxide percolating networks as a suspension electrode for an asymmetric flow capacitor," *ACS Appl. Mater. Interfaces*, vol. 6, pp. 8886–8893, 2014.

[169] H. S. Nam, J. S. Kwon, K. M. Kim, J. M. Ko, and J. D. Kim, "Supercapacitive properties of a nanowire-structured MnO2 electrode in the gel electrolyte containing silica," *Electrochim. Acta*, vol. 55, pp. 7443–7446, 2010.

[170] T. Brousse, M. Toupin, R. Dugas, L. Athouël, O. Crosnier, and D. Bélanger, "Crystalline MnO[sub 2] as Possible Alternatives to Amorphous Compounds in Electrochemical Supercapacitors," *J. Electrochem. Soc.*, vol. 153, p. A2171, 2006.

[171] P. Ragupathy, D. H. Park, G. Campet, H. N. Vasan, S. J. Hwang, J. H. Choy, and N.

Munichandraiah, "Remarkable capacity retention of nanostructured manganese oxide upon cycling as an electrode material for supercapacitor," *J. Phys. Chem. C*, vol. 113, pp. 6303–6309, 2009.

[172] X. Wang, X. Wang, W. Huang, P. J. Sebastian, and S. Gamboa, "Sol-gel template synthesis of highly ordered MnO2 nanowire arrays," *J. Power Sources*, vol. 140, pp. 211–215, 2005.

[173] a. Bello, O. O. Fashedemi, M. Fabiane, J. N. Lekitima, K. I. Ozoemena, and N. Manyala, "Microwave assisted synthesis of MnO2 on nickel foam-graphene for electrochemical capacitor," *Electrochim. Acta*, vol. 114, pp. 48–53, 2013.

[174] H. Y. Lee, H. Y. Lee, J. B. Goodenough, and J. B. Goodenough, "BRIEF COMMUNICATION Supercapacitor Behavior with KCl Electrolyte," *J. Solid State Chem.*, vol. 223, pp. 220–223, 1999.

[175] C. Hu and T. Tsou, "Ideal capacitive behavior of hydrous manganese oxide prepared by anodic deposition," *Electrochem. commun.*, vol. 4, pp. 105–109, 2002.

[176] M. Toupin, M. Toupin, T. Brousse, T. Brousse, D. Bélanger, and D. Bélanger, "Influence of Microstucture on the Charge Storage Properties of Chemically Synthesized Manganese Dioxide," *Chem. Mater.*, vol. 14, no. 9, pp. 3946–3952, 2002.

[177] P. Yang, Y. Ding, Z. Lin, Z. Chen, Y. Li, P. Qiang, M. Ebrahimi, W. Mai, C. P. Wong, and Z. L. Wang, "Low-cost high-performance solid-state asymmetric supercapacitors based on MnO2 nanowires and Fe2O3 nanotubes.," *Nano Lett.*, vol. 14, no. 2, pp. 731–6, Feb. 2014.

[178] K. Rajendra Prasad and N. Miura, "Electrochemically synthesized MnO 2-based mixed oxides for high performance redox supercapacitors," *Electrochem.*

commun., vol. 6, no. 10, pp. 1004–1008, 2004.

[179] V. Khomenko, E. Raymundo-Piñero, and F. Béguin, "Optimisation of an asymmetric manganese oxide/activated carbon capacitor working at 2 v in aqueous medium," *J. Power Sources*, vol. 153, no. 1, pp. 183–190, 2006.

[180] R. K. Sharma, H.-S. Oh, Y.-G. Shul, and H. Kim, "Carbon-supported, nano-structured, manganese oxide composite electrode for electrochemical supercapacitor," *J. Power Sources*, vol. 173, no. 2, pp. 1024–1028, 2007.

[181] T. Cottineau, M. Toupin, T. Delahaye, T. Brousse, and D. Bélanger, "Nanostructured transition metal oxides for aqueous hybrid electrochemical supercapacitors," *Appl. Phys. A Mater. Sci. Process.*, vol. 82, pp. 599–606, 2006.

[182] V. Subramanian, H. Zhu, and B. Wei, "Synthesis and electrochemical characterizations of amorphous manganese oxide and single walled carbon nanotube composites as supercapacitor electrode materials," *Electrochem. commun.*, vol. 8, no. 5, pp. 827–832, 2006.

[183] S.-B. Ma, K.-W. Nam, W.-S. Yoon, X.-Q. Yang, K.-Y. Ahn, K.-H. Oh, and K.-B. Kim, "Electrochemical properties of manganese oxide coated onto carbon nanotubes for energy-storage applications," *J. Power Sources*, vol. 178, no. 1, pp. 483–489, 2008.

[184] D. P. Dubal, D. S. Dhawale, R. R. Salunkhe, S. M. Pawar, and C. D. Lokhande, "A novel chemical synthesis and characterization of Mn 3 O 4 thin films for supercapacitor application," *Appl. Surf. Sci.*, vol. 256, no. 14, pp. 4411–4416, 2010.

[185] D. P. Dubal and R. Holze, "Successive Ionic Layer Adsorption and Reaction (SILAR) Method to Induce Mn3O4 Nanospots on CNTs for Supercapacitor," *New J. Chem.*, no. ii, pp. 403–408, 2012.

[186] F. Yang, M. Zhao, Q. Sun, and Y. Qiao, "A novel hydrothermal synthesis and characterisation of porous Mn 3 O 4 for supercapacitors with high rate capability," *RSC Adv.*, vol. 5, pp. 9843–9847, 2015.

[187] W. Gao, S. Ye, and M. Shao, "Solution-combusting preparation of mono-dispersed Mn3O4 nanoparticles for electrochemical applications," *J. Phys. Chem. Solids*, vol. 72, no. 9, pp. 1027–1031, 2011.

[188] D. P. Dubal, D. S. Dhawale, R. R. Salunkhe, V. J. Fulari, and C. D. Lokhande, "Chemical synthesis and characterization of Mn3O4 thin films for supercapacitor application," *J. Alloys Compd.*, vol. 497, no. 1–2, pp. 166–170, 2010.

[189] A. Baykal, H. Kavas, Z. Durmuş, M. Demir, S. Kazan, R. Topkaya, and M. S. Toprak, "Sonochemical synthesis and chracterization of Mn3O4 nanoparticles," *Cent. Eur. J. Chem.*, vol. 8, no. 3, pp. 633–638, 2010.

[190] K. V. Sankar, S. T. Senthilkumar, L. J. Berchmans, C. Sanjeeviraja, and R. K. Selvan, "Effect of reaction time on the synthesis and electrochemical properties of Mn3O4 nanoparticles by microwave assisted reflux method," *Appl. Surf. Sci.*, vol. 259, pp. 624–630, 2012.

[191] C.-L. Liu, K.-H. Chang, C.-C. Hu, and W.-C. Wen, "Microwave-assisted hydrothermal synthesis of Mn3O4/reduced graphene oxide composites for high power supercapacitors," *J. Power Sources*, vol. 217, pp. 184–192, 2012.

[192] T. Zhou, S. Mo, S. Zhou, W. Zou, Y. Liu, and D. Yuan, "Mn3O4/worm-like mesoporous carbon synthesized via a microwave method for supercapacitors," *J. Mater. Sci.*, vol. 46, pp. 3337–3342, 2011.

[193] S. K. Apte, S. D. Naik, R. S. Sonawane, B. B. Kale, N. Pavaskar, a. B. Mandale, and B. K. Das, "Nanosize Mn3O4 (Hausmannite) by microwave irradiation method,"

Mater. Res. Bull., vol. 41, pp. 647–654, 2006.

[194] J. Jiang and A. Kucernak, "Electrochemical supercapacitor material based on manganese oxide: Preparation and characterization," *Electrochim. Acta*, vol. 47, no. 15, pp. 2381–2386, 2002.

[195] J. Chang and W. Tsai, "Effects of temperature and concentration on the structure and Effects of temperature and concentration on the structure and specific capacitanceof manganese oxide deposited in manganese acetate solution," *J. Appl. Electrochem.*, vol. 34, pp. 953–961, 2004.

[196] A. Taguchi, S. Inoue, S. Akamaru, M. Hara, K. Watanabe, and T. Abe, "Phase transition and electrochemical capacitance of mechanically treated manganese oxides," *J. Alloys Compd.*, vol. 414, no. 1–2, pp. 137–141, 2006.

[197] Y.-T. Wu and C.-C. Hu, "Aspect Ratio Controlled Growth of MnOOH in Mixtures of Mn3O4 and MnOOH Single Crystals for Supercapacitors," *Electrochem. Solid-State Lett.*, vol. 8, no. 5, pp. A240–A244, 2005.

[198] B. Djurfors, J. N. Broughton, M. J. Brett, and D. G. Ivey, "Electrochemical oxidation of Mn/MnO films: Formation of an electrochemical capacitor," *Acta Mater.*, vol. 53, no. 4, pp. 957–965, 2005.

[199] N. Nagarajan, H. Humadi, and I. Zhitomirsky, "Cathodic electrodeposition of MnOx films for electrochemical supercapacitors," *Electrochim. Acta*, vol. 51, no. 15, pp. 3039–3045, 2006.

[200] G. An, P. Yu, M. Xiao, Z. Liu, Z. Miao, K. Ding, and L. Mao, "Low-temperature synthesis of Mn3O4 nanoparticles loaded on multi-walled carbon nanotubes and their application in electrochemical capacitors.," *Nanotechnology*, vol. 19, p. 275709, 2008.

[201] B. Wang, J. Park, C. Wang, H. Ahn, and G. Wang, "Mn3O4 nanoparticles embedded into graphene nanosheets: Preparation, characterization, and electrochemical properties for supercapacitors," *Electrochim. Acta*, vol. 55, no. 22, pp. 6812–6817, 2010.

[202] D. P. Dubal and R. Holze, "All-solid-state flexible thin film supercapacitor based on Mn3O4 stacked nanosheets with gel electrolyte," *Energy*, vol. 51, pp. 407–412, 2013.

[203] Y. Qiao, Q. Sun, H. Cui, D. Wang, F. Yanga, and X. Wang, "Synthesis of micro/nano-structured Mn3O4 for supercapacitor electrode with excellent rate performance," *RSC Adv.*, 2015.

[204] A. F. Wells, *Structural Inorganic Chemistry*, 5th ed. Oxford Science Publications, 1984.

[205] N. Greenwood, *Chemistry of the Elements*, 2nd ed. Butterworth–Heinemann, 1997.

[206] T. Nathan, M. Cloke, and S. R. S. Prabaharan, "Electrode properties of Mn 2 O 3 nanospheres synthesized by combined sonochemical/solvothermal method for use in electrochemical capacitors," *J. Nanomater.*, vol. 1, 2008.

[207] X. Chen, X. Li, Y. Jiang, C. Shi, and X. Li, "Rational synthesis of MnO2 and Mn 2O3 nanowires with the electrochemical characterization of MnO2 nanowires for supercapacitor," *Solid State Commun.*, vol. 136, pp. 94–96, 2005.

[208] W. Li, J. Shao, Q. Liu, X. Liu, X. Zhou, and J. Hu, "Facile synthesis of porous Mn2O3 nanocubics for high-rate supercapacitors," *Electrochim. Acta*, vol. 157, pp. 108–114, 2015.

[209] N. K. Chiang, M. Clokec, G. Z. Chena, E. Engineering, E. Capacitor, M. Oxide, and S.

Route, “Nano-sized Mn2O3 preparedby a novel solvolysis route as an electrochemical capacitor,” *Inst. Eng. Malaysia*, vol. 69, no. 3, pp. 31–36, 2006.

[210] Z. Chen, S. Zhang, S. TAn, F. Li, J. Wang, S. Jin, and Y. Zhang, “Preparation and electron spin resonance effect of nanometer-sized Mn2O3,” *J. Cryst. Growth*, vol. 180, pp. 280–283, 1997.

[211] W. He, Y. Zhang, X. Zhang, H. Wang, and H. Yan, “Low temperature preparation of nanocrystalline Mn2O3 via ethanol-thermal reduction of MnO2,” *J. Cryst. Growth*, vol. 252, pp. 285–288, 2003.

[212] C. Yu, L. Zhang, J. Shi, J. Zhao, J. Gao, and D. Yan, “A simple template-free strategy to synthesize nanoporous manganese and nickel oxides with narrow pore size distribution, and their electrochemical properties,” *Adv. Funct. Mater.*, vol. 18, no. 10, pp. 1544–1554, 2008.

[213] L. L. Zhang, T. Wei, W. Wang, and X. S. Zhao, “Manganese oxide-carbon composite as supercapacitor electrode materials,” *Microporous Mesoporous Mater.*, vol. 123, no. 1–3, pp. 260–267, 2009.

[214] X. Wang, L. Liu, X. Wang, L. Yi, C. Hu, and X. Zhang, “Mn2O3/carbon aerogel microbead composites synthesized by in situ coating method for supercapacitors,” *Mater. Sci. Eng. B Solid-State Mater. Adv. Technol.*, vol. 176, no. 15, pp. 1232–1238, 2011.

[215] S. W. Zhang and G. Z. Chen, “Manganese oxide based materials for supercapacitors,” *Energy Mater. Mater. Sci. Eng. Energy Syst.*, vol. 3, no. 3, pp. 186–200, 2008.

[216] W. Wei, X. Cui, W. Chen, and D. G. Ivey, “Manganese oxide-based materials as electrochemical supercapacitor electrodes.,” *Chem. Soc. Rev.*, vol. 40, no. 3, pp.

1697–721, Mar. 2011.

[217] K. Ozoemena, N. Kuznetsova, and T. Nyokong, "Photosensitized transformation of 4-chlorophenol in the presence of aggregated and non-aggregated metallophthalocyanines," *J. Photochem. Photobiol. A Chem.*, vol. 139, no. 2–3, pp. 217–224, 2001.

[218] T. Nyokong and E. Antunes, "Influence of nanoparticle materials on the photophysical behavior of phthalocyanines," *Coord. Chem. Rev.*, vol. 257, no. 15–16, pp. 2401–2418, 2013.

[219] G. N. Ngubeni, J. Britton, J. Mack, E. New, I. Hancox, M. Walker, T. Nyokong, T. S. Jones, and S. Khene, "Spectroscopic and nonlinear optical properties of the four positional isomers of 4α-(4-tert-butylphenoxy)phthalocyanine," *J. Mater. Chem. C*, 2015.

[220] K. Sanusi, E. K. Amuhaya, and T. Nyokong, "Enhanced Optical Limiting Behavior of an Indium Phthalocyanine − Single-Walled Carbon Nanotube Composite: An Investigation of the E ff ects of Solvents," 2014.

[221] M. P. Siswana, K. I. Ozoemena, and T. Nyokong, "Electrocatalysis of asulam on cobalt phthalocyanine modified multi-walled carbon nanotubes immobilized on a basal plane pyrolytic graphite electrode," *Electrochim. Acta*, vol. 52, no. 1, pp. 114–122, 2006.

[222] T. Higuchi, T. Murayama, E. Itoh, and K. Miyairi, "Electrical properties of phthalocyanine based field effect transistors prepared on various gate oxides," *Thin Solid Films*, vol. 499, no. 1–2, pp. 374–379, Mar. 2006.

[223] F. Bedioui, S. Griveau, T. Nyokong, a J. Appleby, C. a Caro, M. Gulppi, G. Ochoa, and J. H. Zagal, "Tuning the redox properties of metalloporphyrin- and

metallophthalocyanine-based molecular electrodes for the highest electrocatalytic activity in the oxidation of thiols.," *Phys. Chem. Chem. Phys.*, vol. 9, no. 26, pp. 3383–96, Jul. 2007.

[224] B. Agboola, K. I. Ozoemena, and T. Nyokong, "Comparative efficiency of immobilized non-transition metal phthalocyanine photosensitizers for the visible light transformation of chlorophenols," *J. Mol. Catal. A Chem.*, vol. 248, no. 1–2, pp. 84–92, Apr. 2006.

[225] S. Pillay, J. Pillay, P. M. Ejikeme, K. Makgopa, and K. I. Ozoemena, "Nanostructured Cobalt(II) Tetracarboxyphthalocyanine Complex Supported Within the MWCNT Frameworks: Electron Transport and Charge Storage Capabilities," *Electroanalysis*, vol. 27, pp. 1707 – 1718, 2015.

[226] P. Simon and Y. Gogotsi, "Materials for electrochemical capacitors.," *Nat. Mater.*, vol. 7, no. 11, pp. 845–854, Nov. 2008.

[227] K. I. Ozoemena, D. Nkosi, and J. Pillay, "Influence of solution pH on the electron transport of the self-assembled nanoarrays of single-walled carbon nanotube-cobalt tetra-aminophthalocyanine on gold electrodes: Electrocatalytic detection of epinephrine," *Electrochim. Acta*, vol. 53, no. 6, pp. 2844–2851, Feb. 2008.

[228] A. T. Chidembo and K. I. Ozoemena , "Electrochemical Capacitive Behaviour of Multiwalled Carbon Nanotubes Modified with Electropolymeric Films of Nickel Tetraaminophthalocyanine," *Electroanalysis*, vol. 22, no. 21, pp. 2529–2535, Nov. 2010.

[229] D. K. Gosser, *Cyclic voltammetry: simulation and analysis of reaction mechanisms.* New York: VCH, 1993.

[230] J. N. Lekitima, "Supercapacitive properties of nanocarbons modified with

manganese oxide nanoparticles and metallotetrapyrazinoporphyrazines," M.Sc. Thesis, University of Pretoria, 2013.

[231] R. Signorelli, D. C. Ku, J. G. Kassakian, and J. E. Schindall, "Electrochemical double-layer capacitors using carbon nanotube electrode structures," *Proc. IEEE*, vol. 97, no. 11, pp. 1837–1847, 2009.

[232] B. E. Conway and W. G. Pell, "Double-layer and pseudocapacitance types of electrochemical capacitors and their applications to the development of hybrid devices," *J. Solid State Electrochem.*, vol. 7, no. 9, pp. 637–644, 2003.

[233] W. Plieth, *Electrochemistry for Materials Science*, 1st ed. Elsevier B.V, 2008.

[234] Y. Gao, S. Chen, D. Cao, G. Wang, and J. Yin, "Electrochemical capacitance of Co3O4 nanowire arrays supported on nickel foam," *J. Power Sources*, vol. 195, no. 6, pp. 1757–1760, 2010.

[235] D. Weingarth, a. Foelske-Schmitz, and R. Kötz, "Cycle versus voltage hold – Which is the better stability test for electrochemical double layer capacitors?," *J. Power Sources*, vol. 225, pp. 84–88, Mar. 2013.

[236] S. Brockman, "Basics of Electrochemical Impedance Spectroscopy," *Appl. note*, no. 1, pp. 1–13, 2012.

[237] A. R. Clarke and C. N. Eberhardt, *Microscopy techniques for materials science*. Cambridge: Woodhead Publishing Ltd, 2002.

[238] J. J. Bozzola and L. D. Russell, *Principles and Techniques for Biologists*. Sudbury: Jones & Bartlett Learning, 1999.

[239] P. University, "Scanning Electron Microscope." [Online]. Available: https://www.purdue.edu/ehps/rem/rs/sem.htm. [Accessed: 02-Jun-2015].

[240] B. D. Williams and C. B. Carter, *Transmission Electron Microscopy: A Textbook for Materials Science*, no. Chapter 1. New York, USA: Springer, 1996.

[241] L. Reimer, *Transmission Electron Microscopy: Physics of Image Formation and Microanalysis*. New York, USA: Springer-verlag Berlin Heidelberg, 1984.

[242] R. F. Egerton, *Physical principles of electron microscopy: an introduction to TEM, SEM, and AEM,* 1st ed. New York, USA: Springer, 2005.

[243] "Basic principle of transmission electron microscope." [Online]. Available: http://www.hk-phy.org/atomic_world/tem/tem02_e.html. [Accessed: 20-Jul-2015].

[244] Oxford Instruments, "EDS in the TEM Explained," *The Business of Science*. [Online]. Available: http://www.oxford-instruments.com/products/microanalysis/energy-dispersive-x-ray-systems-eds-edx/eds-for-tem. [Accessed: 03-Jun-2015].

[245] B. D. Cullity and S. R. Stock, *Elements of X-Ray Diffraction*, 3rd ed. New Jersey: Prentice Hall International Inc, 2001.

[246] D. M. Moore and R. C. Reynolds Jr, *X-ray diffraction and the identification and analysis of clay minerals*. Oxford University Press, 1989.

[247] "Physical Electronics, A division of ULVAC-PHI, Surface Analysis Techniques." [Online]. Available: https://www.phi.com/surface-analysis-techniques/xps-esca.html. [Accessed: 03-Sep-2015].

[248] "Thermo Scientific, What is X-Ray Photoelectron Spectroscopy (XPS)?" [Online]. Available: http://xpssimplified.com/whatisxps.php. [Accessed: 03-Sep-2015].

[249] H. H. Willard, L. L. Merritt Jr., and J. A. Dean, *Instrumental methods of analysis*, 5th ed. New York-Wokingham: Van Nostrand Reinhold Company, 1974.

[250] D. A. Skoog, D. M. West, F. J. Holler, and S. R. Crouch, *Fundamentals of analytical chemistry*, 8th ed. Califonia: Thomson-Brooks/Cole, 2004.

[251] "Coulter, Gas Adsorption Analysis." [Online]. Available: http://www.cyto.purdue.edu/cdroms/cyto2/6/coulter/ss000107.htm. [Accessed: 03-Sep-2015].

[252] Y. S. Bae, a. Ö. Yazayd'n, and R. Q. Snurr, "Evaluation of the BET method for determining surface areas of MOFs and zeolites that contain Ultra-Micropores," *Langmuir*, vol. 26, no. 8, pp. 5475–5483, 2010.

[253] S. Brunauer, L. S. Deming, W. Deming, and E. Teller, "On a theory of the van der Waals adsorption of gases," *J. Am. Chem. Soc.*, vol. 62, no. 6, pp. 1723–1732, 1940.

[254] D. J. Gardiner, P. R. Graves, and H. J. Bowley, *Practical Raman spectroscopy*. Germany: springer-verlag heidelberg, 1989.

[255] H. A. Szymanski, *Raman Spectroscopy: Theory and Practice*, 2nd ed. New York, USA: Plenum Press springer, 1970.

[256] K. I. Sasaki, "Basic principles of raman spectroscopy for graphene," *NTT Tech. Rev.*, vol. 11, no. 8, 2013.

Chapter 3: Experimental Techniques and Methods

3.1 Materials and Reagents

All the materials and chemical reagents used for synthesizing the ECs electrode materials are listed in Table 3.1.

Table 3.1: List of materials and reagents used in this study.

Reagents and materials	Purity and specifications	Supplier
$Mn(NO_3)_2·4H_2O$	≥ 97 %	Sigma-Aldrich
$KMnO_4$	≥ 99 %	Sigma-Aldrich
$Co(NO_3)_2·6H_2O$	≥ 98 %	Associated Chemical Enterprises (ACE)
$AlN_3O_9·9H_2O$	≥ 98 %	Fluka Analytical
Na_2SO_4	≥ 99 %	Sigma Aldrich
H_2O_2	30 %	Sigma-Aldrich
Electrolytic Manganese Dioxide (EMD)	-	Delta EMD (Pty) Ltd
Multi-Walled Carbon Nano Tubes (MWCNT)	Bundles ≥ 94 % Diameter 10 – 20 nm Length 5 – 20 µm	NanoLab
H_2SO_4	98 %	Sigma-Aldrich
HNO_3	-	Sigma-Aldrich
NH_4OH	28 %	Sigma-Aldrich
HCl	37 %	Sigma-Aldrich
Carbon Black	Control number: 030520	PRINTEX XE-2-B
Polyvinylidene Fluoride (PVDF)	≥ 99.5 %	MTI Corp
N-methyl-2-pyyolidone (NMP)	99.5 %	Sigma Aldrich
Nanodiamond (ND)	98-99 %	NaBond Technologies
Graphite	-	Asbury Graphite Mills
Activated Carbon		SUPELCO Analytical
Nickel Foam	-	-

3.2 Synthesis of Materials

This section takes account of the synthesis of all electrode materials utilised in ECs applications. All chemicals were of analytical grade and used as received. De-ionized water is used throughout the synthesis process.

3.2.1 Synthesis of Onion-Like Carbon (OLC)

OLC was synthesized from nanodiamond (ND) powder with a purity of 98-99 % (NaBond Technologies) and thoroughly characterized [1]. Briefly, ND powder was placed in a closed-lid cylindrical graphite crucibles (30 mm in diameter and 20 mm in height) and thermally annealed in a water-cooled high-temperature vacuum furnace with tungsten heaters (Model: 1100-3580-W1, Thermal Technology Inc.). The heating and cooling rates were both 15 °C min^{-1} and the chamber pressure ranged between 10 and 100 mPa. The final OLC is annealed at 1750 °C for 3 h.

3.2.2 Functionalization of Multiwalled carbon nanotubes (CNT)

Multi-walled carbon nanotubes obtained from Nanolab (purity: > 94%, diameter: 10-20 nm, length: 5-20 μm), were converted to short and uncapped nanotubes bearing acidic functional groups (mainly: -COOH) by following the established multi-step acid treatment procedures 1-6, just referred to in this work as CNT.

A 1 g of pristine CNTs was refluxed in 140 mL of 2.6 M Nitric acid (HNO_3) for 48 h. Sediments of carbon nanotube were separated from the reaction and washed with de-ionized H_2O. The clean deposits were sonicated in a mixture of conc. H_2SO_4/HNO_3 (3:1 ratio, 95-97%, and 65% purity, respectively) for 24 h, followed by washing with de-ionised H_2O and stirred at 70 ° C for 30 min. in a mixture of H_2SO_4/H_2O_2 (4:1, piranha solution, 95-97% and 30% purity, respectively). The black powder was finally washed with de-ionized H_2O and dried at 50 °C for 24 h. Figure 3.1 shows a schematic representation of the outlined method in acid functionalization of MWCNT.

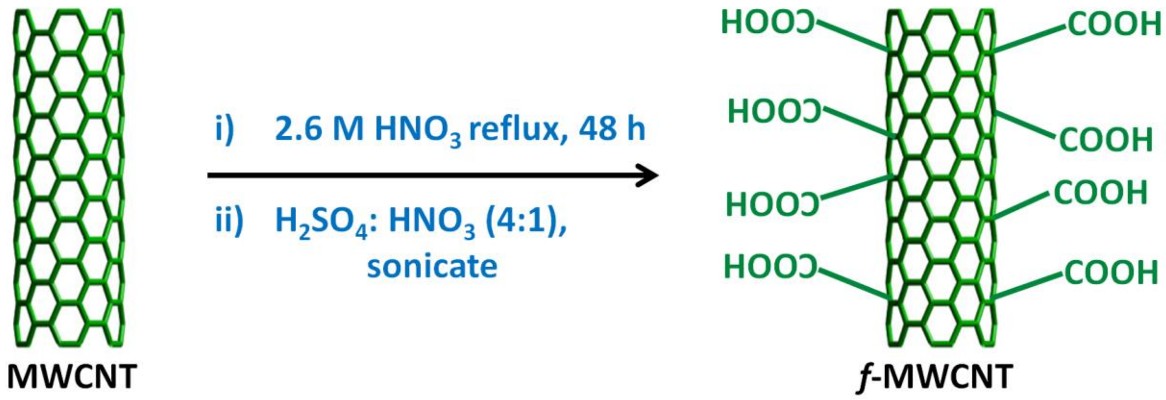

Figure 3.1: A schematic representation of acid functionalization of MWCNT.

N.B.: Activated carbon (AC) was purchased from SUPELCO analytical and used as received.

3.2.3 Synthesis of Graphene Oxide (GO)

Graphene oxide (GO) was prepared from expanded graphite powder. The expanded graphite is obtained from the graphite powder using a well-established method [2]. Briefly, a natural graphite powder (5.0 g) and conc. H_2SO_4 (15 mL) were first mixed and stirred in the round bottom flask, followed by addition of fuming nitric acid (HNO_3) and the mixture was stirred for 24 h at room temperature. After stirring, 50 mL of de-ionized H_2O was slowly added to the mixture and centrifuged for 10 min at the speed of 4000 rpm. After decanting the supernatant, the solid material was then centrifuged three times (3x) with de-ionized H_2O and dried at 60 ^{o}C for 24 h as to obtain a graphite intercalation compound (GIC) powder. The as-synthesized GIC powder was thermally expanded at 1050 °C for 15 s as to get the expanded graphite (EG). The synthesis of GO was carried out using the well-known modified Hummers method. This approach is outlined as follows: 1.0 g EG was mixed and stirred with 200 mL of concentrated H_2SO_4

in a 500 mL three-necked flask. Followed by a very slow addition of 10 g Potassium permanganate ($KMnO_4$), then the mixture was transferred into an ice bath where 200 mL de-ionized H_2O, and 50 mL H_2O_2 were added slowly resulting in a color change of the suspensions to light brown. After stirring for 30 minutes, the as prepared GO particles were then washed with an aqueous HCl (9:1 H_2O: HCl by volume), then washed by centrifugation with de-ionized H_2O until the pH is adjusted about 5 to 6 and dried overnight at 80 °C [2], [3].

3.2.4 Synthesis of Carbon/Birnessite-MnO_2 Nanohybrid

The carbon/MnO_2 nanohybrid electrode materials (i.e., OLC/MnO_2, CNT/MnO_2, GO/MnO_2, and AC/MnO_2) were prepared using the conventional hydrothermal reduction technique. Typically, ~ 40 mg of various carbon materials (i.e., OLC, CNT, GO, and AC) were individually dispersed by sonication in 30 mL of 0.02 M $KMnO_4$ (Merck). Subsequently, the mixture (pH = 7.05) of each was refluxed at 130 °C in an oil bath for 24 h with continuous magnetic stirring. The resultant dispersion was then centrifuged and washed several times with deionized water, and finally dried at 60 °C overnight in a vacuum oven. All chemicals were of analytical grade and used as received. De-ionized water was used throughout the synthesis process. Figure 3.1 shows the schematic representation of the synthesis procedure.

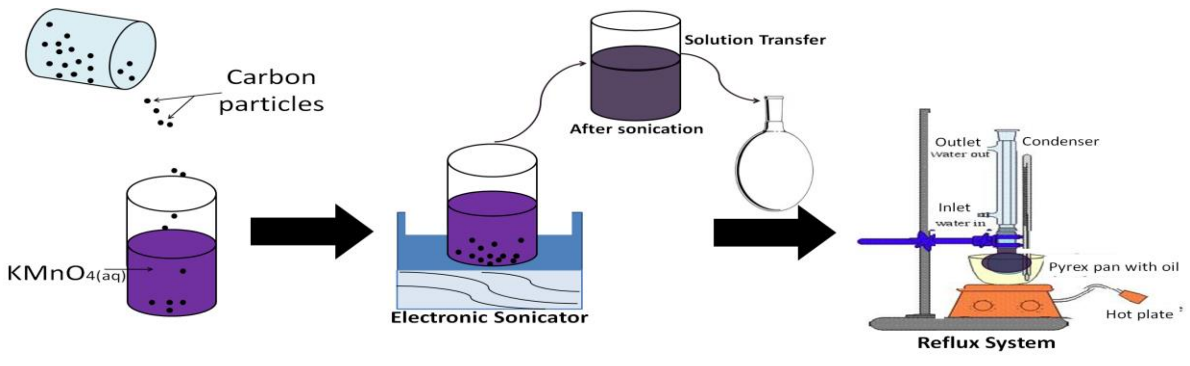

Figure 3.2: A scheme depicting the synthetic process of birnessite-type MnO_2 on the surface of the carbon.

3.2.5 Synthesis of Hausmannite Mn_3O_4 and Carbon/Hausmannite Mn_3O_4 Nanohybrid

Tetragonal hausmannite Mn_3O_4 nanoparticles were synthesised from Electrolytic Manganese Dioxide (EMD) through the annealing process. EMD powder was placed in a horizontal tube furnace and ramped from room temperature to 1000 °C at 10 °C min^{-1} in the air and kept at this temperature for 40 h. Carbon/Mn_3O_4 nanohybrid electrode materials (i.e., OLC/Mn_3O_4, CNT/Mn_3O_4, GO/Mn_3O_4, and AC/Mn_3O_4) were obtained by dispersing both carbon material (i.e., OLC, CNT, GO or AC) and Mn_3O_4 nanoparticles, (1: 1 mass ratio, Carbon: Mn_3O_4), in ethanol. Then the mixture was ultrasonicated for 24 h using a table-top ultrasonic cleaner (VWR B1500-A MTH, operated at 50 W). After which samples were washed by centrifugation with copious de-ionized H_2O and finally dried at 60 °C overnight.

3.2.6 Synthesis of NiTAPc and GO/NiTAPc

Nickel (II) tetraaminophthalocyanine (NiTAPc) was synthesised and characterised following the well-known procedure introduced by Acher and Jayasree [4]. The GO/NiTAPc composite was obtained by dispersing both GO and NiTAPc precursors, (1: 1 mass ratio, GO: NiTAPc), in ethanol, followed by ultrasonicated for 2 h. Then the samples were washed by centrifugation with copious de-ionized H_2O and finally dried at 60 °C overnight.

3.3 Microscopic and Spectroscopic Characterization Equipment

This section takes account of the microscopic and spectroscopic techniques used in the analysis of the as-synthesised electrode materials utilised in ECs applications.

3.3.1 Scanning Electron Microscopy (SEM)

The surface morphology and microstructure of all samples in this work were investigated using a Zeiss Ultra Plus 55 field emission scanning electron microscope (FE-SEM) operated at 2 kV in secondary electron detection mode. The samples are prepared by placing the powder on the carbon stickers attached to an aluminium holder.

3.3.2 Energy dispersive X-ray spectra (EDX)

Energy dispersive X-ray spectra (EDX) were measured with an EDX system (Oxford Instruments) at five different positions. The chemical composition was calculated using the AZtec energy analysis software (Oxford Instruments).

3.3.3 Transmission electron microscopy (TEM)

Transmission electron microscopy (TEM) samples were prepared by dispersing powders in ethanol and placing the solution over a copper grid with a lacey carbon film. All measurements were carried out with a 2100F microscope (JEOL) operating at 200 kV.

3.3.4 X-ray diffraction (XRD)

X-ray diffraction (XRD) patterns of the samples were collected using a X'Pert-Pro MPD diffractometer (PANalytical) with theta/theta geometry (step width: 0.0263°s^{-1}), operating a copper tube at 40 kV and 40 mA. The instrumental resolution function is characterized with the NIST SRM 660a (LaB_6) standard. The XRD patterns were carried out in the range of 5-148 ° 2θ. Qualitative phase analysis of the samples was conducted using Bruker EVA using the PDF database.

3.3.5 Raman Analysis

Raman spectra were recorded with a Renishaw inVia Raman microscope using a Nb-YAG laser with an excitation wavelength of 532 nm and a grating with 1800 lines mm^{-1} yielding a spectral resolution of *ca.* 1.2 cm^{-1}. The spot size of the sample was in the focal plane *ca.* 2 μm using an output power of 0.5 mW. Spectra were recorded for 30 s and accumulated 50 times to eliminate cosmic rays and to obtain a high signal-to-noise and signal-to-background ratio. Peak fitting is achieved by employing Lorentzian peaks assuming four components for the carbon spectrum between 1000 and 1800 cm^{-1}.

3.3.6 Fourier infrared spectroscopy (FTIR)

Fourier infrared spectroscopy (FTIR) analyses were carried out using Perkin Elmer FT-IR spectrophotometer. OLC and OLC/MnO_2 nanohybrids were analyzed as KBr pellets (10 scans).

3.3.7 X-ray photoelectron spectroscopy (XPS)

X-ray photoelectron spectroscopy (XPS) experiments were carried out on a Kratos Axis Ultra-DLD system (Shimadzu) with monochromated Al Kα radiation (1486.6 eV). Binding energies were calibrated using the containment carbon (C 1s @ 284.6 eV). The spectra analysis was carried out with the XPS Peak 4.1 program, and a Shirley function was used to subtract the background.

3.3.8 Nitrogen gas sorption

Nitrogen gas sorption measurements have been conducted with a Quantachrome Autosorb iQ system. The samples were outgassed at 150 °C for 10 h under vacuum condition. Gas sorption was performed in liquid nitrogen (-196 °C) with a relative pressure range from 10^{-7} to 0.95 in 68 steps. The specific surface area (SSA) was calculated with the ASQwin-software using Brunauer-Emmett-Teller (BET) equation [5] in the relative pressure range 0.01-0.2. We also calculated SSA and pore size distribution (PSD) via quenched-solid density functional theory (QSDFT)[6] with a hybrid model for slit and cylindrical pores and pore size between 0.56 and 37.5 nm.

3.4 Electrochemical Characterization Procedure

3.4.1 Fabrication of Carbon/MnO_2 Nanohybrid Electrodes for Electrochemical Capacitors

Electrochemical measurements were performed in a single cell configuration using Swagelok cells (see Fig. 3.3.). Before use, the nickel foam (current collector) was cleaned in a 1 M HCl solution, washed with de-ionized water, and dried under vacuum. Both the positive and the negative electrodes were prepared by mixing one of the nanohybrid, carbon black (CB) and polyvinylidene fluoride (PVDF) in a weight percentage of 80:15:5 respectively using pestle and mortar with a few drops of anhydrous N-methyl-2-pyrrolidone (NMP) to produce a homogeneous paste. The CB and PVDF served as the conductive agent and binder, respectively. The resulting slurry was coated onto the nickel foam substrate with a spatula. The electrode was then dried at 80 °C overnight in a vacuum oven and pressed to a thickness of 250 µm. For comparison, all other electrodes used in this work were prepared using the above-outlined procedure.

3.4.2 Electrochemical Procedure

All electrochemical measurements were carried out using a Bio-Logic VMP 300 potentiostat/galvanostat (driven by EC-Lab® v10.40 software) using a two-electrode (full cell) configuration for a symmetric pseudocapacitor. A 1 M Na_2SO_4 was used as an electrolyte and a porous glass fiber (Whatman Grade GF/D Glass Microfiber Filters) served as the separator. The cyclic voltammetry (CV), tests were carried out in the potential range of 0 to 0.8 V at various scan rates (i.e., 5 mV s^{-1} to 100 mV s^{-1}). The galvanostatic charge-discharge (GCD) tests were carried out at varying current densities (i.e., 0.1 A g^{-1} to 10 A g^{-1}). Electrochemical impedance spectroscopy (EIS) measurements were conducted in the frequency range from 0.1 Hz to 100 kHz with an open circuit potential and Z-fit tool was used for EIS data analysis (fitting). Aqueous 1 M Na_2SO_4 was used throughout as electrolyte. Voltage-holding (floating) experiments are carried out for 10 h at 0.8 V, then galvanostatically charged-discharged between 0.0 and 0.8 V at 1 A g^{-1}, repeating the process for five times (i.e., a total of 50 h).

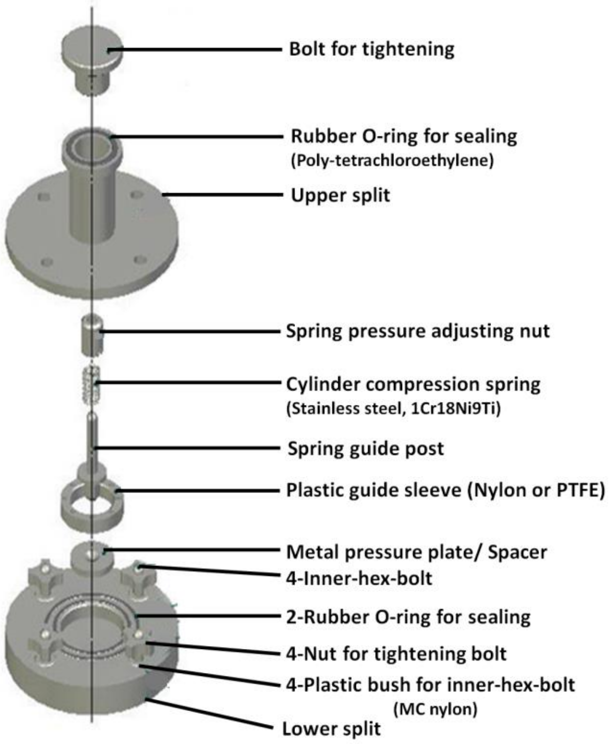

Figure 3.3: A cell configuration depicting Swagelok cell used for fabrication of electrodes materials in symmetric energy storage pseudocapacitor.

References

[1] D. Weingarth, M. Zeiger, N. Jäckel, M. Aslan, G. Feng, and V. Presser, "Graphitization as a Universal Tool to Tailor the Potential-Dependent Capacitance of Carbon Supercapacitors," *Adv. Energy Mater.*, vol. 4, no. 13, pp. 1–13, 2014.

[2] S. H. Aboutalebi, M. M. Gudarzi, Q. Bin Zheng, and J.-K. Kim, "Spontaneous Formation of Liquid Crystals in Ultralarge Graphene Oxide Dispersions," *Adv. Funct. Mater.*, vol. 21, no. 15, pp. 2978–2988, Aug. 2011.

[3] J. William S. Hummers and R. E. Offeman, "Preparation of Graphitic Oxide," *J. Am. Chem. Soc*, vol. 80, no. 1937, p. 1339, 1958.

[4] B. . Achar and P. . Jayasree, "Novel `synthetic metals' based on symmetrically tetrasubstituted nickel phthalocyanines," *Synth. Met.*, vol. 104, no. 2, pp. 101–106, Jul. 1999.

[5] S. Brunauer, P. H. Emmett, and E. Teller, "Gases i n Multimolecular Layers," *J. Am. Chem. Soc.*, vol. 60, no. 2, pp. 309 – 319, 1938.

[6] G. Y. Gor, M. Thommes, K. a. Cychosz, and A. V. Neimark, "Quenched solid density functional theory method for characterization of mesoporous carbons by nitrogen adsorption," *Carbon N. Y.*, vol. 50, no. 4, pp. 1583–1590, Apr. 2012.

Chapter 4: Carbon/birnessite-type Manganese Oxide (C/MnO_2) Nanohybrids as Pseudocapacitor Materials [1]

[1]The following publication resulted from part of the research work presented in this chapter and is not referenced further:
K. Makgopa, P. M. Ejikeme, C. J. Jafta, K. Raju, M. Zeiger, V. Presser, and K. I. Ozoemena, A high-rate aqueous symmetric pseudocapacitor based on highly graphitized onion-like carbon/birnessite-type manganese oxide nanohybrids, *J. Mater. Chem. A*. **3** (2015) 3480–3490

4.1 Introduction

There have been extensive studies of varieties of carbon materials for ECs application because of their large specific surface area (SSA), high conductivity, facile availability, and chemical stability [1], [2]. Amongst the carbon nanomaterials, onion-like carbon (OLC), carbon nanotube (CNT), graphene oxide (GO) and activated carbon (AC) have attracted significant research interests as electrode materials for energy storage. For example, advanced anode electrodes for lithium ion batteries [3]–[5], pseudocapacitors [6]–[11] and ultrahigh-power electric double-layer capacitors. The major attractions stem from the ability to prepare them on a large-scale and the superior power handling capacity [12]. OLCs consist of multi-shell fullerenes [13] that exhibit a high electrical conductivity commonly in the range of 2-4 S cm^{-1} and are prepared by thermal annealing of nanodiamonds [14]. However, the limited surface area of OLCs (200-600 m^2 g^{-1} range) has also resulted in limited double-layer capacitance (usually between 25 and 50 F g^{-1}, equivalent up to 2 Wh kg^{-1} at 1 V) [12], [14]. OLCs derived from thermal treatment of nanodiamonds (ND) [15] are highly graphitic spherical particles (5-10 nm) that consist of concentric carbon shells [16]. Alternative synthesis methods may also yield larger OLCs with diameters of more than 10 nm [5], [17] and include condensation of carbon vapor, [18] or electron beam irradiation.[19] However, thermal annealing of ND [20] at temperatures between 1000 and 2000 °C is the preferred technique to synthesize OLC since significant amounts of material can be obtained [21]. Also, a narrow size distribution of the ND precursor translates into a narrow size distribution of resulting onion-like carbons [6]. Carbon nanotubes (CNT) can be modified at the surfaces with functional groups such as carboxylic acid (-COOH) and sulfonic acid (-SO_3H) to give functionalized carbon nanotubes (*f*-CNTs where *f* = -COOH or (-SO_3H) [22]. Due to its intrinsic properties fine-tuned, CNT has found its path as the energy storage electrode material in ECs application [23], [24]. Graphene and graphene oxide have almost similar chemical properties as compared to other carbon allotropes. Due to graphene's high theoretical specific surface area, graphene has found attention as a potential electrode material for ECs application [25]–[30]. Apart from its many uses, activated carbon (AC) has been widely used also as an ECs electrode [31].

Birnessite-type MnO_2 (in this thesis referred to just "MnO_2") exhibits a two-dimensional layered structure (see Fig. 4.1) displaying edge-sharing MnO_6 octahedra in the sheets, metal cations (for example K^+) and water molecules in the interlayer region. Hence, an appropriate chemical representation would be $K_xMn_2O_4{\cdot}yH_2O$ (with $x \leq 0.5$ and $y \leq 1.5$) [32]. This metal oxide has become an attractive electrode material for an efficient and low-cost development of supercapacitor due to its natural abundance and environmental compatibility. However, because of its low electrical conductivity (10^{-6}-10^{-5} S cm^{-1}) and reduced power handling capability, electrochemical performance of MnO_2 electrodes is rather low, which significantly limits its potential applications as high-power supercapacitors [33]. The capacitive performance, redox activity of MnO_2 is improved by the addition of conductive materials [8], [34], [35]. For a detailed explanation, see Chapter 2.

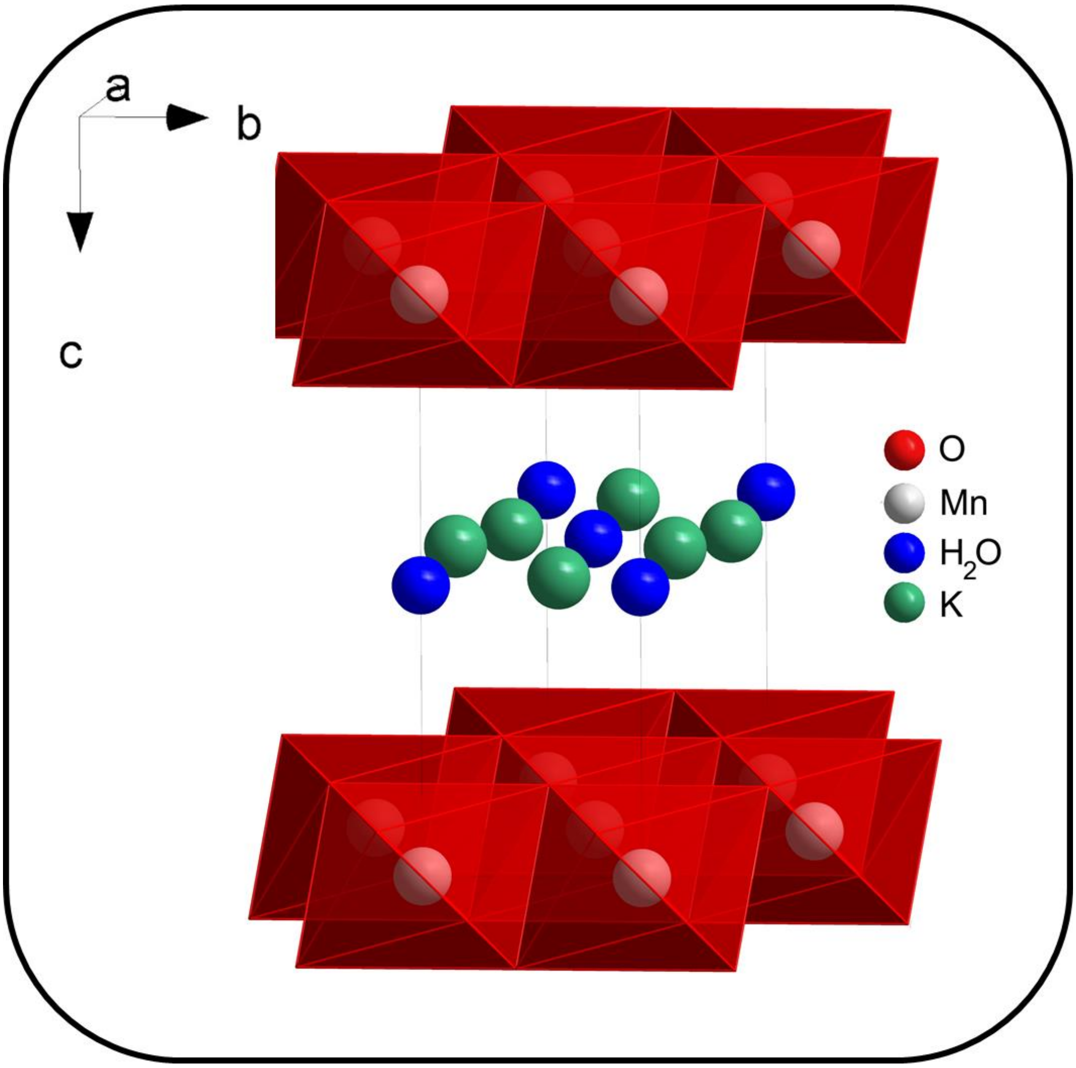

Figure 4.1: Crystal structure of a birnessite-type MnO_2 (with molecular formula represented as $K_xMn_2O_4 \cdot yH_2O$).

4.2 Results and Discussion

4.2.1 SEM and TEM analysis

The surface morphologies of the synthesized electrode materials (i.e., OLC/MnO_2, CNT/MnO_2, GO/MnO_2, and AC/MnO_2) were studied using FESEM as shown in Fig. 4.2 and TEM as shown in Fig. 4.3. The synthesized OLC/MnO_2, CNT/MnO_2, GO/MnO_2, and AC/MnO_2 nanohybrids exhibited different morphologies in comparison to each other. The morphology of the OLC/MnO_2 (Fig. 4.2a), CNT/MnO_2 (Fig. 4.2b), GO/MnO_2 (Fig. 4.2c) and AC/MnO_2 (Fig. 4.2d) clearly show the interaction of MnO_2 nanoparticles with the carbon support. This observation clearly indicates a successful decoration of MnO_2 in the carbon support samples.

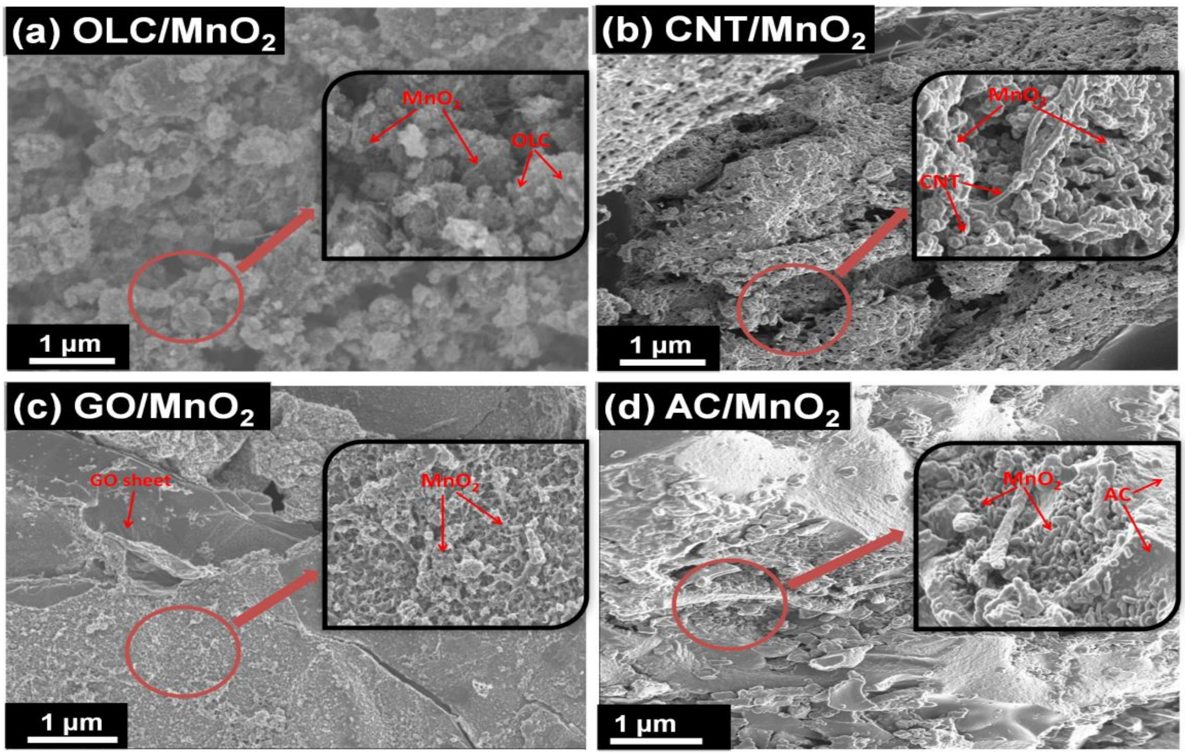

Figure 4.2: SEM images of (a) OLC/MnO_2, (b) CNT/MnO_2, (c) GO/MnO_2 and (d) AC/MnO_2 nanohybrids. Inset in (a-d) is the high magnification SEM image of respective nanohybrids.

Figure 4.3 compares the TEM micrographs of OLC/MnO_2 (Fig. 4.3a), CNT/MnO_2 (Fig. 4.3b), GO/MnO_2 (Fig. 4.3c), and AC/MnO_2 (Fig. 4.3d), nanohybrid electrode materials. The onion-like structure of the OLC decorated with the MnO_2 nanoparticle is clear shown on the high magnification TEM image (inset on Fig. 4.3a), indicating a successful synthesis of OLC/MnO_2 nanohybrid. A clear visibility of the carbon nanotubes covered by the MnO_2 nanoparticle confirms a successful integration of the CNT/MnO_2 nanohybrid as shown in Fig. 4.3b. The primary particle size of both carbon onions and carbon nanotubes is in the range of a few nanometers as seen from the TEM images which are in agreement with our previous findings [36], [37]. This primary particle size is maintained for the OLC/MnO_2 and CNT/MnO_2 nanohybrids (Fig. 4.3a and Fig. 4.3b, respectively). The MnO_2 nanoparticle is clearly distinguished from the graphene oxide sheet and the activated carbon structure as shown in both GO/MnO_2 and AC/MnO_2 nanohybrids (Fig. 4.3c and Fig. 4.3d, respectively). All these results are in good agreement with the results obtained from the SEM images, indicating a successful synthesis of the hybrid materials.

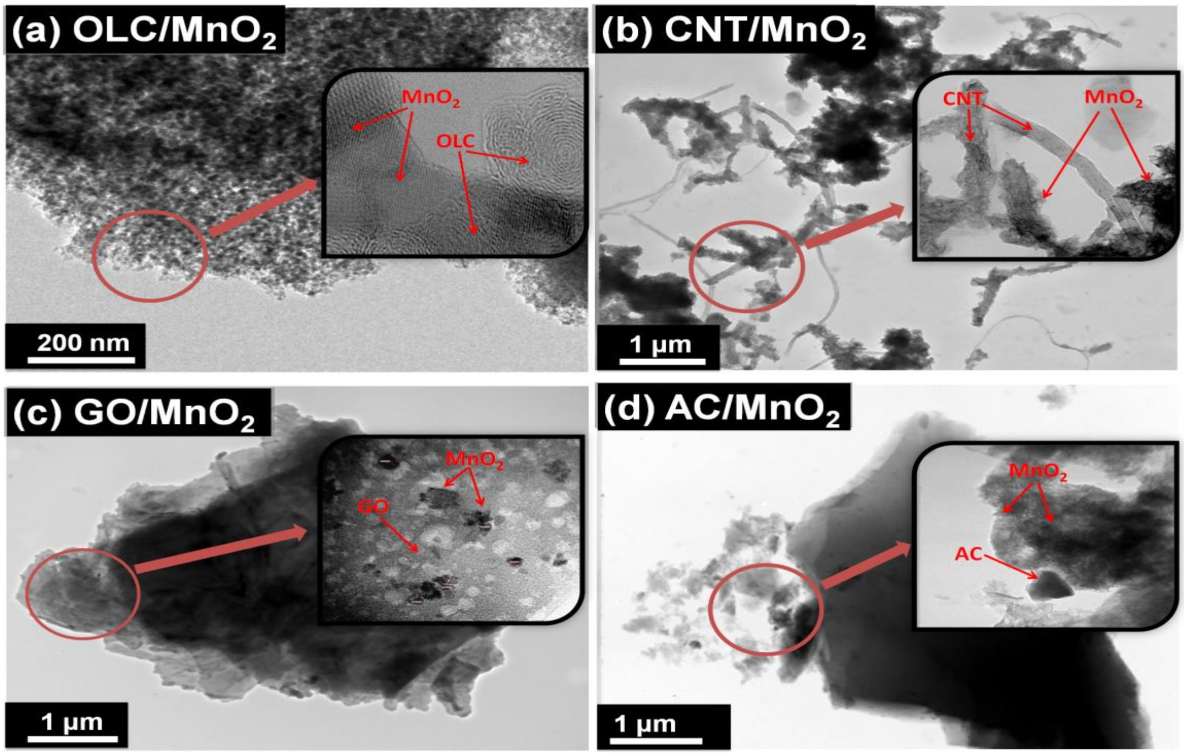

Figure 4.3: TEM images of (a) OLC/MnO_2, (b) CNT/MnO_2, (c) GO/MnO_2 and (d) AC/MnO_2 nanohybrids. Inset in (a-d) is the high magnification TEM image of respective nanohybrids.

4.2.2 XRD, Raman, FTIR, EDX, and XPS studies

Since X-ray powder diffraction (XRD) is deemed to be a fundamental analytical tool for the characterization and phase identification of crystalline powder materials, this technique has been employed for the analysis of the synthesised materials. Figure 4.4 illustrates X-ray diffraction pattern of synthesized nanohybrid electrode materials (i.e., OLC/MnO_2, CNT/MnO_2, GO/MnO_2, and AC/MnO_2) and various carbon materials (i.e., OLC, CNT, GO, and AC). Figure 4.4a show the XRD patterns of the nanohybrid materials with peaks that can be indexed to those of birnessite-type MnO_2 structure (Sys.: monoclinic, lattice: end-centered, space-group: C2/m (12), *a*: 0.515 nm, b: 0.284 nm, *c*: 0.716 nm) in accordance with JCPDS card of birnessite-type MnO_2 (JCPDS 42-1317). The peak at 2θ values of 12.57°, 25.30°, 37.26° and 66.00° correspond to the

(001), (002), (200), and (020) planes of end-centered monoclinic birnessite-type MnO_2, respectively. All these peaks are observed in the nanohybrid materials, suggesting a successful decoration of MnO_2 nanoparticles onto the surface of the carbon materials. The XRD patterns of all the carbon materials are shown in Fig. 4.4b. The peaks at 2θ values of 25.23° and 43.76° correspond to the (002) and (101) planes and can be indexed to those of hexagonal graphitic carbon (JCPDS card 75-1621, Sys.: hexagonal, lattice: primitive, d-spacing: 0.334 nm, space-group: P63mc (186) a: 0.247 nm, c: 0.679 nm, a/b: 1.0000, b/c: 0.3638 and c/a: 2.7490). Upon oxidation of graphite, the (002) peak shifts to 10.54° as seen in pure GO (without MnO_2 particles) in Fig. 4.4b [38]. It is worth mentioning the presence of graphite peaks in the nanohybrid materials. The peak of (001) plane in the GO/MnO_2 nanohybrid material, overlaps with the (002) plane of the oxidized form of graphite (GO) and can be clearly seen in other carbon-based nanohybrid materials (i.e., OLC/MnO_2, CNT/MnO_2, and AC/MnO_2). In the same manner, the peak associated with the (002) plane of the birnessite-type MnO_2 overlaps with the graphitic carbon peak associated with the (002) plane as it can be clearly observed on GO/MnO_2 diffractograms (Fig. 4.4a). All diffraction peaks of the metal oxide in the OLC/MnO_2, CNT/MnO_2, and AC/MnO_2 nanohybrids are broad indicating the nanocrystalline nature of the MnO_2 with an average coherence length (domain size) in the range of 5-10 nm. The calculated carbon d-spacing for the (002) plane is around 0.352 nm and remains at that value with or without the presence of MnO_2 in all the nanohybrid materials. The above calculated d-spacing represents a small increase in lattice spacing as compared to an ideal graphite crystal (i.e., 0.344 nm) [39]. The successful decoration of MnO_2 nanoparticles on the surface of carbon is confirmed by the presence of the carbon in the nanohybrid, which will also be shown by Raman analysis.

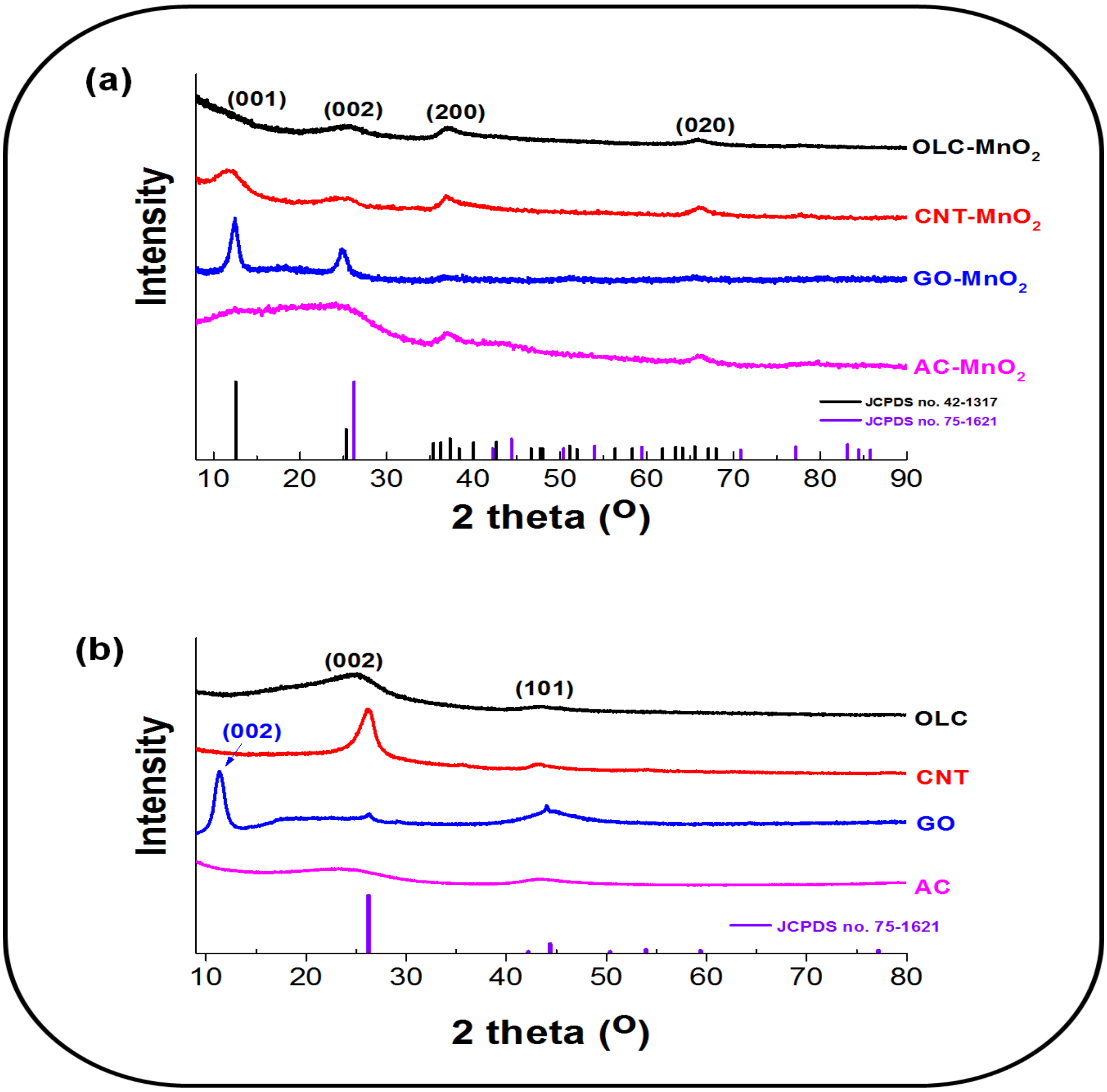

Figure 4.4: X-ray diffraction pattern for (a) OLC/MnO_2, CNT/MnO_2, GO/MnO_2, and AC/MnO_2 nanohybrids, and (b) OLC, CNT, GO, and AC.

Figure 4.5 illustrates Raman spectra of synthesized nanohybrid electrode materials (i.e., OLC/MnO_2, CNT/MnO_2, GO/MnO_2, and AC/MnO_2) and various carbon allotropes (i.e., OLC, CNT, GO, and AC). The presence of MnO_2 is confirmed by a strong Raman signal at around 565 cm^{-1} in all the nanohybrid electrode materials (Fig. 4.5a) [40]. The presence of the carbon in the hybrid electrode materials is confirmed by Raman peaks associated with the carbon D-mode (1350 cm^{-1}) and G-mode (1590 cm^{-1}) (Fig. 4.5a) which are similar to the carbon D-mode and G-mode observed in the pure carbon samples shown in Fig. 4.5b. Peak analysis indicates that the hydrothermal synthesis only insignificantly changes the carbon structure: both D- and G-mode remain almost unchanged in all the nanohybrid materials. In particular, the I_D/I_G ratios before and after MnO_2 deposition are virtually identical with values of 1.20 and 1.25, respectively for OLC/MnO_2 nanohybrid. The FWHM for both the D-mode and the G-mode were measured to 73.1 cm^{-1} and 69.8 cm^{-1} before the deposition and to 78.5 cm^{-1} and 65.4 cm^{-1} after the MnO_2 deposition for the OLC/MnO_2 nanohybrid. The CNT/MnO_2 nanohybrid I_D/I_G ratios before and after MnO_2 deposition have values of 0.95 and 1.00, respectively. The FWHM for both the D-mode and the G-mode were measured to 50.8 cm^{-1} and 43.1 cm^{-1} before the deposition and to 57.2 cm^{-1} and 53.3 cm^{-1} after the MnO_2 deposition for the CNT/MnO_2 nanohybrid. The GO/MnO_2 nanohybrid have values (I_D/I_G ratios) of 0.95 and 0.96, respectively, with the FWHM for both the D-mode and the G-mode measured to be 128.9 cm^{-1} and 83.51 cm^{-1} before the deposition and to 131.2 cm^{-1} and 85.4 cm^{-1} after the MnO_2 deposition for the GO/MnO_2 nanohybrid. The intensity ratio (I_D/I_G) of the AC/MnO_2 nanohybrid before and after MnO_2 deposition exhibited values of 1.06 and 1.08, respectively, while the FWHM for both the D-mode and the G-mode were measured as 123.3 cm^{-1} and 93.8 cm^{-1} before the deposition and as 134.2 cm^{-1} and 102.7 cm^{-1} after the MnO_2 deposition. There is a minor change related to the carbon signal at ~ 1100 to 1200 cm^{-1} which may be due to a small amount of functionalized carbon on the nanohybrids [39]. The Raman modes of the carbon allotropes are observed at similar time in their respective nanohybrids, thus, the results obtained from the XRD are in agreement with the results obtained from the Raman analysis, confirming that the birnessite-type MnO_2 was formed during the hydrothermal treatment (i.e., reflux process) in the presence of the carbon supports.

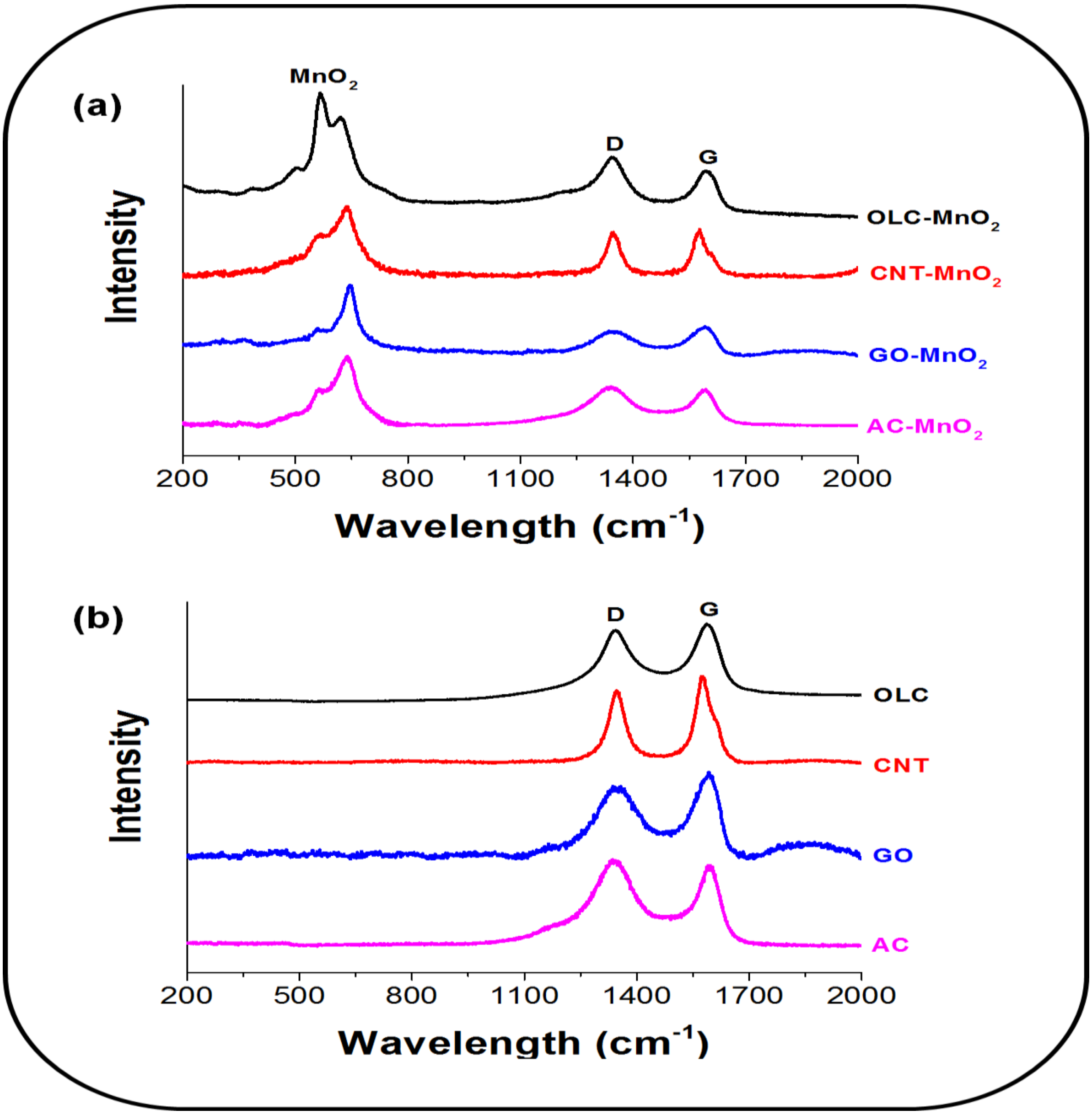

Figure 4.5: Raman spectra for (a) OLC/MnO_2, CNT/MnO_2, GO/MnO_2, and AC/MnO_2 nanohybrids, and (b) OLC, CNT, GO, and AC.

Figure 5.6 shows a deconvoluted Raman spectra using a Lorentzian Fit, for the nanohybrid materials (i.e., OLC/MnO_2, CNT/MnO_2, GO/MnO_2, and AC/MnO_2), Fig. 5.6a, and also for carbon materials (i.e., OLC, CNT, GO, and AC), Fig. 5.6b. It is well known that the D1-mode arise from the defects present in the atomic layers of carbon materials whereas, the D2-mode is related to a lattice vibration corresponding to that of the G mode [41], [42]. The D3-mode originates from the distribution of amorphous carbon on interstitial sites in the disturbed lattice of graphite or carbonaceous material [43], [44]. The D4-mode has been found to be related to lattice vibrations corresponding to sp^2-sp^3 bonds [45], [46]. The Raman curve fitting presented in Fig. 5.6 agree well with Raman data reported for other carbonaceous material (e.g. soot)[45].

The I_D/I_G ratio in all the nanohybrid materials has been observed to remain almost unchanged suggesting that, the synthesised nanohybrid materials experienced a similar amount of defects. However, there exists a level of amorphousness within the nanohybrid materials (shown by the presence of D3-mode), except for the CNT/MnO_2 as witnessed by the absence of D3-mode. The AC/MnO_2 and GO/MnO_2 nanohybrid materials exhibited much higher amorphousness relative to the OLC/MnO_2 and suggested by the intensity increase in the area between the D- and G-mode ranges (1440-1550 cm^{-1}) which overlaps with the D3-mode. Nonetheless, the structural stability of all the nanohybrid materials is maintained since there is no much difference in the deconvoluted Raman spectra of the nanohybrid materials and those of the carbon supports.

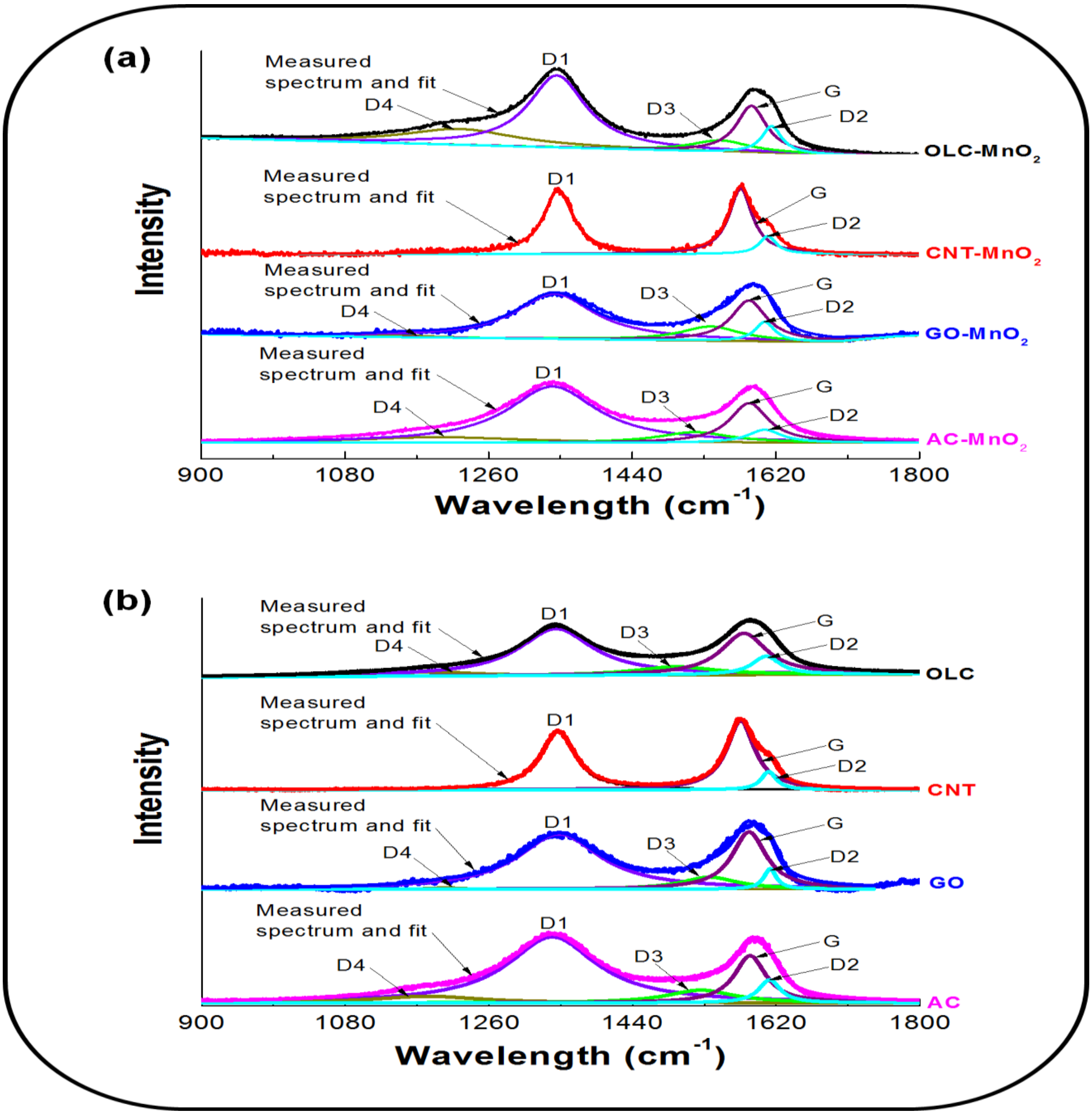

Figure 4.6: A deconvoluted Raman spectra for (a) OLC/MnO_2, CNT/MnO_2, GO/MnO_2, and AC/MnO_2 nanohybrids, and (b) OLC, CNT, GO, and AC.

Figure 4.7 illustrates the FTIR spectra comparing nanohybrid electrode materials (i.e., OLC/MnO_2, CNT/MnO_2, GO/MnO_2, and AC/MnO_2) as shown in Fig. 4.7a and various carbon allotropes (i.e., OLC, CNT, GO, and AC) as shown in Fig. 4.7b. The well pronounce peak at 550 cm^{-1} is due to Mn-O-Mn asymmetric stretching vibration (see Fig. 4.7a) indicating the presence of MnO_2 nanoparticles in all the nanohybrids. The broad peak at 3450 cm^{-1} assigned to hydroxyl groups suggests the presence of water molecules in the interlayers (see also structure given in Fig. 4.1) [47]. The bands at ~ 1070 cm^{-1}, ~ 1200 cm^{-1} and ~ 1720 cm^{-1} in Fig. 4.7b are assigned to the C–O alkoxy stretching, C–O epoxy stretching and C=O carbonyl stretching vibrations, respectively [48]. It is worth noting that the vibration bands mentioned above are due to the functionalization of the graphite materials (i.e., GO and CNT) while the intensity of these vibration bands are minimal in the OLC and AC since they have not been functionalised. The similar broad peak at 3450 cm^{-1} assigned to hydroxyl groups also appears in the pure carbon materials (without MnO_2) in Fig. 4.7b, resulting from the moisture exposure on the carbon precursor such as OLC and AC, while on the carbon precursor such as CNT and GO, in addition to moisture, there exist hydroxyl functional groups from the synthetic procedure. All these results agree with the results obtained from SEM and TEM analysis and thus indicating a successful decoration of MnO_2 to form hybrid electrode materials.

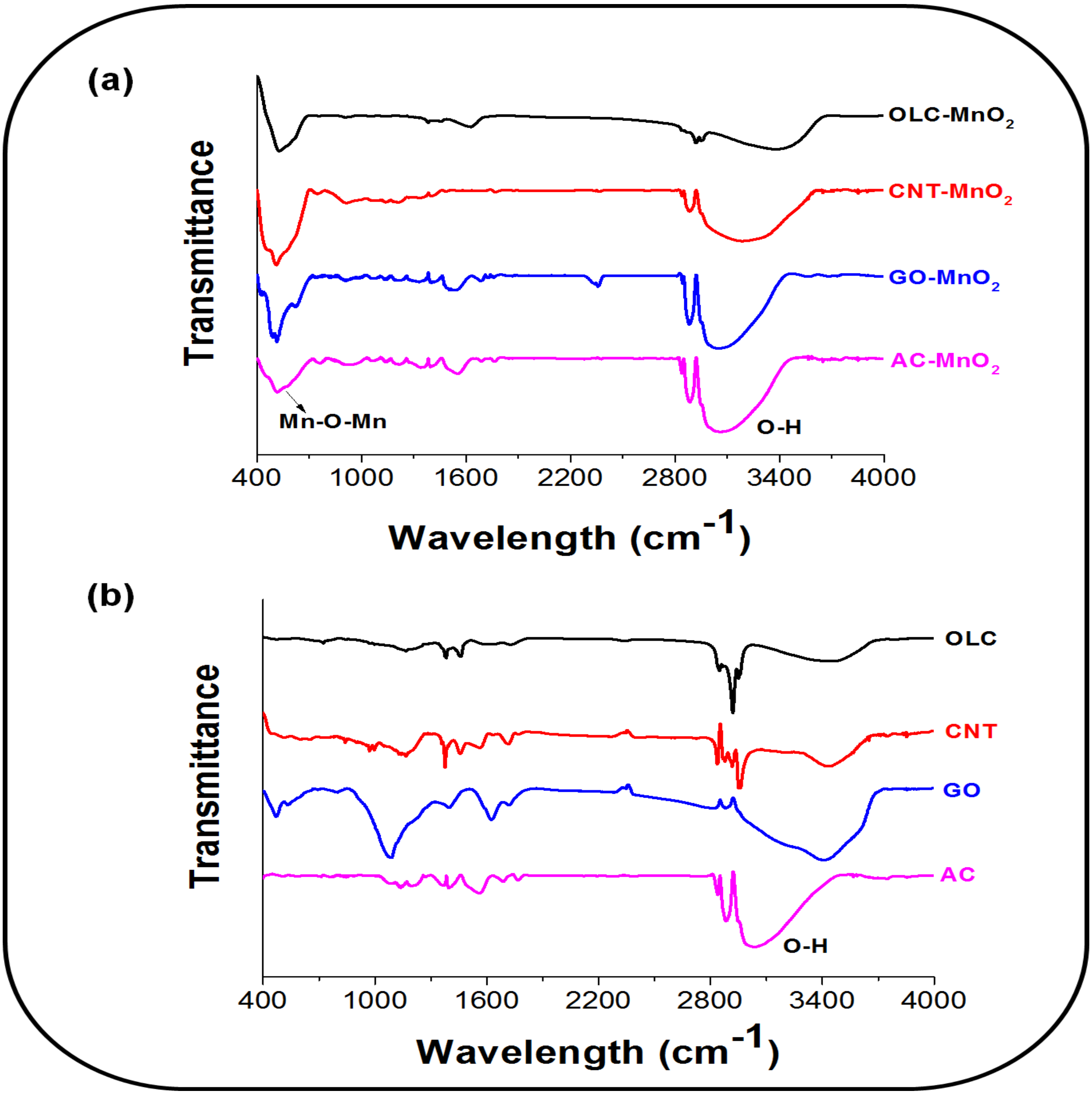

Figure 4.7: FTIR spectra comparison for (a) OLC/MnO_2, CNT/MnO_2, GO/MnO_2 and AC/MnO_2 nanohybrids and (b) OLC, CNT, GO, and AC.

Figure 4.8 illustrates Energy dispersive X-ray (EDX) spectra comparing OLC and OLC/MnO_2 nanohybrid (Fig. 4.8a) and X-ray photoelectron spectrum (XPS) of the OLC/MnO_2 nanohybrid (Fig. 4.8b). Chemical analysis confirms the presence of birnessite, meaning, not of pure MnO_2 but of material following the average formula $K_xMn_2O_4{\cdot}yH_2O$ as depicted in Fig. 4.1.

Semi-quantitative analysis of OLC EDX spectra (Fig. 4.8a and Table 4.1) show less than 0.2 mass% of impurities alongside *ca.* 9 mass% of surface oxygen. The metal oxide shows an average molar Mn: K ratio of 4.6:1 which is somewhat larger than the maximum stoichiometric value of 4:1. The small difference might indicate the presence of minor amounts of residual $KMnO_4$. We note that the previously reported non-carbon content of around 47 mass% is in agreement with our EDX data (54.3 weight %). Only minor impurities of Si and Na can be detected which stem from impurities in the $KMnO_4$. XPS analysis of OLC/MnO_2 (Fig. 4.8b) shows the binding energy peaks of Mn and C. The Mn 2p region consisted of a spin-orbit doublet with Mn $2p_{1/2}$ and Mn $2p_{3/2}$ having binding energies of 654.2 eV and 642.3 eV, respectively.[49] The energy separation between Mn $2p_{1/2}$ and Mn $2p_{3/2}$, of 11.9 eV is an indication of Mn in a +4 oxidation state [50]–[52]. From the XPS survey scan, we also see the presence of significant amounts of K in addition to Mn, C, and O.

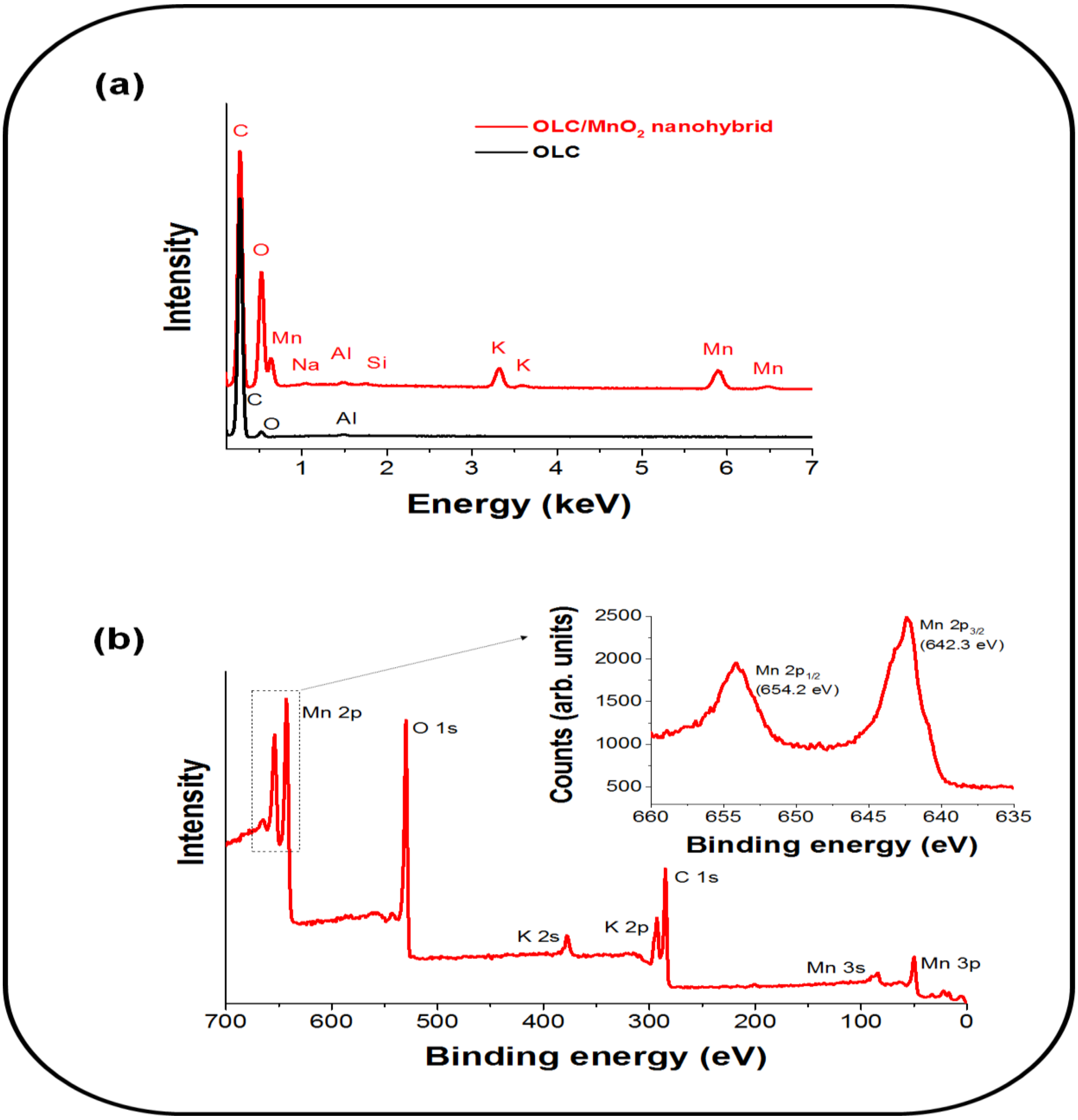

Figure 4.8: (a) Energy dispersive X-ray (EDX) spectra of OLC and OLC/MnO_2 nanohybrid and (b) X-ray photoelectron spectrum (XPS) of the OLC/MnO_2 nanohybrid.

Table 4.1: Chemical composition of OLC and OLC/MnO_2 nanohybrid

(mass%)	C	O	Na	Al	Si	K	Mn
OLC	90.8±1.7	9.1±1.7	-	0.2±0.1	-	-	-
OLC/MnO_2	45.7±1.4	20.3±1.9	0.2±0.1	0.3±0.1	0.2±0.1	4.5±1.2	28.9±2.6

(atom%)	C	O	Na	Al	Si	K	Mn
OLC	93.0±1.3	7.0±1.3	-	0.1±0.1	-	-	-
OLC/MnO_2	66.3±1.5	22.1±1.7	0.1±0.1	0.2±0.1	0.1±0.1	2.0±0.6	9.2±1.0

4.2.3 Cyclic Voltammetric (CV) analysis of various carbon-MnO_2 based electrodes on Ni foam.

The investigation of the OLC/MnO_2, CNT/MnO_2, GO/MnO_2, and AC/MnO_2 nanohybrids as a full cell symmetric supercapacitor was carried out using nickel foam as the current collector considering its lower cost, better pore size distribution and good surface area. Figure 4.11 compares cyclic voltammograms for OLC/MnO_2, CNT/MnO_2, GO/MnO_2, AC/MnO_2 nanohybrids and OLC in aqueous 1 M Na_2SO_4 at the scan rate of 5 mV s^{-1}. All the cyclic voltammograms of the nanohybrid have exhibited a rectangular shape which depicts the contribution of EDL storage mechanism resulting from the presence carbon in the nanohybrids. The slight deviation from a perfect rectangular shape is due to the pseudocapacitive storage mechanism arising from the metal oxide (i.e., MnO_2) in the nanohybrid electrode materials.

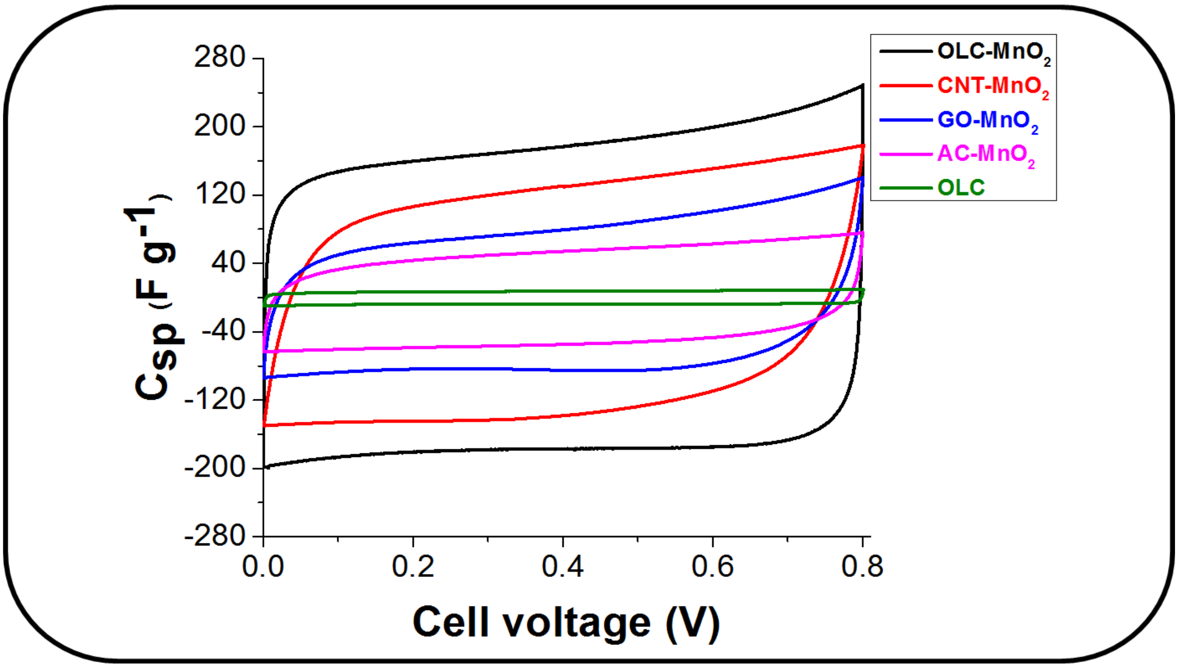

Figure 4.9: Comparative cyclic voltammograms for OLC/MnO_2, CNT/MnO_2, GO/MnO_2, AC/MnO_2 nanohybrids and OLC in aqueous 1 M Na_2SO_4 at 5 mV s^{-1}.

The entire nanohybrid electrode materials exhibited better electrochemical performance as compared to each other. However, the nanohybrid resulting from the decoration of MnO_2 on the surface of the OLC (i.e., OLC/MnO_2 nanohybrid) displayed much higher current response and maximum charge separation followed by the CNT/MnO_2, GO/MnO_2 and AC/MnO_2 nanohybrids respectively. This type of behaviour is a good indication of a good pseudocapacitive behaviour of the electrode materials. From the results observed in Fig. 4.9, it is clear that the introduction of various carbon allotropes (i.e., OLC, CNT, GO, AC) has attributed a good synergistic effect that has enhanced the electrochemical properties of the nanohybrids resulting in an improved pseudocapacitive behaviour of the MnO_2.

Figure 4.10 shows cyclic voltammograms (a) OLC/MnO_2, (b) CNT/MnO_2, (c) GO/MnO_2, and (d) AC/MnO_2 nanohybrids at the scan rates of 5, 10, 25, 50 and 100 mV s^{-1} in the potential range of 0–0.8 V using 1 M Na_2SO_4 aqueous solution as the electrolyte. It is clearly visible that the CV shapes of OLC/MnO_2 nanohybrid are almost ideally rectangular from the scan rates between 5-100 mV s^{-1} (see Fig. 4.10a). However, the CV curves of CNT/MnO_2, GO/MnO_2, and AC/MnO_2 nanohybrids gradually change into an oval shape with the increase of the scan rate, particularly in the scan rate of 50 and 100 mV s^{-1}. The reason for such change in the CV shapes on the other nanohybrids other than OLC/MnO_2 may be due to the internal resistance of the electrode material inhibiting the charge movements within their porous structure and also the low conductivity of the Na_2SO_4 aqueous electrolyte [50]. The same phenomenon was observed in graphene oxide/MnO_2 and CNT/MnO_2 composites studies by Li *et al*. and Zhang *et al.* respectively [50], [53]. Comparing the CV curve of the pure OLC as a representative of other carbon precursors, it is clear that these carbon allotropes have a significant contribution to the electrochemical behaviour of the MnO_2. Thus, OLC has proved to be the best in opening the channels of the MnO_2 by reducing its resistance thus increasing the conductivity which resulted in the OLC/MnO_2 showing better electrochemical performance. Hence, the CV curve of OLC/MnO_2 nanohybrid continued to retain its rectangular shape even at high scan rate (100 mV s^{-1}) indicating an ideal electrochemical capacitive behaviour with rapid diffusion and easy transportation of electrolyte ions to the interface of the electrode.

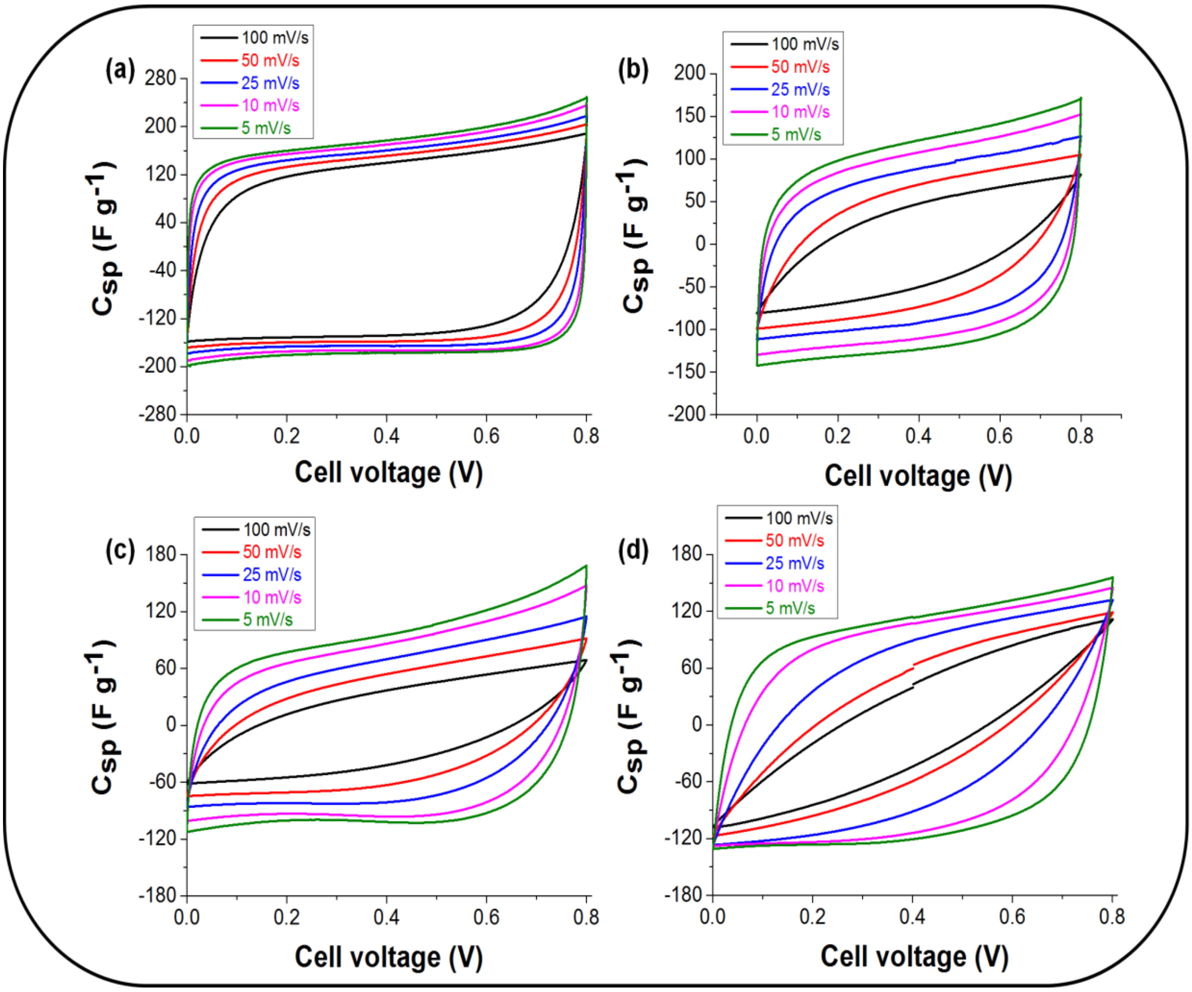

Figure 4.10: Comparison of cyclic voltammograms for (a) OLC/MnO_2, (b) CNT/MnO_2, (c) GO/MnO_2, and (d) AC/MnO_2 nanohybrids at various scan rates. Electrolyte: aqueous 1M Na_2SO_4.

4.2.4 Galvanostatic Charge-Discharge (GCD) analysis of various carbon-MnO_2 based electrodes on Ni foam.

Galvanostatic charge-discharge technique was adopted as it is believed to be a reliable electrochemical method for the evaluation of the electro-capacitive behavior of the electrode materials in energy storage device. Figure 4.11a shows the galvanostatic charge-discharge curves comparing OLC/MnO_2, CNT/MnO_2, GO/MnO_2, AC/MnO_2 nanohybrids and OLC at 0.3 A g^{-1} with a cell voltage varied from 0.0 to 0.8 V in aqueous 1 M Na_2SO_4. The electrodes materials displayed linear charge-discharge curves that resemble an isosceles triangle, suggesting that the electrodes possess an ideal capacitive performance and splendid electrochemical reversibility contributed by both faradaic and non-faradaic charge storage mechanisms. According to the galvanostatic discharge curves, the specific capacitances (C_{sp}), maximum specific energy (E_{sp}) and power (P_{max}) densities can be calculated using equation 2.16 to 2.18 with the internal resistance of the cell calculated using equation 2.19 obtained in chapter 2. For a better analysis of the capacitive behaviour of the as-synthesised nanohybrid materials, studies were made using various current densities (see Fig. 4. 12) and are shown in Fig. 4.11b. The specific capacitance values obtained in Fig. 4.11b were calculated using the equations mentioned above. In agreement with the experimental data from the cyclic voltammetry, galvanostatic charge-discharge data of OLC/MnO_2 nanohybrid showed much better pseudocapacitive performance as compared to the other nanohybrid electrode materials. The OLC/MnO_2 nanohybrid exhibited a higher specific capacitance of ~ 254 F g^{-1} followed by CNT/MnO_2 with a specific capacitance of 220 F g^{-1}, while the GO/MnO_2 was found to be 176 F g^{-1} and AC/MnO_2 exhibited the least value of 148 F g^{-1} at a current density of 0.1 A g^{-1} in aqueous 1 M Na_2SO_4 electrolyte. As expected, the specific capacitance of pure OLC (without the presence of MnO_2 nanoparticles) was found to be 14 F g^{-1} which was remarkably smaller than that of its nanohybrid (OLC/MnO_2) and the other carbon-MnO_2 nanohybrids. It is worth mentioning that although the high specific capacitance originates from the contribution of MnO_2, the conductivity of the nanohybrids also plays a major role in its capacitance. Although all carbon nanohybrids have MnO_2 content, the corresponding specific capacitance is decreasing from the OLC, CNT, GO and AC based on their conductivity.

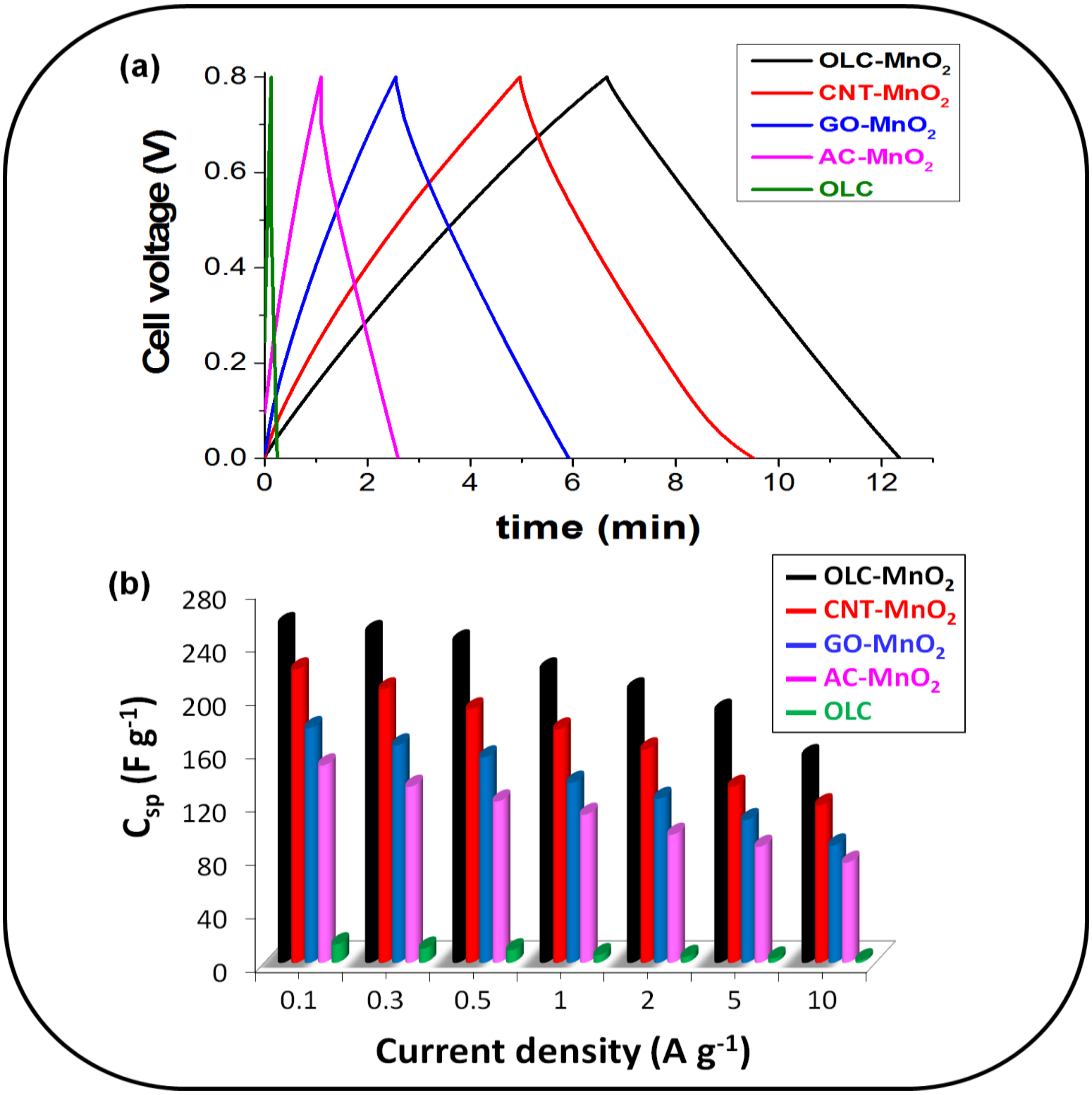

Figure 4.11: Comparative (a) galvanostatic charge-discharge curves at 0.3 A g^{-1} and (b) C_{sp} *vs.* current density plot, for OLC/MnO_2, CNT/MnO_2, GO/MnO_2, AC/MnO_2 nanohybrids and OLC in aqueous 1 M Na_2SO_4.

The C_{sp} of nanohybrids (as observed from Fig. 4.11b and Fig. 4.12) decreased with increase in current density with OLC/MnO_2 nanohybrid (Fig. 4.12a) ranging from 248 F g^{-1} (at 0.3 A g^{-1}) to 155 F g^{-1} (at 10 A g^{-1}), CNT/MnO_2 nanohybrid (Fig. 4.12b) ranging from 205 F g^{-1} (at 0.3 A g^{-1}) to 118 F g^{-1} (at 10 A g^{-1}), GO/MnO_2 nanohybrid (Fig. 4.12c) ranging from 176 F g^{-1} (at 0.3 A g^{-1}) to 88 F g^{-1} (at 10 A g^{-1}) and AC/MnO_2 nanohybrid (Fig. 4.12d) ranging from 148 F g^{-1} (at 0.3 A g^{-1}) to 75 F g^{-1} (at 10 A g^{-1}) whereas the pure OLC ranged from 11 F g^{-1} (at 0.3 A g^{-1}) to 2.0 F g^{-1} (at 10 A g^{-1}) as shown in Fig. 4.11b. It is worth mentioning that OLC/MnO_2 nanohybrid exhibit low internal resistance at high current densities when compared to the other electrode materials. The GCD curve of the GO/MnO_2 shows in addition to the IR-drop, more internal resistance as the cell voltage is towards 0.8 V, indicated the resistivity of charges mobility at the electrode-electrolyte interface. The pseudocapacitive performances of these nanohybrid electrode materials with much higher specific capacitance as compared to the ones reported in the literature suggests that these electrode materials are suitable for high power energy storage applications.

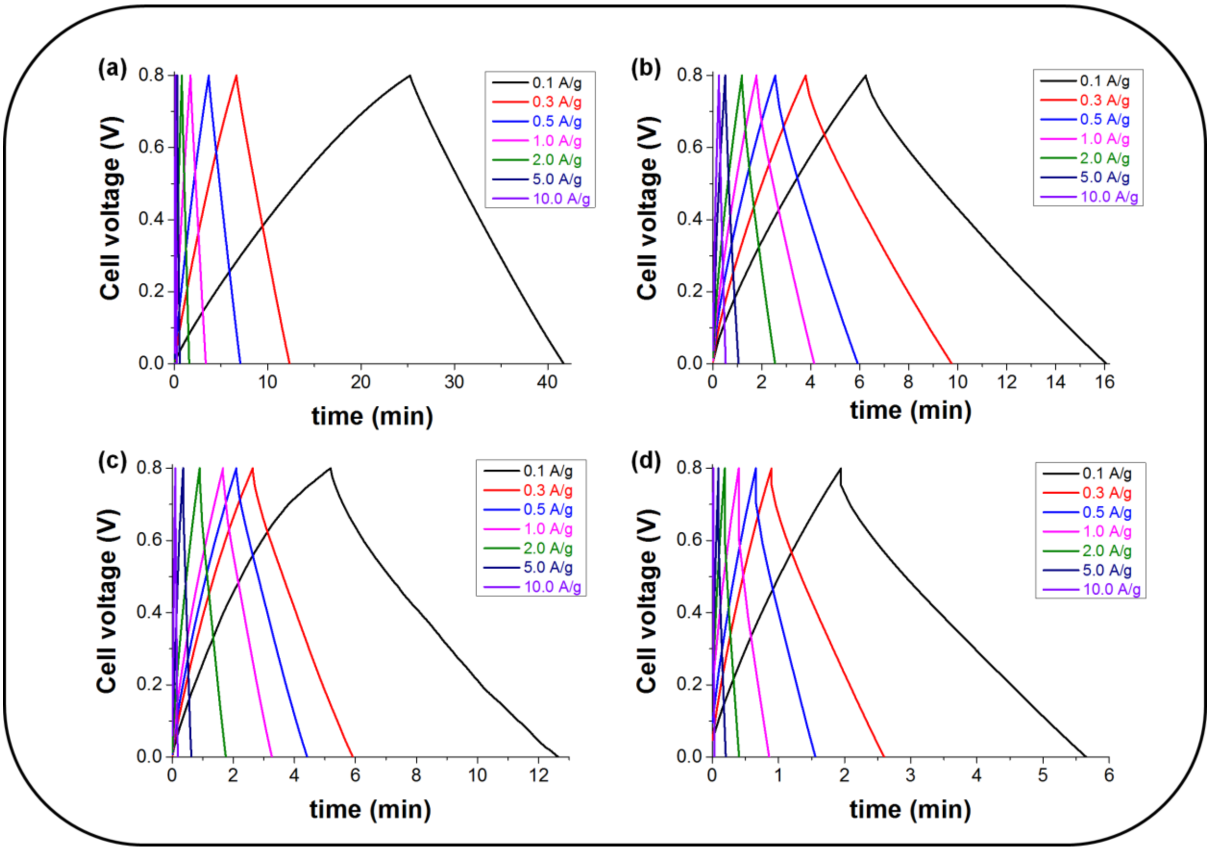

Figure 4.12: Comparison of galvanostatic charge-discharge curves for (a) OLC/MnO_2, (b) CNT/MnO_2, (c) GO/MnO_2, and (d) AC/MnO_2 nanohybrids at various current densities. Electrolyte: aqueous 1M Na_2SO_4.

Figure 4.13 shows a Ragone plot comparing energy and power densities for OLC/MnO_2, CNT/MnO_2, GO/MnO_2, and AC/MnO_2 nanohybrids. As showed from the other electrochemical analysis such as CV and GCD, OLC/MnO_2 nanohybrid continued leading with regard to the pseudocapacitive performance as compared to other carbon/MnO_2-based electrode materials. The maximum energy and power densities of OLC/MnO_2 nanohybrid is apparently higher with values of ~5.6 Wh kg^{-1} and ~74.8 kW.kg^{-1}, respectively. The maximum energy and power density values of CNT/MnO_2 nanohybrid were found to be ~4.9 Wh kg^{-1} and ~55.1 kW.kg^{-1}, respectively. The GO/MnO_2 nanohybrid showed maximum energy and power density values of ~3.9 Wh kg^{-1} and ~35.8 kW.kg^{-1}, respectively, whereas AC/MnO_2 nanohybrid showed maximum energy and power density values of ~3.3 Wh kg^{-1} and ~30.1 $kW.kg^{-1}$, respectively. It is worth mentioning that these remarkable rate capabilities of the nanohybrid electrode materials are much higher than those reported in the literature as shown in Table 4.2.

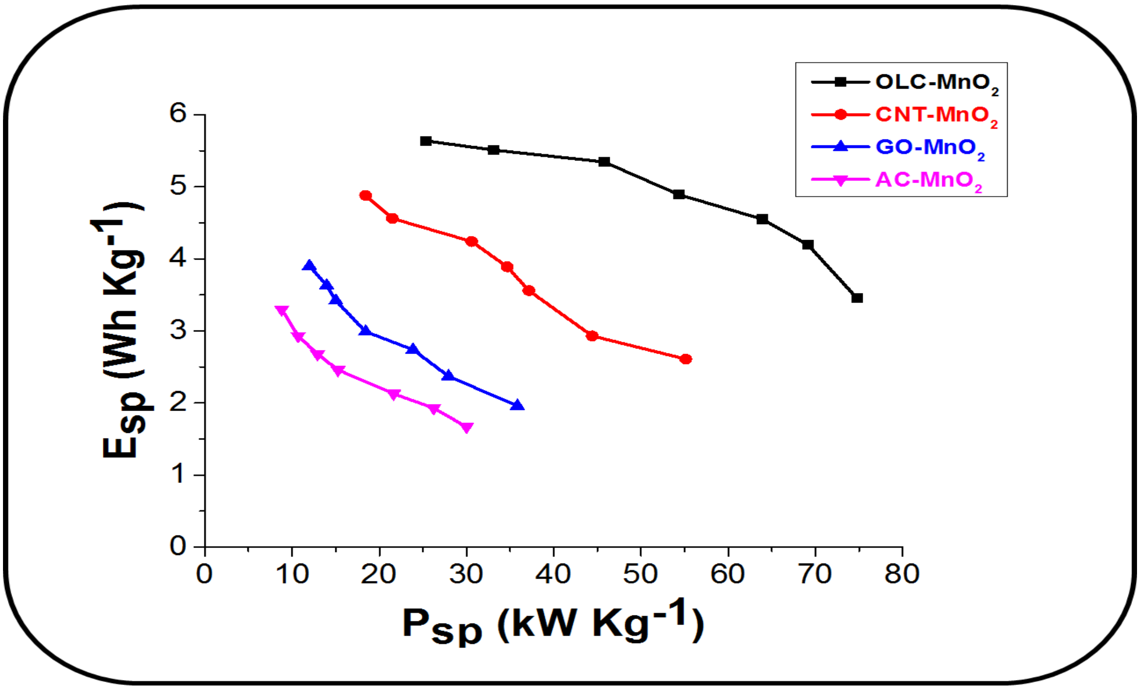

Figure 4.13: Ragone plot is indicating Energy vs. Power densities for OLC/MnO_2, CNT/MnO_2, GO/MnO_2, and AC/MnO_2 nanohybrids. Electrolyte: aqueous 1M Na_2SO_4.

Table 4.2 summarizes the values of the capacitance parameters obtained in comparison with literature, and it is evident that OLC/MnO_2, CNT/MnO_2, GO/MnO_2, and AC/MnO_2 nanohybrids exhibit higher performances (regarding power density or rate capability) than many state-of-the-art MnO_2-based pseudocapacitors. Note that there is no known report on symmetric supercapacitor based on birnessite-type MnO_2 in the literature so far; yet, the latter is of utmost importance to transition to actual devices and not just laboratory-relevant data.

Figure 9-11 summarized the key findings as follows:

(i) The electrochemical performance (i.e., specific capacitance, charge separation, stability, cyclability, energy and power densities) of the MnO_2

was extensively improved by the addition of various carbon allotropes (i.e., OLC, CNT, GO, and AC).

(ii) The OLC/MnO_2 nanohybrid displayed much better electrochemical performance compared to the rest of the nanohybrids, followed by CNT/MnO_2.

(iii) Thus, the nanohybrids of GO/MnO_2 and AC/MnO_2 show the least electrochemical performance, and the latter exhibited poorer electrochemical performance as compared to other nanohybrid electrode materials.

(iv) All the nanohybrid electrode materials displayed much better electrochemical performance compared to those of their respective carbon allotropes (Note: OLC was used as a representative of the contributing effect of the carbon allotropes as shown in Fig. 4.9 and Fig. 4.11).

(v) The introduction of various carbon materials has significantly improved both the stability and cyclability of MnO_2 nanoparticles.

Table 4.2: Comparison of electrochemical performance of some MnO_2-based aqueous symmetric electrochemical capacitors.

Aqueous Electrolyte	Electrode Material	Cell Voltage (V)	Specific Capacitance (F g^{-1})	Current Density/ Scan Rate	Energy (Wh kg^{-1})	Power/ (kW kg^{-1})	Ref.
Na_2SO_4	OLC	0.8	12	0.1 A g^{-1}	0.3	2.9	This work
Na_2SO_4	OLC/MnO_2	0.8	254	0.1 A g^{-1}	5.6	74.8	This work
Na_2SO_4	CNT/MnO_2	0.8	220	0.1 A g^{-1}	4.9	55.0	This work
Na_2SO_4	GO/MnO_2	0.8	176	0.1 A g^{-1}	3.8	35.6	This work
Na_2SO_4	AC/MnO_2	0.8	148	0.1 A g^{-1}	3.1	29.7	This work
Na_2SO_4	Ni-MnO_2	1.0	685	2 mA cm^{-2}	-	-	[54]
Na_2SO_4	Co-MnO_2	1.0	560	2 mA cm^{-2}	-	-	[54]
Na_2SO_4	a-MnO_2/CNT	-	140	2 mV/s	-	-	[55]
Na_2SO_4	CNT/PPy/MnO_2	-	149	1 mA cm^{-2}	-	-	[56]
Na_2SO_4	MnO_2	1.0	198	0.28 A g^{-1}	-	-	[57]
KOH	MnO_2	1.0	401	0.28 A g^{-1}	-	-	[57]
Na_2SO_4	MnO_2/CNT-textile	1.0	410	50 mV/s	20.0	13.0	[58]
H_2SO_4	aMEGO/MnO_2	1.0	256	0.25 A g^{-1}	-	-	[59]
KOH	GN-(γ-MnO_2/CNT)	1.0	310	20 mV/s	43.0	26.0	[60]
Na_2SO_4	MnO_2/AC	1.2	49	0.1 A g^{-1}	9.7	3.0	[11]
Na_2SO_4	GF/ MnO_2	1.0	240	0.1 A g^{-1}	8.3	20.0	[61]
Na_2SO_4	C/MnO_2 DNTAs	0.8	161	5 mV/s	35.0	16.0	[62]
H_2SO_4	CNOs/MnO_2	1.0	575	0.5 A g^{-1}	19.95*	2.25*	[17]
KOH	α-MnO_2	1.0	775	2 mV/s	76.0	6.5	[63]
Na_2SO_4	MnO_2/PDDA/CNO	0.9	219	-	6.1	-	[64]
Na_2SO_4	α-MnO_2/a-MCMB	1.0	357	0.14 A g^{-1}	-	-	[65]

Key: GN = graphene nanosheet; GF = graphene foam; CNT = carbon nanotube; DNTA = double-walled nanotube array; CNOs = carbon nano-onions; PDDA: polydiallyldimethylammonium, aMEGO = activated microwave expanded graphite oxide, a-MCMB= activated mesocarbon microbeads. NB: *= values are based on the published corrections from the authors

4.2.5 Electrochemical Impedance Spectroscopy (EIS) analysis of various carbon-MnO_2 based electrodes on Ni foam.

EIS data were acquired prior and post-floating experiments to understand the fundamental pseudocapacitive processes taking place at the electrode/electrolyte interface of the nanohybrid electrode materials as shown in Fig. 4.14 measured in the frequency range of 100 kHz to 10 mHz in aqueous 1 M Na_2SO_4. Figure 4.14a shows a Nyquist plot comparison for the nanohybrid electrode materials (i.e., OLC/MnO_2, CNT/MnO_2, GO/MnO_2 and AC/MnO_2) and the inset represents the expanded portion of the high-frequency region of the compared Nyquist plots. The equivalent distributed resistance (EDR), comprising of both the equivalent series resistance (ESR) and the ionic resistance within the porous structure (i.e., RC semicircle), was obtained by extrapolating the vertical portion of the plot to the real axis. The OLC/MnO_2 device shows a lower EDR value (3.1 Ω cm^2) compared to that of CNT/MnO_2 (with the EDR value of 4.8 Ω cm^2), GO/MnO_2 (with the EDR value of 7.6 Ω cm^2) and AC/MnO_2 device (with the EDR value of 9.1 Ω cm^2). However, these values are larger than that of OLC alone (1.6 Ω cm^2). The RC semicircle of the OLC/MnO_2 is slightly smaller (~ 1.8 Ω cm^2) compared to that of the CNT/MnO_2 (~ 1.9 Ω cm^2), GO/MnO_2 (~ 4.8 Ω cm^2) and AC/MnO_2 (~ 4.4 Ω cm^2). Nevertheless, these values are smaller than those calculated for OLC alone (~ 0.9 Ω cm^2), meaning that the ionic resistance of the porous structure of the pure EDLC (OLC alone) increased for the nanohybrid pseudocapacitor. Figure 4.14b shows a Bode plot comparison for the nanohybrid electrode materials (i.e., OLC/MnO_2, CNT/MnO_2, GO/MnO_2 and AC/MnO_2) and pure OLC (without MnO_2). From the Bode plots, the phase angle of the pure OLC is -85^0 (which is close to the -90^0 for an ideal EDLC) compared to that of the OLC/MnO_2 nanohybrid which is -80^0, CNT/MnO_2 nanohybrid which is -79^0, GO/MnO_2 nanohybrid which is -74^0 and AC/MnO_2

nanohybrid which is -75^0 further indicating the pseudocapacitive behavior of the nanohybrid devices. The knee frequency (f_o, ϕ = -45°) describes the maximum frequency at which the capacitive behavior is dominant, and is a measure of the power capability of ECs. The higher the f_o, the faster the supercapacitor can be charged and discharged. The values of the f_o were *ca.* 25 Hz for the OLC/MnO_2 (time constant ~ 40 ms) and *ca.* 22 Hz (time constant ~ 45 ms) for the CNT/MnO_2. The GO/MnO_2 displayed f_o value of *ca.* 17 Hz (time constant ~ 59 ms) and AC/MnO_2 *ca.* 15 Hz (time constant ~ 67 s). These values further corroborate the higher-power performance of the nanohybrid electrode materials. Also, these results show that most of the stored energy in the nanohybrid electrode materials is accessible with power output available on millisecond time scale. It is worth noting that most commercially available supercapacitors, including those designed for higher power applications, operate at frequencies less than 1 Hz [66].

To better understand the pseudocapacitive behaviour of these devices, the EIS data (shown in Fig. 4.14a) were fitted with the electrical equivalent circuit (EEC) which comprise Voigt RC elements (Fig. 4.14c), involving a series resistance (R_s), charge-transfer resistance (R_{ct}) and constant phase elements (CPE or Q). From Table 4.3, the R_s of the OLC (0.25 Ohm) are lower than that of the OLC/MnO_2 (0.38 Ohm), CNT/MnO_2 (0.95 Ohm), GO/MnO_2 (0.97 Ohm) and AC/MnO_2 (1.53 Ohm). Also, the R_{ct} value of the OLC (0.38 Ohm) is lower than that of the OLC/MnO_2 (0.94 Ohm), CNT/MnO_2 (1.64 Ohm), GO/MnO_2 (2.46 Ohm) and AC/MnO_2 (3.27 Ohm) (Table 4.3). These results further suggest that the OLC component serves to reduce the internal resistance of the OLC/MnO_2, thereby improving the conductivity and capacitance of the OLC/MnO_2-based symmetric pseudocapacitor as compared to other carbon supports (i.e., CNT, GO and AC) on their subsequence nanohybrid electrode materials. The equation gives the impedance of CPE (4.1) [67]:

$$Z_{CPE} = \frac{1}{[Q(jw)^n]} \tag{4.1}$$

where Q represents the frequency-independent constant relating to the electroactive surface properties, w is the radial frequency; the exponent n arises from the slope of log Z vs. log f (and has values $-1 \leq n \leq 1$). If n = 0, the CPE behaves like a pure resistor; $n = 1$, CPE acts as a pure capacitor, $n = -1$, CPE behaves as an inductor; while $n = 0.5$ corresponds to Warburg impedance (Z_w) which is related to the diffusion of the ions. The n values observed for these electrodes are > 0.7, explicitly confirming porous nanohybrid electrode materials with pseudocapacitive behaviour, corroborating the CV and GCD data of Fig. 4.9 and Fig. 4.11, respectively.

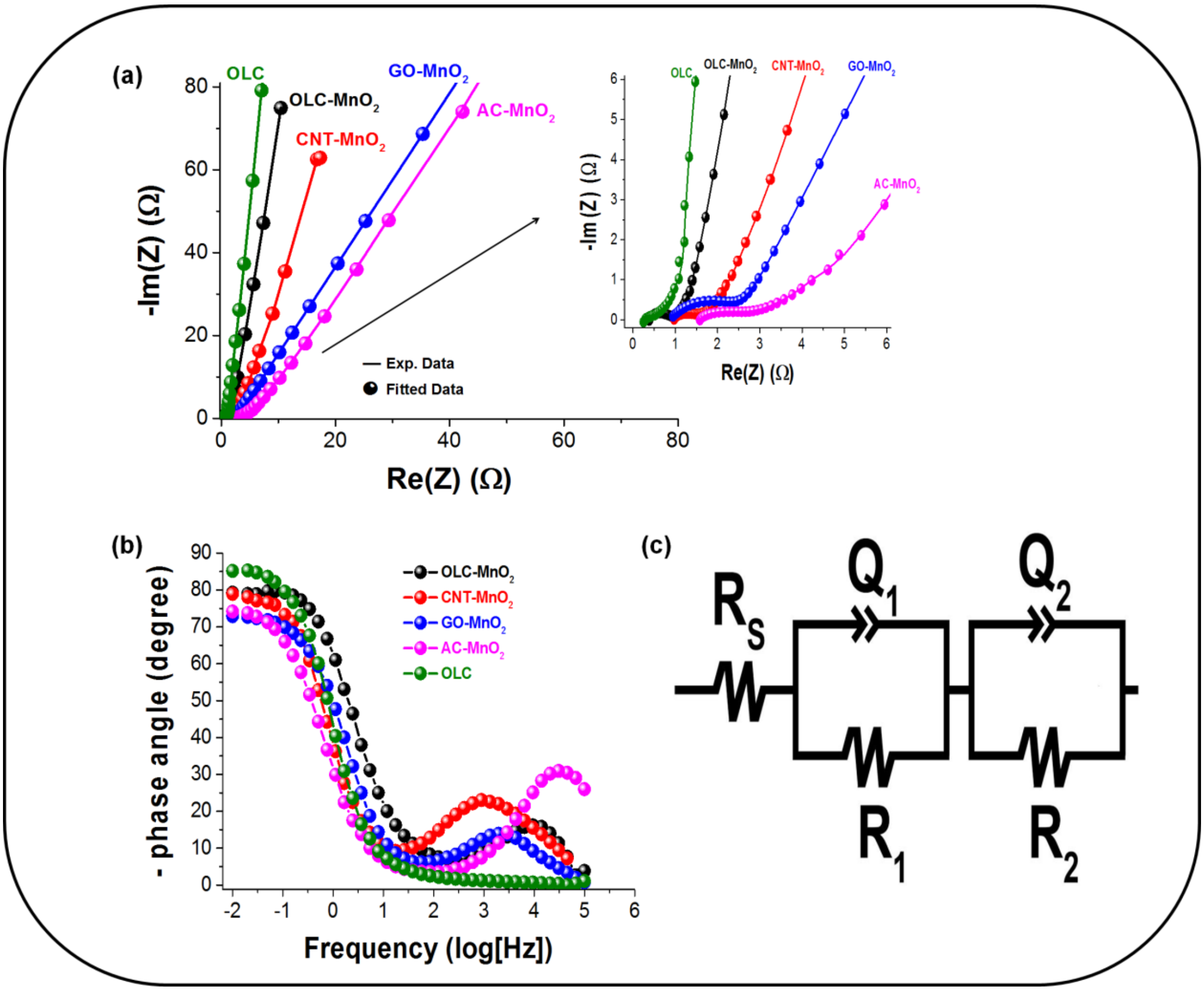

Figure 4.14: Comparative (a) Nyquist, (b) Bode plots for OLC/MnO_2, CNT/MnO_2, GO/MnO_2, and AC/MnO_2 nanohybrids in aqueous 1 M Na_2SO_4 and (c) The Electrical

Equivalent Circuit (EEC) used to fit the experimental EIS data. The inset in (a) is the expanded portion of the high-frequency region.

Table 4.3: Comparative fitting parameters for the EIS data for the CNT/MnO_2, CNT/MnO_2, GO/MnO_2 and AC/MnO_2 nanohybrid using the Voigt equivalent circuit.

Parameter	**OLC/MnO_2**	**CNT/MnO_2**	**GO/MnO_2**	**AC/MnO_2**
R_s / Ω	0.38± 0.20	0.95± 0.31	0.97± 0.23	1.53± 0.12
Q_1 / mF.s$^{(\alpha-1)}$	2.28± 1.06	2.11± 0.96	2.51± 0.10	4.33± 0.52
n_1	0.79± 0.17	0.73± 0.17	0.71± 0.11	0.72± 1.02
R_{ct1} / Ω	0.94± 0.13	1.64± 0.13	2.46± 0.95	3.27± 1.22
Q_2 / mF.s$^{(\alpha-1)}$	3.14± 0.41	3.58± 0.68	3.43± 0.25	1.63± 0.11
n_2	0.86± 0.25	0.81± 0.25	0.59± 0.22	0.66± 1.80
R_{ct2} / Ω	1.65± 1.54	4.71± 1.54	7.76± 1.80	17.09± 1.67

Voltage-holding (or floating) experiments represent a reliable analysis method for establishing the long-term stability of ECs electrodes [68], [69]. In this work, the stability for OLC/MnO_2, CNT/MnO_2, GO/MnO_2, and AC/MnO_2 nanohybrid was interrogated using voltage-holding, and EIS data was required to understand the behavior of the electrodes prior and post voltage-holding experiments as shown in Fig. 4.15. In this work, the OLC/MnO_2 nanohybrid exhibited excellent stability during voltage-holding over 50 h at 1 A g^{-1} as represented by a small internal resistance after voltage-holding (Fig. 4.15a). Subsequently, CNT/MnO_2, GO/MnO_2, and AC/MnO_2 nanohybrid exhibited a decrease in stability as compared to the OLC/MnO_2 nanohybrid as depicted by an increase in internal resistance after voltage-holding experiments and shown in Fig. 4.15b-d, respectively. The OLC/MnO_2 performance as explained above, has been illustrated by the gradual decrease in the specific capacitance as the current is kept constant at a high potential, retaining 200 F g^{-1} (i.e., approximately 90% of its initial capacitance of 220 F g^{-1}). The excellent stability of the OLC/MnO_2 nanohybrid showed that this device can be charged and discharged without significant deterioration in its efficiency (Fig. 4.15a). The stability of the CNT/MnO_2 nanohybrid as shown in Fig. 4.15b exhibited a steady decrease, resembling that of OLC/MnO_2 while showing a much decrease in C_{sp} as compared to the OLC/MnO_2 after 50 h voltage-holding, retaining 120 F g^{-1} (i.e., approximately 70% of its initial capacitance of 174 F g^{-1}). These devices can be charged and discharged without significant deterioration in their efficiency. The above values correspond with a maximum specific energy of 5.6 Wh kg^{-1} and an excellent power density of 74.8 kW kg^{-1} for OLC/MnO_2 and maximum specific energy of 4.9 Wh kg^{-1} and a good power density of 55.1 kW kg^{-1} for CNT/MnO_2 nanohybrid. Both the GO/MnO_2 (Fig. 4.15c) and AC/MnO_2 (Fig. 4.15d) depicted exponential decrease in C_{sp} as compared to the OLC/MnO_2 and CNT/MnO_2. A drop in C_{sp} for AC/MnO_2 after 50 h voltage-holding cost the nanohybrid approximately 44% of its initial capacitance and thus retaining 73 F g^{-1} (i.e., approximately 66% of its original capacitance of 110 F g^{-1}). The above calculated pseudocapacitive performances of all the nanohybrids are compared as shown in Fig. 4.16. It is worth noting that although the nanohybrids performed invariably as compared to each other, their pseudocapacitive performances are still much better than some values obtained in the literature. The improved performance of this hybrid symmetric pseudocapacitor is attributed to the combination of the high electrical conductivity of various carbon supports with the highly reversible redox reactions (pseudocapacitance) arising from the nanostructured MnO_2 material. This chapter has shown that the use of different carbon supports has a significant contribution to the pseudocapacitive performance of the MnO_2, improving its stability through the synergistic effect resulting from the conductive porous carbon support. The OLC proves to be the best carbon support (compared to CNT, GO, and AC) yielding much better electrochemical performance from the birnessite-type MnO_2.

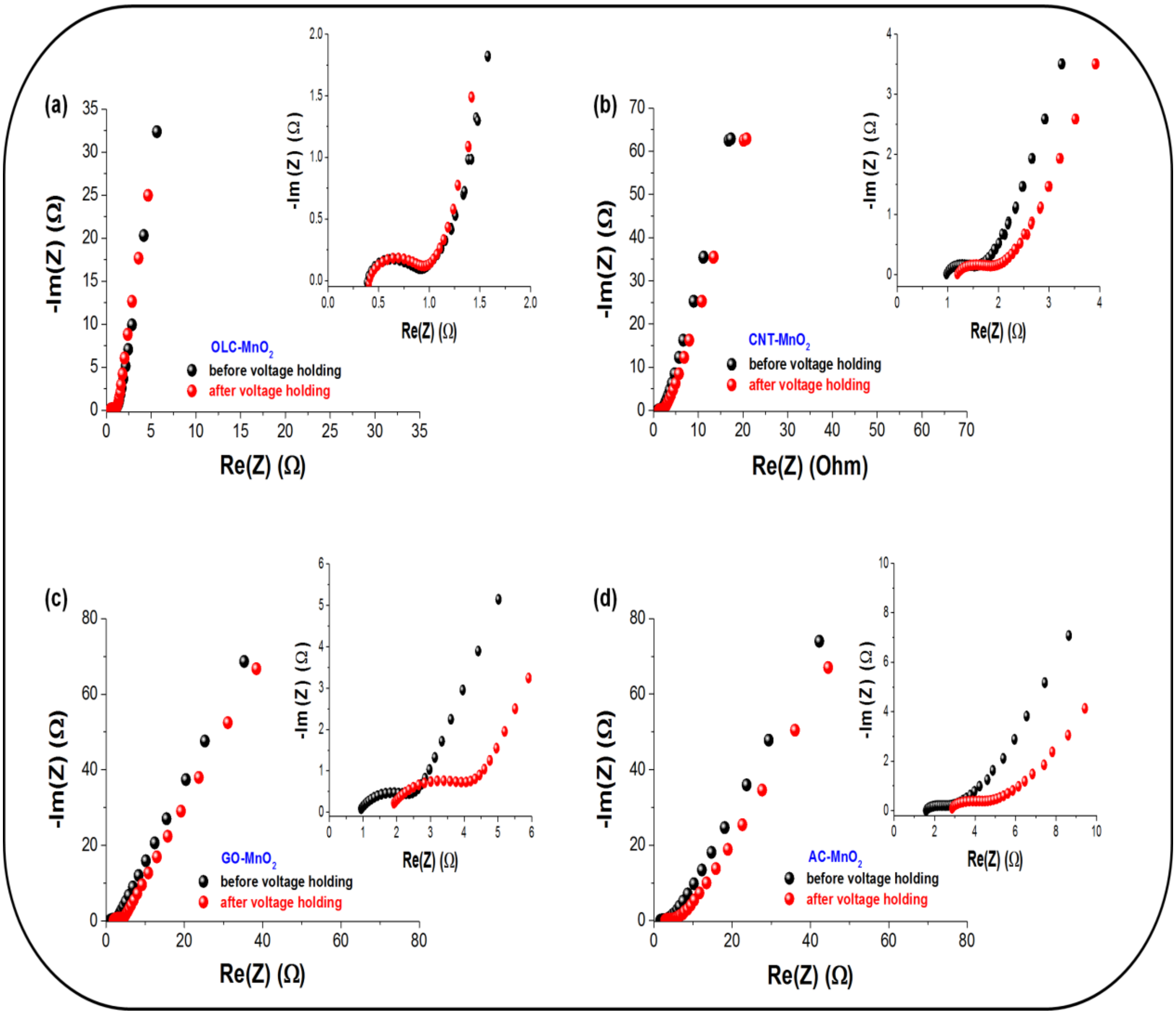

Figure 4.15: Nyquist plots for (a) OLC/MnO_2, (b) CNT/MnO_2, (c) GO/MnO_2, and (d) AC/MnO_2 nanohybrids before and after voltage holding in aqueous 1 M Na_2SO_4. The inset in (a-d) is the expanded portion of the high-frequency region.

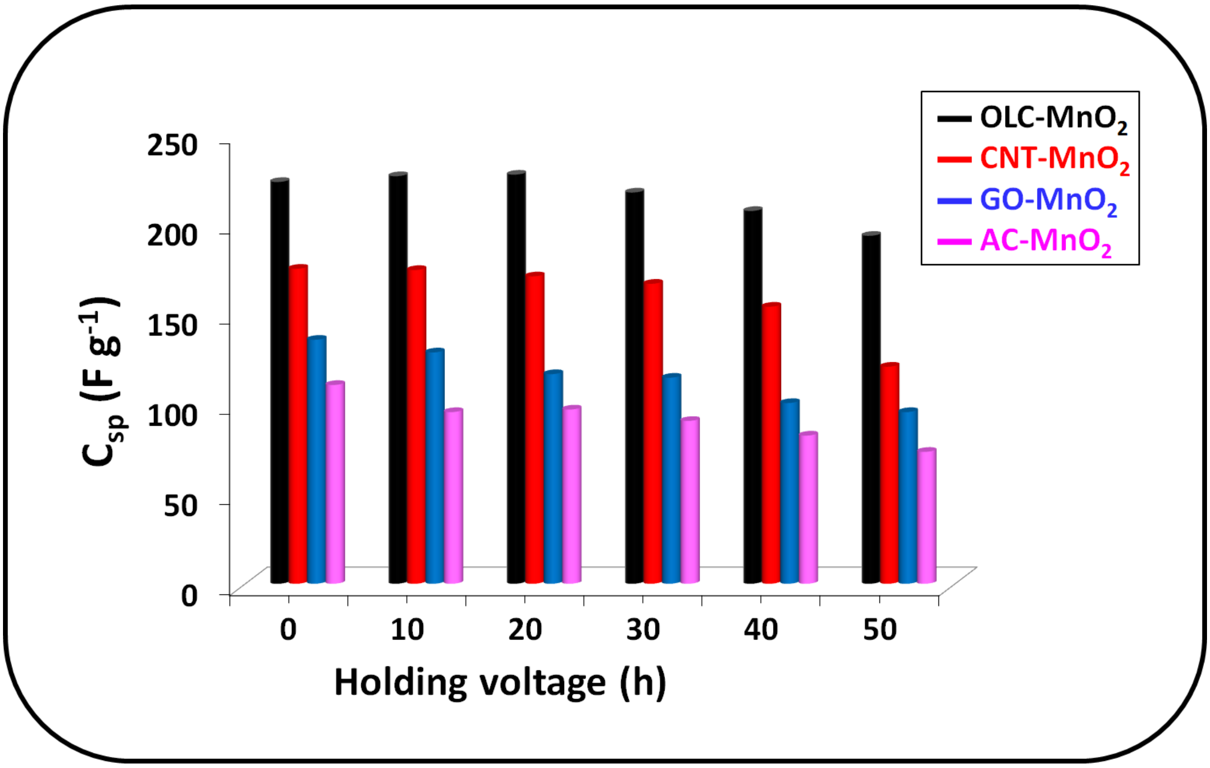

Figure 4.16: A 50 h voltage-holding experimental comparison for OLC/MnO_2, CNT/MnO_2, GO/MnO_2, and AC/MnO_2 nanohybrids at 0.8 V cell voltage. Electrolyte: aqueous 1 M Na_2SO_4.

The results obtained from the deconvoluted Raman spectra, and XRD spectra confirm the trend of electrochemical performance from CV, GCD, and EIS data. The OLC/MnO_2 (due to the small particle size of both the OLC and MnO_2 together with the crystallinity of the nanohybrid) exhibited the best specific capacitance and followed by the CNT/MnO_2 nanohybrids (due to its crystallinity and good interaction of CNT with MnO_2). Subsequently, GO/MnO_2 and AC/MnO_2 nanohybrid materials exhibited much smaller specific capacitance than the nanohybrid materials mentioned above.

4.2.6 TGA and Gas sorption analysis

The OLC/MnO_2 nanohybrid showed better pseudocapacitive performance than other nanohybrids. Therefore, further analyses were done on the nanohybrid to understand the % composition of the MnO_2 decorated on the OLC and its porosity. Similar, the synthetic process was employed for the decoration of the MnO_2 on various carbon allotropes. Therefore, the TGA analysis of OLC/MnO_2 was used to estimate the amount of MnO_2 in the synthesized nanohybrid. The MnO_2 nanoparticles represented 46 mass% of the OLC/MnO_2 nanohybrid material (see Fig. 4.17). Also, the TGA data shows the excellent thermal stability of OLC with an onset of oxidation at around 630 °C as a result of the highly graphitic character of carbon onions synthesized at 1750 °C.

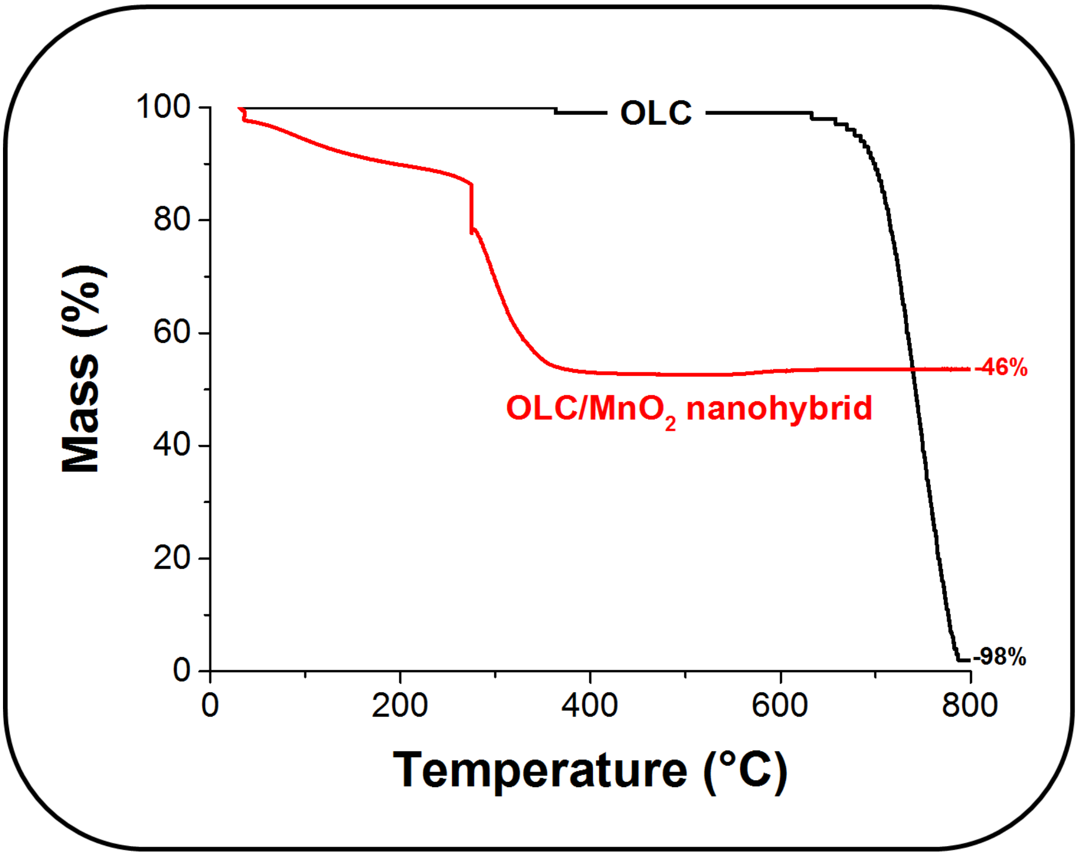

Figure 4.17: TGA of OLC and OLC/MnO_2 nanohybrid.

Figure 4.18 shows nitrogen gas sorption data for synthesized OLC/MnO_2. As noted, OLC/MnO_2 exhibits a DFT SSA of 122 $m^2\,g^{-1}$ with a distribution of micropores (<2 nm) and mesopores (between 2 and 50 nm). This measurement represents a severe loss in the specific surface area compared to OLC with a DFT SSA of 391 $m^2\,g^{-1}$ and is mostly related to the higher molecular mass and higher density of MnO_2 in addition to pore blocking.[70]. Figure 4.18b shows that the overall pore size distribution is preserved after the addition of MnO_2 at a lower total pore volume in OLC/MnO_2 nanohybrid.

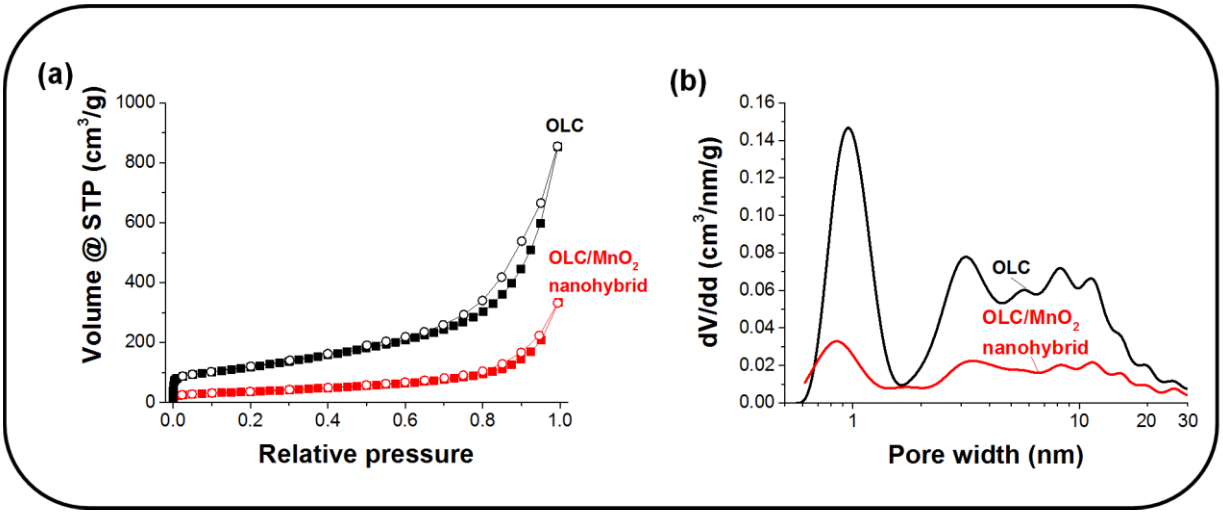

Figure 4.18: (a) Nitrogen adsorption-desorption isotherms at -196 °C and (b) Pore size distribution, overlays of OLC and OLC/MnO_2 nanohybrid.

4.3 Conclusion

This work investigated the electrochemical performance of highly graphitized onion-like carbon (OLC), carbon nanotube (CNT), graphene oxide (GO) and activated carbon (AC) integrated with nanostructured birnessite-type MnO_2 materials (i.e., OLC/MnO_2, CNT/MnO_2, GO/MnO_2 and AC/MnO_2) as electrode materials for symmetric pseudocapacitor devices. From the full-cell experiment, the OLC/MnO_2 nanohybrid exhibited better performance when using Ni foam as the current collector (regarding specific capacitance and rate capability) compared to other nanohybrid electrode materials. The OLC/MnO_2 device gave excellent electrochemical performance with a specific capacity of 255 F g^{-1}, specific energy density of 5.6 Wh kg^{-1}, power density of 74.8 kW kg^{-1}, capacity retention upon long-hour voltage-holding, very low equivalent distributed resistance. As much as the OLC/MnO_2 exhibited much better performance, all the nanohybrids (CNT/MnO_2 with maximum specific capacitance, energy and power density of 174 F g^{-1}, 4.9 Wh kg^{-1} and 55.1 kW kg^{-1}, respectively, GO/MnO_2 with maximum specific capacitance, energy and power density of 135 F g^{-1}, 3.9 Wh kg^{-1} and 35.8 kW kg^{-1}, respectively and AC/MnO_2 with maximum specific capacitance, energy and power density of 110 F g^{-1}, 3.3 Wh kg^{-1} and 30.0 kW kg^{-1}, respectively) have demonstrated to be better electrode materials for high power ECs devices. The symmetric pseudocapacitor devices exhibited "knee frequency" f_0 values of *ca.* 25 Hz for the OLC/MnO_2 (time constant ~ 40 ms) and *ca.* 22 Hz (time constant ~ 45 ms) for the CNT/MnO_2. The GO/MnO_2 displayed f_0 value of *ca.* 17 Hz (time constant ~ 59 ms) and AC/MnO_2 *ca.* 15 Hz (time constant ~ 67 s). These results show that most of the stored energy in the nanohybrid electrode materials is accessible with power output available on millisecond time scale. Using such a nanohybrid materials, it is possible to overcome the main limitation of MnO_2, namely its poor electrical conductivity (10^{-6} – 10^{-5} S cm^{-1})

and to exploit its main advantages, namely low-cost, high abundance, and environmentally-friendliness, for high power energy storage devices. Indeed, the electrochemical properties of OLC/MnO_2 nanohybrid as high-rate energy storage device have great potential for the development of high power aqueous-based supercapacitors that can be deployed for high-power technological applications.

References

[1] C. Largeot, C. Portet, J. Chmiola, P. Taberna, Y. Gogotsi, and P. Simon, "Relation between the Ion Size and Pore Size for an Electric Double-Layer Capacitor," pp. 2730–2731, 2008.

[2] P. Simon and Y. Gogotsi, "Materials for electrochemical capacitors.," *Nat. Mater.*, vol. 7, no. 11, pp. 845–854, Nov. 2008.

[3] X. Liu, C. Chen, Y. Zhao, and B. Jia, "A review on the synthesis of manganese oxide nanomaterials and their applications on lithium-ion batteries," *Journal of Nanomaterials*, vol. 2013. 2013.

[4] Y. Wang, Z. J. Han, S. F. Yu, R. R. Song, H. H. Song, K. (Ken) Ostrikov, and H. Y. Yang, "Core-leaf onion-like carbon/MnO2 hybrid nano-urchins for rechargeable lithium-ion batteries," *Carbon N. Y.*, vol. 64, pp. 230–236, Nov. 2013.

[5] Y. Wang, Z. J. Han, S. F. Yu, R. R. Song, H. H. Song, K. (Ken) Ostrikov, and H. Y. Yang, "Core-leaf onion-like carbon/MnO2 hybrid nano-urchins for rechargeable lithium-ion batteries," *Carbon N. Y.*, vol. 64, pp. 230–236, Nov. 2013.

[6] D. M. Anjos, J. K. McDonough, E. Perre, G. M. Brown, S. H. Overbury, Y. Gogotsi, and V. Presser, "Pseudocapacitance and performance stability of quinone-coated carbon onions," *Nano Energy*, Aug. 2013.

[7] I. Kovalenko, D. G. Bucknall, and G. Yushin, "Detonation Nanodiamond and Onion-Like-Carbon-Embedded Polyaniline for Supercapacitors," *Adv. Funct. Mater.*, vol. 20, no. 22, pp. 3979–3986, Nov. 2010.

[8] H. Xia, Y. Wang, J. Lin, and L. Lu, "Hydrothermal synthesis of MnO2/CNT nanocomposite with a CNT core/porous MnO2 sheath hierarchy architecture for supercapacitors," *Nanoscale Res. Lett.*, vol. 7, no. 1, p. 33, 2012.

[9] Y. Jin, H. Chen, M. Chen, N. Liu, and Q. Li, "Graphene patched CNT / MnO 2

nanocomposite papers for the electrode of high-performance flexible asymmetric supercapacitors," 2013.

[10] Y. Cheng, S. Lu, H. Zhang, C. V. Varanasi, and J. Liu, "Synergistic effects from graphene and carbon nanotubes enable flexible and robust electrodes for high-performance supercapacitors," *Nano Lett.*, vol. 12, no. 8, pp. 4206–4211, 2012.

[11] X. Zhang, X. Sun, H. Zhang, D. Zhang, and Y. Ma, "Development of redox deposition of birnessite-type MnO2 on activated carbon as high-performance electrode for hybrid supercapacitors," *Mater. Chem. Phys.*, vol. 137, no. 1, pp. 290–296, Nov. 2012.

[12] J. K. McDonough, A. I. Frolov, V. Presser, J. Niu, C. H. Miller, T. Ubieto, M. V. Fedorov, and Y. Gogotsi, "Influence of the structure of carbon onions on their electrochemical performance in supercapacitor electrodes," *Carbon N. Y.*, vol. 50, no. 9, pp. 3298–3309, Aug. 2012.

[13] I. Suarez-Martinez, N. Grobert, and C. P. Ewels, "Nomenclature of sp2 carbon nanoforms," *Carbon N. Y.*, vol. 50, no. 3, pp. 741–747, Mar. 2012.

[14] C. Portet, G. Yushin, and Y. Gogotsi, "Electrochemical performance of carbon onions, nanodiamonds, carbon black and multiwalled nanotubes in electrical double layer capacitors," *Carbon N. Y.*, vol. 45, no. 13, pp. 2511–2518, Nov. 2007.

[15] V. N. Mochalin, O. Shenderova, D. Ho, and Y. Gogotsi, "The properties and applications of nanodiamonds.," *Nat. Nanotechnol.*, vol. 7, no. 1, pp. 11–23, Jan. 2012.

[16] D. Pech, M. Brunet, H. Durou, P. Huang, V. Mochalin, Y. Gogotsi, P.-L. Taberna, and P. Simon, "Ultrahigh-power micrometre-sized supercapacitors based on onion-like carbon.," *Nat. Nanotechnol.*, vol. 5, no. 9, pp. 651–4, Sep. 2010.

[17] M. V. K. Azhagan, M. V. Vaishampayan, and M. V. Shelke, "Synthesis and

electrochemistry of pseudocapacitive multilayer fullerenes and MnO2 nanocomposites,” *J. Mater. Chem. A*, vol. 2, no. 7, p. 2152, 2014.

[18] V. L. Kuznetsov, A. L. Chuvilin, Y. V. Butenko, I. Y. Mal’kov, and V. M. Titov, “Onion-like carbon from ultra-disperse diamond,” *Chem. Phys. Lett.*, vol. 222, no. 4, pp. 343–348, May 1994.

[19] Daniel Urgate, “Curling and closure of graphitic networks under electron-beam irradiation.,” *Nature*, vol. 359, no. 6397, pp. 707–709, 1992.

[20] S. Iijima, “DIRECT OBSERVATION OF THE TETRAHEDRAL BONDING IN GRAPHITIZED CARBON BLACK BY,” *J. Christal Growth*, vol. 50, no. 3, pp. 675–683, 1980.

[21] M. Choucair and J. A. Stride, “The gram-scale synthesis of carbon onions,” *Carbon N. Y.*, vol. 50, no. 3, pp. 1109–1115, Mar. 2012.

[22] B. O. Agboola, J. Pillay, K. Makgopa, and K. I. Ozoemena, “Electrochemical Characterization of Mixed Self-Assembled Films of Water-Soluble Single-Walled Carbon Nanotube-Poly(m-aminobenzene sulfonic acid) and Iron(II) Tetrasulfophthalocyanine,” *J. Electrochem. Soc.*, vol. 157, no. 11, p. F159, 2010.

[23] C. Liu and H.-M. Cheng, “Carbon nanotubes for clean energy applications,” *J. Phys. D. Appl. Phys.*, vol. 38, no. 14, pp. R231–R252, 2005.

[24] M. F. L. De Volder, S. H. Tawfick, R. H. Baughman, and a J. Hart, “Carbon nanotubes: present and future commercial applications.,” *Science*, vol. 339, no. 6119, pp. 535–9, 2013.

[25] Y. Wang, Y. Wu, Y. Huang, F. Zhang, X. Yang, Y. Ma, and Y. Chen, “Preventing Graphene Sheets from Restacking for High-Capacitance Performance,” *J. Phys. Chem. C*, vol. 115, no. 46, pp. 23192–23197, Nov. 2011.

[26] Y. Zhu, S. Murali, M. D. Stoller, K. J. Ganesh, W. Cai, P. J. Ferreira, A. Pirkle, R. M.

Wallace, K. A. Cychosz, and M. Thommes, "Carbon-based supercapacitors produced by activation of graphene," *Science (80-.).*, vol. 332, no. 6037, pp. 1537–1541, 2011.

[27] Y. Chen, X. Zhang, D. Zhang, P. Yu, and Y. Ma, "High performance supercapacitors based on reduced graphene oxide in aqueous and ionic liquid electrolytes," *Carbon N. Y.*, vol. 49, no. 2, pp. 573–580, Feb. 2011.

[28] Z. Bo, X. Shuai, S. Mao, H. Yang, J. Qian, J. Chen, J. Yan, and K. Cen, "Green preparation of reduced graphene oxide for sensing and energy storage applications.," *Sci. Rep.*, vol. 4, p. 4684, Jan. 2014.

[29] C. Liu, Z. Yu, D. Neff, A. Zhamu, and B. Z. Jang, "Graphene-Based Supercapacitor with an Ultrahigh Energy Density.," *Nano Lett.*, pp. 4863–4868, Nov. 2010.

[30] M. D. Stoller, S. Park, Y. Zhu, J. An, and R. S. Ruoff, "Graphene-based ultracapacitors.," *Nano Lett.*, vol. 8, no. 10, pp. 3498–502, Oct. 2008.

[31] B. Xu, Y. Chen, G. Wei, G. Cao, H. Zhang, and Y. Yang, "Activated carbon with high capacitance prepared by NaOH activation for supercapacitors," *Mater. Chem. Phys.*, vol. 124, no. 1, pp. 504–509, 2010.

[32] C. Julien, "Raman spectra of birnessite manganese dioxides," *Solid State Ionics*, vol. 159, no. 3–4, pp. 345–356, Apr. 2003.

[33] P. Yang, Y. Ding, Z. Lin, Z. Chen, Y. Li, P. Qiang, M. Ebrahimi, W. Mai, C. P. Wong, and Z. L. Wang, "Low-cost high-performance solid-state asymmetric supercapacitors based on MnO2 nanowires and Fe2O3 nanotubes.," *Nano Lett.*, vol. 14, no. 2, pp. 731–6, Feb. 2014.

[34] Z.-S. Wu, W. Ren, D.-W. Wang, F. Li, B. Liu, and H.-M. Cheng, "High-energy MnO2 nanowire/graphene and graphene asymmetric electrochemical capacitors.," *ACS Nano*, vol. 4, no. 10, pp. 5835–42, Oct. 2010.

[35] H. Yang, J. Jiang, W. Zhou, L. Lai, L. Xi, Y. M. Lam, Z. Shen, B. Khezri, and T. Yu, "Influences of graphene oxide support on the electrochemical performances of graphene oxide-MnO2 nanocomposites.," *Nanoscale Res. Lett.*, vol. 6, no. 1, p. 531, Jan. 2011.

[36] D. Weingarth, M. Zeiger, N. Jäckel, M. Aslan, G. Feng, and V. Presser, "Graphitization as a Universal Tool to Tailor the Potential-Dependent Capacitance of Carbon Supercapacitors," *Adv. Energy Mater.*, vol. 4, no. 13, pp. 1–13, 2014.

[37] A. T. Chidembo, K. I. Ozoemena, B. O. Agboola, V. Gupta, G. G. Wildgoose, and R. G. Compton, "Nickel(ii) tetra-aminophthalocyanine modified MWCNTs as potential nanocomposite materials for the development of supercapacitors," *Energy Environ. Sci.*, vol. 3, no. 2, p. 228, 2010.

[38] B. P. Vinayan, R. Nagar, V. Raman, N. Rajalakshmi, K. S. Dhathathreyan, and S. Ramaprabhu, "Synthesis of graphene-multiwalled carbon nanotubes hybrid nanostructure by strengthened electrostatic interaction and its lithium ion battery application," *J. Mater. Chem.*, vol. 22, no. 19, p. 9949, 2012.

[39] K. Bogdanov, A. Fedorov, V. Osipov, T. Enoki, K. Takai, T. Hayashi, V. Ermakov, S. Moshkalev, and A. Baranov, "Annealing-induced structural changes of carbon onions: High-resolution transmission electron microscopy and Raman studies," *Carbon N. Y.*, vol. 73, pp. 78–86, Jul. 2014.

[40] T. K. Gupta, B. P. Singh, V. N. Singh, S. Teotia, A. P. Singh, I. Elizabeth, S. R. Dhakate, S. K. Dhawan, and R. B. Mathur, "MnO2 decorated graphene nanoribbons with superior permittivity and excellent microwave shielding properties," *J. Mater. Chem. A*, vol. 2, no. 12, p. 4256, 2014.

[41] G. Dresselhaus, M.S. Dresselhaus, *Topics in applied physics*. Berlin: Springer-Verla, 1982.

[42] Y. Wang, D. C. Alsmeyer, and R. L. Mccreery, "Raman spectroscopy of carbon materials: structural basis of observed spectra," *Carbon N. Y.*, no. 10, pp. 557–563, 1990.

[43] a Cuesta, P. Dhamelincourt, and J. Laureyns, "Raman microprobe studies on carbon materials," *Carbon N. Y.*, vol. 32, no. 8, pp. 1523–1532, 1994.

[44] T. Jawhari, A. Roid, and J. Casado, "Raman spectroscopiccharacterization of some commercially available carbon black materials," *Carbon N. Y.*, vol. 33, no. 11, pp. 1561–1565, 1995.

[45] A. Sadezky, H. Muckenhuber, H. Grothe, R. Niessner, and U. P??schl, "Raman microspectroscopy of soot and related carbonaceous materials: Spectral analysis and structural information," *Carbon N. Y.*, vol. 43, no. 8, pp. 1731–1742, 2005.

[46] B. Dippel, H. Jander, and J. Heintzenberg, "NIR FT Raman spectroscopic study of flame soot," *Phys. Chem. Chem. Phys.*, vol. 1, no. 20, pp. 4707–4712, 1999.

[47] D. Yang and M. Wang, "Syntheses and characterization of well-crystallized birnessite," *Chem. Mater.*, vol. 13, no. 8, pp. 2589–2594, 2001.

[48] H. Zhang, D. Hines, and D. L. Akins, "Synthesis of a nanocomposite composed of reduced graphene oxide and gold nanoparticles.," *Dalton Trans.*, vol. 43, no. 6, pp. 2670–5, 2014.

[49] F.-J. Liu, "Electrodeposition of manganese dioxide in three-dimensional poly(3,4-ethylenedioxythiophene)–poly(styrene sulfonic acid)–polyaniline for supercapacitor," *J. Power Sources*, vol. 182, no. 1, pp. 383–388, Jul. 2008.

[50] Z. Li, Y. Mi, X. Liu, S. Liu, S. Yang, and J. Wang, "Flexible graphene/MnO2 composite papers for supercapacitor electrodes," *J. Mater. Chem.*, vol. 21, no. 38, p. 14706, 2011.

[51] Y.-K. Hsu, Y.-C. Chen, Y.-G. Lin, L.-C. Chen, and K.-H. Chen, "Birnessite-type

manganese oxides nanosheets with hole acceptor assisted photoelectrochemical activity in response to visible light," *J. Mater. Chem.*, vol. 22, no. 6, p. 2733, 2012.

[52] M. C. Biesinger, B. P. Payne, A. P. Grosvenor, L. W. M. Lau, A. R. Gerson, and R. S. C. Smart, "Resolving surface chemical states in XPS analysis of first row transition metals, oxides and hydroxides: Cr, Mn, Fe, Co and Ni," *Appl. Surf. Sci.*, vol. 257, no. 7, pp. 2717–2730, Jan. 2011.

[53] H. Zhang, G. Cao, Z. Wang, and Y. Yang, "Growth of Manganese Oxide Nanoflowers on Vertically-Aligned Carbon Nanotube Arrays for High-Rate Electrochemical Capacitive Energy," no. 1, pp. 1–6, 2008.

[54] K. Rajendra Prasad and N. Miura, "Electrochemically synthesized MnO 2-based mixed oxides for high performance redox supercapacitors," *Electrochem. commun.*, vol. 6, no. 10, pp. 1004–1008, 2004.

[55] E. Raymundo-Piñero, V. Khomenko, E. Frackowiak, and F. Béguin, "Performance of Manganese Oxide/CNTs Composites as Electrode Materials for Electrochemical Capacitors," *J. Electrochem. Soc.*, vol. 152, no. 1, p. A229, 2005.

[56] S. R. Sivakkumar, J. M. Ko, D. Y. Kim, B. C. Kim, and G. G. Wallace, "Performance evaluation of CNT/polypyrrole/MnO2 composite electrodes for electrochemical capacitors," *Electrochim. Acta*, vol. 52, no. 25, pp. 7377–7385, 2007.

[57] H.-Q. Wang, G. Yang, Q.-Y. Li, X.-X. Zhong, F.-P. Wang, Z.-S. Li, and Y. Li, "Porous nano-MnO2: large scale synthesis via a facile quick-redox procedure and application in a supercapacitor," *New J. Chem.*, vol. 35, no. 2, p. 469, 2011.

[58] L. Hu, W. Chen, X. Xie, Nian Liu, Y. Yang, H. Wu, Y. Yao, M. Pasta, H. N. Alshareef, and Y. Cui, "Symmetrical MnO2 Carbon Nanotube-Textile Nanostructures for Wearable Pseudocapacitors with High Mass Loading," *ACS Nano*, vol. 5, no. 11, pp. 8904–8913, 2011.

[59] X. Zhao, L. Zhang, S. Murali, M. D. Stoller, Q. Zhang, Y. Zhu, and R. S. Ruoff, "Incorporation of manganese dioxide within ultraporous activated graphene for high-performance electrochemical capacitors.," *ACS Nano*, vol. 6, no. 6, pp. 5404–12, Jun. 2012.

[60] R. B. Rakhi, W. Chen, D. Cha, and H. N. Alshareef, "Nanostructured Ternary Electrodes for Energy-Storage Applications," *Adv. Energy Mater.*, vol. 2, no. 3, pp. 381–389, Mar. 2012.

[61] A. Bello, O. O. Fashedemi, J. N. Lekitima, M. Fabiane, D. Dodoo-Arhin, K. I. Ozoemena, Y. Gogotsi, A. T. Charlie Johnson, and N. Manyala, "High-performance symmetric electrochemical capacitor based on graphene foam and nanostructured manganese oxide," *AIP Adv.*, vol. 3, pp. 0–9, 2013.

[62] Q. Li, X.-F. Lu, H. Xu, Y.-X. Tong, and G.-R. Li, "Carbon/MnO(2) double-walled nanotube arrays with fast ion and electron transmission for high-performance supercapacitors.," *ACS Appl. Mater. Interfaces*, vol. 6, no. 4, pp. 2726–33, Feb. 2014.

[63] S. Maiti, A. Pramanik, and S. Mahanty, "Interconnected network of MnO2 nanowires with a 'cocoonlike' morphology: Redox couple-mediated performance enhancement in symmetric aqueous supercapacitor," *ACS Appl. Mater. Interfaces*, vol. 6, no. 13, pp. 10754–10762, 2014.

[64] R. Borgohain, J. P. Selegue, and Y.-T. Cheng, "Ternary composites of delaminated-MnO 2 /PDDA/functionalized-CNOs for high-capacity supercapacitor electrodes," *J. Mater. Chem. A*, vol. 2, no. 47, pp. 20367–20373, Oct. 2014.

[65] Z. Li, Z. Liu, D. Li, and H. Wang, "Facile synthesis of a -MnO 2 nanowires / spherical activated carbon composite for supercapacitor application in aqueous neutral electrolyte," *J. Mater. Sci.*, vol. 26, pp. 353–359, 2015.

[66] J. R. Miller, "Battery-Capacitor Power Source for Digital Communication-

Simulations Using Advanced Electrochemical Capacitors," *Electrochem. Soc. Proc. Ser.*, vol. PV95–29, pp. 246–254, 1996.

[67] M. E. Orazem, J.-B. Jorcin, N. Pébère, and B. Tribollet, "CPE analysis by local electrochemical impedance spectroscopy," *Electrochim. Acta*, vol. 51, no. 8, pp. 1473–1479, 2006.

[68] D. Weingarth, a. Foelske-Schmitz, and R. Kötz, "Cycle versus voltage hold – Which is the better stability test for electrochemical double layer capacitors?," *J. Power Sources*, vol. 225, pp. 84–88, Mar. 2013.

[69] P. Ratajczak, K. Jurewicz, and F. Béguin, "Factors contributing to ageing of high voltage carbon/carbon supercapacitors in salt aqueous electrolyte," *J. Appl. Electrochem.*, vol. 44, no. 4, pp. 475–480, Nov. 2013.

[70] Y. V. Butenko, V. L. Kuznetsov, a. L. Chuvilin, V. N. Kolomiichuk, S. V. Stankus, R. a. Khairulin, and B. Segall, "Kinetics of the graphitization of dispersed diamonds at 'low' temperatures," *J. Appl. Phys.*, vol. 88, no. 7, p. 4380, 2000.

Chapter 5: Carbon/hausmannite-type manganese oxide (C/Mn_3O_4) nanohybrids as pseudocapacitor materials [2]

[2]The following publication resulted from part of the research work presented in this chapter and is not referenced further:
K. Makgopa, and K. I. Ozoemena, A high-rate aqueous symmetric pseudocapacitor based on highly graphitized onion-like carbon/hausmanite-type manganese oxide (Mn_3O_4) nanohybrids, *RSC Advances*, (***Submitted)***.

5.1 Introduction

The rapid developmental growth of the economy and significant social advancement necessitate many kinds of energy storage and conversion devices, thus more research on alternative energy storage and conversion devices is critical (see Chapter 1&2). Nanomaterials of about the length scale of less than 100 nm, have received increasing interest owing to their fundamental scientific significance as well as their potential applications that derive from their fascinating electrical, magnetic, and catalytic properties [1], [2]. As compared to the bulk active electrode materials, the corresponding nanomaterials possess more excellent electrochemical activity, such as higher capacitance, larger surface areas, and relatively good conductivity, thereby; nanomaterials have vast potential application in electrochemistry field [3]. It is well known that the electrochemical performance of the electrochemical capacitor device depends on the morphological properties (i.e., size, shape, surface area, and architecture) of the electrode materials [4]. Considerable attention is devoted to manganese oxide based materials, especially because of their environmental friendliness in character. Among these electrode materials, manganese oxides, characterized by their high theoretical specific surface area (1370 m^2 g^{-1}), high theoretical capacitance, low-cost, abundance and environmentally friendly in nature, have attracted significant interest as electrode active materials for ECs [3], [5]–[11]. Recently, a tetragonal hausmannite metal oxide, Mn_3O_4, which has some polymorphs, has attracted considerable attention because of a variety of applications such as energy storage, ion exchange, and molecular adsorption [12]. Moreover, Mn_3O_4 is known to be a potential candidate as electrode materials for electrochemical capacitors (ECs) applications due to the most stable oxide of manganese, non-toxic and cost-effective [13]. Hausmannite, Mn_3O_4, is one of the oxides of manganese which contain both the diand trivalent manganese (Mn^{2+} and Mn^{3+}, respectively). This type of oxide material belongs to the spinel group, and it forms a crystal structure of a tetragonal. Figure 5.1 shows the molecular crystal structure of the tetragonal hausmannite, Mn_3O_4, obtained with Diamond crystal structure software using ICSD file number 68174. The Mn^{2+} atom is coordinated by four oxygen atoms situated at the corners of a tetragonal prism. The Mn^{3+} is also coordinated by four oxygen atoms at the equatorial position to show square-planar coordination geometry (see inset of Fig. 5.1).

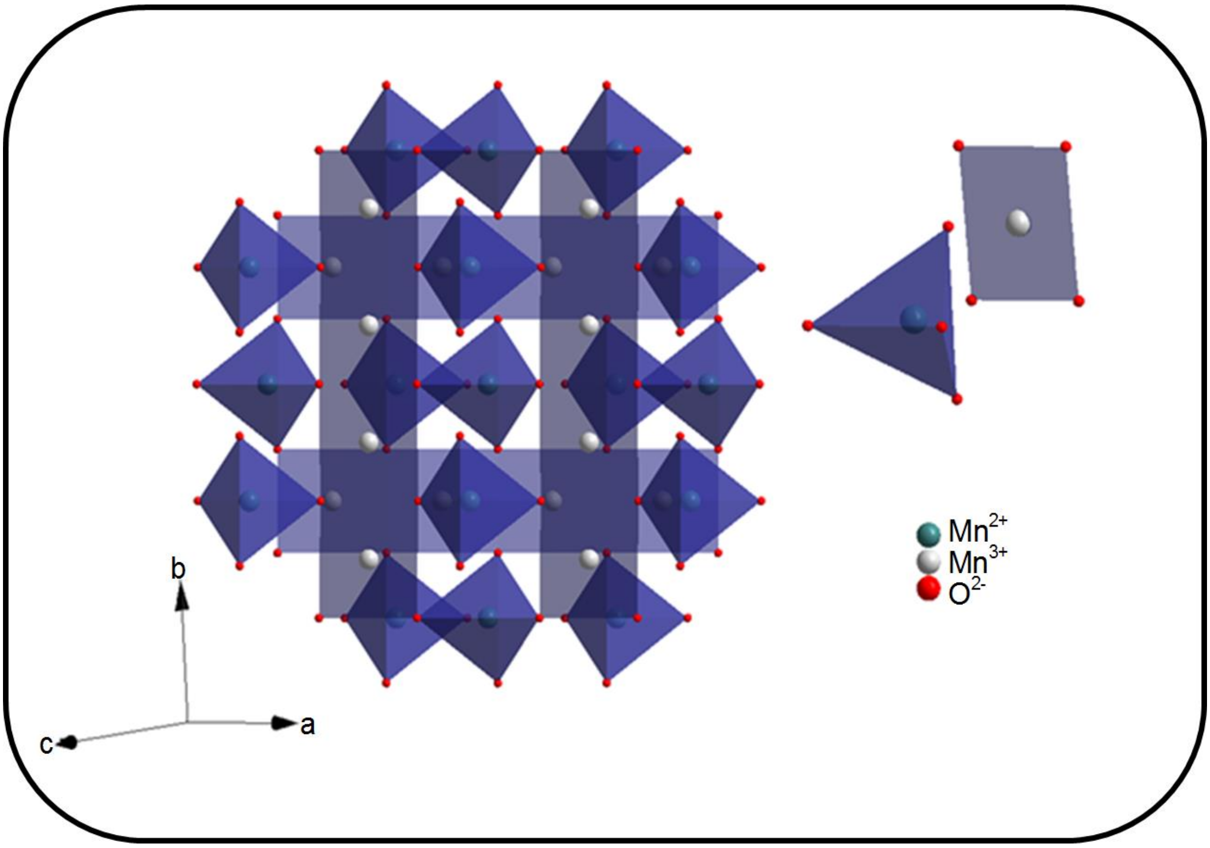

Figure 5.1: Crystal structure of tetragonal hausmannite Mn_3O_4.

5.2 Results and Discussion

5.2.1 SEM and TEM analysis

The surface morphology of all synthesized materials was investigated using FESEM. Figure 5.2 displays FESEM images of various synthesized materials (i.e., OLC/Mn_3O_4, CNT/Mn_3O_4, GO/Mn_3O_4, and AC/Mn_3O_4). Variation in morphology for the synthesized OLC/Mn_3O_4 (Fig. 5.2a), CNT/Mn_3O_4 (Fig. 5.2b), GO/Mn_3O_4 (Fig. 5.2c), and AC/Mn_3O_4 (Fig. 5.2d) nanohybrids is easily noticed from the FESEM images. The inset in Fig. 5.2 represents the high magnification of the respective nanohybrid electrode materials. An explicit interaction of Mn_3O_4 nanoparticles is present in the nanohybrid electrode materials with the carbon support being clearly distinguishable, indicating a successful decoration of Mn_3O_4 in the synthesized nanohybrid electrode materials (Fig 5.2). The particles of OLC and Mn_3O_4 in OLC/Mn_3O_4 nanohybrid have a similar appearance (regarding size). The entangled CNT in the presence of Mn_3O_4 illustrates a successful decoration of Mn_3O_4 in CNT/Mn_3O_4 nanohybrid. The GO/Mn_3O_4 morphology exhibited particles of Mn_3O_4 intercalated between the sheets of the GO. This arrangement of Mn_3O_4 sandwiched between GO sheets in GO/Mn_3O_4 helps in preventing the restacking of the GO sheets which would have distorted the performance of nanohybrid.

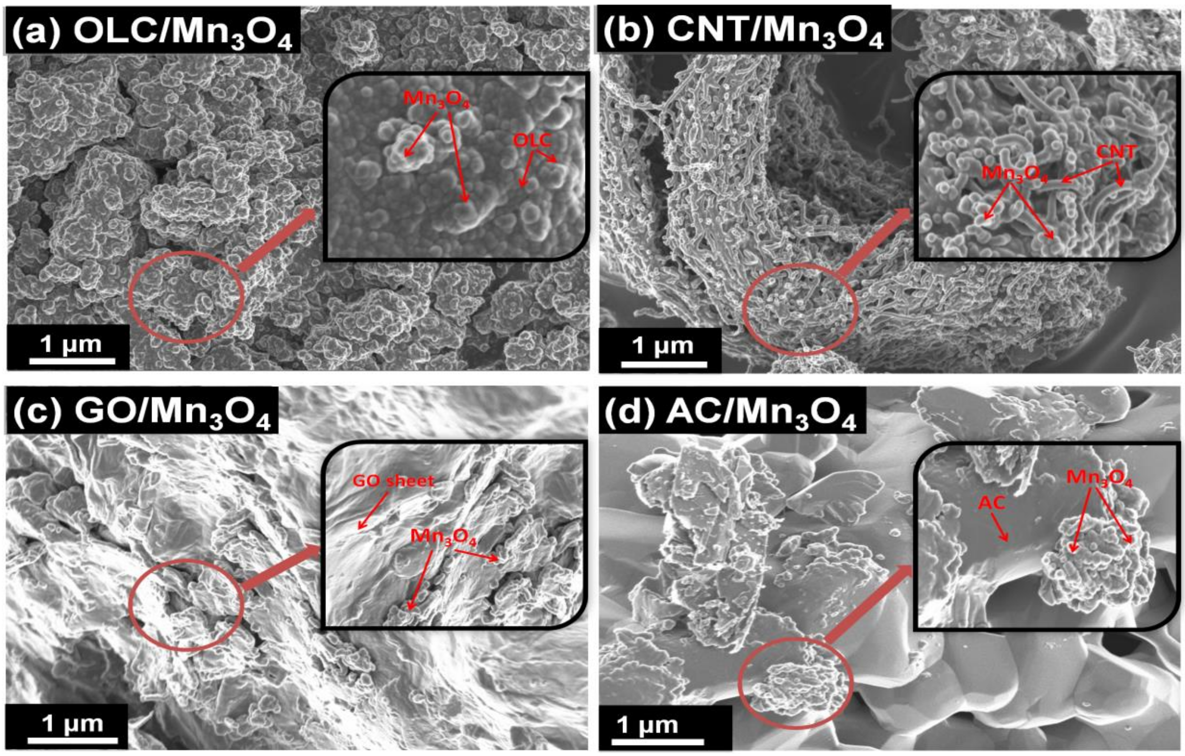

Figure 5.2: SEM images of (a) OLC/Mn_3O_4, (b) CNT/Mn_3O_4, (c) GO/Mn_3O_4 and (d) AC/Mn_3O_4 nanohybrids. Inset in (a-d) is the high magnification SEM image of respective nanohybrids.

Figure 5.3 compares the TEM images which further interrogates the surface morphologies of various synthesized electrode materials (i.e., OLC/Mn_3O_4, CNT/Mn_3O_4, GO/Mn_3O_4, and AC/Mn_3O_4). The result is shown in Fig. 5.3a represents the onion-like structure of the OLC decorated with the Mn_3O_4 nanoparticle to form OLC/Mn_3O_4 nanohybrid. It is clearly shown (by a clear visibility of both the OLC and Mn_3O_4) on the high magnification TEM image (inset on Fig. 5.3a), that a successful synthesis of OLC/Mn_3O_4 nanohybrid is achieved. In Fig. 5.3b, a clear visibility of carbon nanotubes (CNT) covered by the Mn_3O_4 nanoparticle confirms a successful synthesis of the CNT/Mn_3O_4 nanohybrid. The primary particle size of both carbon onions and carbon nanotubes is in the range of a few nanometers as seen from the TEM images which are in agreement with our previous findings [14], [15]. The primary particle size is maintained for the OLC/Mn_3O_4 and CNT/Mn_3O_4 nanohybrids (Fig. 5.3a and Fig. 5.3b, respectively). The Mn_3O_4 nanoparticle can also be clearly spotted from the graphene oxide sheet as shown in GO/Mn_3O_4 nanohybrid (Fig. 5.3c). The manganese oxide nanoparticles (Mn_3O_4) are randomly scattered on the piece of graphene. Similar morphology is displayed on AC/Mn_3O_4 nanohybrid (Fig. 5.3d) indicating the presence of both AC and Mn_3O_4 nanoparticles. All these results are in good agreement with the results obtained from SEM images, showing a successful synthesis of the nanohybrid materials.

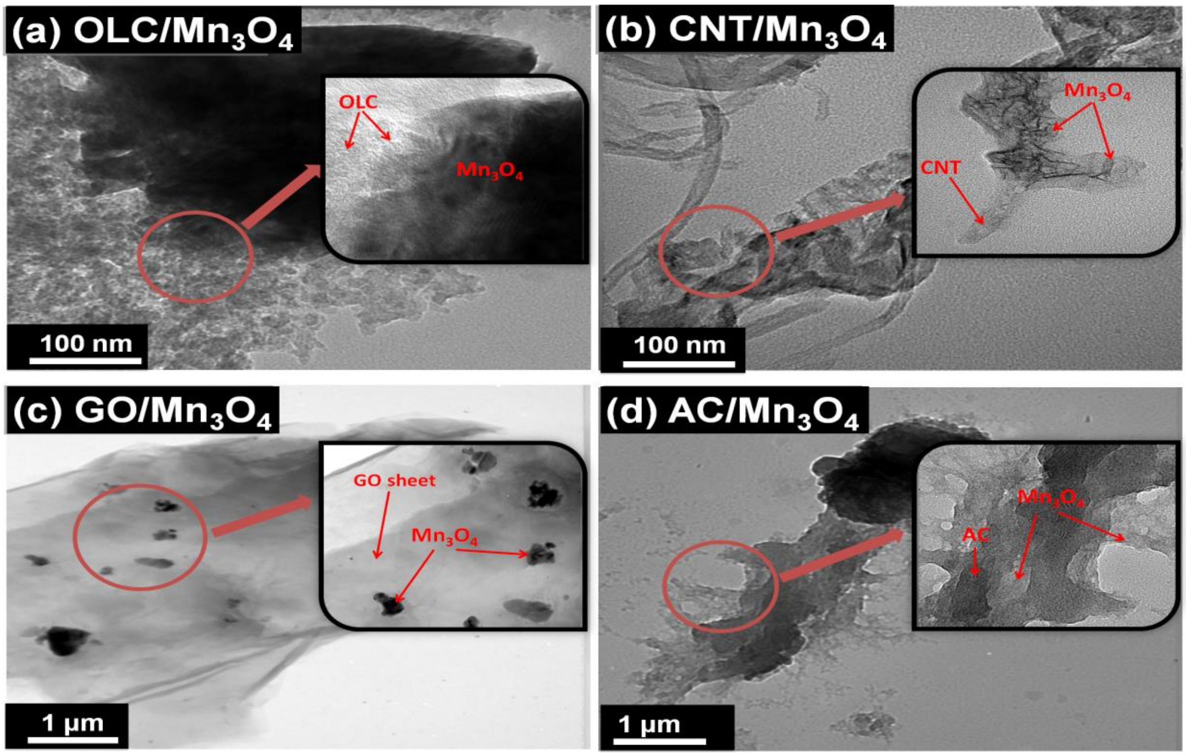

Figure 5.3: TEM images of (a) OLC/Mn_3O_4, (b) CNT/Mn_3O_4, (c) GO/Mn_3O_4 and (d) AC/Mn_3O_4 nanohybrids. Inset in (a-d) is the high magnification TEM image of respective nanohybrids.

5.2.2 XRD, Raman, FTIR, EDX, and XPS studies

X-ray powder diffraction (XRD) is a fundamental analytical tool for the characterization and phase identification of crystalline powder materials. Figure 5.4 illustrates a typical X-ray diffraction pattern of synthesized nanohybrid electrode materials (i.e., OLC/Mn_3O_4, CNT/Mn_3O_4, GO/Mn_3O_4, and AC/Mn_3O_4), overlaid with that of pure tetragonal hausmannite (Mn_3O_4) nanoparticles (Fig. 5.4a) and various carbon allotropes (i.e., OLC, CNT, GO, and AC) (Fig. 5.4b). From the XRD patterns of the electrode materials shown in Fig. 5.4a, it is revealed that the XRD peaks in the pattern can be indexed as those of tetragonal hausmannite (Mn_3O_4) structure (Sys.:tetragonal, lattice: body centered, space-group: $I\ 4_1$/amd (141) a: 0.576 nm, c: 0.944 nm, a/b: 1.0000, b/c: 0.6106 and c/a: 1.6378) in accordance with JCPDS card of tetragonal hausmannite (Mn_3O_4). These parameters are also confirmed by ICSD card of tetragonal hausmannite, Mn_3O_4, (JCPDS 18-0803/ICSD-68174). The peak at 2θ values of 18.14°, 29.04°, 32.53°, 36.29°, 38.15°, 44.59°, 50.89°, 58.69°, 60.06° and 64.78° correspond to the (101), (112), (103), (211), (004), (220), (105), (321), (224), and (400) planes of body-centered tetragonal hausmannite Mn_3O_4, respectively, and this similar peaks are witnessed in nanohybrid materials [16]. The other peaks present in the nanohybrid electrode materials can be indexed as those of graphitic carbon using the JCPDS card 75-1621 and also confirmed by graphite ICSD card 31170 (Sys.: hexagonal, lattice: primitive, space-group: P63mc (186) a: 0.247 nm, c: 0.679 nm, a/b: 1.0000, b/c: 0.3638 and c/a: 2.7490). These peaks indicate the presence of carbon in the nanohybrid [17], [18]. This graphitic carbon peaks can also be observed in the pure carbon diffractograms (Fig. 5.4b) confirming the results found from the nanohybrids XRD patterns. The width of all diffraction peaks for the metal oxide, Mn_3O_4, in both pure tetragonal hausmannite (Mn_3O_4) and the nanohybrid electrode materials are narrow, indicating the crystalline nature of the Mn_3O_4. The strong intensities of the diffraction peaks relative to the background signal means that the resultant product has a high purity Mn_3O_4 tetragonal phase [19]. For graphite, an intense crystalline peak occurs at a 2θ value of 24.97° as seen from the OLC, CNT, and AC, which is the characteristic peak of the (002) plane in hexagonal graphite. Upon oxidation of graphite, the (002) peak shifts to a 2θ value of 10.65° as seen in pure GO (without Mn_3O_4 nanoparticles) in Fig. 5.4b [20]. The calculated *d*-spacing for the (002) plane at 24.97°of carbon is 0.356 nm and remains at that value with or without the presence of Mn_3O_4 in nanohybrid. This value represents a small increase in lattice spacing compared to an ideal graphite crystal (i.e., 0.340 nm) at a 2θ value of 26.23° as well-known for the carbon structure [18]. Though, the carbon is expected to influences the electrochemical properties of the metal oxide, Mn_3O_4, but it does not alter the tetragonal crystal structure of the Mn_3O_4 material.

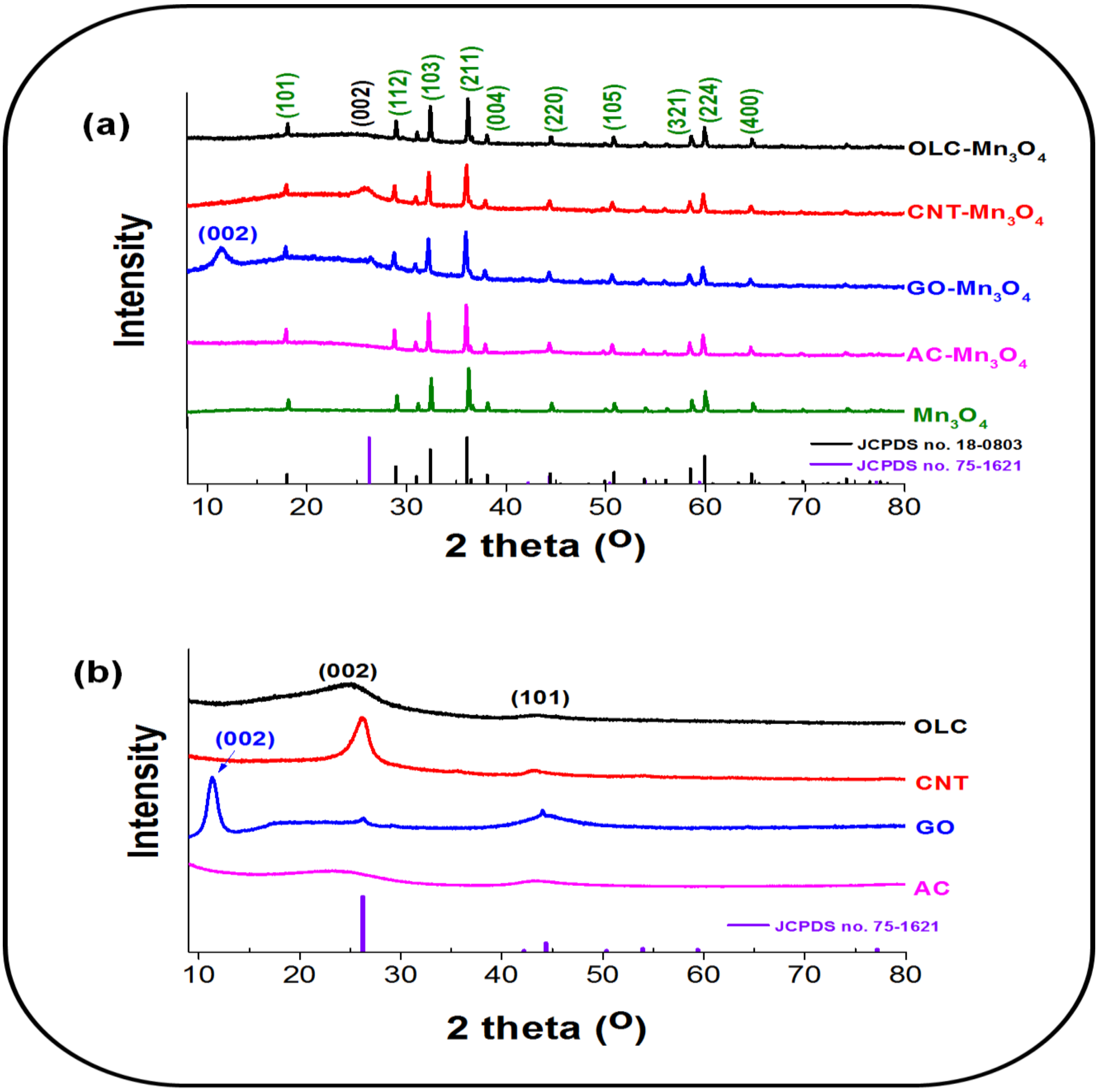

Figure 5.4: X-ray diffraction pattern for (a) OLC/Mn_3O_4, CNT/Mn_3O_4, GO/Mn_3O_4, and AC/Mn_3O_4 nanohybrids, and (b) OLC, CNT, GO, and AC.

Raman spectroscopy is a fundamental analytical tool for the characterization of carbon-based materials to understand their chemical bonding. This technique can precisely distinguish sp^2 and sp^3 hybridized bonding of carbon atoms and also indicates the purity of the carbon samples by providing the defects vibrational peak of the synthesised material [21]. Figure 5.5 illustrates Raman spectra of synthesized nanohybrid materials (i.e., OLC/Mn_3O_4, CNT/Mn_3O_4, GO/Mn_3O_4, and AC/Mn_3O_4), overlaid with pure Mn_3O_4 nanoparticles (Fig. 5.5a) and that of various carbon allotropes (i.e., OLC, CNT, GO, and AC) (Fig. 5.5b). The presence of Mn_3O_4 is confirmed by a strong Raman signal at around 652 cm^{-1} in all the nanohybrid electrode materials (Fig. 5.5a) [22], [23]. The presence of the carbon in the hybrid electrode materials is confirmed by Raman peaks associated with the carbon D-mode (1350 cm^{-1}) and G-mode (1590 cm^{-1}) (Fig. 5.5a) which are in agreement with the peaks observed from pure carbon-based materials (i.e., without Mn_3O_4) shown in Fig. 5.5b. The G-mode is allocated to the E_{2g} phonon of sp^2 carbon atoms, and the D-mode is assigned to the extent of defects in the carbon sample [8], [22], [24]. The ratio of D-mode and G-mode intensities (I_D/I_G) validates the extent of its defects in the carbon samples. In particular, the I_D/I_G ratios before and after Mn_3O_4 deposition are almost identical with values of 0.98 and 0.97, respectively for OLC/Mn_3O_4 nanohybrid. The FWHM for both the D-mode and the G-mode were measured to 73.1 cm^{-1} and 69.8 cm^{-1} before the deposition and to 74.9 cm^{-1} and 98.6 cm^{-1} after the Mn_3O_4 deposition for the OLC/Mn_3O_4 nanohybrid. The CNT/Mn_3O_4 nanohybrid I_D/I_G ratios before and after Mn_3O_4 deposition have values of 0.95 and 1.01, respectively. The FWHM for both the D-mode and the G-mode are measured to 50.8 cm^{-1} and 43.1 cm^{-1} before the deposition and to 57.45 cm^{-1} and 72.6 cm^{-1} after the Mn_3O_4deposition for the CNT/Mn_3O_4 nanohybrid. The intensity ratio (I_D/I_G) of the GO/Mn_3O_4 nanohybrid before and after Mn_3O_4 deposition has a value of 0.95 and 0.98, respectively. The FWHM for both the D-mode and the G-mode measured to be 128.9 cm^{-1} and 83.51 cm^{-1} before the deposition and to 154.6 cm^{-1} and 168.4 cm^{-1} after the Mn_3O_4 deposition. The intensity ratio (I_D/I_G) of the AC/Mn_3O_4 nanohybrid before and after Mn_3O_4 deposition has the value of 1.06 and 1.15, respectively. The FWHM for both the D-mode and the G-mode were measured to 123.3 cm^{-1} and 93.8 cm^{-1} before the deposition and to 118.3 cm^{-1} and 90.1 cm^{-1} after the Mn_3O_4 deposition. The

Raman bands for the carbon allotropes are observed at the similar time in their respective nanohybrids. Thus, these results suggest a successful decoration of Mn_3O_4 to produce nanohybrid electrode materials. This data is in good agreement with the data obtained from the XRD analysis.

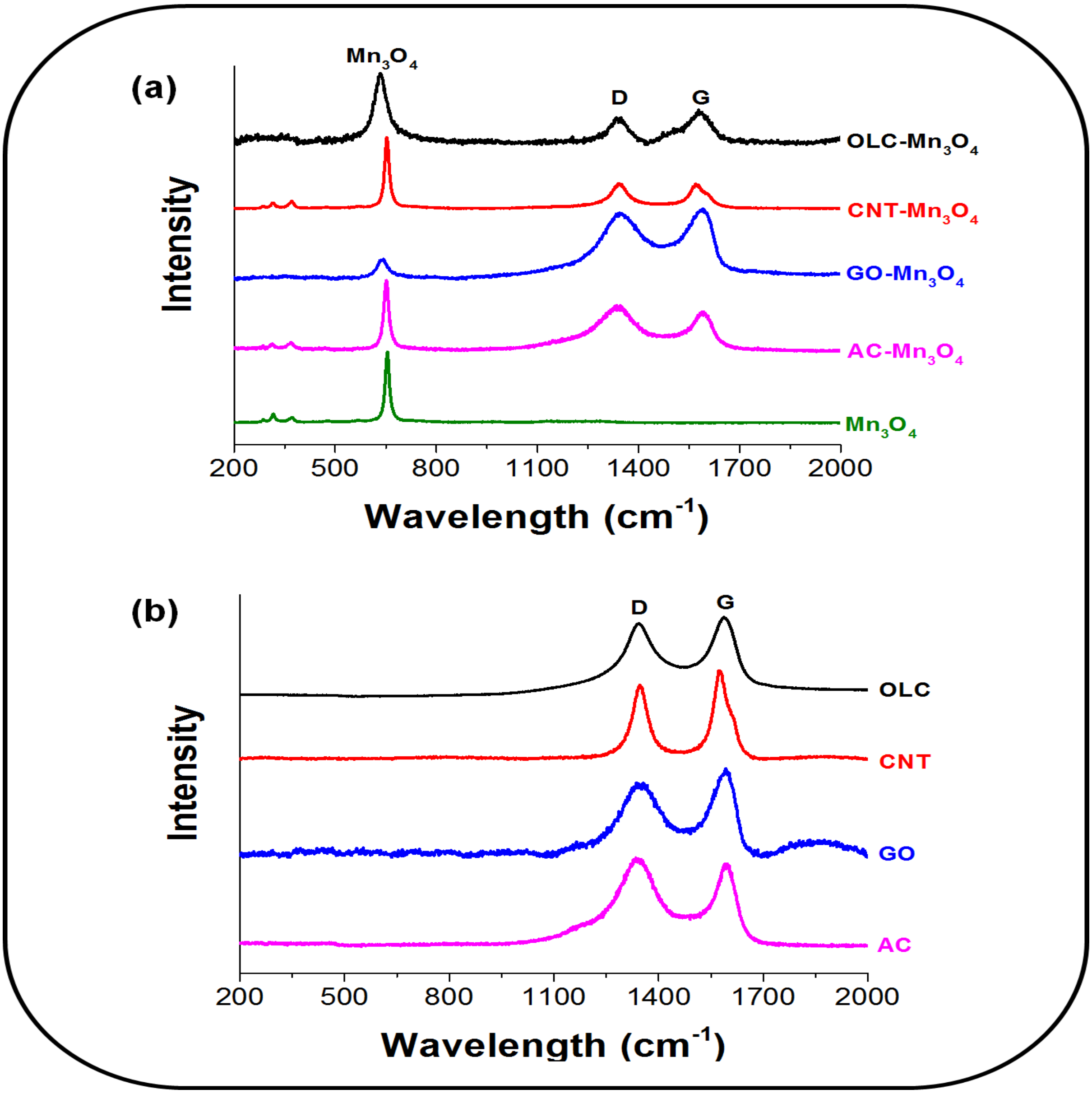

Figure 5.5: Raman spectra for (a) OLC/Mn_3O_4, CNT/Mn_3O_4, GO/Mn_3O_4, and AC/Mn_3O_4 nanohybrids, overlaid with pure Mn_3O_4 and (b) OLC, CNT, GO, and AC.

Figure 5.6 shows a deconvoluted Raman spectra (Lorentzian Fit) for the nanohybrid materials (i.e., OLC/Mn_3O_4, CNT/Mn_3O_4, GO/Mn_3O_4, and AC/Mn_3O_4), Fig. 5.6a, and also for carbon materials (i.e., OLC, CNT, GO, and AC), Fig. 5.6b. The D1-mode has been suggested to arise from the defects present in the atomic layers of carbon materials [24]. The D2-mode is related to a lattice vibration corresponding to that of the G mode [25]. The D3-mode originates from the distribution of amorphous carbon on interstitial sites in the disturbed lattice of graphite or carbonaceous material [26], [27]. The D4-mode is related to lattice vibrations corresponding to sp^2-sp^3 bonds [28], [29]. The Raman curve fitting presented in Fig. 5.6 agree well with Raman data reported for other carbonaceous material (e.g. soot)[28].

In all the nanohybrid materials, the I_D/I_G remains almost unchanged suggesting the similar amount of defects in the materials. However, there exists a level of amorphousness within the nanohybrid materials (shown by the presence of D3-mode), except for the CNT/Mn_3O_4 as witnessed by the absence of D3-mode. The AC/Mn_3O_4 and GO/Mn_3O_4 nanohybrid materials exhibit much higher amorphousness relative to the OLC/Mn_3O_4, and this observation is indicated by the intensity increase in the area between the D- and G-mode range (1440-1550 cm^{-1}) which overlaps with the D3-mode. Nonetheless, the structural stability of all the nanohybrid materials is maintained since there is no much difference in the deconvoluted Raman spectra of the nanohybrid materials and those of the carbon supports.

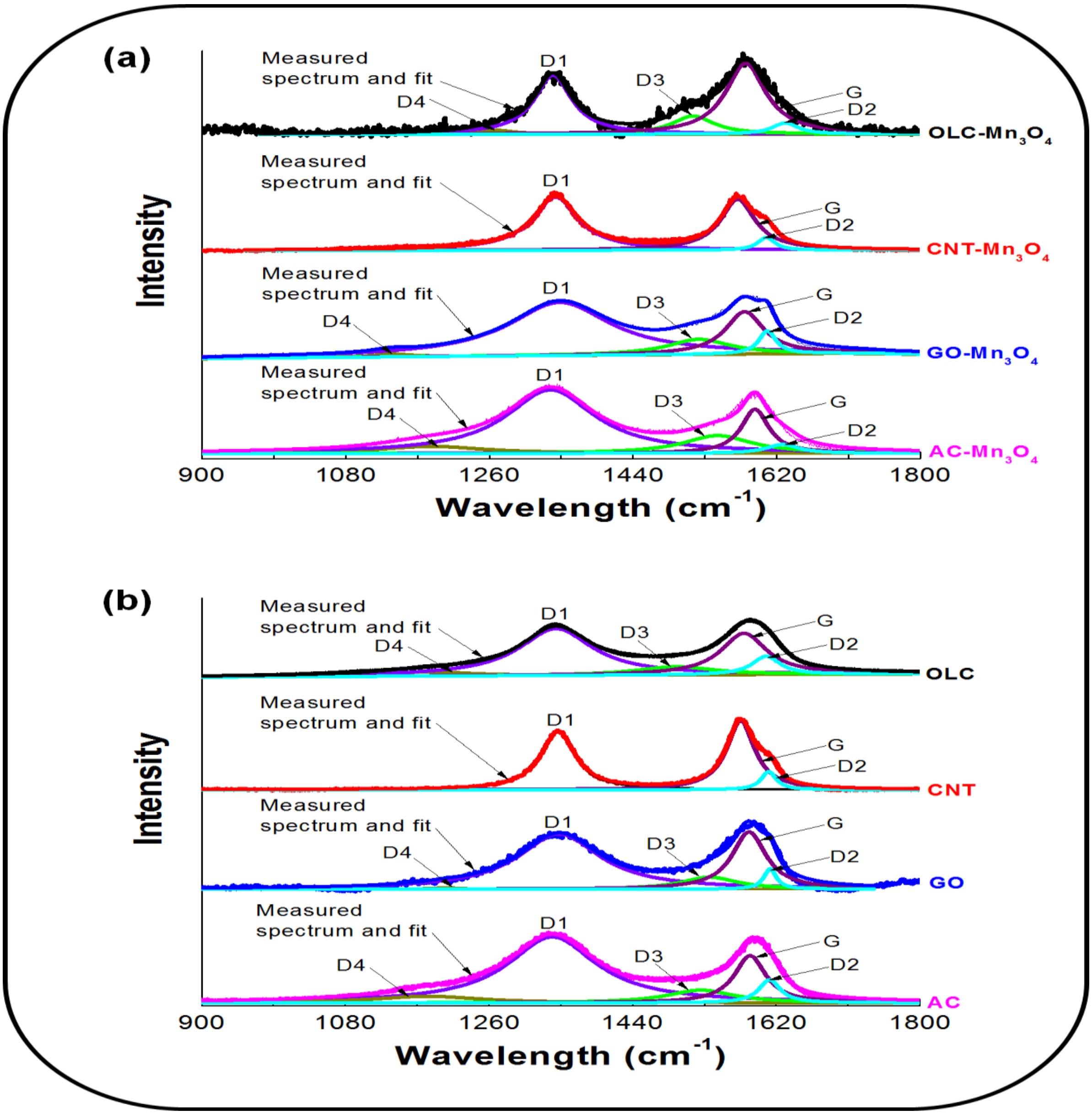

Figure 5.6: A deconvoluted Raman spectra for (a) OLC/Mn_3O_4, CNT/Mn_3O_4, GO/Mn_3O_4, and AC/Mn_3O_4 nanohybrids, and (b) OLC, CNT, GO, and AC.

To further differentiate the structure of Mn_3O_4 nanoparticles in the nanohybrid materials, FTIR analyses of OLC/Mn_3O_4, CNT/Mn_3O_4, GO/Mn_3O_4, and AC/Mn_3O_4 nanohybrids overlaid with pure Mn_3O_4 were carried out. The above results compared with the FTIR analyses of the various carbon allotropes (i.e., OLC, CNT, GO, and AC) without Mn_3O_4, and their corresponding spectra comparison are presented in Figure 5.7. As seen from Fig. 5.7a, there are two well pronounce peaks at 489 cm^{-1} and

617 cm^{-1} corresponding to the vibration of the Mn–O stretching modes, associated with Mn in tetrahedral and octahedral sites, respectively [30]. The broad peak at 3450 cm^{-1} is assigned to hydroxyl groups which suggest that there are water molecules in the synthesized materials [31]. It is worth noting that this broad peak assigned to –OH group is pronounced in GO and GO/Mn_3O_4 due to the intensive exposure to harsh acidic environment during synthesis [32]. These peaks are clearly shown from the FTIR spectra of pure carbon samples (without Mn_3O_4) shown in Fig. 5.7b. The C–H stretching, carbonyl/carboxyl C=O, aromatic C=C, epoxy C–O, alkoxy C–O and carboxyl C–O functional groups are seen at 2912, 1722, 1580, 1414, 1384 and 1106 cm^{-1}, respectively [32]. Moreover, the intensity of the absorption peaks related to the oxidized groups decreased slightly in the FTIR spectra of the various nanohybrid materials as compared to those in the relative spectrum of pure carbon samples, indicating the presence of the Mn_3O_4 in the synthesised nanohybrid materials. There is a good agreement between the results obtained in this FTIR analysis with those obtained from the above discussion (i.e., SEM, TEM, XRD, and Raman), thus indicating a successful decoration of Mn_3O_4 to form nanohybrid electrode materials.

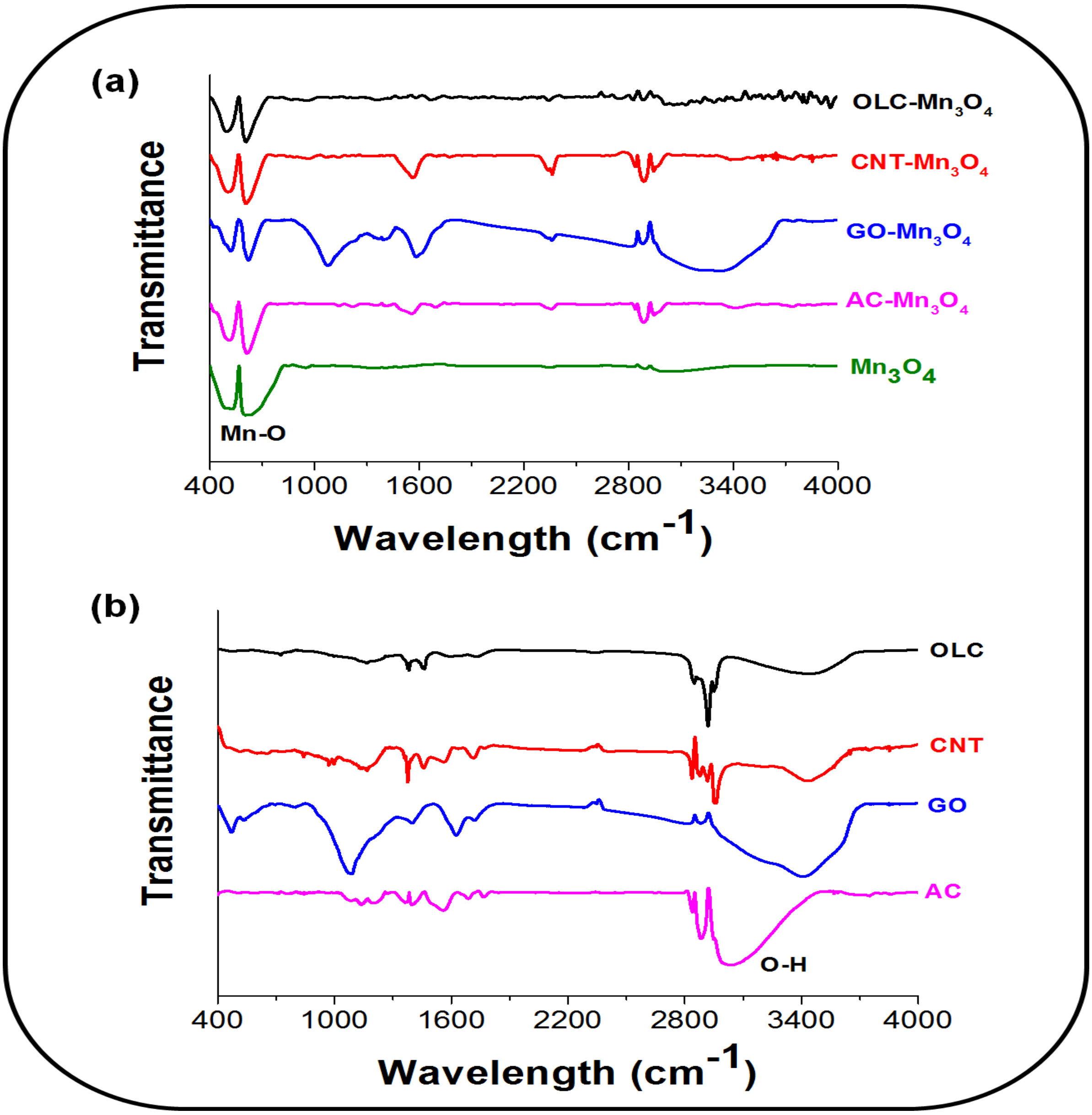

Figure 5.7: FTIR spectra comparison for (a) OLC/Mn_3O_4, CNT/Mn_3O_4, GO/Mn_3O_4 and AC/Mn_3O_4 nanohybrids and (b) OLC, CNT, GO, and AC.

5.2.3 Cyclic Voltammetric (CV) analysis of various carbon/Mn_3O_4-based electrodes on Ni foam.

Cyclic voltammetry is a potentiodynamic electroanalytical technique that is used to provide qualitative information about electrochemical processes that happen at the electrode/electrolyte interphase in a voltaic cell. This method is used with the aim of collecting electrochemical information regarding the synthesised electrode materials. The investigation of the OLC/Mn_3O_4, CNT/Mn_3O_4, GO/Mn_3O_4, AC/Mn_3O_4 nanohybrids and Mn_3O_4 as a full cell symmetric supercapacitor was carried out using nickel foam as the current collector considering its lower cost, better pore size distribution and good surface area. Figure 5.8 compares cyclic voltammograms for OLC/Mn_3O_4, CNT/Mn_3O_4, GO/Mn_3O_4, AC/Mn_3O_4 nanohybrids and pure Mn_3O_4 in aqueous 1 M Na_2SO_4 at the scan rate of 5 mV s^{-1}. All the cyclic voltammograms of the nanohybrid materials have exhibited a rectangular shape which depicts the contribution of EDL storage mechanism resulting from the presence of graphitic carbon in the nanohybrid materials. The slight deviation from a perfect rectangular shape is due to the pseudocapacitive storage mechanism arising from the metal oxide, Mn_3O_4, in the nanohybrid electrode materials. As seen from Fig. 5.8, the entire nanohybrid electrode materials exhibited better electrochemical performance as compared to each other, but the nanohybrid resulting from the decoration of Mn_3O_4 on the surface of the OLC (i.e., OLC/Mn_3O_4 nanohybrid) displayed much higher current response and maximum charge separation as compared to other nanohybrid electrode materials. The electrochemical performance (i.e., current response and charge separation) of the rest of the nanohybrid electrode materials decreased from CNT/Mn_3O_4, GO/Mn_3O_4, and AC/Mn_3O_4 nanohybrids, respectively. This type of behaviour is a good indication of a good pseudocapacitive behaviour of the electrode materials as a result of the synergistic effect coming from Mn_3O_4 and the introduction of various carbon allotropes (i.e., OLC, CNT, GO, AC) in the nanohybrids. As can be seen from the CV of Mn_3O_4; it exhibited a small current response and charge separation, indicating poor electrochemical behaviour. But the electrochemical properties of the nanohybrids have been enhanced resulting in an improved pseudocapacitive performance of the Mn_3O_4.

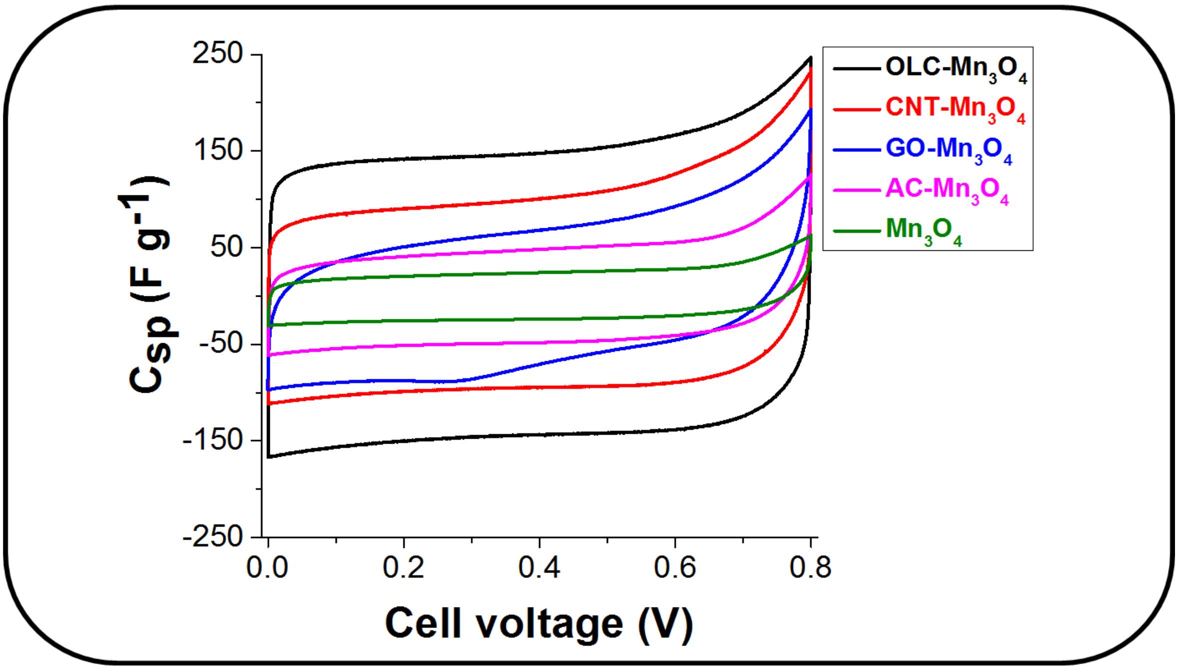

Figure 5.8: Comparative cyclic voltammograms for OLC/Mn_3O_4, CNT/Mn_3O_4, GO/Mn_3O_4, AC/Mn_3O_4 nanohybrids and Mn_3O_4 in aqueous 1 M Na_2SO_4 at 5 mV s^{-1}.

Figure 5.9 shows cyclic voltammograms for (a) OLC/Mn_3O_4, (b) CNT/Mn_3O_4, (c) GO/Mn_3O_4, and (d) AC/Mn_3O_4 nanohybrids at various scan rates (from 2 to 100 mV s^{-1}) in the potential range of 0–0.8 V, using 1 M Na_2SO_4 aqueous solution as the electrolyte. The CV shapes of the entire nanohybrid electrode materials are almost ideally rectangular from the scan rates between 5-100 mV s^{-1}. However, these CV curves exhibit a gradual change into a sharp apex towards the voltage of 0.8 V with the decrease of the scan rate, particularly in the scan rate of 10 to 5 mV s^{-1}. The reason for such change in the CV shapes on the nanohybrids may be due to the internal resistance of the electrode material inhibiting the charge movements within their porous structure and also the low conductivity of the Na_2SO_4 aqueous electrolyte [33]. Is seen that OLC/Mn_3O_4 nanohybrid exhibited a small internal resistance as compared to the others and followed by the CNT/Mn_3O_4 indicating that both the OLC and CNT contributed significantly to improving the conductivity of Mn_3O_4 nanoparticles, resulting in improved charge mobility towards the electrode/ electrolyte interface.

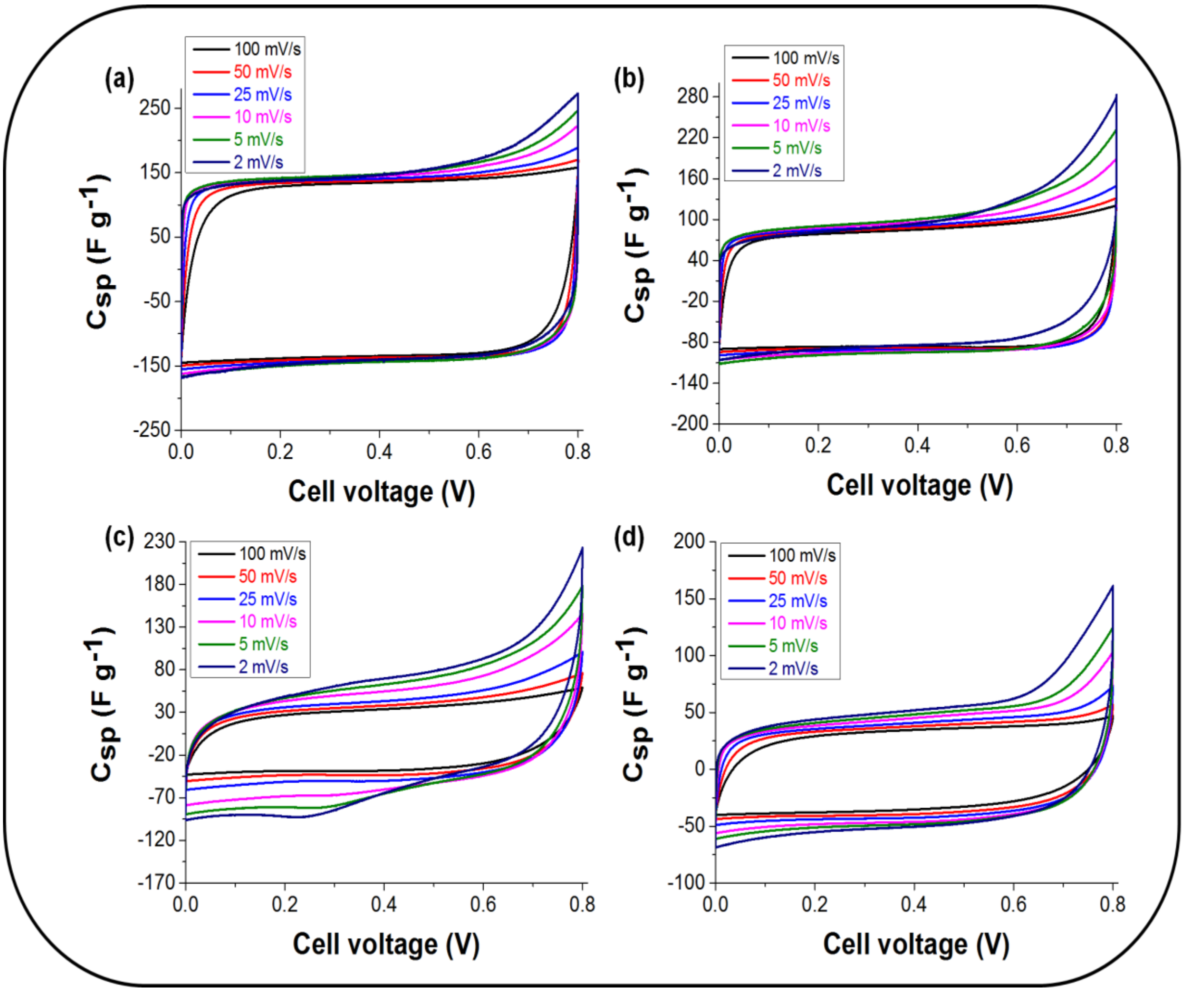

Figure 5.9: Comparison of cyclic voltammograms for (a) OLC/Mn_3O_4, (b) CNT/Mn_3O_4, (c) GO/Mn_3O_4, and (d) AC/Mn_3O_4, nanohybrids at various scan rates. Electrolyte: aqueous 1M Na_2SO_4.

5.2.4 Galvanostatic Charge-Discharge (GCD) analysis of various carbon/Mn_3O_4-based electrodes on Ni foam.

The galvanostatic charge-discharge technique is a reliable electrochemical method for the evaluation of the electro-capacitive behavior of the electrode materials in energy storage device. Thus, this approach is adopted for further interrogation of the nanohybrid electrode materials. Figure 5.10a shows the galvanostatic charge-discharge curves comparing OLC/Mn_3O_4, CNT/Mn_3O_4, GO/Mn_3O_4, AC/Mn_3O_4 nanohybrids and Mn_3O_4 nanoparticles at 0.3 A g^{-1} with a cell voltage varied from 0.0 to 0.8 V in aqueous 1 M Na_2SO_4. The electrodes materials displayed linear charge-discharge curves that resemble an isosceles triangle, which suggests that the electrode materials possess an ideal capacitive performance and splendid electrochemical reversibility contributed by both faradaic and non-faradaic charge storage mechanisms. According to the galvanostatic discharge curves, the specific capacitances (C_{sp}), maximum specific energy (E_{sp}) and power (P_{max}) densities can be calculated using equation 2.16 to 2.18 with the internal resistance of the cell calculated using equation 2.19 (see chapter 2). For a better analysis of the capacitive behaviour of the as-obtained nanohybrid electrode materials, studies were made using different current densities (see Fig. 5. 11) and their values are presented in Fig. 5.10b. The specific capacitance values obtained in Fig. 5.10b were calculated using the equations mentioned above. The experimental data obtained from galvanostatic charge-discharge are in good agreement with the experimental data obtained from cyclic voltammetry with OLC/Mn_3O_4 nanohybrid still exhibiting much better pseudocapacitive performance as compared to the other nanohybrid electrode materials. The OLC/Mn_3O_4 nanohybrid showed higher specific capacitance of 195 F g^{-1} followed by CNT/Mn_3O_4 with a specific capacitance of 180 F g^{-1} while that of GO/Mn_3O_4 was found to be ~ 160 F g^{-1}. The AC/Mn_3O_4 exhibited the least specific capacitance of

124 F g^{-1} compared to other nanohybrids at the current density of 0.1 A g^{-1} in aqueous 1 M Na_2SO_4 electrolyte. It is worth noting that the specific capacitance of pure Mn_3O_4 (without the presence of any carbon allotropes) was found to be ~ 69 F g^{-1} at the current density of 0.1 A g^{-1} (in aqueous 1 M Na_2SO_4 electrolyte) which was extremely smaller than that of the nanohybrid energy storage devices. Although the high specific capacitance observed from the nanohybrids originates from the contribution of Mn_3O_4, the conductivity of the nanohybrid electrodes also played a significant role. Thus, the carbon supports played a major role in the improvement of the pseudocapacitance of Mn_3O_4 as witnessed by fairly small specific capacitance seen from pure Mn_3O_4 (Fig. 5.10).

For a further understanding of the electrochemical behaviour of the prepared electrodes (i.e., OLC/Mn_3O_4, CNT/Mn_3O_4, GO/Mn_3O_4, AC/Mn_3O_4 nanohybrids and Mn_3O_4 nanoparticles), the GCD was performed at different current densities (0.1 to 10 A g^{-1}) current density as shown in Fig. 5.11. The C_{sp} of OLC/Mn_3O_4 nanohybrid as observed from Fig. 11a have decreased with an increase in current density with values ranging from 188 F g^{-1} (at 0.3 A g^{-1}) to 110 F g^{-1} (at 10 A g^{-1}). The C_{sp} of CNT/Mn_3O_4 nanohybrid as observed from Fig. 11b have decreased with an increase in current density with values ranging 167 F g^{-1} (at 0.3 A g^{-1}) to 88 F g^{-1} (at 10 A g^{-1}) whereas, the C_{sp} of GO/Mn_3O_4 nanohybrid as observed from Fig. 11c have decreased with an increase in current density with values ranging from 148 F g^{-1} (at 0.3 A g^{-1}) to 65 F g^{-1} (at 10 A g^{-1}). The C_{sp} of AC/Mn_3O_4 nanohybrid as observed from Fig. 11d have also decreased with an increase in current density with values ranging from 116 F g^{-1} (at 0.3 A g^{-1}) to 30 F g^{-1} (at 10 A g^{-1}) whereas that of pure Mn_3O_4 ranged from 53 F g^{-1} (at 0.3 A g^{-1}) to 10 F g^{-1} (at 10 A g^{-1}). It is worth mentioning that OLC/Mn_3O_4 nanohybrid exhibit low internal resistance even at the high current density compared to the other electrode materials, and this observation is also seen from the CV as shown in Fig. 5.9a.

The GCD curve of the GO/Mn_3O_4 shows more internal resistance as the cell voltage is towards 0.8 V indicating the resistivity of charges mobility at the electrode-electrolyte interface. The pseudocapacitive performances of these nanohybrid electrode materials with much higher specific capacitance as compared to the ones reported in the literature suggests that these electrode materials are suitable for high power energy storage applications. In conclusion, the OLC/Mn_3O_4 nanohybrid pseudocapacitor electrode has shown to be the best as compared to the nanohybrid pseudocapacitors arose from the combination of CNT, GO, and AC with Mn_3O_4 nanoparticle (CNT/Mn_3O_4, GO/Mn_3O_4, and AC/Mn_3O_4 nanohybrid, respectively).

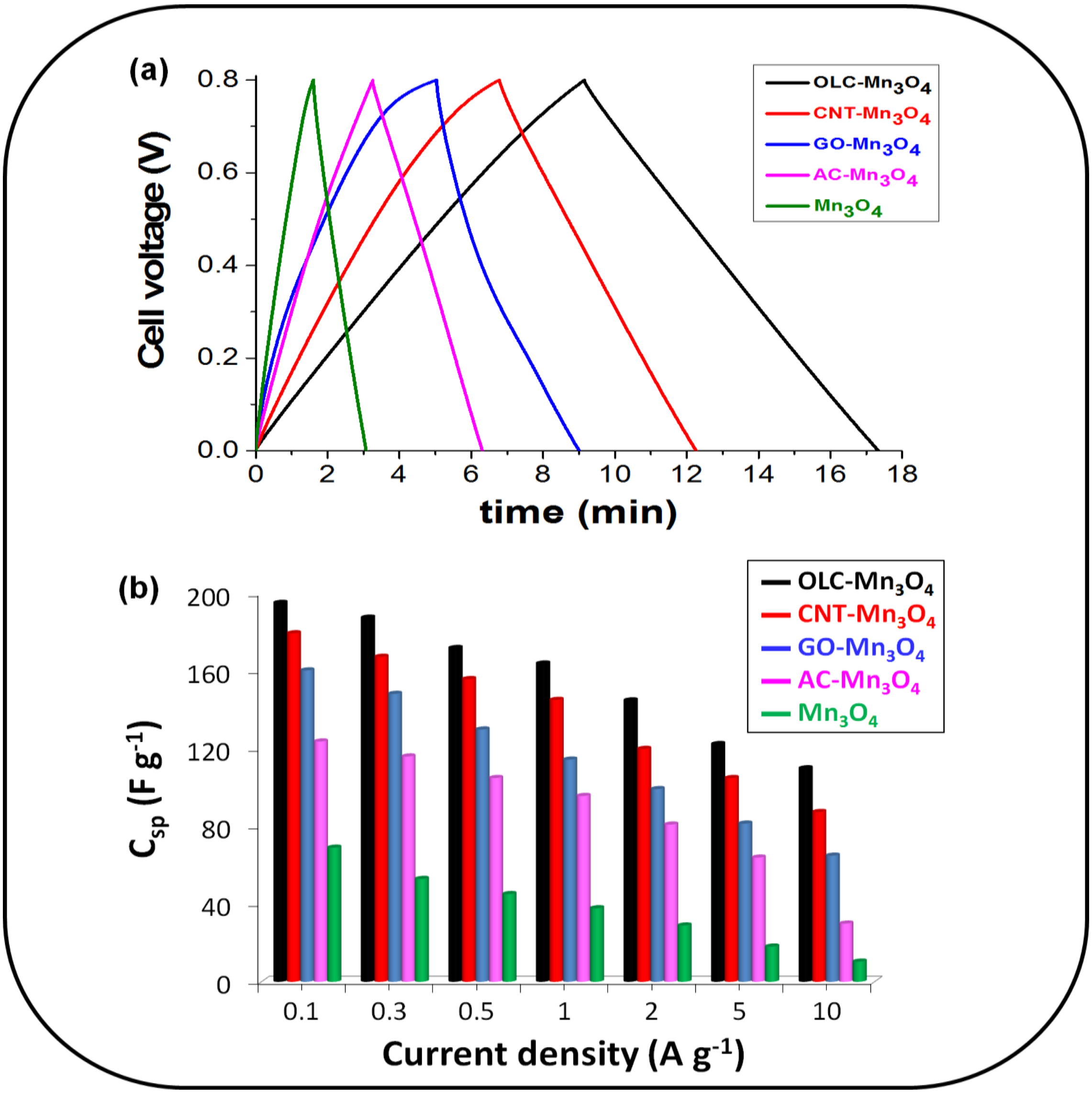

Figure 5.10: Comparative (a) galvanostatic charge-discharge curves at 0.3 A g^{-1} and (b) C_{sp} *vs.* current density plot, for OLC/Mn_3O_4, CNT/Mn_3O_4, GO/Mn_3O_4, AC/Mn_3O_4 nanohybrids and Mn_3O_4 in aqueous 1 M Na_2SO_4.

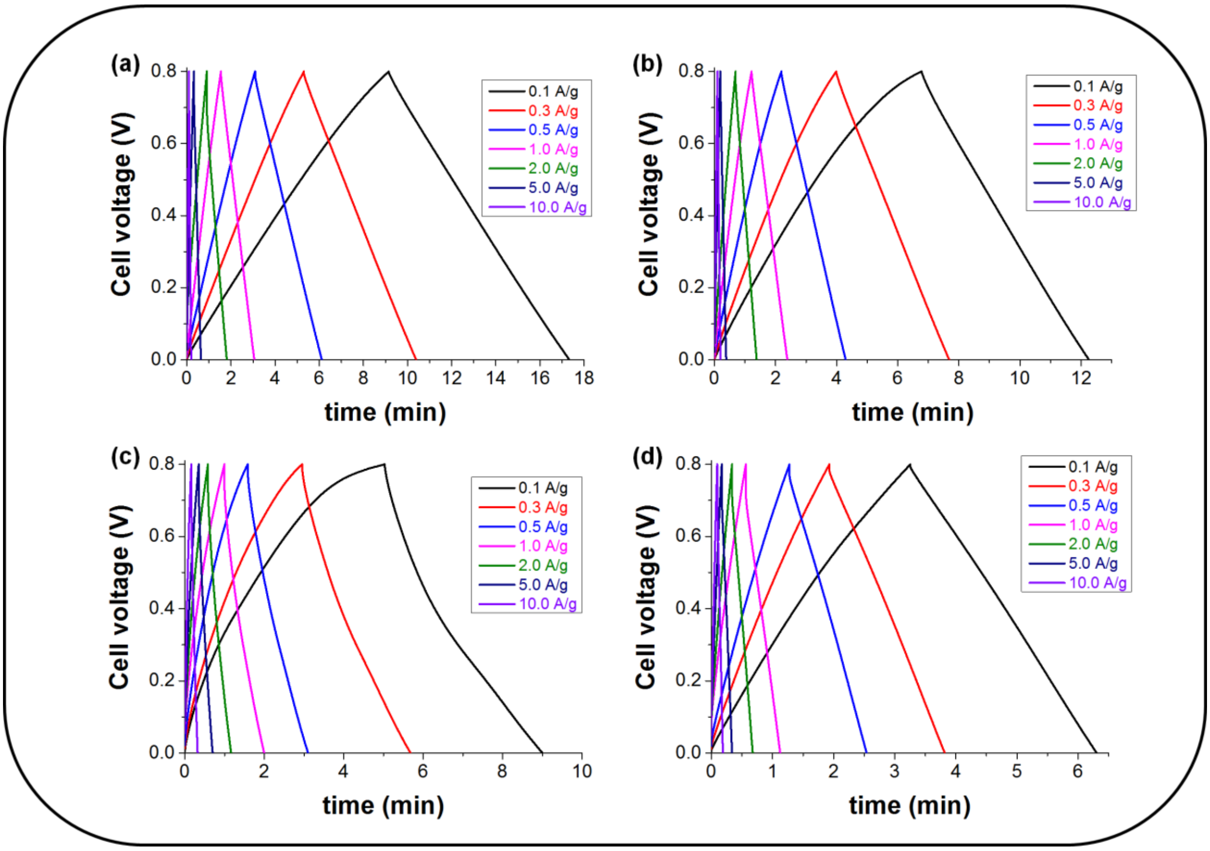

Figure 5.11: Comparison of galvanostatic charge-discharge curves for (a) OLC/Mn_3O_4, (b) CNT/Mn_3O_4, (c) GO/Mn_3O_4, and (d) AC/Mn_3O_4 nanohybrids at various current densities. Electrolyte: aqueous 1M Na_2SO_4.

Figure 5.12 shows a Ragone plot comparing energy and power densities for OLC/Mn_3O_4, CNT/Mn_3O_4, GO/Mn_3O_4, AC/Mn_3O_4 nanohybrids and Mn_3O_4. As showed from other electrochemical analysis such as CV and GCD, OLC/Mn_3O_4 nanohybrid continued leading with regard to the pseudocapacitive performance as compared to those of CNT/Mn_3O_4, GO/Mn_3O_4, AC/Mn_3O_4 nanohybrids and Mn_3O_4 based electrode materials. The maximum energy and power density of OLC/Mn_3O_4 nanohybrid are apparently higher with calculated values of 4.3 Wh kg^{-1} and 52 kW kg^{-1}, respectively. The maximum energy and power density values of CNT/Mn_3O_4 nanohybrid were found to be 3.9 Wh kg^{-1} and 33 kW kg^{-1}, respectively. The GO/Mn_3O_4 nanohybrid showed maximum energy and power density values of 3.6 Wh kg^{-1} and 24 kW kg^{-1}, respectively, whereas AC/Mn_3O_4

nanohybrid showed maximum energy and power density values of 2.8 Wh kg^{-1} and 18 kW kg^{-1}, respectively. A pure Mn_3O_4 nanoparticle showed maximum energy and power density values of 1.5 Wh kg^{-1} and 8 kW kg^{-1}, respectively. The electrochemical performance of the nanohybrids has consistently proved to be much better than those of the pure Mn_3O_4 indicating that indeed Mn_3O_4 coupled with suitable support, possess a great potential for its deployment in the high-power, energy storage devices. It is worth mentioning that these remarkable rate capabilities of the nanohybrid electrode materials are much higher than those reported in the literature, and this is due to the calcination process involved in synthesizing the Mn_3O_4 together with the presence of graphitic carbon in the nanohybrid electrode materials.

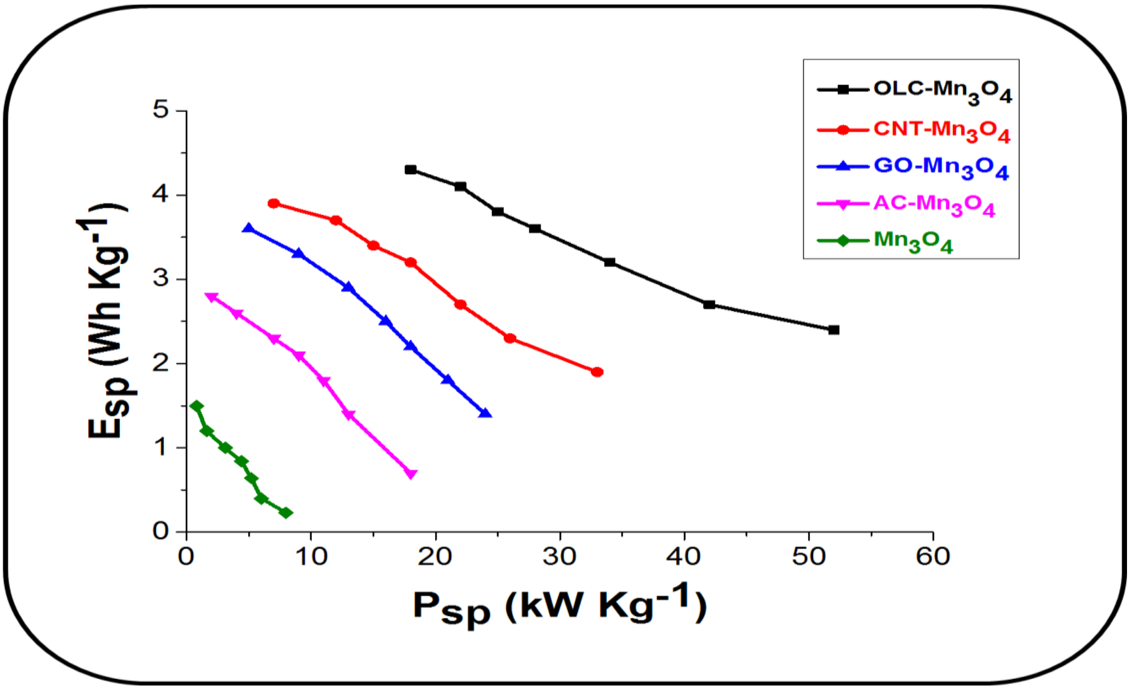

Figure 5.12: Ragone plot is indicating Energy vs. Power densities for OLC/Mn_3O_4, CNT/Mn_3O_4, GO/Mn_3O_4, AC/Mn_3O_4 nanohybrids and Mn_3O_4. Electrolyte: aqueous 1M Na_2SO_4.

5.2.5 Electrochemical Impedance Spectroscopy (EIS) analysis of various carbon/Mn_3O_4 based electrodes on Ni foam.

The electrochemical impedance spectroscopy (EIS) has gained popularity as a vital electrochemical characterization technique that can measure and give feedback on the electrical resistance of several systems such as ECs and LIBs [34]. In this study, EIS was employed to understand the solution phenomenon/mechanisms occurring at the electrode/electrolyte interface of the synthesised electrode materials and thus, EIS data were acquired prior and post-floating experiments as shown in Fig. 5.13 (measured in the frequency range of 100 kHz to 10 mHz in aqueous 1 M Na_2SO_4). Figure 5.13a shows a Nyquist plot comparison for the electrode materials (i.e., OLC/Mn_3O_4, CNT/Mn_3O_4, GO/Mn_3O_4, AC/Mn_3O_4 and Mn_3O_4) and the inset represents the expanded portion of the high-frequency region of the compared Nyquist plots. The equivalent distributed resistance (EDR), comprising of both the equivalent series resistance (ESR) and the ionic resistance within the porous structure (i.e., RC semicircle), was obtained by extrapolating the vertical portion of the plot to the real axis [35]. The OLC/Mn_3O_4 device shows a lower EDR value (12.1 Ω cm^2) compared to that of CNT/Mn_3O_4 (with the EDR value of 17.5 Ω cm^2), GO/Mn_3O_4 (with the EDR value of 23.5 Ω cm^2) and AC/Mn_3O_4 device (with the EDR value of 30.1 Ω cm^2). However, these EDR values are smaller than that of Mn_3O_4 alone (51.5 Ω cm^2) indicating the high resistivity of the metal oxide nanoparticles. Also, the RC semicircle for the OLC/Mn_3O_4 is slightly smaller (7.1 Ω cm^2) than that of the CNT/Mn_3O_4 (10.4 Ω cm^2), GO/Mn_3O_4 (14.1 Ω cm^2) and AC/Mn_3O_4 (18.6 Ω cm^2). Nevertheless, these values are smaller than those calculated for Mn_3O_4 nanoparticles (44.2 Ω cm^2), meaning that ionic resistance within the porous structure of pure Mn_3O_4 decreased for the nanohybrid pseudocapacitor. Bode plot, (plotted as a function of frequency) is one of the crucial ways of representing the gain and phase of an electrochemical system. It is referred to as the frequency domain behaviour of a system. Figure 5.13b shows a Bode plot comparison for the nanohybrid electrode materials (i.e., OLC/Mn_3O_4, CNT/Mn_3O_4, GO/Mn_3O_4 and AC/Mn_3O_4) as well as pure Mn_3O_4. The pseudocapacitive behavior of the nanohybrid devices was emphasized as seen from the Bode plots. The phase angle for the OLC/Mn_3O_4 nanohybrid is -74^o, CNT/Mn_3O_4 nanohybrid is -69^o, GO/Mn_3O_4 nanohybrid is -65^o, AC/Mn_3O_4 nanohybrid is -66^o and Mn_3O_4 are -66^o. This values may further be compared to that of a pure OLC with a phase angle of -85^o (the value close to -90^o for an ideal EDLC) as shown in Chapter 4 (Fig. 4.13b). The knee frequency (f_o, ϕ = -45°) describes the maximum frequency at which the capacitive behavior is dominant, and also measure the power capability of ECs. The higher the $f_{o,}$ the faster the supercapacitor can be charged and discharged or the higher the power density is achieved from the supercapacitor.

The values of the f_o were *ca.* 21 Hz for the OLC/Mn_3O_4 (time constant ~ 48 ms) and *ca.* 18 Hz (time constant ~ 55 ms) for the CNT/Mn_3O_4The GO/Mn_3O_4 displayed f_o value of *ca.* 14 Hz (time constant ~ 71 ms) and AC/Mn_3O_4 *ca.* 12 Hz (time constant ~ 83 ms). These values further corroborate the higher-power performance of the nanohybrid electrode materials. Also, these results show that most of the stored energy in the nanohybrid electrode materials is accessible with power output available on millisecond time scale. It should be worth noting that most commercially available supercapacitors, including those designed for higher power applications, operate at frequencies less than 1 Hz [36]. For a better understanding of the capacitive behaviour of the devices, the EIS data (presented in Fig. 5.13a) were fitted with the electrical equivalent circuit (EEC). The EEC comprise of Voigt RC elements, involving a series resistance (R_s), charge-transfer resistance (R_{ct}) and constant phase elements (CPE or Q) as shown in Fig. 5.13c. The parameters obtained from this analysis are tabulated and presented in Table 5.1.

From Table 5.1, the R_s value of the OLC/Mn_3O_4 (1.64 Ohm), is lower than that of the CNT/Mn_3O_4 (2.38 Ohm), Mn_3O_4 (2.45 Ohm), GO/Mn_3O_4 (3.41 Ohm) and AC/Mn_3O_4 (3.93 Ohm). Also, the R_{ct} value of the OLC/Mn_3O_4 (4.05 Ohm) is lower than that of the CNT/Mn_3O_4 (5.78 Ohm), GO/Mn_3O_4 (7.98 Ohm), AC/Mn_3O_4 (10.05 Ohm) and Mn_3O_4 (15.97 Ohm). These results further suggest that the OLC component serves to reduce the internal resistance of the OLC/Mn_3O_4. Thereby, improving the conductivity and capacitance of the OLC/Mn_3O_4-based symmetric pseudocapacitor as compared to other carbon supports (i.e., CNT, GO, and AC) with respect to their subsequence nanohybrid (CNT/Mn_3O_4, GO/Mn_3O_4, and AC/Mn_3O_4) electrode materials. As shown from Table 5.1 and Fig. 5.13, Mn_3O_4 electrode material seem to behave in such a way of resisting charge mobility within its internal structure, thus giving poor electrochemical performances as compared to the Mn_3O_4 decorated on a carbon support (nanohybrids). The equation 5.1 gives the impedance of CPE [37]:

$$Z_{CPE} = \frac{1}{[Q(jw)^n]} \tag{5.1}$$

where Q represents the frequency-independent constant relating to the electroactive surface properties, w is the radial frequency; the exponent n arises from the slope of log Z vs. log f (and has values $-1 \leq n \leq 1$). If n = 0, the CPE behaves like a pure resistor; $n = 1$, CPE acts as a pure capacitor, $n = -1$, CPE behaves as an inductor; while $n = 0.5$ corresponds to Warburg impedance (Z_w) which is related to the diffusion of the ions. The n values observed for these electrodes are > 0.75, explicitly confirming porous nanohybrid electrode materials with pseudocapacitive behaviour, corroborating the CV and GCD data of Fig. 5.10 and Fig. 5.13, respectively.

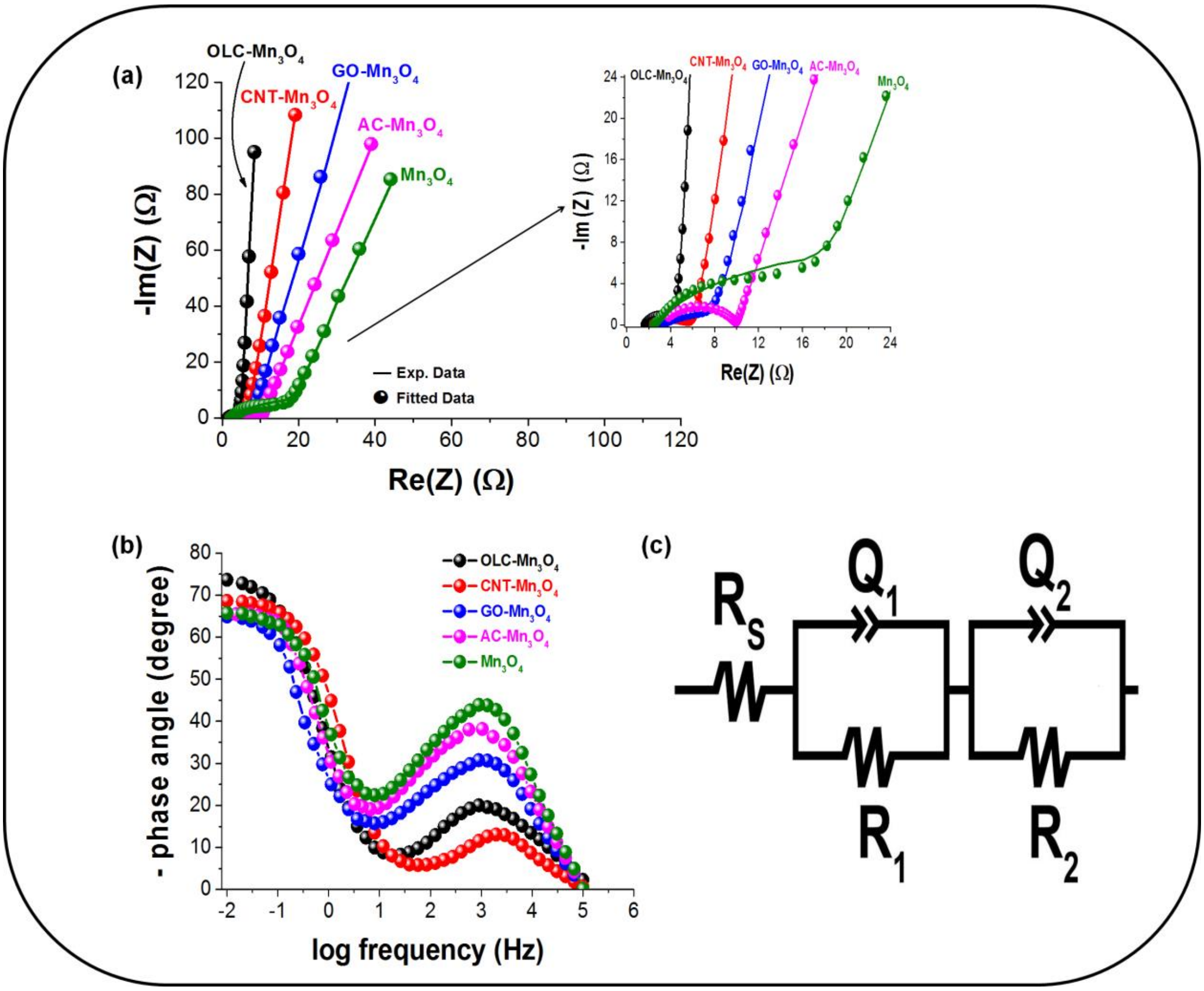

Figure 5.13: Comparative (a) Nyquist, (b) Bode plots for OLC/Mn_3O_4, CNT/Mn_3O_4, GO/Mn_3O_4, and AC/Mn_3O_4 nanohybrids in aqueous 1 M Na_2SO_4 and (c) The Electrical Equivalent Circuit (EEC) used to fit the experimental EIS data. The inset in (a) is the expanded portion of the high-frequency region.

Table 5.1: Comparative fitting parameters for the EIS data for the Mn_3O_4, OLC/Mn_3O_4, CNT/Mn_3O_4, GO/Mn_3O_4, and AC/Mn_3O_4 nanohybrids using the Voigt equivalent circuit.

Parameter	**OLC/Mn_3O_4**	**CNT/Mn_3O_4**	**GO/Mn_3O_4**	**AC/Mn_3O_4**	**Mn_3O_4**
R_s / Ω	1.64±0.72	2.38±0.09	3.41±0.56	3.93± 0.93	2.45±0.16
Q_1 / mF.s$^{(\alpha-1)}$	2.62±0.13	2.39±0.99	1.36±0.71	1.03±0.11	0.73±0.14
n_1	0.84±0.08	0.82±0.23	0.79±0.14	0.77±0.21	0.75±0.31
R_{ct1} / Ω	4.05±0.84	5.78±0.64	7.98±1.29	10.05±0.12	15.97±1.29
Q_2 / mF.s$^{(\alpha-1)}$	3.78±0.29	3.08±0.23	5.00±1.64	1.54±0.07	2.33±0.69
n_2	0.79±0.17	0.76±1.94	0.68±0.18	0.80±0.2	0.61±0.14
R_{ct2} / Ω	7.93±1.27	9.36±1.38	13.19±2.06	15.38±0.48	24.58±4.94

It has been established that voltage-holding (also known as floating) experiments represent a reliable analysis method for determining the long-term stability of electrochemical capacitor electrodes [38], [39]. In this study, the stability for OLC/Mn_3O_4, CNT/Mn_3O_4, GO/Mn_3O_4, and AC/Mn_3O_4 nanohybrid was interrogated using voltage-holding and the EIS data was required to understand the behavior of the electrodes prior and post voltage-holding experiments as shown in Fig. 5.14. The OLC/Mn_3O_4 nanohybrid exhibited excellent stability during voltage-holding over 50 h at 1 A g^{-1} as represented by a small internal resistance after voltage-holding (Fig. 5.14a). Subsequently, CNT/Mn_3O_4, GO/Mn_3O_4, and AC/Mn_3O_4 nanohybrid exhibited a decrease in stability as compared to the OLC/Mn_3O_4 nanohybrid as depicted in Fig. 5.14b-d, respectively. The better performance of OLC/Mn_3O_4 nanohybrid has been illustrated by the gradual decrease in the specific capacitance as the current is kept constant at a high potential, retaining *ca.* 134 F g^{-1} (i.e., approximately 83% of its initial capacitance of *ca.* 161 F g^{-1}). The stability of the CNT/Mn_3O_4 nanohybrid showed a steady decrease in specific capacitance as compared to that of OLC/Mn_3O_4 after 50 h voltage-holding, retaining *ca.* 118 F g^{-1} (i.e., approximately 80% of its initial capacitance of *ca.* 146 F g^{-1}). This excellent stability of the OLC/Mn_3O_4 and CNT/Mn_3O_4 nanohybrids showed that these devices can be charged and discharged without significant deterioration in its efficiency (Fig. 5.15). The stability of GO/Mn_3O_4 and AC/Mn_3O_4 nanohybrids exhibited much decrease in specific capacitance compared to OLC/Mn_3O_4 and CNT/Mn_3O_4 after 50 h voltage-holding. GO/Mn_3O_4 retained specific capacitance of 68 F g^{-1} (i.e., approximately 59% of its initial capacitance of 116 F g^{-1}) and AC/Mn_3O_4 retained 51 F g^{-1} (i.e., approximately 53% of its original capacitance of 96 F g^{-1}). The above values correspond with a maximum specific energy of 4.3 Wh kg^{-1} and an excellent power density of 52 kW kg^{-1} for OLC/Mn_3O_4 and a maximum specific energy of 3.9 Wh kg^{-1} and an excellent power density of 33 kW kg^{-1} for CNT/Mn_3O_4 nanohybrid. The above values for GO/Mn_3O_4 nanohybrid correspond with a maximum specific energy of 3.6 Wh kg^{-1} and power density of 24 kW kg^{-1}, whereas, the AC/Mn_3O_4 nanohybrid values correspond with the maximum specific energy of 2.8 Wh kg^{-1} and power density of 18 kW kg^{-1}. It is worth noting that although the nanohybrids performed differently as compared to each other, their pseudocapacitive performances are still much better than some values obtained in the literature. The enhanced performance of these hybrid electrochemical capacitor devices is due to the combination of the high electrical conductivity of various carbon supports with the highly reversible redox reactions (pseudocapacitance) arising from the nanostructured Mn_3O_4 material. This Chapter has shown that the electrochemical performance of Mn_3O_4 nanomaterial is enhanced by the use of various conductive carbon supports and thus improving its stability through the synergistic effect resulting from the porous carbon with Mn_3O_4.

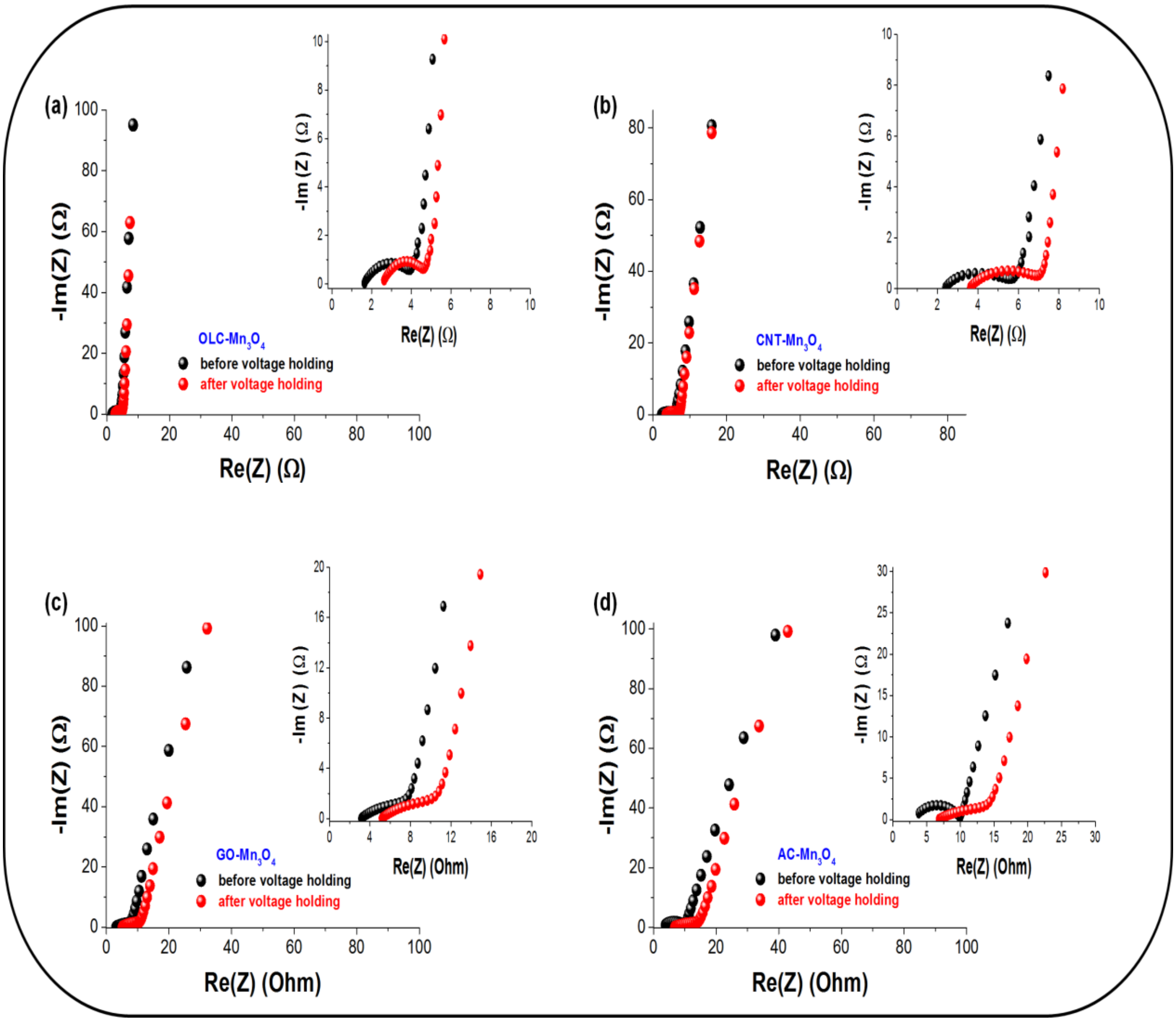

Figure 5.14: Nyquist plots for (a) OLC/Mn_3O_4, (b) CNT/Mn_3O_4, (c) GO/Mn_3O_4, and (d) AC/Mn_3O_4 nanohybrids before and after voltage-holding in aqueous 1 M Na_2SO_4. The inset in (a-d) is the expanded portion of the high-frequency region.

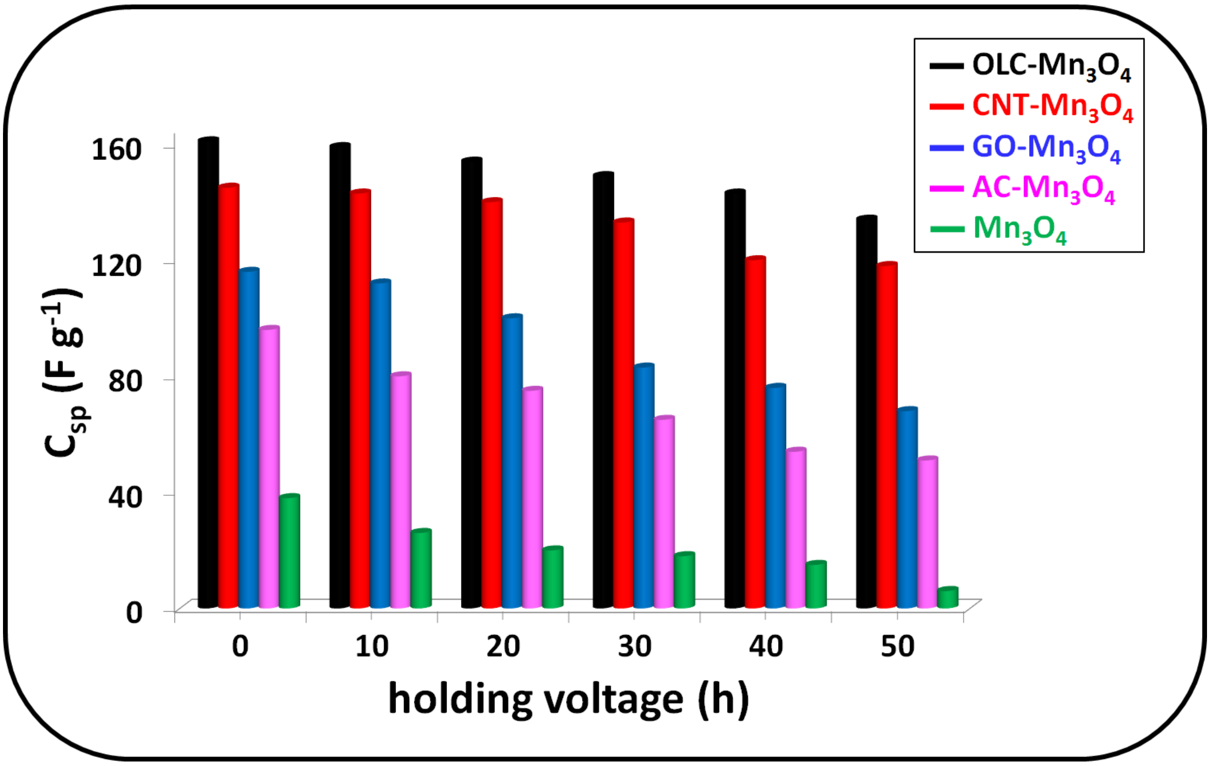

Figure 5.15: A 50 h voltage-holding experimental comparison for OLC/Mn_3O_4, CNT/Mn_3O_4, GO/Mn_3O_4, and AC/Mn_3O_4 nanohybrids at 0.8 V cell voltage. Electrolyte: aqueous 1 M Na_2SO_4.

The as-discussed results from Fig. 5.8 confirms the trend of electrochemical performance observed from CV, GCD, and EIS data, with the OLC/Mn_3O_4 (due to the particle small particle size and its crystallinity) giving the best specific capacitance and followed by the CNT/Mn_3O_4 nanohybrids (due to its crystallinity). Subsequently, GO/Mn_3O_4 and AC/Mn_3O_4 nanohybrid materials exhibit much smaller specific capacitance than the nanohybrids mentioned above but still shows an improved specific capacitance compared to the pure Mn_3O_4 nanoparticles (without carbon sample).

5.3 Conclusion

This work investigated the electrochemical performance of a highly graphitized onion-like carbon (OLC), carbon nanotube (CNT), graphene oxide (GO) and activated carbon (AC) decorated with nanostructured tetragonal hausmannite (Mn_3O_4) particles (i.e., OLC/Mn_3O_4, CNT/Mn_3O_4, GO/Mn_3O_4 and AC/Mn_3O_4), and their application in a symmetrical pseudocapacitor device. The results demonstrate that all nanohybrid electrode materials have better electrochemical performance, regarding specific capacitance and rate capability as energy storage devices. Among the four synthesized nanohybrid electrode materials, OLC/Mn_3O_4 has shown to have much better pseudocapacitive performance as compared to other nanohybrid electrode materials and followed by CNT/Mn_3O_4 GO/Mn_3O_4, and AC/Mn_3O_4 nanohybrid, respectively. The OLC/Mn_3O_4 device gave an excellent electrochemical performance with a maximum specific capacitance of ~ 195 F g^{-1}, the specific energy density of 4.3 Wh kg^{-1}, the power density of 52 kW kg^{-1}. This nanohybrid material also shows capacity retention upon long-hour voltage-holding and cycling, very low equivalent distributed resistance Although, the OLC/Mn_3O_4 nanohybrid exhibited much better performance than the rest, all the nanohybrids (CNT/Mn_3O_4 with maximum specific capacitance, energy and power density of 180 F g^{-1}, 3.9 Wh kg^{-1} and 33 kW kg^{-1}, respectively, GO/Mn_3O_4 with maximum specific capacitance, energy and power density of 160 F g^{-1}, 3.6 Wh kg^{-1} and 24 kW kg^{-1}, respectively and AC/Mn_3O_4 with maximum specific capacitance, energy and power density of 124 F g^{-1}, 2.8 Wh kg^{-1} and 18 kW kg^{-1}, respectively) demonstrated to be better electrode materials for high power ECs device. The symmetric pseudocapacitor devices exhibited "knee frequency" f_o values of *ca.* 21 Hz for the OLC/Mn_3O_4 (time constant ~ 48 ms) and *ca.* 18 Hz (time constant ~ 55 ms) for the CNT/Mn_3O_4The GO/Mn_3O_4 displayed f_o value of *ca.* 14 Hz (time constant ~ 71 ms) and AC/Mn_3O_4 *ca.* 12 Hz (time constant ~

83 ms). These results show that most of the stored energy in the nanohybrid electrode materials is accessible with power output available on millisecond time scale.

By the use of these nanohybrid electrode materials, the main limitation of Mn_3O_4 electrode material, namely its poor electrical conductivity was overcome, and we managed to exploit the main advantages (i.e., low-cost, high abundance, and environmentally-friendliness) for application in high-power energy storage devices. Indeed, it has been shown that the electrochemical properties of OLC/Mn_3O_4, CNT/Mn_3O_4, GO/Mn_3O_4 and AC/Mn_3O_4 nanohybrid electrode materials as high-rate energy storage devices have great potential for the development of high power aqueous-based electrochemical capacitors that are deployed for high-power technological applications.

References

[1] C. Burda, X. Chen, R. Narayanan, and M. A. El-sayed, "Chemistry and Properties of Nanocrystals of Different Shapes," *Chem. Rev.*, vol. 105, no. 4, pp. 1025– 1102, 2005.

[2] Y. Tan, L. Meng, Q. Peng, and Y. Li, "One-dimensional single-crystalline Mn3O4 nanostructures with tunable length and magnetic properties of Mn3O4 nanowires.," *Chem. Commun. (Camb).*, vol. 47, no. 4, pp. 1172–4, Jan. 2011.

[3] D. Yan, S. Cheng, R. F. Zhuo, J. T. Chen, J. J. Feng, H. T. Feng, H. J. Li, Z. G. Wu, J. Wang, and P. X. Yan, "Nanoparticles and 3D sponge-like porous networks of manganese oxides and their microwave absorption properties.," *Nanotechnology*, vol. 20, no. 10, p. 105706, Mar. 2009.

[4] C. Largeot, C. Portet, J. Chmiola, P. Taberna, Y. Gogotsi, and P. Simon, "Relation between the Ion Size and Pore Size for an Electric Double-Layer Capacitor," pp. 2730–2731, 2008.

[5] C. J. Jafta, F. Nkosi, L. le Roux, M. K. Mathe, M. Kebede, K. Makgopa, Y. Song, D. Tong, M. Oyama, N. Manyala, S. Chen, and K. I. Ozoemena, "Manganese oxide/graphene oxide composites for high-energy aqueous asymmetric electrochemical capacitors," *Electrochim. Acta*, pp. 2–7, Jul. 2013.

[6] A. T. Chidembo, S. H. Aboutalebi, K. Konstantinov, C. J. Jafta, H. K. Liu, and K. I. Ozoemena, "In situ engineering of urchin-like reduced graphene oxide–Mn2O3–Mn3O4 nanostructures for supercapacitors," *RSC Adv.*, vol. 4, no. 2, p. 886, 2014.

[7] R. Borgohain, J. P. Selegue, and Y.-T. Cheng, "Ternary composites of delaminated-MnO 2 /PDDA/functionalized-CNOs for high-capacity supercapacitor electrodes," *J. Mater. Chem. A*, vol. 2, no. 47, pp. 20367–20373, Oct. 2014.

[8] Z.-S. Wu, W. Ren, D.-W. Wang, F. Li, B. Liu, and H.-M. Cheng, "High-energy MnO2 nanowire/graphene and graphene asymmetric electrochemical capacitors.," *ACS Nano*, vol. 4, no. 10, pp. 5835–42, Oct. 2010.

[9] V. Subramanian, H. Zhu, R. Vajtai, P. M. Ajayan, and B. Wei, "Hydrothermal synthesis and pseudocapacitance properties of MnO2 nanostructures," *J. Phys. Chem. B*, vol. 109, no. 43, pp. 20207–20214, 2005.

[10] Z. Yu, B. Duong, D. Abbitt, and J. Thomas, "Highly ordered MnO_2 nanopillars for enhanced supercapacitor performance.," *Adv. Mater.*, vol. 25, no. 24, pp. 3302–6, Jun. 2013.

[11] Y. Wang, S. F. Yu, C. Y. Sun, T. J. Zhu, and H. Y. Yang, "MnO2/onion-like carbon nanocomposites for pseudocapacitors," *J. Mater. Chem.*, vol. 22, no. 34, p. 17584, 2012.

[12] P. Li, C. Nan, Z. Wei, J. Lu, Q. Peng, and Y. Li, "Mn3O4 nanocrystals: Facile synthesis, controlled assembly, and application," *Chem. Mater.*, vol. 22, no. 14, pp. 4232–4236, 2010.

[13] R. Dong, Q. Ye, L. Kuang, X. Lu, Y. Zhang, X. Zhang, G. Tan, Y. Wen, and F. Wang, "Enhanced supercapacitor performance of Mn3O4 nanocrystals by doping transition-metal ions," *ACS Appl. Mater. Interfaces*, vol. 5, pp. 9508–9516, 2013.

[14] D. Weingarth, M. Zeiger, N. Jäckel, M. Aslan, G. Feng, and V. Presser, "Graphitization as a Universal Tool to Tailor the Potential-Dependent Capacitance of Carbon Supercapacitors," *Adv. Energy Mater.*, vol. 4, no. 13, pp. 1–13, 2014.

[15] A. T. Chidembo, K. I. Ozoemena, B. O. Agboola, V. Gupta, G. G. Wildgoose, and R. G. Compton, "Nickel(ii) tetra-aminophthalocyanine modified MWCNTs as potential nanocomposite materials for the development of supercapacitors," *Energy*

Environ. Sci., vol. 3, no. 2, p. 228, 2010.

[16] S. Nagamuthu, S. Vijayakumar, and G. Muralidharan, “Synthesis of Mn3O4-Amorphous Carbon Nanoparticles as ElectrodeMaterial for High Performance Supercapacitor Applications,” *energy & Fuels*, vol. 27, pp. 3508–3515, 2013.

[17] L. Peng, J. Zhang, Z. Xue, B. Han, J. Li, and G. Yang, “Large-pore mesoporous Mn3O4 crystals derived from metal-organic frameworks.,” *Chem. Commun. (Camb).*, vol. 49, no. 99, pp. 11695–7, 2013.

[18] K. Bogdanov, A. Fedorov, V. Osipov, T. Enoki, K. Takai, T. Hayashi, V. Ermakov, S. Moshkalev, and A. Baranov, “Annealing-induced structural changes of carbon onions: High-resolution transmission electron microscopy and Raman studies,” *Carbon N. Y.*, vol. 73, pp. 78–86, Jul. 2014.

[19] H. W. Park, H. J. Lee, S.-M. Park, and K. C. Roh, “Synthesis and Electrochemical Properties of Mn 3 O 4 Nanocrystals with Controlled Morphologies Grown from Compact Ion Layers,” *RSC Adv.*, vol. DOI: 10.10, 2016.

[20] B. P. Vinayan, R. Nagar, V. Raman, N. Rajalakshmi, K. S. Dhathathreyan, and S. Ramaprabhu, “Synthesis of graphene-multiwalled carbon nanotubes hybrid nanostructure by strengthened electrostatic interaction and its lithium ion battery application,” *J. Mater. Chem.*, vol. 22, no. 19, p. 9949, 2012.

[21] M. F. L. De Volder, S. H. Tawfick, R. H. Baughman, and a J. Hart, “Carbon nanotubes: present and future commercial applications.,” *Science*, vol. 339, no. 6119, pp. 535–9, 2013.

[22] L. Wang, Y. Li, Z. Han, L. Chen, B. Qian, X. Jiang, J. Pinto, and G. Yang, “Composite structure and properties of Mn3O4/graphene oxide and Mn3O4/graphene,” *J. Mater. Chem. A*, no. 1, pp. 8385–8397, 2013.

[23] M. Bernard, A. H. Goff, B. V. Thi, C. Physique, U. Pierre, and S. C. De Torresi, "ELECTROCHEMICAL SCIENCE AND TECHNOLOGY: Electrochromic Reactions in Manganese Oxides !.," *J. Electrochem. Soc.*, vol. 140, no. 11, pp. 3065–3070, 1993.

[24] Y. Wang, D. C. Alsmeyer, and R. L. Mccreery, "Raman spectroscopy of carbon materials: structural basis of observed spectra," *Carbon N. Y.*, no. 10, pp. 557–563, 1990.

[25] G. Dresselhaus, M.S. Dresselhaus, *Topics in applied physics*. Berlin: Springer-Verla, 1982.

[26] a Cuesta, P. Dhamelincourt, and J. Laureyns, "Raman microprobe studies on carbon materials," *Carbon N. Y.*, vol. 32, no. 8, pp. 1523–1532, 1994.

[27] T. Jawhari, A. Roid, and J. Casado, "Raman spectroscopiccharacterization of some commercially available carbon black materials," *Carbon N. Y.*, vol. 33, no. 11, pp. 1561–1565, 1995.

[28] A. Sadezky, H. Muckenhuber, H. Grothe, R. Niessner, and U. P??schl, "Raman microspectroscopy of soot and related carbonaceous materials: Spectral analysis and structural information," *Carbon N. Y.*, vol. 43, no. 8, pp. 1731–1742, 2005.

[29] B. Dippel, H. Jander, and J. Heintzenberg, "NIR FT Raman spectroscopic study of flame soot," *Phys. Chem. Chem. Phys.*, vol. 1, no. 20, pp. 4707–4712, 1999.

[30] D. P. Dubal, D. S. Dhawale, R. R. Salunkhe, V. J. Fulari, and C. D. Lokhande, "Chemical synthesis and characterization of Mn3O4 thin films for supercapacitor application," *J. Alloys Compd.*, vol. 497, no. 1–2, pp. 166–170, 2010.

[31] D. Yang and M. Wang, "Syntheses and characterization of well-crystallized birnessite," *Chem. Mater.*, vol. 13, no. 8, pp. 2589–2594, 2001.

[32] H. Zhang, D. Hines, and D. L. Akins, “Synthesis of a nanocomposite composed of reduced graphene oxide and gold nanoparticles.,” *Dalton Trans.*, vol. 43, no. 6, pp. 2670–5, 2014.

[33] B. Wang, J. Park, C. Wang, H. Ahn, and G. Wang, “Mn3O4 nanoparticles embedded into graphene nanosheets: Preparation, characterization, and electrochemical properties for supercapacitors,” *Electrochim. Acta*, vol. 55, no. 22, pp. 6812–6817, 2010.

[34] S. Brockman, “Basics of Electrochemical Impedance Spectroscopy,” *Appl. note*, no. 1, pp. 1–13, 2012.

[35] D. Z. S. Dr. Stryzhakova N., Dr.Maletin Y., “Testing methodology manual,” 2012.

[36] J. R. Miller, “Battery-Capacitor Power Source for Digital Communication-Simulations Using Advanced Electrochemical Capacitors,” *Electrochem. Soc. Proc. Ser.*, vol. PV95–29, pp. 246–254, 1996.

[37] M. E. Orazem, J.-B. Jorcin, N. Pébère, and B. Tribollet, “CPE analysis by local electrochemical impedance spectroscopy,” *Electrochim. Acta*, vol. 51, no. 8, pp. 1473–1479, 2006.

[38] D. Weingarth, a. Foelske-Schmitz, and R. Kötz, “Cycle versus voltage hold – Which is the better stability test for electrochemical double layer capacitors?,” *J. Power Sources*, vol. 225, pp. 84–88, Mar. 2013.

[39] P. Ratajczak, K. Jurewicz, and F. Béguin, “Factors contributing to ageing of high voltage carbon/carbon supercapacitors in salt aqueous electrolyte,” *J. Appl. Electrochem.*, vol. 44, no. 4, pp. 475–480, Nov. 2013.

Chapter 6: Graphene Oxide/Nickel (II)Tetraaminophthalocyanine (GO/NiTAPc) Composite as Pseudocapacitor Material[3]

[3]The following publication resulted from part of the research work presented in this chapter and is not referenced further:
K. Makgopa, P. M. Ejikeme, and K. I. Ozoemena, Graphene oxide-modified nickel (II) tetra-aminophthalocyanine nanocomposites for high-power symmetric pseudocapacitor, *Electrochemica Acta*, (**Accepted**)

6.1 Introduction

Thus far, the role of carbon allotropes as the prime electrode material for ECs has been extensively emphasized especially in Chapter 2, 4 and 5. In this chapter, Graphene Oxide (GO) has been selected as the template of choice and its interaction with transition metal phthalocyanines (MPc's) is interrogated. The interest on GO began after Graphene, a two-dimensional honeycomb lattice of sp^2-bonded carbon atoms brought to general attention in 2004 by Novoselov and Geim [1], displayed a significantly lower capacitance value. The poor performance of graphene results from aggregation, agglomeration, and possible poor wetting by various electrolytes. Several researcher highly esteemed graphene more than graphene oxide, due to its high theoretical surface area (2630 m^2/g), high electrical conductivity, high (electro)chemical stability, and excellent mechanical properties [2]–[4]. To maintain a high surface area of the assembled, macroscopic electrode and avoiding graphene restacking due to van der Waals interactions between the layers, remains a major challenge [4] and thus, graphene oxide (GO) has been considered as an electrode material instead of pure graphene [5], [6]. GO is an intermediate product during the synthesis of graphene and has particularly attracted attention mainly due to its cheap production on a large scale from graphite through modification of Hummer's method [7], [8]. GO can be in situ activated to show a large specific surface area via ion insertion in organic electrolytes yielding up to 220 F/g (in 1 M TEA-BF_4) [9].

Transition-metal phthalocyanines (MPc's) as electrode active materials have been introduced as pseudocapacitors [10], [11]. A significant aspect of the development of advanced ECs is the improvement of their energy density without sacrificing their high power density and cycle ability by designing composite material with high surface area, excellent conductivity, and proper pore size distribution.

Metallophthalocyanine (MPc) complexes and their derivatives are well-known classes of N4-macrocyclic metal compounds with attractive physical and chemical properties [12]. They have been widely studied for a possible range of technological applications such as electrochemical capacitors, sensors, field effect transistors photocatalysis and electrocatalysts [13]–[16], see chapter 2. MPc complexes such as nickel (II) tetraaminophthalocyanine (NiTAPc) have been supported on multi-walled carbon nanotubes (MWCNTs) and tested as a pseudocapacitance device in 1 M H_2SO_4 electrolyte and has shown exciting electrochemical capacitive performance [17], [18]. These promising results have motivated us to investigate supercapacitors devices based on GO and NiTAPc. The efficient combination of GO with NiTAPc is expected to prevent restacking and also improves the conductivity of the composite thereby leading to the improved electrochemical performance of the electrode material.

6.2 Results and Discussion

6.2.1 SEM, TEM, XRD and UV-vis analysis

In this study, we examined the morphologies of GO, NiTAPc, and GO/NiTAPc composite by SEM and TEM. Fig. 6.1a-d shows the SEM images of exfoliated GO sheets, NiTAPc nanoparticles, and GO/NiTAPc composite with a diameter of several hundred nanometers to a few micrometers. Compared with GO sheets (Fig. 1a) and NiTAPc particles (Fig. 6.1b), GO/NiTAPc composite displays an obviously different morphology (Fig 1c at low magnification and Fig. 1d at high magnification) to that of its precursors, which showed successful decoration of NiTAPc on the GO sheets. An efficient overlapping is achieved that in some cases give isolated composite structures. The flakes of exfoliated GO appear thicker and with a rounded morphology which provides a direct demonstration on the π−π stacking interaction. It is evident from the SEM images of the GO/NiTAPc composite (Fig. 6.1c, d) that the nanoparticles of the NiTAPc were randomly scattered on the surface of the graphene oxide sheets.

Fig. 6.2a-c shows the TEM images of exfoliated GO sheets, NiTAPc particles, and GO/NiTAPc composite. The black spots in Fig. 6.2c illustrate the adsorption of NiTAPc molecules on GO sheets. The TEM results are in agreement with those obtained from SEM. Investigations have revealed that the self-assembly of the conjugated molecular systems via intermolecular π−π interactions can form structures with different morphologies [18], [19]. Hence, elaborate characterizations tools are of a great deal in comprehending the interaction of the as-synthesized composite material.

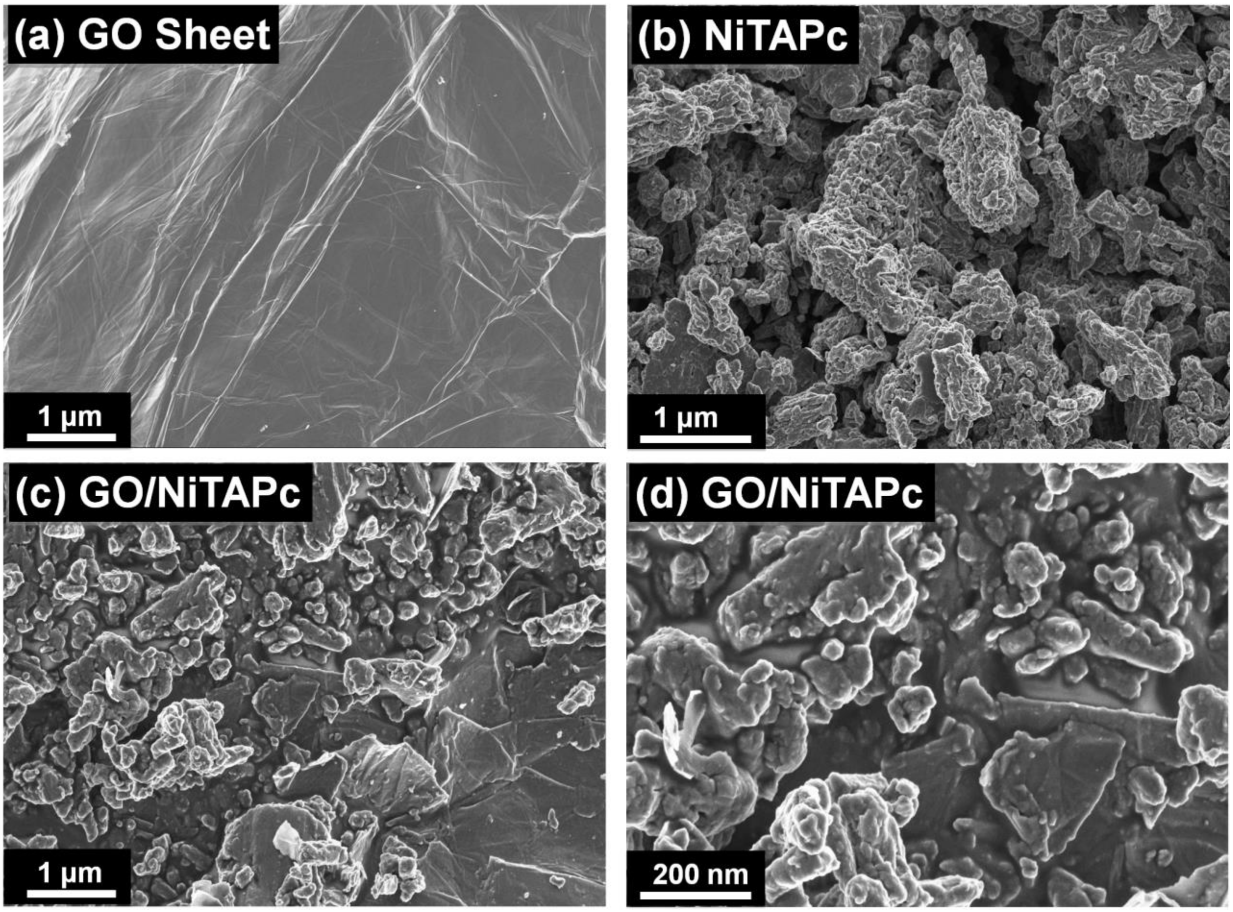

Figure 6.1: SEM images of (a) GO, (b) NiTAPc, (c) GO/NiTAPc composite (low mag.) and (d) GO/NiTAPc composite (high mag.)

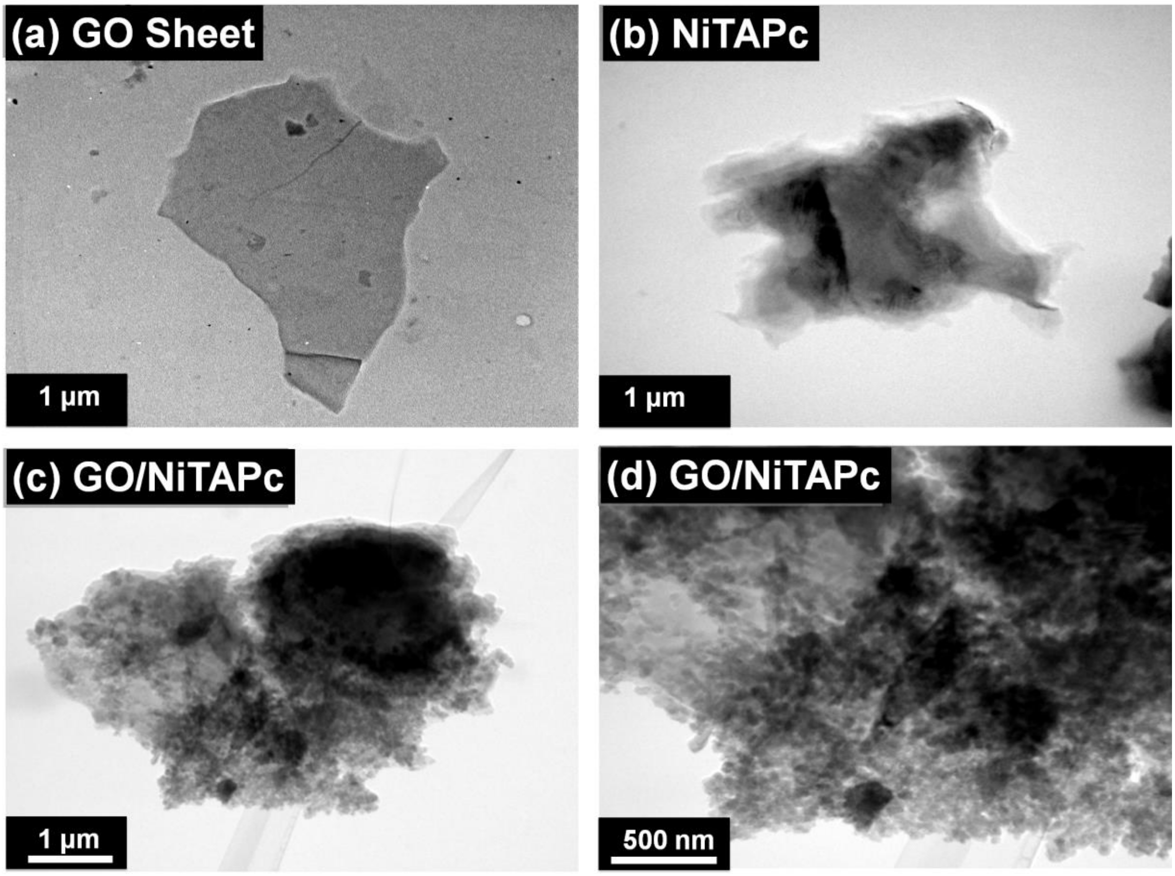

Figure 6.2: TEM images of (a) GO, (b) NiTAPc, (c) GO/NiTAPc composite (low mag.) and GO/NiTAPc composite (high mag.)

Figure 6.3 shows the UV-vis spectra comparing GO, NiTAPc, and GO/NiTAPc composite. There is an absorption peak at around 260 nm on the GO spectrum due to π–π* overlap. NiTAPc showed the characteristic Q band at 730 nm which is due to aggregation and a vibrational Q_{0-0} band at 630 nm, a weak band around 430 nm due to metal–ligand charge transfer transition, and a B band at 310 nm. Upon integration with the GO, there is a significant disappearance of Q-band of NiTAPc at 430 nm and while the B band at 310 nm of NiTAPc has overlapped with the GO peak in GO/NiTAPc composite. This change in the UV-vis spectrum is a clear indication of the interaction between the GO and NiTAPc via strong co-facial aggregation (face-to-face assembly) to form a GO/NiTAPc composite which has led to maximum contact between the NiTAPc molecules.

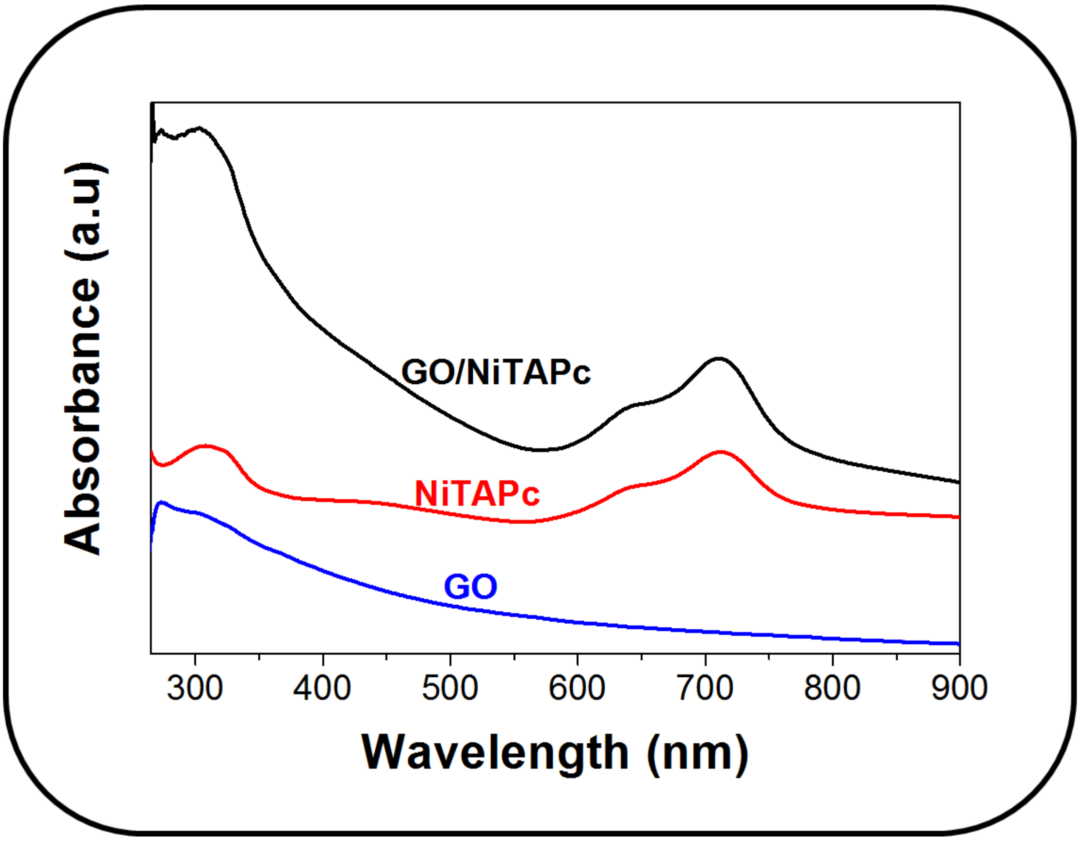

Figure 6.3: UV spectra of GO, NiTAPc, and GO/NiTAPc in DMF.

Figure 6.4 illustrate XRD patterns of GO, NiTAPc, and GO/NiTAPc hybrid. The pattern of GO reveals an intense, sharp peak centred at 2θ = 12.5°, corresponding to the (001) inter-planar spacing of 0.79 nm. Due to its aggregation, NiTAPc exhibits several weak reflections with one at 2θ = 31.8° (0.34 nm), corresponding to the interplanar distance between two adjacent macrocycles and the other one at 2θ = 16.6° (0.62 nm) [19], [20]. Compared with GO and NiTAPc, the XRD pattern of the GO/NiTAPc composite shows a peak at 2θ = 13.7° (0.75 nm), which is lower than that of pristine GO which is an indication of the presence of GO within the composite and a weak peak at 2θ = 31.8° (0.34 nm) is still presence yet its intensity overshadowed due to the interaction of GO with NiTAPc indicating the presence of phthalocyanine macrocycles within the composite.

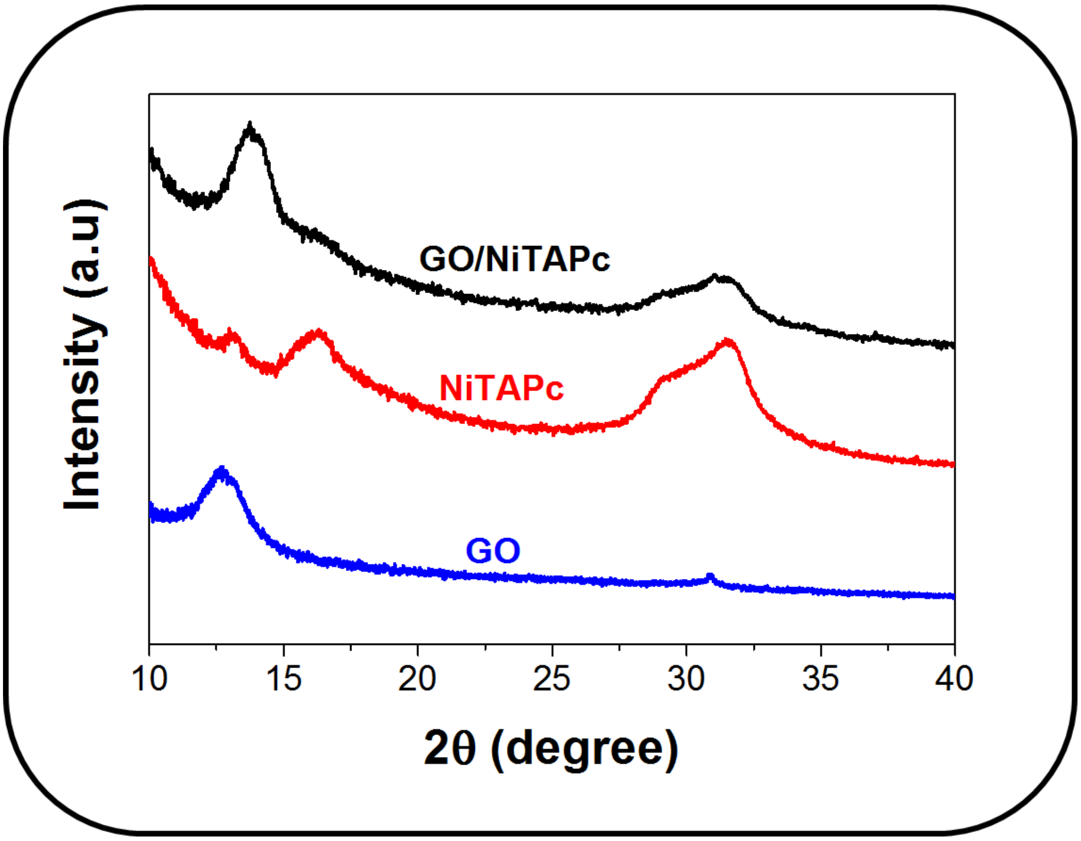

Figure 6.4: XRD patterns of GO, NiTAPc, and GO/NiTAPc composite.

6.2.2 The comparative electrochemical performance of GO/NiTAPc electrode material.

Electrochemical measurements were carried out in two-electrode systems and the ECs device was fabricated in a symmetric-type cell. The electrochemical behavior of the ECs electrodes was investigated by cyclic voltammetry, galvanostatic charge–discharge and electrochemical impedance spectroscopy. Figure 6.5 shows, cyclic voltammograms acquired at the scan rate of 25 mV s^{-1} (Fig. 6.5a), galvanostatic charge-discharge curves acquired at the constant current density of 0.5 A g^{-1} (Fig. 6.5b), comparing GO, NiTAPc and GO/NiTAPc composite-based electrode materials, scan rate studies (Fig. 6.5c) and rate capability studies of the GO/NiTAPc composite (Fig. 6.5d), in 1 M Na_2SO_4 aqueous electrolyte at the potential range of 0 to 0.8 V. CV curve of graphene oxide impregnated with Ni (II) Tetraamine Phthalocyanines (GO/NiTAPc) composite exhibited better quasi-rectangular shape with the largest charge separation, suggesting the highest specific capacitance and also indicating that this hybrid material would be more desired as electrode material for the supercapacitor application as compared to its precursors (GO and/or NiTAPc). The galvanostatic charge/discharge curves of the GO/NiTAPc composite (Fig. 6.5b) displayed good electro-capacitive performance that is in agreement with the results shown from the CV in Fig. 6.5a. Furthermore, the scan rate studies of the GO/NiTAPc composite were performed, and the electrode materials continued to display a stable capacitive performance even at the higher scan rate of 100 mV s^{-1} (see Fig. 6.5c), maintaining the quasi-rectangular shape and high charge separation. The galvanostatic charge/discharge behavior of GO/NiTAPc electrode was further studied at various current densities of 0.5, 1, 2 and 10 A g^{-1} (see Fig. 6.5d). These charge/discharge curves were almost linear (symmetrical), and the isosceles triangles indicated excellent supercapacitor behaviors. The ability of the GO/NiTAPc composite to be cycled at a very high current densities (up to 10 A g^{-1}, Fig. 6.5d), shows that this electrode material it can be suitable for high power energy storage applications. According to the galvanostatic discharge curves, the specific capacitances (C_{sp}), maximum specific energy (E_{sp}) and power (P_{max}) densities can be calculated using equation 2.16 to 2.18 with the internal resistance of the cell calculated using equation 2.19 (see chapter 2)[21].

A symmetric two-electrode device, fabricated with the Ni foam, of GO/NiTAPc composite showed a large specific capacitance (C_{sp}) of 163 F g^{-1} and maximum specific energy density (E_{sp}) of 3.6 Wh kg^{-1}, which were much higher than that of its precursors NiTAPc and GO with specific capacitance (C_{sp}) of 60 F g^{-1} and 15 F g^{-1}, specific energy density (E_{sp}) of 1.3 Wh kg^{-1} and 0.3 Wh kg^{-1}, respectively at the current density of 0.1 A g^{-1} and between the potential range of 0 to 0.8 V in 1 M Na_2SO_4 aqueous electrolyte. The GO/NiTAPc electrode material showed an excellent maximum power density (P_{sp}) of 140.0 kW kg^{-1} at a higher current density of 10 A g^{-1}. A higher specific capacitance of GO/NiTAPc composite could be attributed to the synergic contributions of both the GO and NiTAPc precursors and thus resulting in an improved electrochemical performance of the composite. The galvanostatic charge/discharge behavior of (GO/NiTAPc) electrode was further studied at various current densities of 0.3, 0.5, and 1 A/g. (Fig. 6.5c). These curves with the technique adopted to test the performance of electrochemical capacitor electrodes exhibits charge/discharge curves that have a symmetric nature (approximately isosceles), suggesting the excellent capacitive performance.

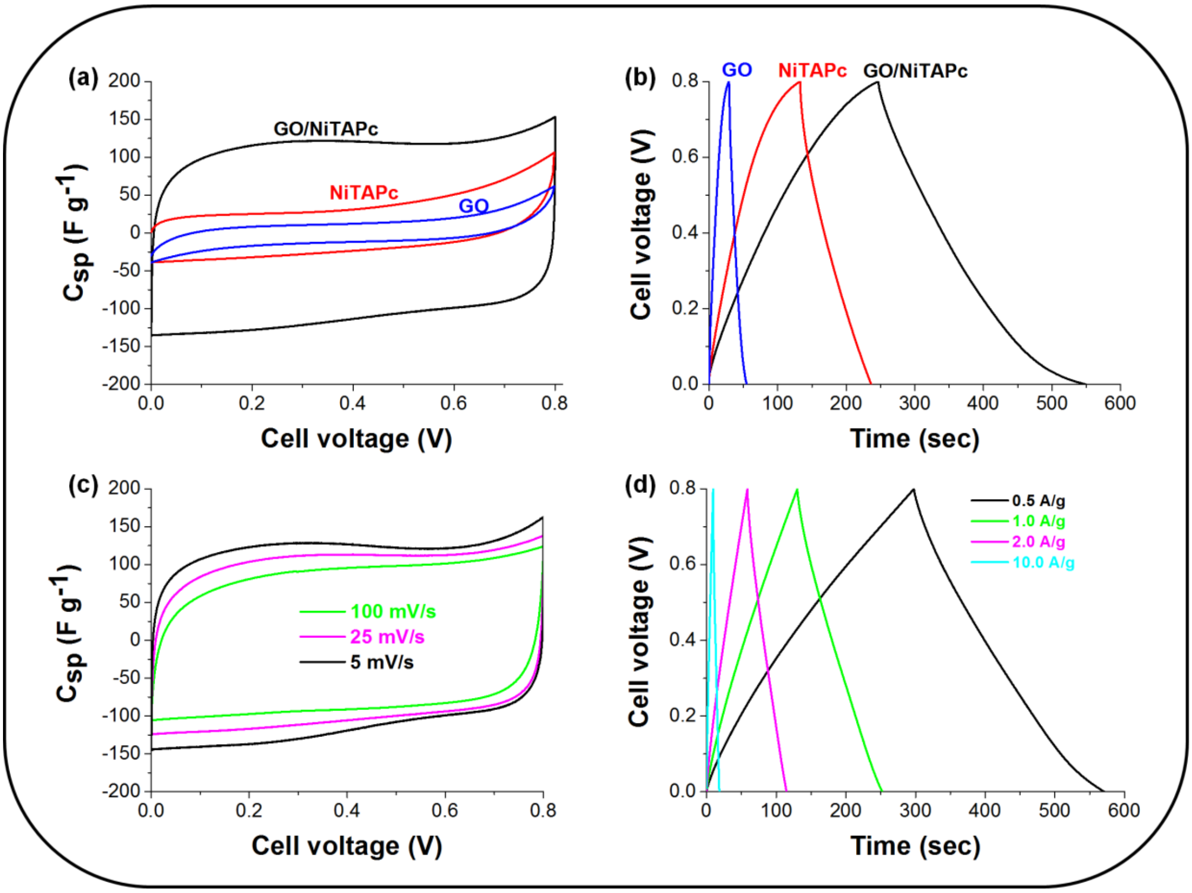

Figure 6.5: Nickel foam based 2-electrode (symmetric) configuration: (a) comparative cyclic voltammograms for GO, NiTAPc and GO/NiTAPc at 5 mV/s, (b) comparative galvanostatic charge-discharge curves for GO, NiTAPc and GO/NiTAPc at 0.5 A g^{-1}, (c) CVs at different scan rates for GO/NiTAPc and, (d) comparative galvanostatic charge-discharge curves for GO/NiTAPc at different current densities. Electrolyte: aqueous 1M Na_2SO_4.

The capacitive performance for the GO/NiTAPc-based symmetric pseudocapacitor cell is compared with other related MPc-based composites from literature. The GO/NiTAPc-based device is characterized by high power compared to related MPc-based complexes and even other Carbon/MnO_2 systems shown in Table 6.1.

Table 6.1: Comparison of capacitive performance of various metallophthalocyanines-based and some carbon/MnO_2-based symmetric (two-electrode) systems.

Aqueous Electrolyte	Electrode material	Device configuration	Voltage window (V)	Specific Capacitance	Specific energy Wh kg^{-1}	Specific power/ kW kg^{-1}	Ref.
1 M Na_2SO_4	GO/NiTAPc	Symmetric	0.8	163 F g^{-1}	3.6	140.0	This work
1 M Na_2SO_4	NiTAPc	Symmetric	0.8	60 F g^{-1}	1.3	-	This work
1 M Na_2SO_4	GO	Symmetric	0.8	15 F g^{-1}	0.3	-	This work
EtOH($C_2HF_3O_2$)	TNFePc	Symmetric	0.8	63 F g^{-1}	-	-	[22]
1 M Na_2SO_4	GO/CoTPyzPz	Asymmetric	1.6	500 F g^{-1}	44.0	31.0	[23]
PVA/H_3PO_4	CNPs/MnO_2	Symmetric	0.8	800 F g^{-1}	4.8	39.0	[24]
1 M Na_2SO_4	GF/MnO_2	Symmetric	1.0	240 F g^{-1}	8.3	20.0	[25]
1 M Na_2SO_4	AC/MnO_2	Symmetric	1.2	49 F g^{-1}	9.7	3.0	[26]

Key: CoTPyzPz = Cobalt (II) Tetrapyrazyl porphyrazine; CNT = Carbon Nanotubes; GF = Graphene foam; GO = Graphene Oxide; CNPs = Carbon nano-particles; TNFePc = Iron Tetranitrophthalocyanine; EtOH = Ethanol solution; $C_2HF_3O_2$ = Trifluoroacetic acid.

EIS is a very powerful tool used to investigate the electrochemical characteristics of the electrode/electrolyte interface using a Nyquist plot, which is a representation of the real and imaginary parts of the impedance in a sample. The Nyquist plots of GO, NiTAPc, and GO/NiTAPc composite are shown in Fig. 6.6a. The intercept in the high frequency region on the x-axis corresponds to the resistance of the electrolyte solution (Rs), and is also referred to as the equivalent series resistance (ESR), which consists of the resistance of the aqueous electrolyte, the intrinsic resistance of the composite material, and the contact resistance at the electrode. The ESR values for the GO, NiTAPc, and GO/NiTAPc electrodes were 1.8, 2.0 and 3.4 respectively, as observed from Fig. 6.6a. It is worth stating that for ideal supercapacitors, the EIS (Nyquist) plot should be a line perpendicular to the real axis at low frequency. However, comparing both samples, the Nyquist plots of GO/NiTAPc composite is much closer to the ideal behavior due to the small charge transfer of GO and NiTAPc, thus indicating a better capacitive behavior. This improved electrochemical performance is due to the synergistic effect between GO and NiTAPc, leading to the improved conductivity of the hybrid and a decrease in the internal resistance of the electrode. It is worth mentioning that, to the best of our knowledge, there is no literature report on the use of GO with NiTAPc to prepare supercapacitor composite of GO/NiTAPc in a two-electrode cell (symmetric cell). This composite material show an excellent power handling ability as is still capable of maintaining almost 50% of its original specific capacitance at the higher current density of 1 A g^{-1} and further exhibit a small drop in specific capacitance as a function of the current density (up to A g^{-1} range), Fig. 6.6b.

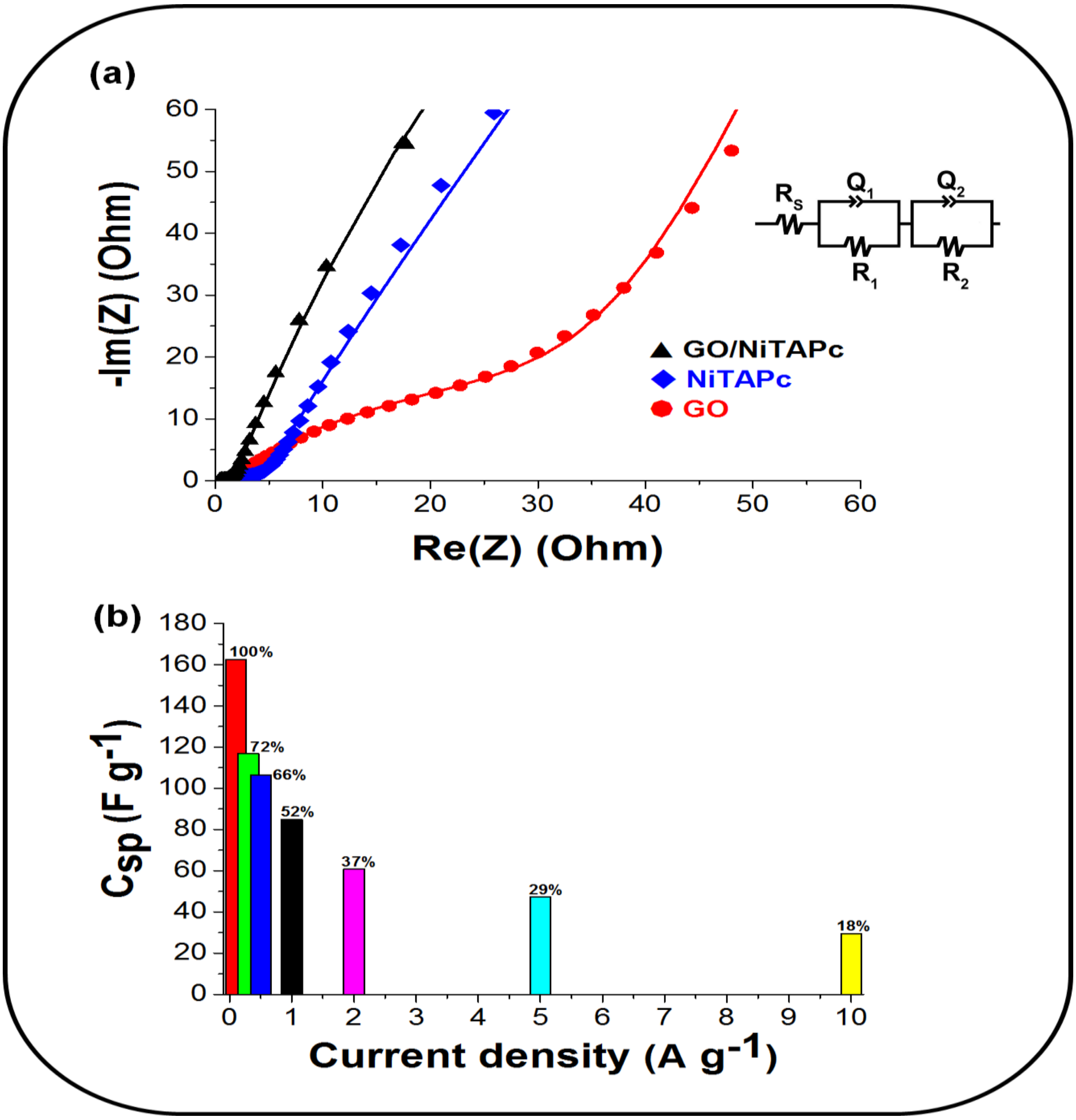

Figure 6.6: (a) Nyquist plot comparing GO, NiTAPc, and GO/NiTAPc symmetric pseudocapacitor, and (b) plot of specific capacitance versus gravimetric currents for the GO/NiTAPc composite. All data were acquired from nickel-foam-based symmetric cells of the electrode materials in 1M Na_2SO_4 aqueous solutions.

For clearer insights into the capacitive behaviour of the devices, the EIS data were fitted with the electrical equivalent circuit (EEC) which comprise Voigt RC elements (Fig. 6C inset), involving a series resistance (R_s), charge-transfer resistance (R_{ct}) and constant phase elements (CPE or Q). From Table 6.2, the R_s of the GO/NiTAPc (~ 0.31 Ohm) are lower than that of the NiTAPc (~ 3.02 Ohm) and GO (~ 2.03 Ohm). Also, the R_{ct} value of the GO/NiTAPc (~ 1.17 Ohm) is lower than that of the NiTAPc (~ 5.15 Ohm) and GO (~ 12.29 Ohm). These results further suggest that the GO component serves to reduce the internal resistance of the NiTAPc, thereby improving the conductivity and capacitance of the GO/NiTAPc-based symmetric pseudocapacitor. The impedance of CPE is given by the equation 6.1 [27]:

$$Z_{CPE} = \frac{1}{[Q(jw)^{n}]} \tag{6.1}$$

where Q represents the frequency-independent constant that describes the electroactive properties of the surface-confined species, w describes the radial frequency, n is obtained from the slope of log Z versus log f (with values in the $-1 \le n \le 1$ range). Note that when n = 0, the CPE describes a pure resistor; when n = 1, CPE describes a pure capacitor, when n = –1, CPE describes an inductor; and when n = 0.5, the CPE describes a Warburg impedance (Z_w) due to the diffusion of the ions. The n values observed for these electrodes are > 0.7, explicitly confirming a porous electrode with pseudocapacitive behaviour, corroborating the CV data of Fig. 6.5a.

Table 6.2: Comparative fitting parameters for the EIS data of the GO, NiTAPc and GO/NiTAPc using the Voigt equivalent circuit.

Parameter	**GO**	**NiTAPc**	**GO/NiTAPc**
R_s / Ω	2.03± 0.56	3.02± 0.51	0.31± 0.28
Q_1 / μF.s$^{(\alpha-1)}$	0.11± 0.53	0.12± 0.25	0.70± 0.26
n_1	0.70± 0.13	0.71± 0.16	0.78± 0.17
R_{ct1} / Ω	12.29± 1.41	5.15± 0.12	1.17± 0.23
Q_2 / mF.s$^{(\alpha-1)}$	6.07± 0.38	1.29± 0.22	3.48± 0.66
n_2	0.80± 0.17	0.80± 0.18	0.88± 0.27
R_{ct2} / Ω	14.86± 1.68	3.78± 0.64	6.51± 0.83

Cycling stability test of the GO/NiTAPc-based symmetric pseudocapacitor was first examined by using the conventional long-term repetitive cycling. As shown in Fig. 6.7, the symmetric pseudocapacitor showed excellent stability upon 1000 continuous cycling at the current density of 1 A g^{-1}, with *ca.* 100% of the initial capacitance retention (see Fig. 6.7). The efficiency of the delivered energy (η / %) was obtained from equation (6.1)

$$\eta(\%) = \frac{t_d}{t_c} \text{ x } 100 \tag{6.1}$$

where t_d is the discharge time and t_c the charge time.

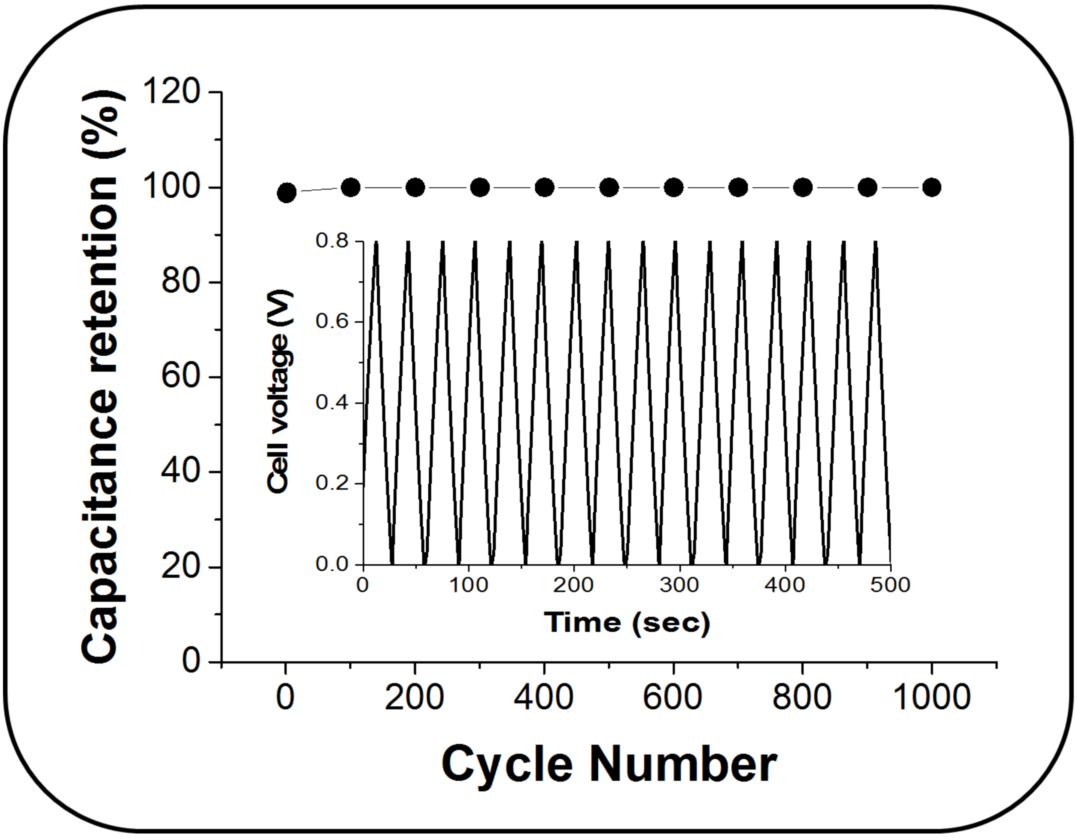

Figure 6.7: Stability test of GO/NiTAPc composite at the current density of 1 A g^{-1}. All data were acquired from nickel-foam-based symmetric cells of the electrode materials in 1M Na_2SO_4 aqueous solutions.

Further stability test of the GO/NiTAPc-based symmetric pseudocapacitor was evaluated using the voltage-holding experiments conducted at 1 A g^{-1} for 50 h (Fig. 6.8a), to complement the traditional long-term cycling analysis. Figs. 6.8b and c show the Nyquist plot and Bode plots, respectively, obtained before and after voltage-holding. The fitted impedimetric parameters are given in Table 6.3. There are no significant differences in the R_s and R_{ct} values before and after 50 h voltage-holding experiments, indicating insignificant loss of power or loss of contact between the GO and NiTAPc or the current collector after long-hour cycling. The superior cycling stability of the GO/NiTAPc nanocomposite is an indication that the pseudocapacitor can quickly undergo charge-discharge cycles with no significant decay in efficiency. The Ragone plot (Fig. 6.8d) is consistent with the expectation at different current densities, with maximum energy and power at 3.6 Wh kg^{-1} and 140 kW kg^{-1}, respectively. The enhanced electrochemical performance of this GO/NiTAPc-based symmetric pseudocapacitor may be ascribed to the efficient distribution and integration of the NiTAPc particles within the GO sheets thus acting as fillers and inhibiting the GO sheets π-π restacking and also resulting in excellent contact between the two materials which allows better conductivity (ionic mobility). The electrochemical cycling stability shows that GO/NiTAPc nanocomposite can undergo continuously charge-discharge without significant decay in power generation efficiency. The results observed under this test are in good agreement with those shown by cycling experiments.

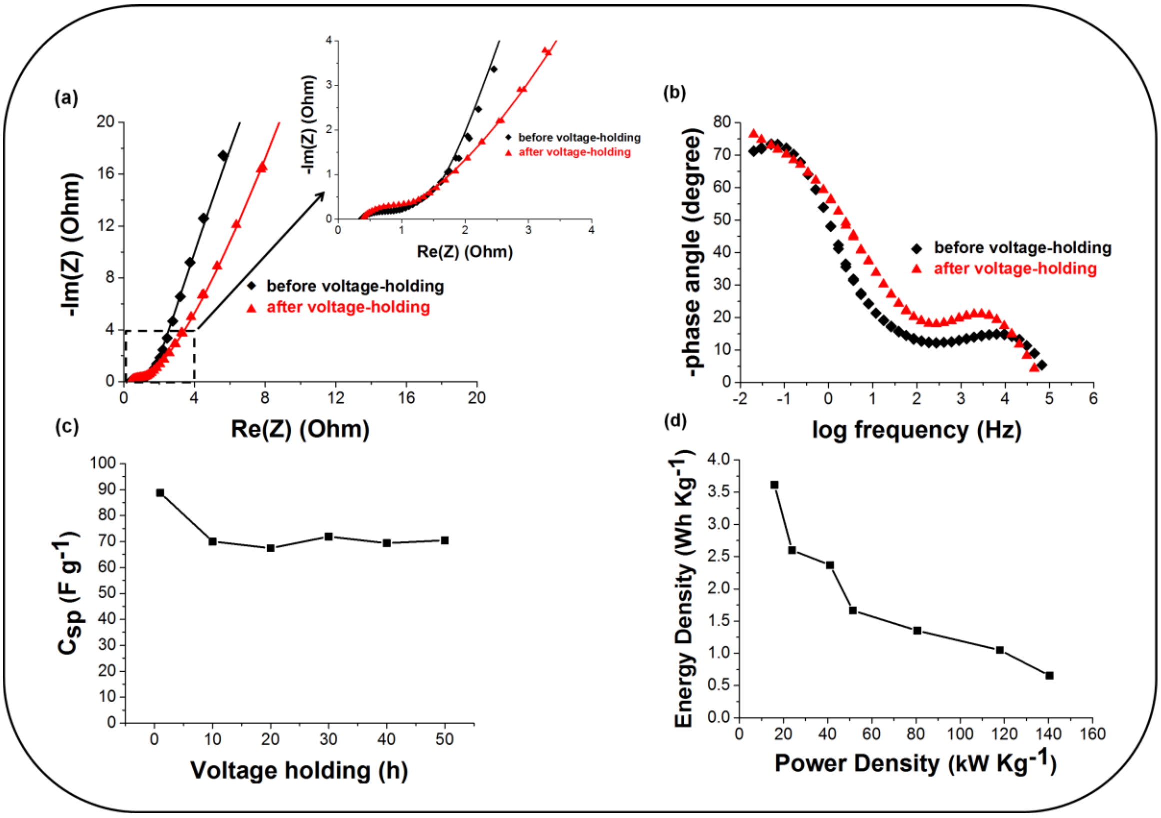

Figure 6.8: Nyquist (a) and Bode (b) plots obtained before and after the 50-h voltage-holding tests, (c) 50 h voltage holding experiments at 0.8 V cell voltage and (d) Ragone plot indicating energy vs. power density, for the GO/NiTAPc symmetric pseudocapacitor.

Table 6.3: Comparative fitting parameters of the EIS data of the GO/NiTAPc-based symmetric pseudocapacitor obtained before and immediately after the 50-h voltage-holding tests. The Voigt electrical equivalent circuit was used in the fitting (see inset, Fig. 6a).

Parameter	GO/NiTAPc-based symmetric Pseudocapacitor	
	Before 50 h **voltage-holding**	**After** 50 h **voltage-holding**
R_s / Ω	0.31± 0.28	0.42± 0.83
Q_1 / μF.s$^{(\alpha-1)}$	0.70± 0.26	0.35± 0.17
n_1	0.78± 0.17	0.80± 0.24
R_{ct1} / Ω	1.17± 0.23	1.55± 0.27
Q_2 / mF.s$^{(\alpha-1)}$	3.48± 0.66	1.72± 0.58
n_2	0.88± 0.27	0.48± 0.26
R_{ct2} / Ω	6.51± 0.83	2.09± 0.27

6.3 Conclusion

This work investigated the electrochemical performance of graphene oxide decorated with particles of nickel (II) tetraaminophthalocyanine (GO/NiTAPc) when used as a symmetrical pseudocapacitor device. The device gave an excellent electrochemical performance with a specific capacitance of (C_{sp}) of 163 F g^{-1} and specific energy density (E_{sp}) of 3.6 Wh kg^{-1}, capacity retention upon long-hour voltage-holding (50h) and long cycling (1000 cycles). The use of GO/NiTAPc composite material exhibits the abilities of MPc's for the development of green and low-cost energy storage devices since they have already found their footing in various applications. The results also show that it is possible to overcome the main limitations of GO while exploiting its main advantages for the development of energy storage devices.

References

[1] K. S. Novoselov, A. K. Geim, S. Morozov, D. Jiang, Y. Zhang, S. Dubonos, I. Grigorieva, and A. Firsov, "Electric field effect in atomically thin carbon films.," *Science*, vol. 306, no. 5696, pp. 666–9, Oct. 2004.

[2] M. D. Stoller, S. Park, Y. Zhu, J. An, and R. S. Ruoff, "Graphene-based ultracapacitors.," *Nano Lett.*, vol. 8, no. 10, pp. 3498–502, Oct. 2008.

[3] Y. Sun, Q. Wu, and G. Shi, "Graphene based new energy materials," *Energy Environ. Sci.*, vol. 4, no. 4, p. 1113, 2011.

[4] C. Liu, Z. Yu, D. Neff, A. Zhamu, and B. Z. Jang, "Graphene-Based Supercapacitor with an Ultrahigh Energy Density.," *Nano Lett.*, pp. 4863–4868, Nov. 2010.

[5] D. Hulicova-Jurcakova, M. Kodama, S. Shiraishi, H. Hatori, Z. H. Zhu, and G. Q. Lu, "Nitrogen-Enriched Nonporous Carbon Electrodes with Extraordinary Supercapacitance," *Adv. Funct. Mater.*, vol. 19, no. 11, pp. 1800–1809, Jun. 2009.

[6] B. Xu, S. Yue, Z. Sui, X. Zhang, S. Hou, G. Cao, and Y. Yang, "What is the choice for supercapacitors: graphene or graphene oxide?," *Energy Environ. Sci.*, vol. 4, no. 8, p. 2826, 2011.

[7] William S. Hummers and Richard E. Offerman, "Preparation of Graphitic Oxide," *J. Am. Chem. Soc.*, vol. 80, pp. 1339–1440, 1957.

[8] S. Stankovich, D. a. Dikin, R. D. Piner, K. a. Kohlhaas, A. Kleinhammes, Y. Jia, Y. Wu, S. T. Nguyen, and R. S. Ruoff, "Synthesis of graphene-based nanosheets via chemical reduction of exfoliated graphite oxide," *Carbon N. Y.*, vol. 45, no. 7, pp.

1558–1565, Jun. 2007.

[9] M. M. Hantel, T. Kaspar, R. Nesper, a. Wokaun, and R. Kötz, "Partially reduced graphite oxide for supercapacitor electrodes: Effect of graphene layer spacing and huge specific capacitance," *Electrochem. commun.*, vol. 13, no. 1, pp. 90–92, Jan. 2011.

[10] L. L. Zhang and X. S. Zhao, "Carbon-based materials as supercapacitor electrodes.," *Chem. Soc. Rev.*, vol. 38, no. 9, pp. 2520–31, Sep. 2009.

[11] P. Simon and Y. Gogotsi, "Materials for electrochemical capacitors.," *Nat. Mater.*, vol. 7, no. 11, pp. 845–854, Nov. 2008.

[12] F. Bedioui, S. Griveau, T. Nyokong, a J. Appleby, C. a Caro, M. Gulppi, G. Ochoa, and J. H. Zagal, "Tuning the redox properties of metalloporphyrin- and metallophthalocyanine-based molecular electrodes for the highest electrocatalytic activity in the oxidation of thiols.," *Phys. Chem. Chem. Phys.*, vol. 9, no. 26, pp. 3383–96, Jul. 2007.

[13] T. Higuchi, T. Murayama, E. Itoh, and K. Miyairi, "Electrical properties of phthalocyanine based field effect transistors prepared on various gate oxides," *Thin Solid Films*, vol. 499, no. 1–2, pp. 374–379, Mar. 2006.

[14] B. O. Agboola, J. Pillay, K. Makgopa, and K. I. Ozoemena, "Electrochemical Characterization of Mixed Self-Assembled Films of Water-Soluble Single-Walled Carbon Nanotube-Poly(m-aminobenzene sulfonic acid) and Iron(II) Tetrasulfophthalocyanine," *J. Electrochem. Soc.*, vol. 157, no. 11, p. F159, 2010.

[15] K. I. Ozoemena, D. Nkosi, and J. Pillay, "Influence of solution pH on the electron

transport of the self-assembled nanoarrays of single-walled carbon nanotube-cobalt tetra-aminophthalocyanine on gold electrodes: Electrocatalytic detection of epinephrine," *Electrochim. Acta*, vol. 53, no. 6, pp. 2844–2851, Feb. 2008.

[16] B. Agboola, K. I. Ozoemena, and T. Nyokong, "Comparative efficiency of immobilized non-transition metal phthalocyanine photosensitizers for the visible light transformation of chlorophenols," *J. Mol. Catal. A Chem.*, vol. 248, no. 1–2, pp. 84–92, Apr. 2006.

[17] A. T. Chidembo and K. I. Ozoemena , "Electrochemical Capacitive Behaviour of Multiwalled Carbon Nanotubes Modified with Electropolymeric Films of Nickel Tetraaminophthalocyanine," *Electroanalysis*, vol. 22, no. 21, pp. 2529–2535, Nov. 2010.

[18] A. T. Chidembo, K. I. Ozoemena, B. O. Agboola, V. Gupta, G. G. Wildgoose, and R. G. Compton, "Nickel(ii) tetra-aminophthalocyanine modified MWCNTs as potential nanocomposite materials for the development of supercapacitors," *Energy Environ. Sci.*, vol. 3, no. 2, p. 228, 2010.

[19] X. Zhang, Y. Feng, S. Tang, and W. Feng, "Preparation of a graphene oxide–phthalocyanine hybrid through strong π–π interactions," *Carbon N. Y.*, vol. 48, no. 1, pp. 211–216, Jan. 2010.

[20] J. Mu, C. Shao, Z. Guo, M. Zhang, Z. Zhang, P. Zhang, B. Chen, and Y. Liu, "Solvothermal synthesis and electrochemical properties of 3D flower-like iron phthalocyanine hierarchical nanostructure," *Nanoscale*, vol. 3, no. 12, p. 5126, 2011.

[21] F. Béguin, V. Presser, A. Balducci, and E. Frackowiak, "Carbons and electrolytes for advanced supercapacitors.," *Adv. Mater.*, vol. 26, no. 14, pp. 2219–51, 2283, Apr. 2014.

[22] J. Mu, C. Shao, Z. Guo, M. Zhang, Z. Zhang, P. Zhang, B. Chen, and Y. Liu, "Solvothermal synthesis and electrochemical properties of 3D flower-like iron phthalocyanine hierarchical nanostructure," *Nanoscale*, vol. 3, no. 12, p. 5126, 2011.

[23] J. N. Lekitima, K. I. Ozoemena, C. J. Jafta, N. Kobayashi, Y. Song, D. Tong, S. Chen, and M. Oyama, "High-performance aqueous asymmetric electrochemical capacitors based on graphene oxide/cobalt(ii)-tetrapyrazinoporphyrazine hybrids," *J. Mater. Chem. A*, vol. 1, no. 8, p. 2821, 2013.

[24] L. Yuan, X.-H. Lu, X. Xiao, T. Zhai, J. Dai, F. Zhang, B. Hu, X. Wang, L. Gong, J. Chen, C. Hu, Y. Tong, J. Zhou, and Z. L. Wang, "Flexible Solid-State Supercapacitors Based on Carbon Nanoparticles/MnO2 Nanorods Hybrid Structure.," *ACS Nano*, vol. 6, no. 1, pp. 656–661, 2012.

[25] A. Bello, O. O. Fashedemi, J. N. Lekitima, M. Fabiane, D. Dodoo-Arhin, K. I. Ozoemena, Y. Gogotsi, A. T. Charlie Johnson, and N. Manyala, "High-performance symmetric electrochemical capacitor based on graphene foam and nanostructured manganese oxide," *AIP Adv.*, vol. 3, pp. 0–9, 2013.

[26] X. Zhang, X. Sun, H. Zhang, D. Zhang, and Y. Ma, "Development of redox deposition of birnessite-type MnO2 on activated carbon as high-performance electrode for hybrid supercapacitors," *Mater. Chem. Phys.*, vol. 137, no. 1, pp. 290–296, Nov. 2012.

[27] M. E. Orazem, J.-B. Jorcin, N. Pébère, and B. Tribollet, "CPE analysis by local electrochemical impedance spectroscopy," *Electrochim. Acta*, vol. 51, no. 8, pp. 1473–1479, 2006.

Chapter 7: General Conclusion and Recommendations

7.1 Concluding Remarks

The performance of the ECs electrode materials and their practicality dependent on two factors: (1) their engineering that is cost effective yet without compromising the electrochemical performance, (2) method of fabrication that increases substrate-electrode contact for an improved mobility of ions. In this study, some of the aspects revolving around the key points above have been considered. This thesis investigated the electrochemical capacitive properties of carbon nanomaterials integrated with nanostructured birnessite-type MnO_2 (Carbon/MnO_2) and tetragonal hausmannite-type Mn_3O_4 (Carbon/Mn_3O_4) as electrode materials for enhanced performance in symmetric pseudocapacitors. This work further explores the synergistic effect of graphene oxide decorated with particles of nickel (II) tetraaminophthalocyanine (GO/NiTAPc composite) as electrode materials for improved performance (power and energy densities) in symmetrical pseudocapacitor device. The physical properties of the synthesised energy storage materials were investigated using scanning electron microscopy (SEM), transmission electron microscopy (TEM), energy dispersive X-ray spectroscopy (EDX), X-ray powder diffraction (XRD), X-ray photoelectron spectroscopy (XPS), gas adsorption technique (i.e BET), infra-red spectroscopy, Raman spectroscopy and thermogravimetric analysis (TGA) techniques while the electrochemical properties were investigated using cyclic voltammetry (CV), galvanostatic charge-discharge (GCD) and electrochemical impedance spectroscopy (EIS). From the study of carbon nanomaterials integrated with nanostructured birnessite-type MnO_2, it has been discovered that OLC/MnO_2 nanohybrid exhibited better performance (regarding specific capacitance, rate capability, and energy density) compared to other nanohybrids such as CNT/MnO_2, GO/MnO_2, and AC/MnO_2. This device gave maximum specific capacitance of 255 F g^{-1}, the specific energy density of 5.6 Wh kg^{-1} and excellent power density of 74.8 kW kg^{-1}. The CNT/MnO_2, exhibited a maximum specific capacitance, energy and power density of 174 F g^{-1}, 4.9 Wh kg^{-1}, and 55.1 kW kg^{-1}, respectively. The stated values of CNT/MnO_2 are closely related to those obtained from OLC/MnO_2. The GO/MnO_2 displayed 135 F g^{-1}, 3.9 Wh kg^{-1}, and 35.8 kW kg^{-1}, and AC/MnO_2 was 110 F g^{-1}, 3.3 Wh kg^{-1}, and 30.0 kW kg^{-1}, respectively. The carbon nanomaterials integrated with nanostructured tetragonal hausmannite-type Mn_3O_4, OLC/Mn_3O_4 nanohybrid exhibited better performance compared to other Mn_3O_4 nanohybrid electrode materials (i.e., CNT/Mn_3O_4 GO/Mn_3O_4, and AC/Mn_3O_4). This device exhibited a maximum specific capacitance of 195 F g^{-1}, the specific energy density of 4.3 Wh kg^{-1} and power density of 52 kW kg^{-1}. The CNT/Mn_3O_4 exhibited a maximum specific capacitance, energy and power density of was 180 F g^{-1}, 3.9 Wh kg^{-1}, and 33 kW kg^{-1}, respectively. While the GO/Mn_3O_4 displayed values of 160 F g^{-1}, 3.6 Wh kg^{-1}, 24 kW kg^{-1} and AC/Mn_3O_4 was 124 F g^{-1}, 2.8 Wh kg^{-1}, 18 kW kg^{-1}, respectively. The synergistic effect of graphene oxide (GO) decorated with particles of nickel (II) tetraaminophthalocyanine (NiTAPc) resulted in GO/NiTAPc nanohybrid displaying better pseudocapacitive performance relative to its precursor (i.e., GO and NiTAPc). This pseudocapacitor device exhibited a maximum specific capacitance of 163 F g^{-1}, the specific energy density of 3.6 Wh kg^{-1} and high-power density of 140 kW kg^{-1}. These values are much higher than those of its individual precursors NiTAPc (60 F g^{-1} and 1.3 Wh kg^{-1}) and GO (15 F g^{-1} and 0.3 Wh kg^{-1}). These symmetric pseudocapacitor device displayed better stability with good capacitance retention upon long-hour voltage-holding (50h) and long cycling (1000 cycles).

In summary, the properties of MnO_2 and Mn_3O_4 can be improved by the use of highly graphitized carbon source that also possess conductivity that is relatively greater than that of MnO_2 for better performance of MnO_2-based ECs electrode material.

Metallophthallocyanines can also be used as energy storage materials for the application in electrochemical capacitors. The synergistic effect of GO and NiTAPc brings an improved performance in a symmetric cell-type configuration. This excellent capacitive performance shows promising opportunities for the development of aqueous-based pseudocapacitors made of carbon nanomaterials with transitional metal oxides and metallophthalocyanine (MPc) complexes (N4-macrocyclic metal compounds).

7.2 Recommendations for Further Research

Further research is necessary for the future to explore the pseudocapacitive behaviour of these investigated electrode materials with a view of improving their properties fully. Such futures studies should include the following:

- Investigation of the carbon/birnessite MnO_2 and carbon/hausmannite Mn_3O_4 using the full-cell asymmetric device for increasing the voltage window, as this is the characteristic that directly influences the energy density of the ECs device.
- Investigation of the GO/NiTAPc composites using the full-cell asymmetric device for increasing the voltage window, as this is the characteristic that directly influences the energy density of the ECs device.
- Exploring the suitability of these electrodes materials in the different electrolytes, such as ionic liquid, organic and non-neutral aqueous. This will be important considering that the findings of this work showed excellent electrochemical performance in aqueous electrolyte.
- There is a need to explore other synthetic routes to make manganese-based electrodes with fine-tuned electrochemical properties (i.e., use of surfactants to eliminates agglomeration and aggregation of metal oxide and metal phthalcyanines.
- Other transition metal oxides (i.e., Co, Ni, Fe, W, V) incorporated on various carbon supports and the ternary composites should be designed for the energy storage applications.
- There is a need to explore other MPc-based electrodes (i.e., CoPc, FePc, NiPc) incorporated on various carbon supports and the ternary composites should be designed for the energy storage applications.

- The use of other different conducting substrates other than Nickel foam to understand the role of a current collector towards the improvement of the electrochemical capacitive performance.

Appendix A

List of Publications Arising from this Thesis

1. **K. Makgopa**, P.M. Ejikeme, C.J. Jafta, K. Raju, M. Zeiger,V. Presser, and K.I. Ozoemena, "High-rate aqueous symmetric pseudocapacitor based on highly graphitized onion-like carbon/Birnessite-type manganese oxide nanohybrids", *Journal of Material Chemistry A*, **3** (2015) 3480–3490,
2. **K. Makgopa**, P.M. Ejikeme, and K.I. Ozoemena, "Graphene oxide-modified nickel (II) tetra-aminophthalocyanine nanocomposites for high-power symmetric pseudocapacitor", *Electrochimica Acta*, (**Accepted**)
3. **K. Makgopa**, P.M. Ejikeme and K.I. Ozoemena, "Effects of highly graphitized onion-like carbon/hausmannite-type manganese oxide (OLC/Mn_3O_4) nanohybrid on symmetric pseudocapacitor", *RSC Advances*, (**Submitted**)
4. **K. Makgopa**, P.M. Ejikeme and K.I. Ozoemena, (2015). Nanostructured manganese oxides in Supercapacitors. In: Nanomaterials in Advanced Batteries and Supercapacitors. K.I. Ozoemena & S. Chen Eds., Springer Publishers, USA. **In Press.**

Appendix B

Conference Presentations Arising from this Thesis

1. **K. Makgopa**, and K.I. Ozoemena, "Electrochemical investigation of symmetric pseudocapacitor based on highly graphitized onion-like carbon/birnessite-type manganese oxide nanohybrids with high rate capability" SACI Young Chemist Symposium, UNISA, Florida, SOUTH AFRICA, November 27, 2015 (ORAL).
2. **K. Makgopa**, and K.I. Ozoemena, "Electrochemical Properties of Graphene Oxide/Manganese Oxide Nanocomposites for Electrochemical Capacitors" 13th Topical Meeting of the ISE, International Conference Centre, CSIR, Pretoria, SOUTH AFRICA, April 07-11, 2013 (ORAL).
3. **K. Makgopa**, and K.I. Ozoemena, "Electrochemical Properties of Graphene Oxide/Manganese Oxide Nanocomposites for Electrochemical Capacitors" 13th Topical Meeting of the ISE, International Conference Centre, CSIR, Pretoria, SOUTH AFRICA, April 07-11, 2013 (ORAL).
4. **K. Makgopa**, and K.I. Ozoemena, "Electrochemical Properties of Graphene Oxide/Manganese Oxide Nanocomposites for Electrochemical Capacitors" 12th International Chemistry Conference Africa, University of Pretoria, Pretoria, SOUTH AFRICA, July 08-12, 2013 (ORAL).
5. **K. Makgopa**, and K.I. Ozoemena, "Supercapacitive properties of nickel oxide (NiO) integrated with nickel (II) tetra- aminophthalocyanine (NiTAPc)" 2nd International Symposium on Electrochemistry, Electrochemistry for Energy, University of the Western Cape, Cape Town, SOUTH AFRICA, July 19-20, 2012 (ORAL).